



HAL
open science

All-dielectric nonlinear nanophotonics

Valerio Flavio Gili

► **To cite this version:**

Valerio Flavio Gili. All-dielectric nonlinear nanophotonics. Material chemistry. Université Sorbonne Paris Cité, 2018. English. NNT : 2018USPCD012 . tel-02329466

HAL Id: tel-02329466

<https://theses.hal.science/tel-02329466>

Submitted on 23 Oct 2019

HAL is a multi-disciplinary open access archive for the deposit and dissemination of scientific research documents, whether they are published or not. The documents may come from teaching and research institutions in France or abroad, or from public or private research centers.

L'archive ouverte pluridisciplinaire **HAL**, est destinée au dépôt et à la diffusion de documents scientifiques de niveau recherche, publiés ou non, émanant des établissements d'enseignement et de recherche français ou étrangers, des laboratoires publics ou privés.



Galilée
Ecole doctorale



UNIVERSITÉS PARIS DIDEROT & PARIS 13
SORBONNE PARIS CITÉ

ÉCOLE DOCTORALE : INSTITUT GALILÉE
LABORATOIRE MATÉRIAUX ET PHÉNOMÈNES
QUANTIQUES

Doctorat en sciences des matériaux
Valerio Flavio Gili

All-dielectric nonlinear nanophotonics

soutenu publiquement le 7 novembre 2018 devant la
commission d'examen composée de:

Azzedine BOUDRIOUA,	Examineur
Alberto BRAMATI,	Rapporteur
Raffaele COLOMBELLI,	Examineur
Costantino DE ANGELIS,	Invité
Aloyse DEGIRON,	Examineur
Alexandre DELGA,	Examineur
Andrei KANAEV,	Codirecteur de thèse
Giuseppe LEO,	Directeur de thèse
Thomas PERTSCH,	Rapporteur

NANOPHOTONIQUE NONLINÉAIRE TOUT DIÉLECTRIQUE

La méta-optique non linéaire tout diélectrique suscite un vif intérêt, grâce à la faisabilité de nanostructures à contraste élevé et indice de réfraction disponible avec la lithographie à semi-conducteurs. Alors que des effets non-linéaires au troisième ordre ont été rapportés dans les nanoantennes silicium sur isolant, la plate-forme AlGaAs-sur-isolant a récemment permis la démonstration de la génération de la seconde harmonique, dû à la non-centrosymétrie de ce matériel. Cette thèse illustre notre activité récente sur les nanoantennes non linéaires AlGaAs-sur-AlOx, où AlOx est obtenu par attaque chimique sélective par voie humide d'une couche épitaxiale d'AlGaAs riche en aluminium d'une épaisseur de quelques micromètres. Un tel substrat à faible indice de réfraction permet de découpler efficacement les modes nanoantenna de la tranche de GaAs (100) sous-jacent. La thèse présente d'abord les méthodes numériques, expérimentales et technologiques utilisées. Une analyse des résultats obtenus dans la génération de signaux non linéaires dans des nanoantennes simples et dans des structures complexes est ensuite présentée. Tous nos résultats expérimentaux ouvrent la voie à la génération et à la manipulation de signaux non linéaires à l'échelle nanométrique et pointent vers des applications telles que l'holographie non linéaire, la goniométrie sans fond et la vision nocturne.

ALL-DIELECTRIC NONLINEAR NANOPHOTONICS

All-dielectric nonlinear meta-optics is attracting a great deal of interest thanks to the feasibility of high refractive-index contrast nanostructures available with semiconductor lithography. While third order nonlinear effects have been reported in silicon-on-insulator nanoantennas, the AlGaAs-on-insulator platform has recently enabled the demonstration of second harmonic generation, owing to the non-centrosymmetry of this material. This PhD thesis illustrates our recent activity on AlGaAs-on-AlOx nonlinear nanoantennas, where AlOx is obtained from selective wet etching of micrometer-thick aluminium-rich AlGaAs epitaxial layer. Such a low refractive index substrate allows to effectively decouple the nanoantenna modes from the underlying GaAs (100) wafer. The thesis first introduces the numerical, experimental and technological methods employed. Afterwards, a review of the results obtained in nonlinear signal generation in single nanoantennas and in complex structures is given. All our experimental results pave the way towards nonlinear signal generation and manipulation at the nanoscale, and point towards applications such as nonlinear holography, background-free goniometry and night vision.

MOTS CLÉS

- Génération de signaux non linéaires
- Plate-forme photonique intégrée
- Meta-surfaces
- Nanoantennes optiques

KEYWORDS

- Nonlinear light generation
- Photonic integrated platform
- Metasurfaces
- Optical nanoantennas

Contents

General introduction	9
1 Elements of nonlinear nano optics	15
1.1 Nonlinear optics	15
1.1.1 Second-order nonlinear processes	16
1.1.2 Third-order nonlinear processes	18
1.1.3 Wave equation in a nonlinear optical medium	19
1.1.4 Phase-matching considerations	21
1.1.5 Phase-matching in sub-wavelength media	22
1.2 Light scattering from a sphere: Mie theory	22
1.3 Elements of Plasmonics	27
1.3.1 Surface Plasmons	27
1.3.2 Second-order nonlinear plasmonics	30
1.3.3 Metals vs dielectrics	31
1.4 Conclusion	33
2 Techniques: numerics, technology and experiments	35
2.1 Numerical calculations	35
2.1.1 Linear scattering calculation in spherical coordinates	36
2.1.2 Cartesian coordinates scattering: the anapole condition	38
2.1.3 Modeling the nonlinear optical response	39
2.2 Fabrication techniques	42
2.2.1 Molecular beam epitaxy	42
2.2.2 Electron beam lithography	43
2.2.3 Electron-beam physical vapour deposition	46
2.2.4 Reactive ion etching	48
2.2.5 Selective oxidation	50
2.3 Experimental methods	54
2.3.1 Confocal optical microscopy	54
2.3.2 Back focal plane imaging	55
2.3.3 Cathodoluminescence spectroscopy	57

2.4	Conclusion	59
3	AlGaAs-on-AlO_x monolithic platform	61
3.1	AlGaAs integrated platform: state-of-the-art	61
3.2	Non-monolithic approaches	62
3.2.1	Epitaxial lift-off	63
3.2.2	Wafer bonding	63
3.3	Monolithic approaches	66
3.4	Monolithic AlGaAs-on-AlO _x platform: fabrication	70
3.4.1	Original fabrication protocol	70
3.4.2	Protocol improvement	76
3.4.3	Impact of dose factor	79
3.4.4	Switch to HSQ	82
3.4.5	AlGaAs-Au hybrid integration	84
3.5	TEM characterization	89
3.5.1	Sample preparation	89
3.5.2	Results and discussion	90
3.6	Conclusion	95
4	Nonlinear response of single AlGaAs nanoantennas	97
4.1	SHG from isolated nanoantennas	97
4.1.1	Numerical modelling	98
4.1.2	Experiments with fixed pump wavelength	100
4.1.3	SHG polarization properties	103
4.1.4	Impact of nonidealities on SH emission properties	106
4.1.5	Experiments with a tunable pump	109
4.2	Nonlinear emission directionality considerations	112
4.3	SH emission shaping through pump reconfiguration	113
4.3.1	Towards nonlinear goniometry at the nanoscale	118
4.4	SH emission shaping through asymmetric diffraction gratings	119
4.4.1	Towards nonlinear background-free holography	124
4.5	Quantum-classical correspondence: SFG and SPDC from isolated nanopillars	125
4.5.1	SFG experiments	126
4.5.2	SPDC experiment	129
4.6	Conclusion	133
5	Nonlinear response of advanced AlGaAs nanostructures	135
5.1	Anapole-driven SHG enhancement: from single pillars to dimers	135
5.1.1	Looking for the anapole in the linear scattering properties of a single pillar	136

5.1.2	Looking for the anapole in the linear scattering properties of a dimer	137
5.1.3	Nonlinear modeling and experiments	140
5.2	SHG enhancement in hybrid AlGaAs-Au nanostructures . . .	143
5.3	SFG from a transparent AlGaAs metasurface	150
5.3.1	Setup	150
5.3.2	SFG measurement	153
5.3.3	SFG-based nonlinear imaging	155
5.4	Beyond plane-wave excitation: Cathodoluminescence spectroscopy of AlGaAs single pillars and dimers	157
5.4.1	Results and discussion	158
5.5	Conclusion	164
General conclusion and perspectives		165
List of acronyms		169
List of publications		175
Bibliography		181

General introduction

Immediately after the advent of the first analogue computers, the need for system miniaturization quickly raised following the rapidly increasing occupied space and consumed power. This demand was later satisfied by the emergence of monolithic integrated circuits, culminating in the Complementary Metal-Oxide-Semiconductor (CMOS) technological standard. The complexity evolution of CMOS circuits has followed in the last decades a constant trend, the so-called Moore's law, which predicts a doubling in the number of transistors on a single integrated circuit every two years.

In the last years this trend has reached a point in which chips with a few centimetre size integrate billions of elements [2]. In parallel, a similar tendency towards miniaturization and integration has been characterizing the field of photonics shortly after the demonstration of the first III-V semiconductor laser diode in 1962 [3], which shortly followed the invention of the laser in 1960 [4] and that of the Light-Emitting Diode (LED) in 1955 [5].

Despite the faster technological development of electronic integration, these two approaches coexisted and evolved separately for several decades. Nowadays instead, the paradigm of Photonic integrated circuit (PIC) is gaining more and more attention as a saturation of Moore's Law on electronic circuits has been predicted to happen in the next decade [6], due to the rapidly approaching physical limit of electronic component integration. So far the success of PICs has been tremendous, with the realization of basic building blocks such as light modulators, detectors, low-loss waveguides, couplers, (de)multiplexers, etc. [8].

In this frame, nonlinear optics plays a major role for the full implementation of electronics-inspired photonic elements [1]. For example, light amplification, which can be achieved by exploiting both second and third order nonlinear effects, such as Four-Wave Mixing (FWM), Sum-Frequency Generation (SFG) or Stimulated Raman Scattering, super-continuum light generation, which takes advantage of Self-Phase Modulation, wavelength conversion and demultiplexing, allowed by a large number of three and four wave mixing effects [8]. Moreover, nonlinear optics is starting to expand its do-

main of interest beyond PICs, for example in data storage and sensors [1].

This urge for efficient on-chip nonlinear optical effects caused the choice of an optimal material to remain an open issue for many years. On the one hand we have Silicon, which is already widely employed in large-scale electronic integrated circuits, whose CMOS technology is at a mature stage, allowing for low-cost and reliable fabrication. Moreover the ability to monolithically integrate Silicon structures on a low refractive index substrate in the so called Silicon-On-Insulator (SOI) platform makes it suitable for both scalability and miniaturization [8]. Nonetheless, its indirect bandgap makes it not suitable as a laser material, and its energy of $\sim 1.1\text{eV}$ hinders nonlinear optical effects at telecom wavelengths due to Multi-photon absorption.

Thus so far the application of SOI PICs has been limited to passive functionalities. On the other hand, the III-V periodic table groups offer a wide range of semiconductor alloys, such as Aluminum Gallium Arsenide (AlGaAs), Indium Gallium Arsenide (InGaAs), Indium Phosphide (InP) and so on, which exhibit the required direct bandgap for a laser material, and in some cases the desired properties to achieve efficient second and third order nonlinear optical response at telecom wavelengths, a necessary condition for active photonic components. Despite these advantages, a monolithic III-V semiconductor-on-oxide platform is still lacking. To overcome this limitation, hybrid III-V-on-SOI platforms were successfully demonstrated, despite the burden of the required non-monolithic bonding step, allowing to integrate on the same chip mode-locked lasers and Si passive elements [2].

Throughout this thesis I will present the work that has been done to demonstrate a monolithic AlGaAs-on-oxide platform for nonlinear frequency conversion, enabled by the selective oxidation of an Al-rich AlGaAs layer, which conversely does not significantly affect the relevant structures, patterned on an AlGaAs layer with low Al content [7]. The platform capabilities have been validated in nanoscale structures ($\sim 100\text{nm}$), for illumination wavelengths at $1.55\mu\text{m}$. With this choice we were able to access the Mie theory regime, which is defined by a size parameter $x = l/\lambda \sim 1$.

The interest for probing this particular regime stems on the one hand from the great number of results achieved in the last two decades within the frame of linear and nonlinear plasmonics, in which the interaction between an impinging electromagnetic wave and the free-electron cloud surrounding a metal gives rise to sub-wavelength field confinement [9]. The employment of a dielectric material instead allows to overcome the limitations caused by ohmic losses, as long as operation at energies below the semiconductor bandgap is granted.

The research activity on optical field confinement at the nanoscale has been recently going in tandem with the new emerging paradigms of meta-

surfaces and meta-optics. The idea at the core of these concepts is to exploit sub-wavelength nanostructuring of a host medium to achieve effective optical phenomenon otherwise not found in nature, with pioneering works dated back to twenty years ago demonstrating blazed binary lens [10], vector vortex-beam formation [11] and polarization control [12].

Only recently however did this research area explode after two milestone works showing a high-NA flat meta-lens [13] and optical Huygens surfaces with full transmission-phase coverage and near-unity transmission [14]. Until recently most of these promising results were achieved in linear optics regime.

Combining the frequency conversion allowed by nonlinear materials and the phase/polarization control over the scattered field in linear metasurfaces represents an appealing goal for several research groups [15], with exciting applications such as background-free holography, sensing, night vision and single-photon generation that could have a potential impact in everyday life.

To sum up, this thesis rests on these three fundamental aspects that have been introduced so far: nonlinear optics, photonic integrated platforms, and nanoscale optical regime. My personal doctoral work has been focused on the design, fabrication and characterization of all-dielectric optical nano-resonators for nonlinear frequency conversion.

The demonstration of such objects has been the result of a collaborative work involving several universities within the EU-funded NANOPHI mobility program¹: University of Brescia, King's College London, Aston University, University of Crete, Friedrich-Schiller-Universität Jena, Université Paris Diderot, Sofia University, Massey University, the Australian National University.

In this framework, my personal contribution has been mainly technological and the MPQ lab has provided AlGaAs-on-AlOx samples to all the partners. Moreover, I have taken advantage of the consortium dynamics and top-level competences in three respects:

- I have actively participated in numerous meetings and exchanges, following step-by-step all the developments in theory, numerical modeling and experiments.
- I have reproduced a part of the simulation work, both linear and non-linear, carried out in Brescia by the group of Costantino De Angelis, thus learning the related numerical techniques and design procedures.
- I have spent a semester at ANU, where I have completed my thesis work with an experimental activity in optical measurements, with the

¹<https://en.unibs.it/research/international-research-and-cooperation/nanophi-project>

successful demonstration of SFG-based nonlinear imaging from a transparent AlGaAs metasurface.

The manuscript is divided into five chapters and it is organised in the following way:

- **Chapter 1** provides an introduction to nonlinear processes on the one hand, with a review on second and (some) third order nonlinear phenomena, accompanied by phase-matching considerations. The second part of the chapter is dedicated to nano optics elements, comprising Mie theory for dielectric nano-objects, and plasmonics for metallic ones. The chapter ends with a comparison between these two nanoscale approaches.
- **Chapter 2** introduces the mechanisms underlying the main numerical, technological and experimental tools that enabled the exploration of nonlinear optical mixing effects in all-dielectric nanoscale objects. In particular, the linear and nonlinear Finite-Element Method (FEM) full-vectorial electromagnetic calculations will be presented in the first part, accompanied by multipolar decomposition methods. The second part will describe the main fabrication steps necessary for monolithic integration of AlGaAs-on-AlO_x nanostructures. Finally in the third part, experimental techniques to probe the linear and nonlinear response of fabricated objects will be presented, comprising confocal microscopy and back focal plane imaging for the nonlinear part, and cathodoluminescence spectroscopy for linear characterization.
- **Chapter 3** goes deeper in detail into the fabrication section, first exploring the state-of-the-art on AlGaAs integrated photonic platforms, and then explaining the novelty of our monolithic approach, following step by step the whole optimization process that finally led to our results. This review will be mainly accompanied Scanning Electron Microscope (SEM) and Transmission Electron Microscope (TEM) characterization, which are the main tools allowing to estimate the fabrication quality of nanostructures.
- **Chapter 4** presents the design and experiments carried out on single AlGaAs nanopillars. The chapter starts with the description of Second-Harmonic Generation (SHG), including studies on the emission polarization and the impact of fabrication nonidealities on the observed nonlinear signal. Subsequently, the problem of nonlinear emission control is presented, in tandem with the description of two solutions we

adopted: pump reconfiguration and surrounding the nanoantenna with a diffraction grating. Finally, the observation of two other second-order conversion effects are taken into account, namely Sum-Frequency Generation (SFG) and Spontaneous Parametric Down-conversion (SPDC), linked together by quantum-classical correspondence.

- **Chapter 5** goes beyond $\chi^{(2)}$ nonlinear effects by single nanoantennas and introduces the measurements performed on advanced structures specifically designed to enhance the SHG yield, namely nanodimers and hybrid AlGaAs-Au nanostructures. Subsequently, nonlinear SFG measurements carried out on transparent AlGaAs metasurfaces is described, as well as some preliminary results on SFG-based nonlinear imaging. Finally, Cathodoluminescence (CL) measurements allow to shed brighter light on the modes supported by AlGaAs pillars and dimers.

The order in which all these subjects are presented is not strictly chronological, as most projects tended to overlap in time. For this reason, an organization by thematic area was privileged in the redaction of this thesis. Finally, this thesis will end with a section providing the general conclusions and the perspective of this doctoral work.

This manuscript does not deal with the research activity I performed on Surface Enhanced Raman Scattering (SERS) with prof. Nordin Felidj, and on ultra-porous alumina characterization with Dr. Andrei Kanaev, since the relative weight of nonlinear nanophotonics driven by the NANOPHI project on my overall thesis work turned out to be more relevant.

Chapter 1

Elements of nonlinear nano optics

This chapter is dedicated to outline the theoretical tools necessary to understand the physical processes in the nanostructures considered during my PhD work. First, a general introduction to nonlinear optics will be given, followed by nano optics, with reference to both cases of metals, i.e. plasmonics, and dielectrics, i.e. Mie theory, with particular emphasis on the latter, as it is predominant in this thesis work.

1.1 Nonlinear optics

Although optics has been investigated for millennia, dating back to the ancient Greeks, to whom we owe the origin of the word “optike”, meaning appearance, look, the domain of nonlinear optics has remained unexplored until the demonstration of the first laser in 1960 [4]. Indeed, the most basic nonlinear optical effect, that is SHG, was first observed in 1961 by using this new invention as a source [16]. The reason is that only after laser invention we could reach the high field intensities required to trigger a nonlinear optical response of a material.

The origin of these effects can be understood in the following way: it is well known from conventional electromagnetism that when an electric field is applied to a homogeneous dielectric material it polarizes according to the following law:

$$P_i = \epsilon_0 \sum_j \chi_{ij}^{(1)} E_j \quad (1.1)$$

where $\chi^{(1)}$ is the linear susceptibility tensor, and ϵ_0 is the free-space permittivity. This simple relation however only holds in the case of linear response

of the material. If we allow for a more general super-linear dependence, the induced polarization can be expressed as a Taylor expansion [17, 18] (we neglect dispersion and losses of the medium):

$$P_i = \epsilon_0 \left(\sum_j \chi_{ij}^{(1)} E_j + \sum_{j,k} \chi_{ijk}^{(2)} E_j E_k + \sum_{j,k,l} \chi_{ijkl}^{(3)} E_j E_k E_l + \dots \right) \quad (1.2)$$

where we call $\chi_{ijk}^{(2)}$ and $\chi_{ijkl}^{(3)}$ respectively second and third order nonlinear susceptibilities. To have an idea of the orders of magnitude, assuming $\chi^{(1)} \sim 1$, $\chi^{(2)} \sim 1 \text{ pm}/V$, and $\chi^{(3)} \sim 1 \text{ (pm)}^2/V^2$. For centrosymmetric materials it is easily shown that all even terms in the expansion vanish:

$$-P^{(2n)} = \epsilon_0 \chi^{(2n)} (-E)^{2n} = \epsilon_0 \chi^{(2n)} E^{2n} \implies \chi^{(2n)} \equiv 0 \quad \forall n \quad (1.3)$$

Indeed a change in the sign of the incident field must be accompanied by a change in the polarization sign, implying that even nonlinear susceptibility tensors should be identically 0. An example of such material is silicon.

In this thesis however I will focus my attention on $\chi^{(2)}$ processes, as they are dominant in non-centrosymmetric materials such as Gallium Arsenide. Second order nonlinear processes can be modelled as three-wave interactions, as will be clear in the next subsection.

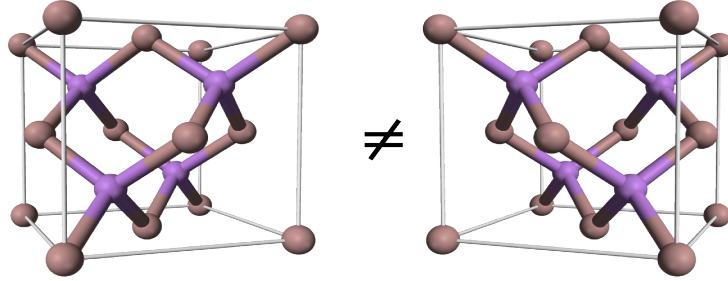


Figure 1: Gallium Arsenide (GaAs) unit cell. This material is non-centrosymmetric, thus enabling second-order nonlinear optical response.

1.1.1 Second-order nonlinear processes

Let us consider as a first approximation a linearly polarized monochromatic plane wave incident field (called pump):

$$E(t) = E_0 e^{-i\omega t} + c.c. \quad (1.4)$$

then the second order polarizability reads

$$P^{(2)}(t) = 2\epsilon_0 \chi^{(2)} E E^* + (\epsilon_0 \chi^{(2)} E^2 e^{-i2\omega t} + c.c.) \quad (1.5)$$

The second term corresponds to SHG, and can be quantum-mechanically understood as the creation of one photon with frequency 2ω by simultaneously annihilating two pump photons with frequency ω (Fig. 2).

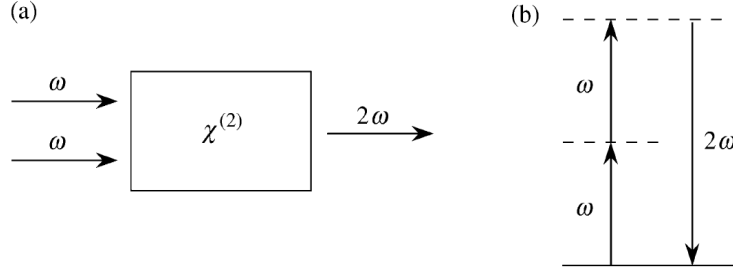


Figure 2: (a) Schematics of Second-Harmonic Generation. (b) Energy level diagram describing the process. It should be noted that the intermediate energy levels correspond to virtual states.

The first term instead refers to the generation of a static field with frequency $\omega - \omega = 0$, called optical rectification, often used to generate terahertz radiation [19]. Let us now allow two pump frequency components instead of a single one:

$$E(t) = E_1 e^{-i\omega_1 t} + E_2 e^{-i\omega_2 t} + c.c. \quad (1.6)$$

we then find a richer second-order nonlinear response:

$$P^{(2)}(t) = 2\epsilon_0 \chi^{(2)} (E_1 E_1^* + E_2 E_2^*) + \epsilon_0 \chi^{(2)} (E_1^2 e^{-i2\omega_1 t} + E_2^2 e^{-i2\omega_2 t} + 2E_1 E_2 e^{-i(\omega_1 + \omega_2)t} + 2E_1 E_2^* e^{-i(\omega_1 - \omega_2)t} + c.c.) \quad (1.7)$$

The first line of the equation describes optical rectification, and the first two terms in the second line refer to SHG from the two pump frequencies. The last two terms are absent in the case of monochromatic pump, and refer to Sum-Frequency Generation (SFG) and Difference-Frequency Generation (DFG), respectively.

One last process to be mentioned is the so-called SPDC, which is the time-reversed process of SFG, thus allowing the generation of two photons with frequency ω_1 and ω_2 starting from a single pump photon at $\omega_1 + \omega_2$ [20]. This SFG-SPDC correspondence is important for our experimental results and will be described in greater detail in the next chapters. SPDC is widely used in quantum optics to generate entangled photon pairs [21]. All $\chi^{(2)}$ processes are summarized in Fig. 3.

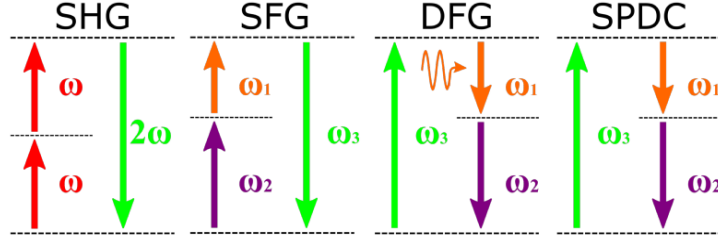


Figure 3: Energy level diagrams of $\chi^{(2)}$ processes.

1.1.2 Third-order nonlinear processes

The third-order response of nonlinear media comprises a large number of effects such as self-focusing, self phase modulation, optical Kerr effect, soliton formation [17, 18]. Here we focus attention on mixing effects, Third-Harmonic Generation (THG) and Four-Wave Mixing (FWM). Let us consider an excitation described by Eq. (4), then the third-order polarizability is

$$P^{(3)}(t) = \epsilon_0 \chi^{(3)} (E_0^3 e^{-i3\omega t} + c.c.) + 3\epsilon_0 \chi^{(3)} (E_0^2 E_0^* e^{-i\omega t} + c.c.) \quad (1.8)$$

The first term describes the THG process, in which a field with frequency 3ω is generated. In complete analogy with SHG, THG can be seen as a particular degenerate case of a broader class of wave-mixing effects, that is FWM. Let us determine the nonlinear response of a $\chi^{(3)}$ medium excited by a superposition of three frequency components:

$$E(t) = E_1 e^{-i\omega_1 t} + E_2 e^{-i\omega_2 t} + E_3 e^{-i\omega_3 t} + c.c. = \sum_{j=\pm 1, \pm 2, \pm 3} E_j e^{-i\omega_j t} \quad (1.9)$$

where $E_{-j} = E_j^*$, and $\omega_{-j} = -\omega_j$. Plugging this expression into $P^{(3)}(t)$ we obtain a sum of $6^3 = 216$ terms which can nonetheless be easily written in terms of a three-indexes sum:

$$P^{(3)}(t) = \epsilon_0 \chi^{(3)} \sum_{j,k,l=\pm 1, \pm 2, \pm 3} E_j E_k E_l e^{-i(\omega_j + \omega_k + \omega_l)t} \quad (1.10)$$

In this way any harmonic component can be obtained by summing the appropriate permutations of j, k, l . Fig. 4 summarizes some possible FWM scenarios, as well as THG.

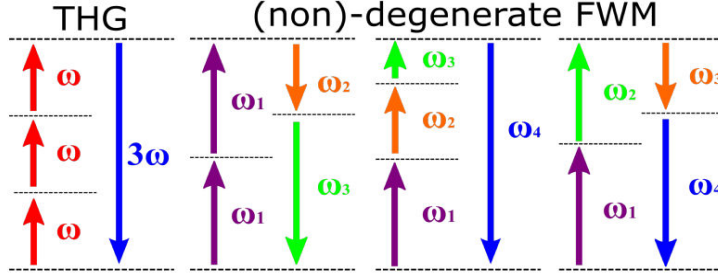


Figure 4: Energy level diagram of $\chi^{(3)}$ processes.

1.1.3 Wave equation in a nonlinear optical medium

So far we have seen that an intense field illuminating a nonlinear medium can give rise to a polarization response comprising new frequency components, according to the properties of the material. These nonlinear polarization frequency components act as a source of new electromagnetic waves.

Therefore, for a more quantitative analysis of second and third order nonlinear processes we need to look at how Maxwell equations describe the frequency mixing in the nonlinear medium and the generation of the nonlinear fields. Let us assume the absence of free charges ($\rho = 0$) and currents ($\mathbf{J} = 0$). Moreover, for simplicity the material is assumed to be non-magnetic ($\mathbf{B} = \mu_0 \mathbf{H}$). The nonlinearity of the medium is expressed by the relation between the displacement and electric fields:

$$\mathbf{D} = \epsilon_0 \mathbf{E} + \mathbf{P} \quad (1.11)$$

where $\mathbf{P} = \mathbf{P}^{(1)} + \mathbf{P}_{NL}$ contains both the linear and the nonlinear polarization response of the medium depending on the intensity of the electric field \mathbf{E} . We can alternatively separate the linear and nonlinear electric displacement contributions as $\mathbf{D} = \mathbf{D}^{(1)} + \mathbf{P}_{NL}$, where $\mathbf{D}^{(1)} = \epsilon_0 \mathbf{E} + \mathbf{P}^{(1)} = \epsilon_0 \epsilon_r \mathbf{E}$. By writing ϵ_r as a real scalar quantity we have implicitly assumed an isotropic and lossless medium as well. Maxwell equations are then given by

$$\nabla \cdot \mathbf{D} = 0 \quad (1.12)$$

$$\nabla \cdot \mathbf{B} = 0 \quad (1.13)$$

$$\nabla \times \mathbf{E} = -\frac{\partial \mathbf{B}}{\partial t} \quad (1.14)$$

$$\nabla \times \mathbf{H} = \frac{\partial \mathbf{D}}{\partial t} \quad (1.15)$$

We then take the curl of the curl of the electric field, change the space and time derivation order on the right side of the equation, and replace it with the curl of the magnetic field. The result of these manipulation is:

$$\nabla \times \nabla \times \mathbf{E} = -\mu_0 \frac{\partial^2 \mathbf{D}}{\partial t^2} \quad (1.16)$$

The left side term can be simplified using the following vector relation:

$$\nabla \times \nabla \times \mathbf{V} = \nabla (\nabla \cdot \mathbf{V}) - \nabla^2 \mathbf{V} \quad (1.17)$$

Under some general assumptions, the divergence term can be neglected even in nonlinear optics where the relation between \mathbf{D} and \mathbf{E} is not trivial [17]. By now using Eqs. 1.11 and 1.17, together with $\mu_0 = 1/\epsilon_0 c^2$, and expliciting the linear and nonlinear polarization components, we can finally write:

$$\left[\nabla^2 - \frac{\epsilon_r}{c^2} \frac{\partial^2}{\partial t^2} \right] \mathbf{E} = \frac{1}{\epsilon_0 c^2} \frac{\partial^2 \mathbf{P}_{NL}}{\partial t^2} \quad (1.18)$$

The form of this equation is that of an inhomogeneous wave where the nonlinear polarization acts as a source. The fields can now be expressed in terms of the linear and nonlinear frequency components:

$$\begin{aligned} \mathbf{E} &= \sum_n \mathbf{E}_n(\mathbf{r}) e^{-i\omega_n t} + c.c. \\ \mathbf{D}^{(1)} &= \sum_n \mathbf{D}_n^{(1)}(\mathbf{r}) e^{-i\omega_n t} + c.c. \\ \mathbf{P}_{NL} &= \sum_n \mathbf{P}_n^{NL}(\mathbf{r}) e^{-i\omega_n t} + c.c. \end{aligned} \quad (1.19)$$

where the summation index n runs over all frequency components present in our system. By substituting the summations in the wave equation, after some manipulation we obtain that each frequency component separately satisfies its own inhomogeneous wave equation:

$$\left[\nabla^2 + \frac{\omega_n^2}{c^2} \epsilon_r(\omega_n) \right] \mathbf{E}_n(\mathbf{r}) = -\frac{\omega_n^2}{\epsilon_0 c^2} \mathbf{P}_n^{NL}(\mathbf{r}) \quad (1.20)$$

here material dispersion is taken into account via the dependence of the relative permittivity on the frequency. The wave equation here derived allows to quantitatively describe the above mentioned nonlinear optical interactions.

1.1.4 Phase-matching considerations

If we solve the nonlinear wave equation, for example in case of SHG, we will find that the nonlinear field will sinusoidally depend on the position along the propagation direction (for example z): $E_{SHG} \sim e^{iz\Delta k}$, where $\Delta k = k_{2\omega} - 2k_\omega$ implying that the nonlinear signal builds up inside the nonlinear medium only for a certain length, and then decreases.

This phenomenon can be understood with the following argument: as the generation of nonlinear light is a local process, it is not trivial in general to achieve macroscopically detectable signals. Indeed, after a certain length called coherence length ($L_c = \Delta k/\pi$), the nonlinear light accumulates a π phase difference with the pump, thus the nonlinear light generated in the next coherence length will be out of phase with respect to the previous one, destructively interfering.

The value of L_c varies upon various parameters including pump wavelength, the nature of the nonlinear process and field confinement in the nonlinear medium. For example, in case of SHG process in GaAs obtained from a $1.55\mu\text{m}$ pump L_c can be as small as a few micrometres [22].

In order to induce constructive interference between the local nonlinear sources throughout the whole crystal it is necessary to match the phase velocity of the pump and that of the nonlinear signal. This results into a relation between k vectors: the so-called phase matching condition. In the case of SHG this reads

$$\Delta k = k_{SH} - k_p - k_p = 0 \quad \Rightarrow \quad k_{SH} = 2k_p \quad (1.21)$$

If we now go back to the local interpretation of nonlinear processes, this relation can be seen as a momentum conservation condition to apply to the SHG process. By recalling Noether's theorem of classical mechanics, every symmetry in a physical system is accompanied by a conserved quantity and vice versa.

Momentum conservation in particular stems from translational invariance, which in first approximation is perfectly consistent with the request that the nonlinear signal propagates throughout the whole nonlinear medium. These considerations will be important in the next sections to understand nonlinear processes at the nanoscale. The reason why this condition is not always easily achieved in real materials becomes evident if we rewrite Eq. 8 as

$$\frac{2\omega n(2\omega)}{c} = \frac{\omega n(\omega)}{c} + \frac{\omega n(\omega)}{c} \quad \Rightarrow \quad n(2\omega) = n(\omega) \quad (1.22)$$

Indeed the nonlinear material's dispersion makes this condition difficult to be fulfilled. Therefore a number of techniques have been developed to overcome

this difficulty, such as Quasi Phase-Matching (QPM) [22, 23, 24], Birefringence Phase-Matching (BPM) and Modal Phase-Matching (MPM) [25].

1.1.5 Phase-matching in sub-wavelength media

All the above considerations on phase-matching apply in the case of propagating nonlinear signals, which implies that the dimensions of the host media should be larger than the signal's wavelength. If we now consider nonlinear effects in sub-wavelength structures, which in the case of optical frequencies means dimensions of the order of a few hundreds nanometres, it becomes intuitively clear that phase-matching conditions are no longer needed in order to have macroscopically significant nonlinear signals.

In other words, as the coherence length L_c is of the orders of several microns, the nonlinear signal intuitively does "not travel enough" in the medium to build up a sufficiently large phase-mismatch to require a condition on wave-vectors.

Indeed in sub-wavelength structures by definition there is no propagation at all. What physically happens and which are the necessary conditions to obtain efficient frequency conversion, is to be understood in an entirely different theoretical framework, the so-called Mie theory, which will be the object of the next section.

1.2 Light scattering from a sphere: Mie theory

Light scattering from dielectric objects is a largely studied subject and gives rise to a large number of interesting effects depending on the dimensions of the object(s) compared to the wavelength λ , reflected in the size parameter $x = l/\lambda$, their refractive index m , and the product of these two. For example, in case of λ much larger than the object(s) dimensions ($x \ll 1$, $x(m-1) \ll 1$) we are in Rayleigh scattering regime, while for the opposite case ($x \gg 1$) we find geometric optics [26, 27].

In 1908 Gustav Mie developed a theory describing the case of $x \simeq 1$, $(m-1) \geq 1$ in an effort to understand the various colors assumed by the scattered and absorbed visible light shined on gold nanoparticles in colloidal solution.

More than a century after, his analytic treatment has brought a vast attention again. Let us consider a homogeneous sphere of radius a and refractive index N_1 , embedded in a medium of index N illuminated by a plane

wave:

$$\mathbf{E}_i = \mathbf{E}_0 e^{-i(\mathbf{k} \cdot \mathbf{x} - \omega t)}, \quad \mathbf{H}_i = \mathbf{H}_0 e^{-i(\mathbf{k} \cdot \mathbf{x} - \omega t)} \quad (1.23)$$

In order to find the correct solutions for the fields scattered by the sphere one must solve the Maxwell equations:

$$\nabla \cdot \mathbf{E} = 0 \quad (1.24)$$

$$\nabla \cdot \mathbf{H} = 0 \quad (1.25)$$

$$\nabla \times \mathbf{E} = i\omega\mu\mathbf{H} \quad (1.26)$$

$$\nabla \times \mathbf{H} = -i\omega\mu\mathbf{E} \quad (1.27)$$

which can be rewritten as the so-called vector-wave equations:

$$(\nabla + k^2) \mathbf{E} = 0, \quad (\nabla + k^2) \mathbf{H} = 0 \quad (1.28)$$

Analytically solving full-vectorial wave equations can be a hard task, but in this case it is possible to simplify the problem. Let us now build a vector function \mathbf{M} from a scalar function ψ and a constant vector \mathbf{c} , such that

$$\mathbf{M} = \nabla \times (\mathbf{c}\psi) \quad (1.29)$$

It should be noted that \mathbf{c} is perpendicular to \mathbf{M} , and is called pivotal vector. As the divergence of the curl of every vector functions is identically 0 we have

$$\nabla \cdot \mathbf{M} = 0$$

and by using vector function properties it can be shown that

$$(\nabla + k^2) \mathbf{M} = \nabla \times [\mathbf{c}(\nabla + k^2)\psi] \quad (1.30)$$

Therefore \mathbf{M} satisfies the vector wave equation if and only if ψ is solution to the scalar wave equation. Having defined \mathbf{M} we can now construct another vector:

$$\mathbf{N} = \frac{1}{k} \nabla \times \mathbf{M} \quad (1.31)$$

This definition implies two properties: \mathbf{N} is divergenceless too:

$$\nabla \cdot \mathbf{N} = 0 \quad (1.32)$$

and it satisfies the vector wave equation:

$$(\nabla + k^2) \mathbf{N} = 0 \quad (1.33)$$

Being built in this way, \mathbf{M} and \mathbf{N} vectors have all the required properties of electromagnetic fields: they are divergence-less, the curl of \mathbf{N} is proportional to \mathbf{M} and vice-versa. We have thus simplified the problem to finding solutions of the scalar wave equation. We shall thus call ψ the generating function for the vector harmonics \mathbf{M} and \mathbf{N} . As we are dealing with scattering from a sphere, the generating function has to be chosen to be solution of the scalar wave equation in spherical coordinates (r, θ, ϕ) .

The symmetry of our problem also dictates the choice of the pivotal vector: if we make the choice $\mathbf{c} \equiv \mathbf{r}$, the radial vector, then $\mathbf{M} = \nabla \times (\mathbf{r}\psi)$ is a solution of the vector wave equation in spherical coordinates. Let us now attempt to find a solution of the scalar wave equation, which in spherical coordinates reads

$$\left[\left(\frac{1}{r^2} \frac{\partial}{\partial r} r^2 \frac{\partial}{\partial r} + \frac{1}{r^2 \sin\theta} \frac{\partial}{\partial \theta} \sin\theta \frac{\partial}{\partial \theta} + \frac{1}{r^2 \sin\theta} \frac{\partial^2}{\partial \phi^2} \right) + k^2 \right] \psi = 0 \quad (1.34)$$

We look for solutions that are separable in spherical coordinates, i.e. $\psi(r, \theta, \phi) = R(r)\Theta(\theta)\Phi(\phi)$. Without entering into too heavy mathematical detail, it is possible to show that the final solution to this problem is given by [27]:

$$\psi_{emn} = \cos(m\phi) P_n^m(\cos\theta) z_n(kr) \quad (1.35)$$

$$\psi_{omn} = \sin(m\phi) P_n^m(\cos\theta) z_n(kr) \quad (1.36)$$

where $\cos(m\phi)$, $\sin(m\phi)$ are two, even (*e*) and odd (*o*), linearly independent solutions for $\Phi(\phi)$; $z_n(kr)$ are any of the four kinds of spherical Bessel functions (as any of those is a solution for $R(r)$); and $P_n^m(\cos\theta)$ are the associated Legendre functions. Finally the vector spherical harmonics generated by these solutions are:

$$\mathbf{M}_{emn} = \nabla \times (\mathbf{r}\psi_{emn}) \quad \mathbf{M}_{omn} = \nabla \times (\mathbf{r}\psi_{omn}) \quad (1.37)$$

$$\mathbf{N}_{emn} = \frac{1}{k} \nabla \times (\mathbf{M}_{emn}) \quad \mathbf{N}_{omn} = \frac{1}{k} \nabla \times (\mathbf{M}_{omn}) \quad (1.38)$$

Now we have all the necessary ingredients to expand our incident plane wave excitation in spherical harmonics and solve our actual scattering problem. Let us choose for simplicity an x-polarized plane wave defined as:

$$\mathbf{E}_{inc} = E_0 e^{ikrcos\theta} \hat{x} \quad (1.39)$$

$$\hat{x} = (\sin\theta\cos\phi)\hat{r} + (\cos\theta\cos\phi)\hat{\theta} - (\sin\phi)\hat{\phi} \quad (1.40)$$

Mathematical details about the full expansion can be found in [27]. Here let us directly give the final expression of the expanded electric field:

$$\mathbf{E}_{inc} = E_0 \sum_{n=1}^{\infty} i^n \frac{2n+1}{n(n+1)} (\mathbf{M}_{o1n}^{(1)} - i\mathbf{N}_{e1n}^{(1)}) \quad (1.41)$$

where the superscript (1) means we have to consider the first type of spherical Bessel function for the radial part in order to have finiteness at the origin. Moreover all $n \neq 1$ terms vanish because of the orthogonality of $(\mathbf{M}_{omn}, \mathbf{M}_{emn})$, $(\mathbf{N}_{omn}, \mathbf{N}_{emn})$, $(\mathbf{M}_{omn}, \mathbf{N}_{omn})$, and $(\mathbf{M}_{emn}, \mathbf{N}_{emn})$ sets. Now we have to find an expression for the scattered field \mathbf{E}_{sca} and the field inside the sphere \mathbf{E}_{int} , then the field outside the sphere is simply given by $\mathbf{E}_{out} = \mathbf{E}_{inc} + \mathbf{E}_{sca}$ and the problem is solved. Given the above orthogonality relations, and remembering the interface conditions

$$(\mathbf{E}_{inc} + \mathbf{E}_{sca} - \mathbf{E}_{int}) \times \hat{\mathbf{e}}_r = (\mathbf{H}_{inc} + \mathbf{H}_{sca} - \mathbf{H}_{int}) \times \hat{\mathbf{e}}_r = 0 \quad (1.42)$$

the internal and scattered field must have the same form of the incident one, i.e.

$$\mathbf{E}_{int} = E_o \sum_{n=1}^{\infty} i^n \frac{2n+1}{n(n+1)} (c_n \mathbf{M}_{o1n}^{(1)} - id_n \mathbf{N}_{e1n}^{(1)}) \quad (1.43)$$

$$\mathbf{E}_{sca} = E_o \sum_{n=1}^{\infty} i^n \frac{2n+1}{n(n+1)} (a_n \mathbf{N}_{o1n}^{(3)} - ib_n \mathbf{M}_{e1n}^{(3)}) \quad (1.44)$$

where for the internal field we choose the spherical Bessel function of the first kind for finiteness at the origin, while for the scattered field we choose the third kind because it asymptotically behaves as an outgoing spherical wave, unlike the fourth kind which would be an incoming one.

As we have written the internal and scattered fields as infinite series in the vector spherical harmonics \mathbf{N}_n and \mathbf{M}_n , the latter take on the meaning of electromagnetic normal modes. In particular, \mathbf{N}_n give rise to modes with zero radial magnetic field component, called electric type modes, while \mathbf{M}_n give rise with zero radial electric field component resonances, i.e. magnetic type modes.

In general, the scattered field is a superposition of normal modes, weighted by the appropriate coefficients a_n (electric) and b_n (magnetic). After some math, an explicit expression for a_n, b_n scattering coefficients can be found:

$$a_n = \frac{m\xi_n^{(1)}(mx)(\xi_n^{(1)}(x))' - \xi_n^{(1)}(x)(\xi_n^{(1)}(mx))'}{m\xi_n^{(1)}(mx)(\xi_n^{(3)}(x))' - \xi_n^{(3)}(x)(\xi_n^{(1)}(mx))'} \quad (1.45)$$

$$b_n = \frac{\xi_n^{(1)}(mx)(\xi_n^{(1)}(x))' - m\xi_n^{(1)}(x)(\xi_n^{(1)}(mx))'}{\xi_n^{(1)}(mx)(\xi_n^{(3)}(x))' - m\xi_n^{(3)}(x)(\xi_n^{(1)}(mx))'} \quad (1.46)$$

In this expression we have introduced the size parameter $x = 2\pi Na/\lambda$, the refractive index ratio $m = N_1/N$ and the Riccati-Bessel functions $\xi_n(x) = xz_n(x)$. Having defined the size parameter we can now quantitatively describe

the physical regime we refer to in saying “sub-wavelength optical nanoparticles”: $x \simeq 1$.

As the coefficients a_n, b_n respectively weight \mathbf{N}_n and \mathbf{M}_n (electric and magnetic normal modes), they are respectively called electric and magnetic multipole coefficients. Their role will be very important to understand the nonlinear response of optical nanoparticles, as it will become clear in the next sections.

Finally, the extinction cross section can be introduced, defined as the total attenuation of energy from the incident beam flux due to both absorption and scattering by the sphere ($C_{ext} = C_{abs} + C_{sca}$).

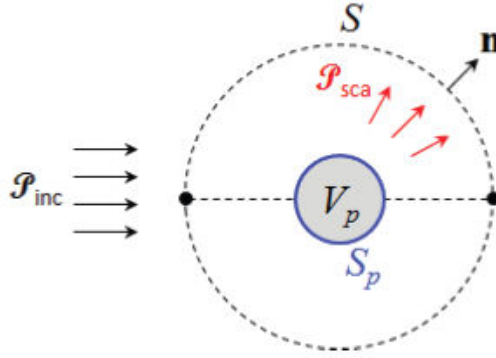


Figure 5: Estimation of extinction and scattering cross sections: An imaginary sphere with surface S is constructed around the nanoparticle and the electromagnetic energy rates across its surface are calculated. S_p and V_p respectively relate to the sphere’s surface and volume.

Let us construct an imaginary sphere with surface S surrounding the sphere and evaluate the rate at which electromagnetic energy crosses its surface \wp_{abs} (Fig. 5). Assuming that the surrounding medium is non-absorbing we have: $\wp_{abs} = -\wp_{sca} + \wp_{ext}$, where each \wp_i is obtained by integrating the corresponding Poynting vector \mathbf{S}_i over the sphere surface S_p :

$$\wp_{sca} = \int_{S_p} \mathbf{S}_{sca} \cdot \hat{\mathbf{n}} dS_p, \quad \wp_{ext} = - \int_{S_p} \mathbf{S}_{ext} \cdot \hat{\mathbf{n}} dS_p \quad (1.47)$$

Finally cross sections can be introduced as $C_{ext} = \wp_{ext}/I_{inc}$ In particular it is possible to derive an expression for the cross sections as a function of the multipole coefficients:

$$C_{sca} = \frac{2\pi}{k^2} \sum_{n=1}^{\infty} (2n+1) (|a_n|^2 + |b_n|^2) \quad (1.48)$$

$$C_{ext} = \frac{2\pi}{k^2} \sum_{n=1}^{\infty} (2n+1) \text{Re}\{a_n + b_n\} \quad (1.49)$$

It should be stressed here that the formula for C_{ext} depends on the polarization and propagation direction of the incident plane wave. For example, in the case of a y-polarized illumination, the real part would have been replaced by the imaginary part. On the contrary, C_{sca} is independent of this choice thanks the presence of the square modulus. Sometimes, instead of cross sections, adimensional quantities misleadingly called efficiencies are used, defined as $Q_j = C_j/\pi r^2$.

Contrarily to what their name suggests, efficiencies often are greater than 1, meaning for example that the nanoparticle is scattering more than would be geometrically possible. As we will see in the next chapter, despite the handiness of this theory, solutions in a closed form are available only for a few particular geometries other than the sphere [28].

Therefore, the only viable approach in most cases is either semi-analytical, which includes the expansion of the fields into an infinite multipole series [29], or numerical, resorting to several techniques such as Finite-Difference Time-Domain (FDTD) [31], FEM [32], or Discrete-Dipole Approximation (DDA) to solve for the fields, followed by multipolar decomposition to identify the involved resonances [33].

1.3 Elements of Plasmonics

Although the physics of metallic nanoparticles and that of dielectric ones are deeply different, they have a common feature: field confinement at the nanoscale under optical excitation. For this reason this next section will be dedicated to a brief introduction to plasmonics and a comparison with dielectric nanoparticles.

1.3.1 Surface Plasmons

Plasmonics deals with the interaction between the free-electron gas surrounding a metal and the incident electromagnetic radiation [9]. The motion of these free electrons can be described by a plasma model, also called Drude model, with a characteristic plasma frequency ω_p . The dielectric function of this free-electron gas can then be derived by solving the free-electron motion differential equation, driven by plane-wave excitation:

$$m \frac{d^2 \mathbf{x}}{dt^2} + m\gamma \frac{d\mathbf{x}}{dt} = -e\mathbf{E}_0 \exp(-i\omega t) \quad (1.50)$$

where γ is the collision frequency between electrons, m the electron mass and e the elementary charge. We look for solutions in the same harmonic form as the driving field $\mathbf{x} = \mathbf{x}_0 e^{-i\omega t}$, and the resulting amplitude will read

$$\mathbf{x}_0 = \mathbf{E}_0 \frac{e}{m(\omega^2 + i\gamma\omega)} \quad (1.51)$$

The induced electric dipole moment per volume unit will be then given by

$$\mathbf{P} = -ne\mathbf{x} = \frac{-ne^2}{m(\omega^2 + i\gamma\omega)} \mathbf{E}_0 \exp(-i\omega t) \quad (1.52)$$

in which n is the electron density. Finally, by recalling that the dielectric function is given by $\epsilon(\omega) = 1 + P(\omega)/\epsilon_0 E(\omega)$ we obtain:

$$\epsilon(\omega) = 1 - \frac{\omega_p^2}{\omega^2 + i\gamma\omega}, \quad \omega_p^2 = \frac{ne^2}{\epsilon_0 m} \quad (1.53)$$

where the characteristic plasma frequency ω_p has been introduced. This simple model works as a first approximation by assuming at least room temperature operation and geometrical confinement smaller than electron-phonon scattering cross-section.

The main message delivered by the equations above is that the interaction between the free-electron gas and the incident electromagnetic field gives rise to coherent collective excitation of these electrons at the metal-dielectric interface called Surface Plasmons (SP). These can occur in two different forms: Surface Plasmon-Polaritons (SPP), which propagate at the metal-dielectric interface between bulk materials, and Localized Surface Plasmons (LSP), which are localized in metallic nanostructures.

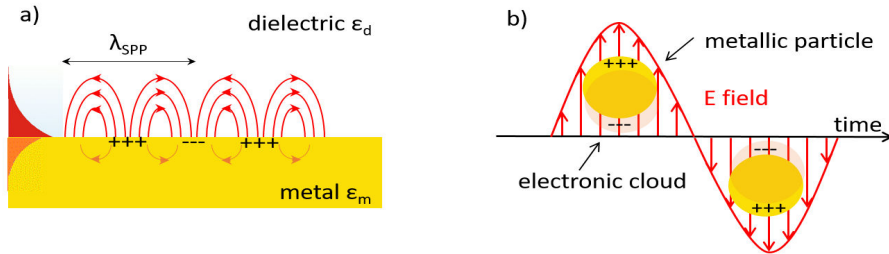


Figure 6: Surface plasmons come in two different forms: (a) propagating SPP at the interface between (bulk) a metal and a dielectric. (b) LSP confined in metallic nanoparticles.

As for the geometry in Fig. 6a, the plasmon field evanescently decays in the z -direction, thus providing sub-wavelength confinement in the proximity of the interface. By solving the wave equation of this system it can be shown that the SPP can be excited only if the impinging radiation has a transverse magnetic component. A dispersion relation for the SPP can then be found by applying field continuity relations at the interface (Fig. 7):

$$\beta^2 = k_0^2 \frac{\epsilon_m \epsilon_d}{\epsilon_m + \epsilon_d} \quad (1.54)$$

where β is the wave vector in the direction parallel to the interface, ϵ_d , ϵ_m are the permittivities of the dielectric and of the metal respectively.

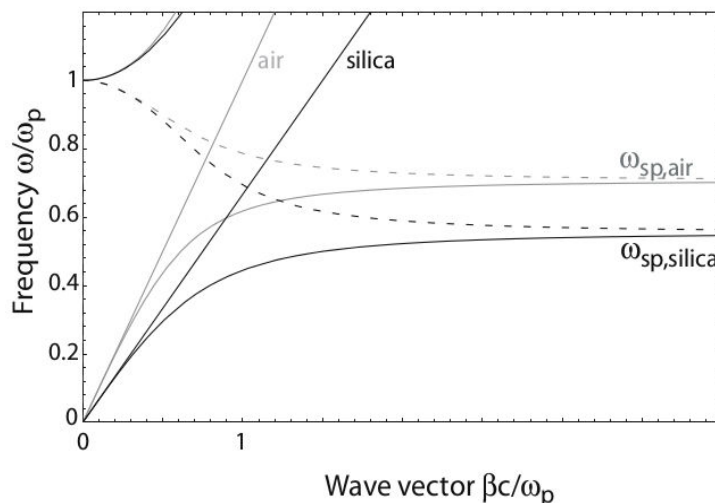


Figure 7: Dispersion relation of a SPP at the interface between a metal and air (gray curve) or silica (black curve). *This plot is reproduced from ref. [9].*

However, coupling of light from free space to SPPs requires special experimental conditions to obtain momentum matching, since the SPP wave-vector is larger than that of propagating light. On the other hand, metallic structures with dimensions on the order of or smaller than the impinging radiation wavelength can support LSP.

Unlike the previous case, LSPs do not require additional momentum matching to be excited, just the appropriate frequency and polarization. It is worth noting that LSPs can be supported as well in the case of subwavelength defects on metallic surfaces, thus enabling the interaction between LSP and SPP [40].

1.3.2 Second-order nonlinear plasmonics

The intense field confinement in subwavelength regions provided by SPs allow weak nonlinear processes, which depend superlinearly on the local field, to be significantly enhanced, both in the case of intrinsic nonlinearity of the metallic structure and in the case of extrinsic nonlinearity belonging to another material placed in its near-field [41].

The intrinsic nonlinear polarizability related to conduction electrons of noble metals can be well described by a hydrodynamic model [44]. The latter holds for a spectral range well below plasma frequency and far away from interband transitions and Coulomb collisions, which occur at high and low frequencies, respectively. The hydrodynamic equation for the conduction band electrons is given by the following expression:

$$mn \left[\frac{\partial \mathbf{v}}{\partial t} + (\mathbf{v} \cdot \nabla) \mathbf{v} + \frac{\mathbf{v}}{\tau} \right] = -en\mathbf{E} - \frac{en}{c} \mathbf{v} \times \mathbf{B} - \nabla p \quad (1.55)$$

where m is the electron effective mass, n the number density, p the gas pressure. The second term on the left side describes convection, while the third one accounts for damping with a characteristic time τ . The right side of the equation includes Lorentz force for both magnetic and electric field components plus the pressure gradient term.

The second-order nonlinear polarization can be then calculated by taking into account the continuity equation $\dot{n} = -(\nabla \cdot \mathbf{j})/e$, where \mathbf{j} is the current density, related to the electron velocity by $\mathbf{v} = \mathbf{j}/ne$.

As the polarization is related to the current density by $\mathbf{j} = \dot{\mathbf{P}}$, the hydrodynamic equation can be expressed in terms of \mathbf{P} , and by adopting a perturbative methodology in the undepleted pump approximation, the nonlinear polarization can be obtained by expanding the currents and electromagnetic fields in the frequency domain and collecting terms up to the second order [45]. In particular, convective and magnetic terms give rise to a second-order nonlinear response [42], while the damping term is responsible for Kerr-type nonlinearity [43].

Unlike the case of dielectric nanoparticles, the second order nonlinear response in metals mainly originates from broken centrosymmetry in the free electron gas, leading to an effective surface $\chi^{(2)}$, which is dominant with respect to the bulk contribution due the high degree of symmetry in their crystalline structure [41]. Conversely third-order effects like THG are mainly due to bulk nonlinearity.

Very recently, record-efficient SHG from gold nanorods was demonstrated, thanks to careful engineering of the gold nanostructures so as to maximize the overlap integral between the resonant modes at ω and 2ω [46].

Although the latter was the best achievement so far in nonlinear plasmonics, the efficiency did not exceed $5 \cdot 10^{-10} W^{-1}$, because of the limitations imposed by ohmic losses.

This suggests that the dielectric approach might be more viable way due to the negligible losses and the possibility to exploit bulk nonlinearities. However before going further into that, a more detailed discussion on the pros and cons of metallic nanostructures compared to dielectric ones is appropriate.

1.3.3 Metals vs dielectrics

Both the approaches above, metals with plasmonic resonances and dielectrics with Mie resonances, can operate at optical frequencies and nanoscale sizes. We have seen as well that the physics of these two system is different, as on the one hand we have the collective oscillation of the free conduction electrons (metals), while on the other hand the induced currents are generated by the displacement of bound valence electrons (dielectrics).

This fact is at the core of most probably the main issue of plasmonics at optical frequencies: ohmic losses [47]. While in dielectrics the displacement currents generated by bound electrons motion do not dissipate energy, SPs undergo ultra-fast dephasing and decay after a few femtoseconds, both by radiative damping and via the formation of hot carriers. These relax in the picosecond timescale by locally increasing the temperature of the nanostructures and their immediate vicinity up to values of $\sim 1000 \text{ }^\circ C$ [48].

This feature can be detrimental for enhanced spectroscopies and bio-applications, as both the organic sample and the metallic nanostructures could be damaged by the high temperatures. Conversely, losses in dielectric nano-objects can be practically neglected as long as we excite them with energies lower than the gap. As a matter of fact, it was recently shown that dielectric nanoantennas can enhance Raman scattering and fluorescence of organic molecules placed in their vicinity with negligible light-to-heat conversion [49].

The sole drawback is that the Raman gain in this case is several orders of magnitude lower than that of metallic nanoparticles due to the reduced field confinement. It would be a mistake however to state that ohmic losses in plasmonics limit all applications. Indeed in the last decade many medical institutions started to successfully employ the fast light-to-heat conversion in gold nanoparticles to kill cancer cells [50].

Another key difference is that metals only support electric type resonances, due to the smaller penetration depth caused by electrostatic screening. This prevents the formation of circulation currents inside the bulk of the

metallic nanoparticle, which are propedeutic to the excitation of magnetic multipole moments. As such, a magnetic response in plasmonic nanostructures can only be achieved through careful engineering of their geometry.

The archetypical example in this sense is the split-ring resonator (Fig. 8a) [51], where the real currents excited by an external field produce a transverse oscillating magnetic field in the center of the ring, which simulates an oscillating magnetic dipole. In contrast, high-index dielectric nanostructures naturally offer Mie-type magnetic resonances as the field is well confined in the bulk due to total internal reflection [35].

Interestingly, in some cases the magnetic response of dielectric nanoparticles can even be higher than the electric one. This happens for example in the case of an AlGaAs nanocylinder with $r=225$ nm and $h=400$ nm, where the Magnetic Dipole (MD) resonance is stronger than the Electric Dipole (ED) one [32]. Such effects have given origin to the concept of “magnetic light”.

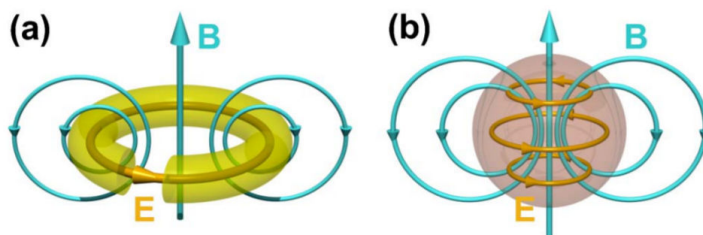


Figure 8: Magnetic dipole resonances supported by plasmonic (a) and dielectric (b) nanostructures. In the metallic case, optical magnetism is artificially obtained by resorting to particular geometries such as the split ring resonator. Conversely, for dielectric nanoparticles optical magnetism occurs naturally as a consequence of high field confinement in the bulk. *Figure taken from [35].*

Despite the advantage of having a mode well confined in the bulk, field enhancements are less important for dielectric nanoparticles. The reason for that is twofold: on the one hand in metals the electromagnetic field does not penetrate much into the bulk, and on the other hand to obtain plasmonic resonances in the visible the typical sizes of the nanostructures are of the order of tens of nanometres. In contrast to excite Mie type resonances in dielectric particles we need the size parameter $x = 2\pi r/\lambda \sim 1$, leading to typical diameters of a few hundreds of nanometres.

For these two reasons the electromagnetic field in plasmonic nanostructures is compressed in smaller volumes very near to the surface, giving rise to field enhancements as high as $E/E_0 \sim 10^3$, while for dielectric structures we have $E/E_0 \sim 10$. This handicap does not reduce the potential of dielectric nanostructures to achieve nonlinear conversion efficiencies many orders

of magnitude higher than with plasmonics.

This happens thanks to the negligible losses and field confinement inside the structures, allowing for greater effective interaction volume between the incident field and the bulk material. These reasons motivated us to make a technological effort to develop an all-dielectric nanophotonic nonlinear platform with high-index AlGaAs nanostructures resting on a low-index AlOx substrate.

1.4 Conclusion

This first thesis chapter has dealt with the necessary theoretical tools to understand the physics of nonlinear optical processes and optical nanostructures (both dielectric and metallic). These allow to define the context of the results we obtained in nonlinear signal generation from monolithic AlGaAs-on-insulator nanoantennas.

This topic will be the subject of chapters number three, four and five. Before going into that, a chapter will be dedicated to a further description of the methods employed throughout this thesis.

Chapter 2

Techniques: numerics, technology and experiments

The aim of this chapter is to review the principal numerical, technological and experimental methods that have been of utmost importance for this thesis work. In the first part I will describe how to simulate the linear and nonlinear response of a nanoparticle using the FEM method, and how to identify the contributions of supported modes by multipolar decomposition.

In the second part of the chapter I will describe the fabrication processes which were most relevant for the fabrication protocols employed in my doctoral work. Particular emphasis will be put on anisotropic etching and thermal wet oxidation, as their optimization required a deeper understanding of the underlying mechanisms compared to the other fabrication steps.

Finally the third part will deal with the main optical experimental methods to probe the linear and nonlinear response of the fabricated nanostructures.

2.1 Numerical calculations

In the general case, an analytical model for finding the Mie-type multipolar resonances of a nanostructure is based on multipolar expansion of the incident, scattered and internal fields, with application of the proper boundary conditions on the nanostructure surface.

The solution in a closed form is however possible in a very limited number of the nanostructure geometries, such as a sphere, spheroids, a cube and a cylinder of infinite length [28]. Unfortunately the fabrication of such structures with standard lithographic techniques is not an easy task compared to that of other structures like nanocylinders.

Despite this limitation, the linear and nonlinear response of optical nanostructures can be numerically calculated using several methods, including FEM [32], FDTD [31] and DDA [30]. Here I will focus my attention on FEM implementation on COMSOL Multiphysics, a commercially available software.

2.1.1 Linear scattering calculation in spherical coordinates

The calculation steps required to implement the FEM on COMSOL and calculate the linear response of a generic nanoparticle can be summarized in the following points:

- The geometry of the problem is defined, comprising the parameters of the nanostructure, a possible substrate, and the host medium, which is usually air. The domain is then surrounded by a Perfectly-Matched Layer (PML), a perfect absorber introduced to avoid non-physical reflections at the boundaries. Usually the domain is not larger than a few wavelengths.
- The illumination parameters are defined, together with the dispersion of the materials involved.
- The domain is discretised into a set of discrete sub-domains. The nanostructure region is the most finely meshed, with elements having a typical dimension of $\lambda/20n$, and a growing factor slightly larger than one, exiting this domain and going towards the PML.
- Initial values and the type of problem are specified.
- Once the field is calculated in every mesh element, scattering and extinction can be evaluated by integrating the relative Poynting vectors.

Very recently, an algorithm has been developed to evaluate the multipole coefficients once the field is numerically calculated [33]. The idea is to build up the scattering density currents

$$\mathbf{J}_s(\mathbf{r}) = -i\omega\epsilon_0(\epsilon_r(\mathbf{r}) - \epsilon_{r,h})\mathbf{E}_{out}(\mathbf{r}) \quad (2.1)$$

where $\epsilon_r(\mathbf{r})$ is the complex permittivity of the system in each coordinate \mathbf{r} , $\epsilon_{r,h}$ is the (real-valued) permittivity of the host medium, $\mathbf{E}(\mathbf{r}) = \mathbf{E}_{inc} + \sum_j \mathbf{E}_{sca,j}$ is the numerically calculated field external to the nano-object(s), consisting of the sum of the incident and the scattered fields. The sum over the index

j is performed in case of nanoparticle arrays. It can be shown that, once the currents are known, the multipole coefficients can be evaluated by performing an inner product with the following formulas:

$$a_E(l, m) = \frac{-i^{l-1}k_0^2\eta O_{lm}}{E_0(\pi(2l+1))^{1/2}} \int_V e^{-im\phi} \{[\xi_l(kr) + \xi_l''(kr)] P_l^m(\cos\theta) \hat{\mathbf{r}} \cdot \mathbf{J}_{s,j}(\mathbf{r}) + \frac{\xi_l'(kr)}{kr} \left[\frac{d}{d\theta} P_l^m(\cos\theta) \hat{\theta} \cdot \mathbf{J}_{s,j}(\mathbf{r}) - \frac{im}{\sin(\theta)} P_l^m(\cos\theta) \right] \hat{\phi} \cdot \mathbf{J}_{s,j}(\mathbf{r}) \} d^3r \quad (2.2)$$

$$a_M(l, m) = \frac{-i^{l-1}k_0^2\eta O_{lm}}{E_0(\pi(2l+1))^{1/2}} \int_V e^{-im\phi} x_l(kr) \left[\frac{im}{\sin(\theta)} P_l^m(\cos\theta) \hat{\theta} \cdot \mathbf{J}_{s,j}(\mathbf{r}) + \frac{d}{d\theta} P_l^m(\cos\theta) \hat{\phi} \cdot \mathbf{J}_{s,j}(\mathbf{r}) \right] d^3r \quad (2.3)$$

where $P_l^m(\cos\theta)$ are Legendre polynomials, $\xi_l(kr) = kr z_l(kr)$ the Riccati-Bessel functions, $z_l(kr)$ the spherical Bessel functions, and

$$O_{lm} = \frac{1}{[l(l+1)]^{1/2}} \left[\frac{(2l+1)(l-m)!}{4\pi(l+m)!} \right]^{1/2}$$

Then, similarly to Mie theory, scattering and extinction cross-sections can be deduced from the individual multipolar contributions:

$$C_{sca} = \frac{\pi}{k^2} \sum_{l=1}^{\infty} \sum_{m=-l}^l (2l+1) (|a_E(l, m)|^2 + |a_M(l, m)|^2) \quad (2.4)$$

$$C_{ext} = \frac{\pi}{k^2} \sum_{l=1}^{\infty} \sum_{m=-l}^l (2l+1) \text{Re}\{m a_E(l, m) + a_M(l, m)\} \quad (2.5)$$

As already explained above, the appearance of the real part in the extinction cross-section formula strictly depends on the pump polarization and propagation direction. Compared to Mie theory formulas, this computational method allows to account for the amount of the z-component of angular momentum of the impinging light, meaning that Mie expansion is a special case of this multipolar approach. Indeed, Mie coefficients can be easily retrieved by setting $a_E(l, m) = a_M(l, m) = 0 \quad \forall m \neq \pm 1$, and $a_{E,M}(l, 1) = -a_{E,M}(l, -1)$.

2.1.2 Cartesian coordinates scattering: the anapole condition

Interestingly, the above derived expression of electric and magnetic multipoles depends on the vector spherical harmonics. As such, these formulas are not invariant under coordinate transformation, and their derivation in other reference frames could provide interesting physical insights. This happens for example if we now expand the source current defined in Eq. 2.1 over multipole coefficients expressed in Cartesian coordinates [53, 54]:

$$\mathbf{J}(\mathbf{r}, t) = \sum_{l=0}^{\infty} \frac{(-1)^l}{l!} B_{i\dots k}^{(l)} \partial_{i\dots k} \delta(\mathbf{r}) \quad (2.6)$$

where $B_{i\dots k}^{(l)}$ is a l -rank tensor given by

$$B_{i\dots k}^{(l)} = \int d^3\mathbf{r} [\mathbf{J}(\mathbf{r}, t) \mathbf{r}_i \dots \mathbf{r}_k] \quad (2.7)$$

which contains all the information about the Cartesian multipoles. As such, the first order $B_i^{(1)} \sim d_i^{(1)}$ consists of the Cartesian ED moment, the second order $B_{ij}^{(2)} \sim Q_{ij}^{(2)} + \mu_i^{(1)}$ contains the Electric Quadrupole (EQ) $Q_{ij}^{(2)}$ and the MD $\mu_i^{(1)}$, and finally the third order $B_{ijk}^{(3)} \sim O_{ijk}^{(3)} + \mu_{ij}^{(2)} + T_i^{(1)}$ includes the Electric Octupole (EO) $O_{ijk}^{(3)}$, the Magnetic Quadrupole (MQ) $\mu_{ij}^{(2)}$ and finally the Toroidal Dipole (TD) $T_i^{(1)}$. The reason why this TD does not appear in Mie theory is that it is associated with a particular configuration of the local current, while in contrast the spherical multipole moments are related to the structure of the scattered light.

This implies that in spherical coordinates the ED and the associated TD cannot be distinguished in the far-field. There are situations, which cannot be fully understood in the frame of spherical multipole decomposition, in which the ED and TD have the same amplitude but phase difference of $\pm\pi$, such that their contributions destructively interfere in the far-field, leading to zero or weak radiation depending on the behaviour of higher order multipoles.

These situations are referred to as anapole (“without any poles” from ancient Greek). Interestingly in such excitation condition energy is highly stored in the bulk of the nanoparticles. For such reason, several different structures and materials were engineered to exploit the anapole mode at the fundamental and boost the nonlinear conversion efficiency [55, 52], intrinsic Surface-Enhanced Raman Scattering [56], and nonlinear amplification in nanolasers [57].

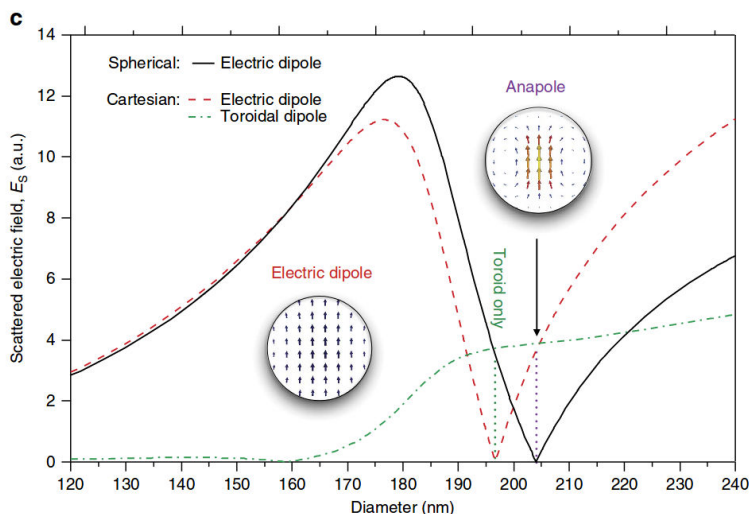


Figure 9: Calculated scattering efficiency contributions from the spherical ED (black), Cartesian electric (red) and toroidal (green) dipole moments. For small particle sizes the TD is negligible whereas the Cartesian and spherical dipoles coincide. The anapole occurs at larger sizes, and is associated with the vanishing spherical electric dipole contribution, while the Cartesian ED and TD are in phase opposition and cancel each other out. *This figure is taken from ref. [53].*

2.1.3 Modeling the nonlinear optical response

The previous sections explained how to numerically calculate the linear response of a nanostructure. In this section I will describe how to calculate its nonlinear response [32]. The idea is to divide the problem in two steps. In the first one the linear response is calculated with COMSOL following the above mentioned procedure. In the second step, the nonlinear polarization induced by the bulk nonlinearity is employed as a source for a second linear study at the nonlinear frequency of interest (for example 3ω for THG in Si, or 2ω in case of SHG from AlGaAs).

In order to better illustrate this point, it is appropriate to describe the example of SHG in AlGaAs nanoantennas, as reported in ref. [32]. All simulation settings were chosen so as to be easily recreated in the laboratory: $\text{Al}_{0.18}\text{Ga}_{0.82}\text{As}$ was chosen as a material to avoid Two-Photon absorption (TPA) at $\lambda=1.55 \mu\text{m}$, referring to [34] for the material dispersion. For Mie theory regime to hold true, the illumination wavelength choice restricts the cylinder dimensions so as to have $x \simeq 1$.

In particular the height was fixed at 400 nm for epitaxial growth reasons, while the radius was spanned in the interval $175 \div 230$ nm. Finally, the

simulations were performed both in the cases of air host medium, and AlOx substrate ($n \simeq 1.6$ at $1.55 \mu\text{m}$), as shown in Fig. 10.

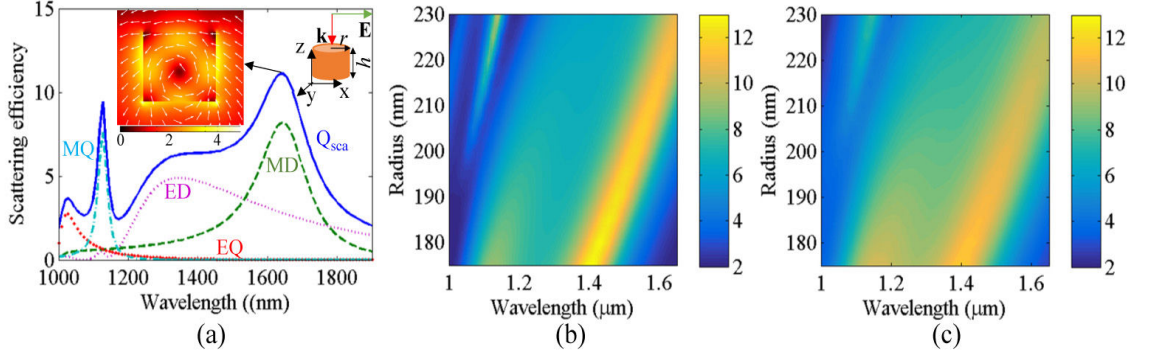


Figure 10: Linear response of an $\text{Al}_{0.18}\text{Ga}_{0.82}\text{As}$ nanocylinder. (a) Scattering efficiency of a cylinder with 225 nm radius, decomposed according to [33] to identify the multipole contributions. The left inset shows the electric field profile at the MD resonance. Scattering efficiency map in the case of air (b) and AlOx (c) substrate. *The figure is taken from [32].*

The illumination geometry is such that the pump k -vector is parallel to the cylinder's symmetry axis, as showed in the right inset of Fig. 10a. The calculated scattering efficiency of a cylinder with radius 225 nm, decomposed according to [33], shows four main contributions coming from electric and magnetic dipoles and quadrupoles (MD, ED, MQ, EQ). In particular the electric field profile at the magnetic dipole resonance ($\lambda_{MD} = 1640 \text{ nm}$) is shown in the left inset, forming an electric current loop inside the cylinder, which is the necessary condition to sustain a magnetic dipole [35].

By varying the radius from 175 nm to 230 nm, it can be seen that the resonances redshift as the radius increases (Fig. 10b). The presence of AlOx substrate does not significantly alter the spectral position of those resonance, with only a slight broadening due to the decreased field confinement in the nanocylinder (Fig. 10c).

$\text{Al}_{0.18}\text{Ga}_{0.82}\text{As}$ is a non-centrosymmetric material with a strong bulk $\chi_{ijk}^{(2)} = 100 \text{ pm/V}$ for $i \neq j \neq k$ [36]; as a consequence the nonlinear response of the nanocylinder is calculated by performing a second linear computation at 2ω , by using the SH term in the nonlinear polarization induced by the bulk $\chi^{(2)}$ as an external current source. Finally the conversion efficiency can be evaluated as

$$\eta_{SHG} = \frac{\int_A \mathbf{S}_{SH} \cdot \hat{\mathbf{n}} dA}{I_0 \pi r^2} \quad (2.8)$$

where \mathbf{S}_{SH} is the Poynting vector of the SH field, A is an imaginary surface enclosing the cylinder, and $I_0 = 1GW/cm^2$ is the incident field intensity. As the strongest resonance in the linear scattering is MD, the expected η_{SHG} should have a maximum when pumping at this frequency. However, Fig 11a shows that the SH efficiency peak is obtained for a slightly higher pump frequency (1680 nm).

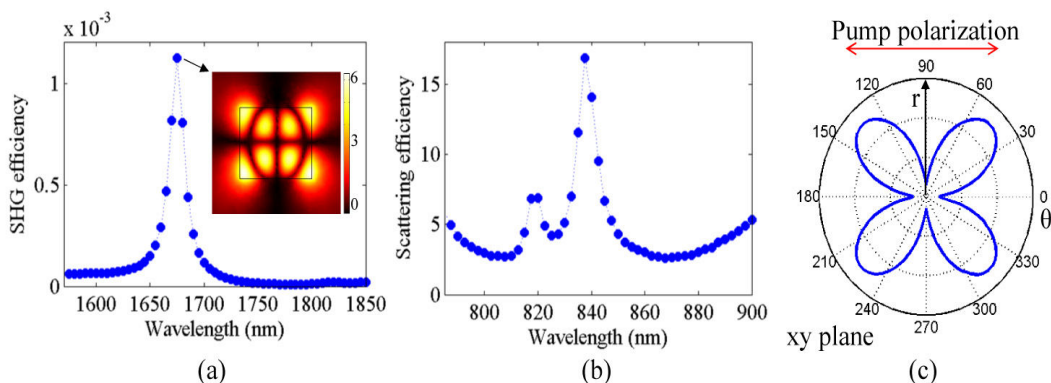


Figure 11: Nonlinear response of an $Al_{0.18}Ga_{0.82}As$ nanocylinder. (a) SHG efficiency of a cylinder with 225 nm radius as a function of the pump frequency, with the inset showing a quadrupolar field profile at the efficiency peak. (b) Linear scattering efficiency calculated at 2ω . (c) SHG far-field radiation pattern in the xy -plane. *The figure appears in ref. [32]*

This point can be understood by calculating the linear scattering at 2ω . Indeed, a sharp resonance is present at exactly half the maximum SHG frequency (Fig. 11b). This behaviour shows that the nonlinear conversion efficiency in this system not only depends on the product of the scattering efficiencies at ω and 2ω ($Q_{FF}^2 \times Q_{SH}$ in particular), but also on the overlap integral between these two resonances. Finally, the inset in Fig. 11a and Fig. 11c show that the excited multipolar mode at 2ω has a quadrupolar nature.

During my thesis, SHG from $Al_{0.18}Ga_{0.82}As$ -on- $AlOx$ nanoantennas was experimentally demonstrated as well [37, 38, 39]. Due to the presence of a substrate with a refractive index higher than 1, the measured conversion efficiency was of the order of 10^{-5} . Despite the two-order of magnitude decreased efficiency with respect to the case of a cylinder in air, these results still represent a record for nonlinear light generation at the nanoscale, especially with respect to plasmonic nanostructures, whose nonlinear properties will be described in the next sections.

2.2 Fabrication techniques

As already stated, III-V semiconductor technology is nowadays at an advanced stage, more than half a century after the first demonstrations of laser diodes and LEDs. These techniques were further developed in the frame of PICs and electronics, involving micro/nano structuring of these semiconductor materials. The basic building block is represented by epitaxial growth, mainly achieved through Molecular Beam Epitaxy (MBE) or Metal-Organic Chemical Vapour Deposition (MOCVD), to define the raw layer stacking to be patterned at a later stage. Here I will describe in particular MBE, as this was the main employed technique during my thesis.

All micro/nano structuring processes can be grouped into two main branches: bottom-up and top-down. This section aims at describing mainly top-down steps, which are fundamental for the fabrication of AlGaAs-on-AlO_x nanostructures. Bottom-up techniques will be introduced as well, as they had an important role in the hybrid semiconductor-metal integration on AlO_x substrate.

2.2.1 Molecular beam epitaxy

MBE is an epitaxial growth technique based on the interaction of different elements adsorbed from molecular beams on a heated crystalline substrate. Molecular beams are generated by the so-called “effusion cells” by evaporating or sublimating high-purity materials contained in radiatively heated crucibles [58].

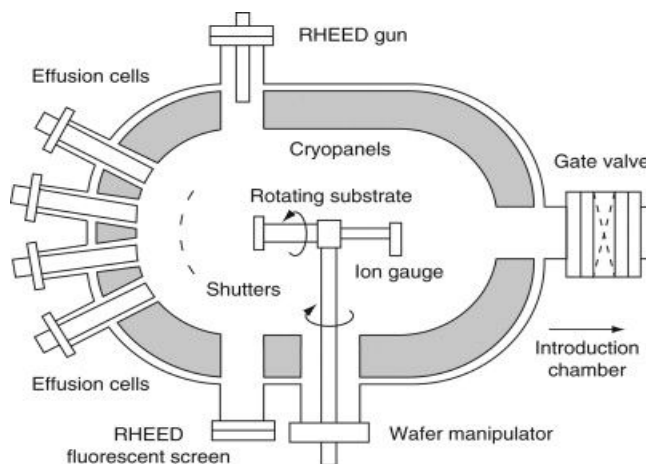


Figure 12: Schematics of a typical MBE system [58].

A typical MBE reactor consists of a stainless steel growth chamber, kept under pressures of the order of 10^{-11} Torr (ultra-high vacuum), so that the

mean free path of molecules in the beams is much greater than the distance between the cells and the substrate. Samples are transferred in and out of the chamber through a vacuum-preserving load-lock system. Molecular beams are individually selected by means of shutters located in front of the effusion cells.

The Reflection High Energy Electron Diffraction (RHEED) technique is often used for in-situ monitoring of the crystal growth. Deposition rates are generally on the order of 10^3 nm/min. Among the advantages of MBE it should be mentioned the ability to grow structures in which carriers are quantum confined in regions smaller than their de Broglie wavelength. Depending if the confinement is on 1D or 3D the structures are denominated quantum wells and quantum dots, respectively.

In our case a GaAs buffer layer of 500 nm is first grown on [100] non-intentionally doped GaAs wafer, followed by 1000 nm of $\text{Al}_{0.98}\text{Ga}_{0.02}\text{As}$ to be later oxidised, sandwiched between two 90 nm transition layers in which the Al molar fraction is linearly varied. Finally, the growth is concluded with a 200 nm or 400 nm $\text{Al}_{0.18}\text{Ga}_{0.82}\text{As}$ layer. In the unit cell of the grown GaAs crystal, Ga and As atoms exist in equal proportions. AlGaAs crystal has the same structure, with a fraction of Ga atoms replaced by Al ones. The lattice constant does not vary much with the Al molar fraction x ($a(x) = 5.6533 + 0.0078x$ Å), therefore AlGaAs can be easily grown on GaAs with minimal stress, and atomic sharp interfaces.

2.2.2 Electron beam lithography

Electron Beam Lithography (EBL) is a technique that allows to transfer a pattern on an electron-sensitive material by selective exposure to an electron beam, the so called resist. When the latter is exposed to electrons it experiences profound structural changes, such that when immersed in a specific basic solution, called developer, the pattern is permanently transferred. It is possible to distinguish two types of resist: positive and negative. The former are such that the exposed areas are etched away after development, while for the latter the opposite occurs.

The choice of electron beam exposure rather than UV light, as in photolithography, is crucial in nanofabrication as it allows sub-10 nm resolution. Photolithography pattern instead hardly exhibit ~ 300 nm features (diffraction limit). Despite the greater accuracy, the patterning rate in EBL is no higher than a few mm/h, much slower than in photolithography.

The beam aperture is usually a key parameter to change the patterning rate, however it has to be carefully chosen, as a bigger aperture comes with a higher rate and with lower resolution. Pushing the latter to the nanoscale

can be a hard task even with EBL: indeed there are two tricky effects that have to be carefully addressed in order to improve the resolution. The first one is the stitching of writing fields, defined as the maximum area that can be exposed in a single stage position.

The origin of the problem is the following: in normal mode the e-beam is deflected in order to expose an user-defined squared area (normally maximum $100\ \mu\text{m}$ sides to avoid aberrations) centered in the non-deflected position. After exposure the beam is blanked and the stage is translated, which could result in superpositions or misalignment in the proximity of the square side (Fig. 13a).

An effective way of anticipating this effect is the writing field alignment. The idea is to choose a reference feature, and move the stage in three positions corresponding to the corners of an user-defined square. At each position the e-beam is deflected as much as to be able to scan that area, an image is taken, and the mismatch with the original position of the reference feature is registered as a correction position. Once all three positions are scanned, the software computes corrective parameters. This procedure is repeated each time defining a smaller square, until no decrease in correction parameters is observed.

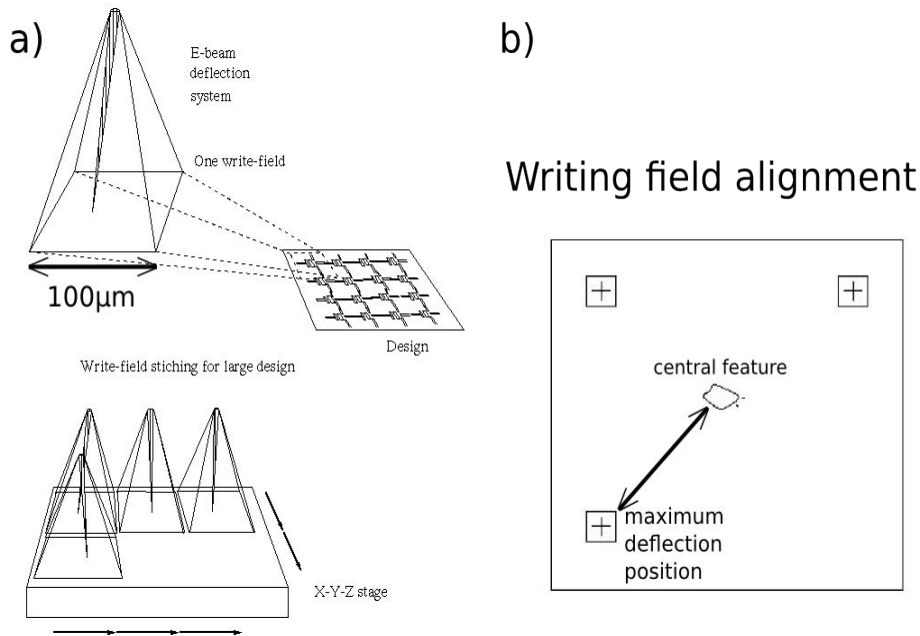


Figure 13: Schematics of the stitching problem in EBL: a) The electron beam is deflected to expose a $100\ \mu\text{m}$ writing field. Misalignments and superpositions between different writing fields are a problem for large designs. b)

Writing field alignment solves the problem by computing corrective parameters from maximum deflection positions with respect to a zero-deflection central feature.

The second, and much more exacerbated source of imperfections are the so called proximity effects, which cause features to be bigger than the nominal values defined in the mask. They can have two possible causes: in case of features close to each other, electrons from the exposure of an adjacent region can spill on the currently written one, effectively enlarging the exposed area and reducing the contrast between the close features.

This problem can be mitigated by reducing the e-beam dose, that is the charge deposited per unit area. The second proximity effect cause are secondary electrons penetrating deep into the substrate and back-scattered into the resist layer, thus contributing again to resist exposure (Fig. 14).

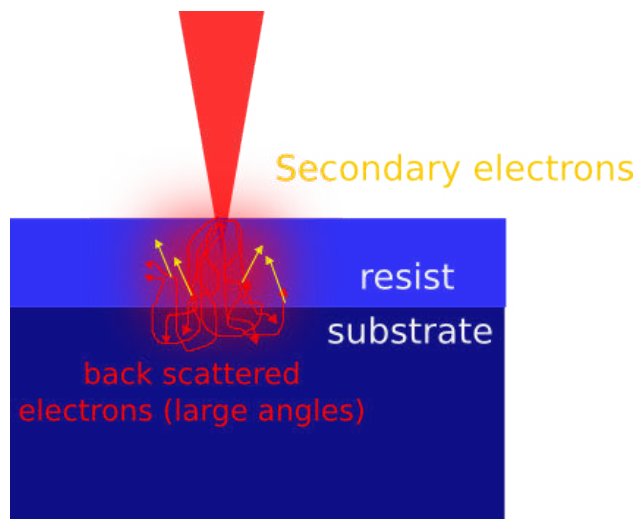


Figure 14: Explicative drawing of proximity effects from back-scattered electrons. The higher the acceleration voltage the deeper electrons penetrate the substrate, increasing the probability of being back-scattered into the substrate with larger angles than the primary electrons, broadening the exposed area.

Smaller acceleration voltages, i.e. electron energy, will reduce the substrate penetration depth, thus hindering electron back-scattering, but at the same time resolution will be reduced too. As a consequence the e-beam acceleration voltage value should be carefully chosen so as to find an optimal compromise between enhanced resolution and proximity effects. Our machine is a Raith PIONEER Two hybrid SEM-EBL system.

Masks are designed with E-line software from the same company, which

allows to easily draw patterns with basic 2D geometric figures as elementary blocks, and saves files in a graphic database format (GDSII), as usually employed in industries for integrated circuits data exchange.

As for the performances of this machine, the optimal acceleration voltage achievable is 20 kV, which, combined with an aperture of 10 μm , is a good compromise between resolution, ease to use, patterning speed and proximity effects.

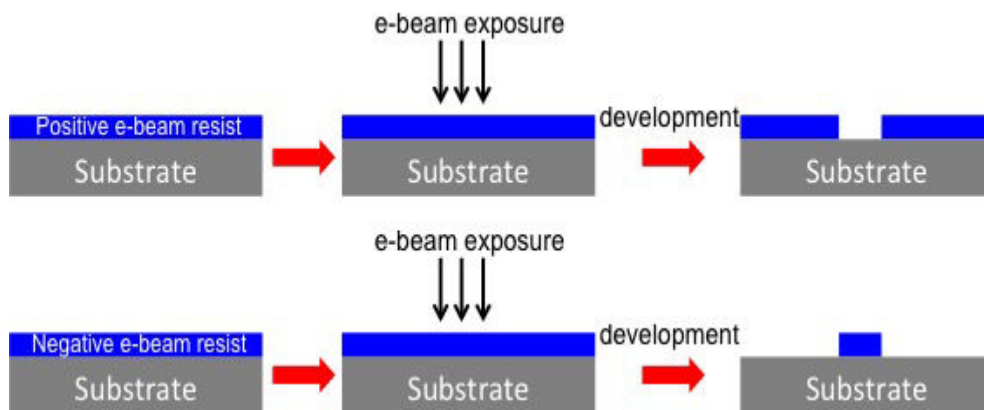


Figure 15: After development, either the exposed resist area or the unexposed one are dissolved, depending on whether the e-beam resist is positive or negative.

Depending on the positive or negative tone of the e-beam resist, after development it is either the exposed or the unexposed resist area respectively that is dissolved in the developer solution (Fig. 15). The choice between these two possibilities strictly depends on the desired structure.

For example, in order to fabricate plasmonic nanostructures, a bottom-up approach is normally preferred, and thus the metals are directly evaporated on a low-index substrate with Electron-Beam Physical Vapour Deposition (EBPVD) on which a positive-tone lithographic mask is patterned.

In contrast, for semiconductor fabrication, a top-down approach is preferable, and thus negative-tone e-beam resist are employed. In this case, especially for nanoscale structures, the patterns are instead transferred to the semiconductor with anisotropic vertical Reactive Ion Etching (RIE).

2.2.3 Electron-beam physical vapour deposition

In case of bottom-up approaches, the desired material, usually a metal, is directly evaporated on the whole surface of the sample through EBPVD. The underlying mechanism is the following: in a high-vacuum chamber ($\sim 10^{-8}$

mbar) a tungsten filament generates an electron beam by thermionic emission which are accelerated to a voltage of 9.37 kV.

Their trajectory is controlled with a magnetic induction field, and is directed towards a crucible shielded from the filament to avoid chemical contaminations, which contains the metal species of interest, with a purity as high as 99.99% (4N in industrial language). Once the electron beam hits the target metal, the local temperature increases up to a point in which the material starts to melt and then to evaporate, spreading itself in all directions.

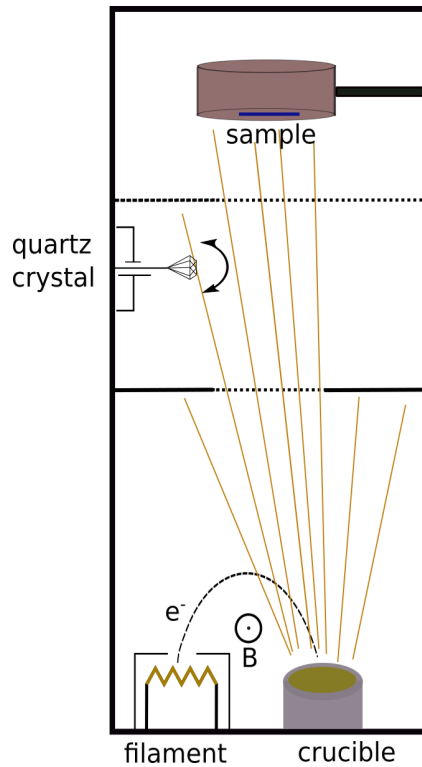


Figure 16: Schematics of a EB-PVD machine.

The access to a second chamber, kept a pressure of $\sim 10^{-7}$ mbar and containing the sample, is controlled by means of a shutter. Once the crucible temperature is high enough to generate the metal vapour, this first shutter opens. In the meantime, in the sample chamber, a constant potential is applied to a quartz, causing it to oscillate with a precise frequency.

As the metal vapour is injected into the sample chamber, its flow will cause a variation in the oscillation frequency. Measuring this difference allows to precisely control the deposition rate. Once the latter reaches the desired value, a second shutter opens and the metal vapour finally reaches the sample, on which it condenses and forms the thin metal layer. Deposition

uniformity is granted by a constant rotation of the sample holder.

Deposition rates can vary in a very wide range, from ~ 0.1 nm/s to ~ 1 $\mu\text{m/s}$, however especially for nanofabrication rates lower than one nanometre are preferable. The reason is twofold: the error on the deposition rate measured with the quartz crystal oscillation variation linearly increases with the rate itself; moreover the non-zero closing time of the shutters must be accounted for as well.

To give an idea of the numbers at play, in case of a 80 nm thin layer deposition at a rate of 0.1 nm/s, the final thickness uncertainty can be as high as ~ 5 nm. As the metal is deposited on the whole sample a subsequent step, called lift-off, is needed to keep the lithographic patterns only. This process is only applicable if and only if the resist thickness is higher than the metal layer thickness. The sample undergoes a hot solvent bath (usually acetone) at a temperature close to the boiling point of the employed chemical.

This causes the unnecessary metal to be lifted-off together with the residual resist. In this way the metallic lithographic patterns only survive this process. In case of Au deposition, a buffer Ti layer of a few nanometres is usually evaporated first to improve adhesion to the substrate and avoid the desired patterns to be lifted-up as well.

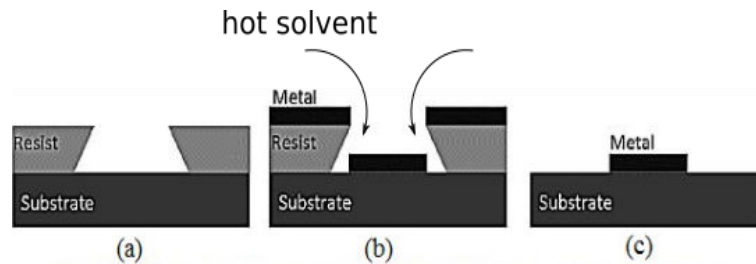


Figure 17: Schematics of the lift-off procedure. (a) Sample surface after EBL and development. (b) Thin layer deposition with EBPVD across the whole sample. (c) After deposition, the sample is placed in a beaker containing solvent at boiling temperature, which causes the residual resist and the metal in excess to be lifted-off.

2.2.4 Reactive ion etching

Once a negative-tone lithographic mask is defined with EBL and development, the patterns can be transferred on the material with anisotropic Reactive Ion Etching (RIE). In particular, I will focus my attention on a particular type of RIE, namely Inductively Coupled Plasma - Reactive Ion Etching (ICP), as it is the most frequently adopted in III-V nanofabrication.

The principle of an ICP machine is the following: the sample is placed

in a vacuum chamber with a load lock system. The high-density plasma is generated in a separated chamber under high-vacuum conditions by sending a Radio Frequency (RF) signal coming from the so called ICP source into a coil. The plasma is then injected into the sample chamber, in which it is submitted to a second RF signal coming from a different source (RF source) connected to the sample holder. This second RF accelerates electrons and ions of the plasma towards the sample.

As electrons have a higher mobility than ions, they strike the sample first, charging it negatively to a value called RF bias. Ions strike the sample in a second moment, performing mechanical sputtering [59].

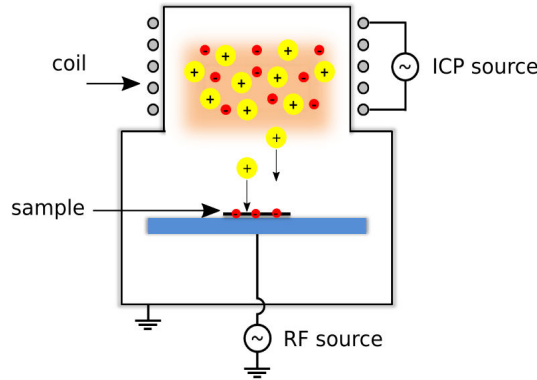


Figure 18: Schematics of an ICP-RIE machine. A high-density plasma is generated by sending a RF signal into a coil. The plasma is then injected into a separated chamber in which a second RF accelerates electrons and ions in the plasma towards the sample.

In reality however, the etching mechanism is much more complex than the sole sputtering, and in most cases a chemical component must be considered as well. The gases we use in our protocols are Argon (Ar) and silicon tetrachloride (SiCl_4). The ICP source ionizes them into Ar^+ and SiCl_4^+ , however collisions within the plasma produce SiCl_x^+ and SiCl_x neutral free radicals. The latter can react chemically with GaAs and AlGaAs.

Even though the sample temperature is kept constant at 10°C during the ICP procedure and this temperature is normally not sufficient to trigger chemical reactions between AlGaAs and the free radicals, the ions locally change the temperature of the surface through collisions, thus enabling the free radicals to chemically react. Despite this chemical component, in our case the mechanical impact of the ions prevails, resulting in rather vertical sidewalls.

In principle, protocols can be optimized to boost chemical reactions on the surface and obtain partially isotropic etchings (see for example [60]).

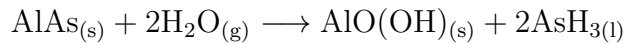
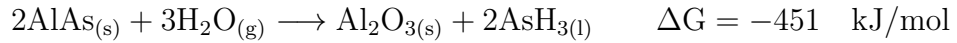
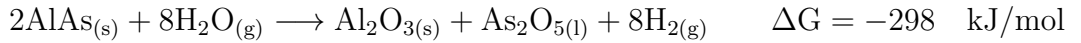
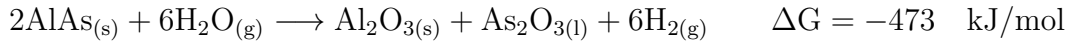
Ions actually play a twofold role in ICP: the products of the reaction between SiCl_x radicals and AlGaAs may not be volatile enough to leave the surface and allow the following “wave” to react. Ions also induce desorption of reactants by mechanical collisions, allowing for a new “wave” of radicals to react.

The role of accelerated ions is therefore double in the etching process. It is important to stress that a pure mechanical etching with Ar gas would not be efficient in our case, as the etching rates of the resist mask and AlGaAs would be the same. This would require a thicker resist than the layer to etch, worsening the resolution.

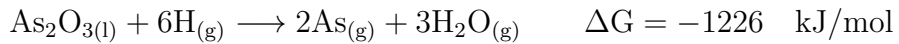
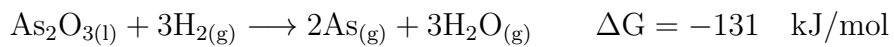
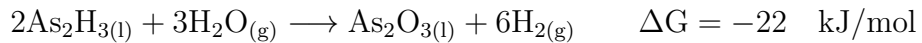
2.2.5 Selective oxidation

Qualitatively speaking, the thermal wet oxidation of AlGaAs enables to eject As atoms from AlGaAs crystal, which combine with water or hydrogen atoms from water, and obtain low-index amorphous AlO_x .

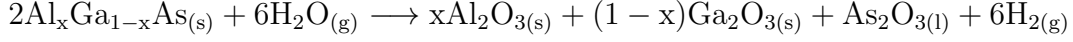
A quantitative model in case of AlAs has been developed in the last two decades, based on Raman spectroscopy [61, 62, 63], secondary-ion mass spectrometer [64] and X-ray absorption fine-structure spectroscopy [65] measurements. All these efforts allowed the community to come up with the following set of equations:



where ΔG is the Gibbs free-energy variation during the process calculated at a temperature of $\sim 700 \text{ K}$ ($\sim 400 \text{ }^\circ\text{C}$), and its negativity ensures the thermodynamic favourability of the reaction. These first stage reactions happen in the so-called “oxidation front” region and have as a by-product the formation of AsH_3 , As_2O_3 and As_2O_5 molecules. These are unstable at 700 K and almost completely degrade into As atoms, which in turn are highly volatile and evacuate through diffusion channels open in the generated amorphous oxide.



Experimental analysis of $\text{Al}_x\text{Ga}_{1-x}\text{As}$ in the range $0.9 < x < 1$ has led to the following modification [66]:



It was also shown that in this case, especially near the interface with the GaAs substrate, the As atoms can form amorphous precipitates, according to [66];



The presence of such precipitates has been shown to alter the AlOx optical properties, including a two-order of magnitude increase in the leakage current and up to 30% increase in the material relative permittivity for $x=0.9$. The employment of $\text{Al}_x\text{Ga}_{1-x}\text{As}$ with $x=0.98$ proved instead to mitigate such effects, with in particular a relative permittivity increase of 7%.

In order to formalize the evolution of the oxidation process, a phenomenological model was developed, following a previous work on Si oxidation [67]. The model assumes that the time $t_{ox}(x)$ necessary to obtain an oxide layer of thickness x is given by the sum of the time necessary to diffuse the oxidant species at the semiconductor/oxide interface situated at the position x , and the typical duration of the chemical reaction:

$$t_{ox}(x) = t_{diff}(x) + t_{reac}(x) \quad (2.9)$$

The two terms in the right side of the equation depend on the thickness x itself and by two parameters A, B in the following way:

$$t_{ox}(x) = \frac{x^2}{A} + x\left(\frac{B}{A}\right)^{-1} \quad (2.10)$$

where A is proportional to the diffusion coefficient D , and B/A is a function of the reaction constant and of the transfer coefficient of the oxidant. As a consequence, the dependence of these two parameters on the temperature will follow the Arrhenius law, as expected from a diffusive process:

$$A = A_0 \exp(-E_a/k_B T) \quad (2.11)$$

$$\frac{B}{A} = \frac{B_0}{A_0} \exp(-E_a/k_B T) \quad (2.12)$$

where k_B is the Boltzmann constant, and E_a is the activation energy, which for this process is usually $\sim 1.5\text{eV}$ [7]. The oxidation rate also depends on various other factors. Most importantly, an exponential drop in the oxidation rate with decreasing Al molar content, which is almost 0 for Al molar

fractions < 0.8 [94, 97, 7] can be appreciated (Fig. 19).

As it will be clear in the next chapter, this feature has been widely exploited in AlGaAs-on-AlOx photonic platforms. In accordance to this, a Transmission Electron Microscope (TEM) analysis of our $\text{Al}_{0.18}\text{Ga}_{0.82}\text{As}$ structures on AlOx showed that, while the $1\ \mu\text{m}$ $\text{Al}_{0.98}\text{Ga}_{0.02}\text{As}$ layer is entirely oxidised, only a few nm oxide layer is present on the nanoantenna surface [70].

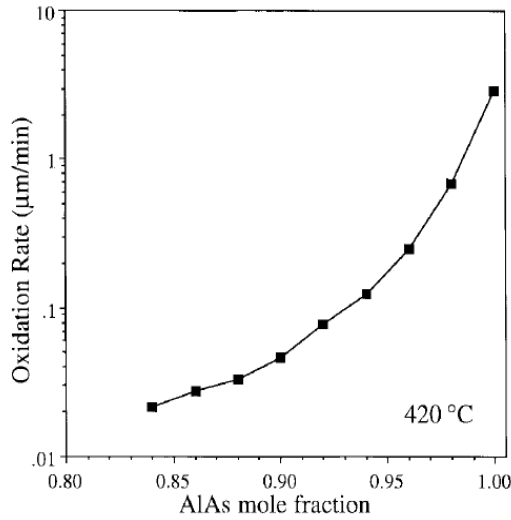


Figure 19: Exponential dependence of the oxidation rate on the Al percentage in the alloy. *The plot is reproduced from [7].*

The oxidation rate was also shown to weakly depend on the layer thickness [7], however when the latter is larger than $\sim 60\text{nm}$ the rate is basically constant (Fig. 20).

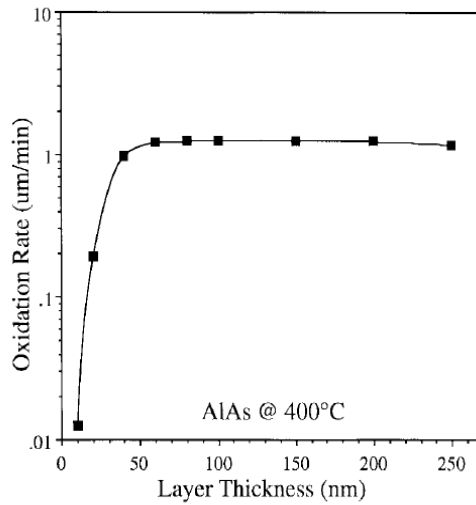


Figure 20: Dependence of the oxidation rate on the layer thickness. For $t > 60\text{nm}$ the plot is almost constant. *Plot taken from [7].*

A less important aspect is represented by the carrier gas, which has been shown to weakly affect the oxidation rate as long as it is not O_2 , which completely suppresses AlGaAs oxidation [7]. Conversely, the temperature of the humid gas mixture consisting of water vapour and carrier gas has a considerable impact, and experiments suggest the adoption of temperatures larger than 90°C , while its flow does not have a significant impact above a certain threshold [7].

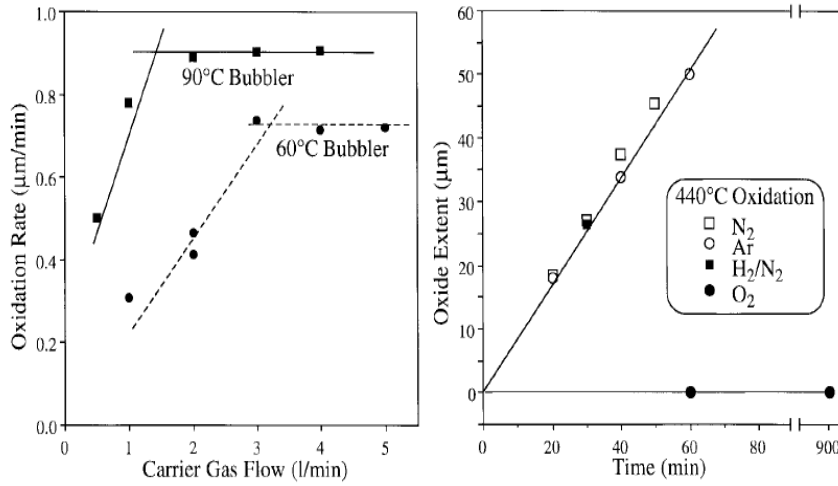


Figure 21: Impact of gas carrier on oxidation. Left: the gas flow does not affect the process after a certain threshold, while a higher temperature ensures a larger oxidation rate. Right: the species of the carrier have a negligible effect apart from O_2 , which completely suppresses the process. *The plot appears in ref. [7].*

Finally, other studies have highlighted the influence of other physical parameters on the oxidation rate, such as composition and thickness of the adjacent layers, which have an impact on the interface strain caused by the volume reduction in controlled oxidation [94]. Interestingly indeed, in controlled oxidation processes, the volume shrinks [71]. In addition, it was shown that the oxidation direction relative to the main crystallographic axes [68], and the doping type [69] can play a role as well.

The dependence of the oxidation rate on this high number of parameters makes it difficult to a-priori predict the oxidation velocity of a given system. For this reason, the oxidation protocol must be carefully calibrated on every desired device. Our oxidation system consists of an oven in which samples

are placed on a carbon holder and kept in vacuum conditions (Fig. 22). The carbon holder supports temperature ramps as high as $40\text{ }^\circ\text{C}/\text{min}$, allowing to reach the desired oxidation temperature (usually $390\text{ }^\circ\text{C}$) in less than 1h.

While the temperature is ramping, the atmosphere inside the chamber is kept constant at 500 mbar by balancing the injection of N_2 and $\text{N}_2:\text{H}_2$ dry gases and vacuum pumping. The humid gas is prepared by injecting in a controlled evaporator mixer at $95\text{ }^\circ\text{C}$ de-ionised water (liquid state) and $\text{N}_2:\text{H}_2$ gas. Once the desired oxidation conditions are met, the humid gas is injected in the chamber and the oxidation begins. The process is monitored with an in-situ optical microscope, enabling the observation of the lateral oxidation front advancement (Fig. 22).

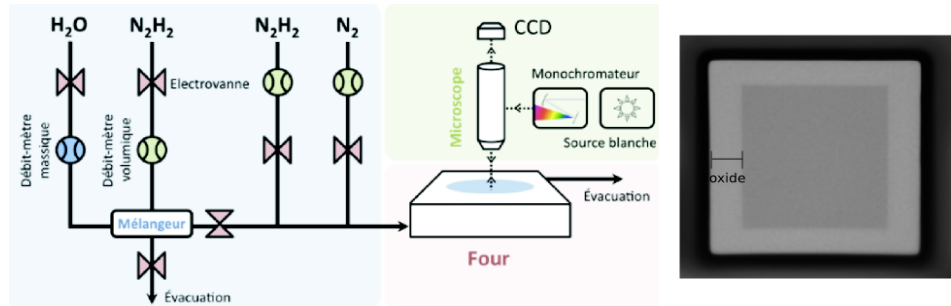


Figure 22: Left: scheme of our oxidation machine. Right: microscope image showing the oxidation front advancing under the structures with low-Al content.

2.3 Experimental methods

Finally, this section will describe the main experimental techniques used during my thesis to investigate the linear and nonlinear response of AlGaAs nanostructures, i.e. Confocal optical microscopy, Back Focal Plane (BFP) imaging and CL spectroscopy.

2.3.1 Confocal optical microscopy

Among all near-field and far-field optical microscopy techniques the one we mainly employed to probe the nonlinear response of AlGaAs nanostructures is the confocal optical microscopy [72]. The setup idea was patented in 1957 [73] and works in epi-illumination, which is the most suitable for samples fabricated according to chapter 2. The principle is the following: collimated light (laser for example) is focused on the sample of interest (point illumination), with a minimum spotsize depending on the Numerical Aperture (NA)

and incoming wavelength according to Abbe's law:

$$\Delta x_{min} = 0.61 \frac{\lambda}{NA} \quad (2.13)$$

The sample emits scattered light at the wavelength λ (elastic scattering) and, in the case of our interest, fluorescence and nonlinear light as well. All the light is collected through the same lens and a Dichroic Mirror (DM) is used to separate the fundamental from the harmonic wavelength. Finally the detection occurs in an optically conjugate plane with a pinhole in front of the detector to eliminate out-of-focus signal.

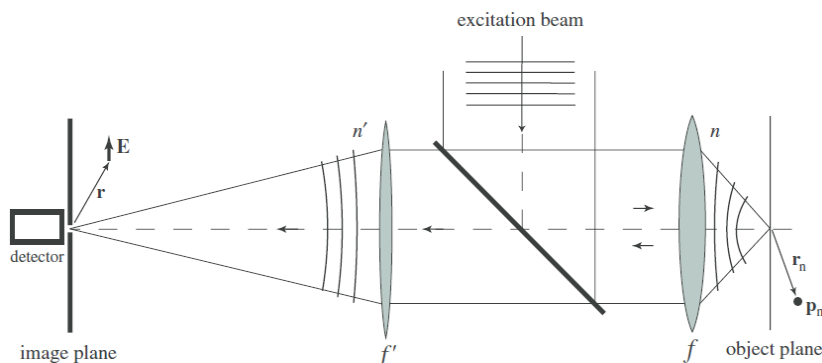


Figure 23: Sketch of a typical confocal optical microscopy setup in reflection geometry [72]. An excitation beam is focused with a lens on a sample placed in the object plane. The light scattered by the sample is collected with the same lens, separated from the pump with a DM, and then focused with another converging lens on a detector. A pinhole is placed just before the detector to improve lateral resolution. *The scheme is reproduced from [72].*

The advantage of this setup is twofold: placing the sample in the focal plane of the lens greatly increases axial resolution, while placing a pinhole in front of the detector enhances lateral resolution [72].

2.3.2 Back focal plane imaging

Although confocal microscopy is a powerful tool to optically characterize objects at the nanoscale, it does not allow to directly visualize the radiation pattern generated by a nanostructure. Among all possible techniques that can be used to this end, I will only detail about BFP imaging, which is a powerful tool we often resorted to in our experiments. Let us consider as a starting point the standard confocal microscopy setup (Fig. 24). In order to get an emission pattern of our nanostructures an experimentally “easy” way

is to try to image the objective BFP with a camera. This can be done using the basic components of Fourier optics, i.e. Bertrand Lens (BL), also called Fourier Lens (FL), and Tube Lens (TL).

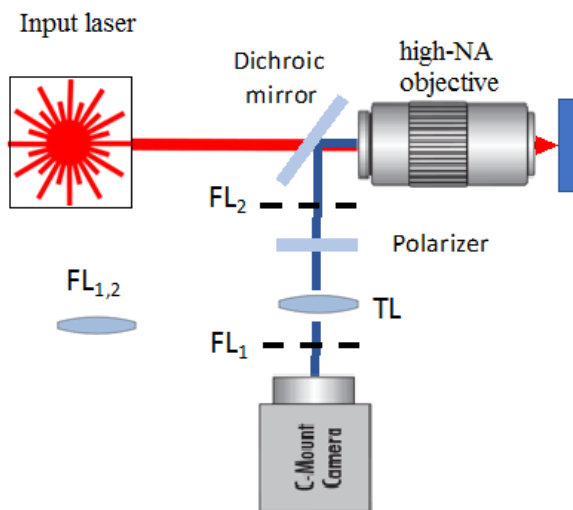


Figure 24: Confocal inverted microscope modified for BFP imaging by adding Fourier optics components, that is TL and FL (also called BL).

Usually a single TL, combined with a single BL are sufficient to effectively image the BFP. As such, there are two possible configurations [74]: in the first one a TL takes the parallel rays coming out of an infinity corrected high-NA objective, and focuses them onto an intermediate image plane, forming a real-space image. The addition of a BL one focal length before the image plane allows to perform a Fourier transform of the object, without changing the position of the conjugate plane. Thus, by placing a detector at its focal length we can effectively re-image the BFP of the objective (Fig. 25(1)).

Interestingly this allows to simply switch between real and Fourier by removing or adding the BL without changing the position of the other optics. In this first configuration however the focal length of the BL is limited to be ≤ 5 cm due to finite accessible space before the image plane, thus hindering the magnification of the BFP image. To overcome these constraints more optics are needed, which however increase the alignment difficulty and decrease the error tolerance.

On the other hand if we still stick to our TL-BL two-lens system, we can overcome all above mentioned limitations by placing the BL between objective and the TL, such to directly focus on the objective's BFP (Fig. 25(2)). The advantage of this configuration compared to the first one is that

it allows for more BFP magnification flexibility, without having to add other optical elements and introduce more curvature or tolerance complications.

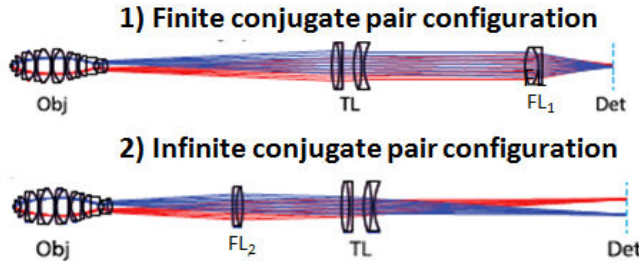


Figure 25: The simplest BFP imaging system only involves a BL and a TL forming a conjugate pair to focus the BFP of an infinity corrected objective onto a detector. In configuration (1) the FL is placed one focal length before the image plane of a TL, while in configuration (2) the FL is placed in the infinity space between objective and TL. This second configuration has a two-fold advantage with respect to the first: improved magnification and stability, due to the fact that in this case the lenses form an infinite conjugate pair. *Figure extrapolated from [74].*

The advantage of the second configuration is motivated by the fact that in this case the BL directly images the objective BFP, therefore forming an infinite conjugate pair with the TL, whereas in the previous configuration they form a finite conjugate pair [74]. Finally, configuration (2) also provides a major advantage during alignment, as deviations in the position of the BL only cause defocusing, while in configuration (1) perturbing the position of the BL causes distortion as well.

2.3.3 Cathodoluminescence spectroscopy

Cathodoluminescence (CL) is the emission from a material in the ultraviolet, Visible (VIS) and Near Infrared (NIR) regions of the electromagnetic spectrum upon fast free electron irradiation, with energies in the range 0.5 keV-300 keV [75]. This definition is of course very broad as many distinct physical effects can give rise to such emission depending on the properties of the material under study.

Traditionally, the physical processes giving rise to CL can be grouped into two main classes: incoherent and coherent emissions. In incoherent CL the phase relation with the excitation is not constant, and as such the emitted light is incoherent, unpolarized and isotropic. This class includes for example situations where valence electrons are promoted to an excited state from which it radiatively decays by emitting a photon.

In coherent CL, conversely the emission and excitation maintain a constant phase relation, with the consequence that the former is strongly polarized. What happens in this case from a physical point of view is that the electron, that is a moving point charge, is accompanied by evanescent vertical and radial electric field (assuming sample illumination at normal incidence) and an azimuthal magnetic field. When such electron sees a change in the background dielectric function, for example at the interface with the sample, these fields can polarize the material, and subsequently light is emitted.

What is attracting for coherent CL is that electromagnetic modes supported by the local structure of the sample can be excited as well, including SPP, LSP, waveguide modes and Mie resonances. Such kind of excitation can be modelled as a vertical electric point dipole aligned along the direction of the e-beam current [76]. The reason for this is that as an electron passes across the interface with the sample, it approaches its image charge, which effectively results in a radiating vertical dipole [77].

Due to the high localization brought about by the very small electron wavelength compared to the nanostructures, it is possible to excite modes that are momentum and symmetry-forbidden for a plane wave [78]. Finally, it is worth noting that CL imaging provides information exclusively on radiative modes [79], so for example the presence of any anapole states cannot be detected with this technique. Non-radiative modes could in principle be detected with Electron Energy Loss Spectroscopy (EELS), which instead couples to the full Electromagnetic Local Density of States [79].

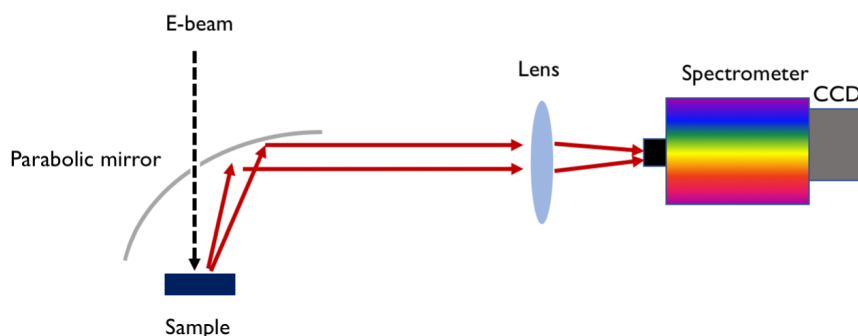


Figure 26: CL spectroscopy experimental setup. An electron beam passes through a hole in a parabolic mirror, and impinges on the sample. The resulting CL emission is collected by the same parabolic mirror and redirected into a VIS/NIR spectrometer.

The CL system employed (SPARC, Delmic) consists of a focused 30 keV electron beam scanning the sample surface. Upon e-beam illumination, the locally excited modes subsequently radiate into the far-field, and their signal is collected by means of a parabolic mirror and directed into either a Si (for the VIS) or an InGaAs (for the NIR) spectrometer (Fig. 26).

2.4 Conclusion

This chapter has described the main numerical, technological and experimental techniques employed throughout my PhD. In the following chapter I will explain how the aforementioned fabrication techniques were used to realise a monolithic AlGaAs-on-AlO_x monolithic photonic platform.

Chapter 3

AlGaAs-on-AlO_x monolithic platform

This chapter aims at describing the technological efforts that have been undertaken to achieve an effective monolithic fabrication of AlGaAs-on-insulator micro and nanostructures. The chapter is organized in the following way: a motivation for this kind of study will first be given, as well as a summary of all the achievements in this field in the last decades; finally a detailed description of the fabrication procedure will be given.

3.1 AlGaAs integrated platform: state-of-the-art

When talking about integrated photonics materials the first thing that comes to mind is SOI. Indeed this platform has been to date the most successful and popular even at an industrial level in both linear and nonlinear PIC [93]. The reason of its success is mainly due to the high field confinement in Si structures, provided by a significant index contrast ($n_{Si} \simeq 3.5$, $n_{SiO_2} \simeq 1.4$ in the NIR).

However, its applications in nonlinear photonics are limited by TPA at telecommunications wavelengths ($1.55 \mu\text{m}$), as no means are currently known to engineer the bandgap of the material (1.1eV). Moreover, as silicon is a centrosymmetric material, it does not allow for second order nonlinear optical mixing. These two limitations have hindered so far the demonstration of optically active components in SOI platforms, slowing down the route towards low-power all-optical computation.

To bridge this gap, different TPA-free non-centrosymmetric materials have been studied, such as lithium niobate (LiNbO_3). In this case however,

its non-stoichiometry complicates the material processing, and its relatively low quadratic nonlinearity ($d_{33} \simeq 27$ pm/V [80]) limits the miniaturization possibilities of integrated chips. On the other hand, aluminium gallium arsenide ($\text{Al}_x\text{Ga}_{1-x}\text{As}$, where $0 < x < 1$), a III-V zinc-blende semiconductor, is a rather promising nonlinear material for the following reasons:

- it has a huge second-order nonlinear coefficient ($d_{14} \simeq 100$ pm/V at $1.55 \mu\text{m}$), and its third-order nonlinearity is comparable to that of silicon ($n_2 \simeq 1.5510^{-13}$ cm²/W).
- Its bandgap can be engineered by modulating the Al molar concentration x , so as to avoid TPA at $1.55 \mu\text{m}$ for $x \geq 0.18$ ($E_g = 1.424 + 1.266x + 0.26x^2$ eV, for $x < 0.45$). Moreover the gap is direct for $x < 0.45$, enabling electrical pumping.
- Its transparency window spans from the VIS to the mid-IR ($0.9 \div 16 \mu\text{m}$).
- Its laser fabrication technology is at a mature stage.

AlGaAs nonlinear platform has attracted the interest of researchers worldwide for at least two decades. Among all different fabrication techniques that have been developed we can distinguish two main approaches: on the one hand we have the monolithic approach, based either on the selective oxidation of an Al-rich layer to achieve a low-index substrate, or on the refractive index variation in $\text{Al}_x\text{Ga}_{1-x}\text{As}$ as a function of x , or on air suspended structures exploiting selective chemical etching.

In all these cases the aim is to obtain a sufficiently high index contrast, and therefore a good field confinement in a nonlinear AlGaAs active layer. On the other hand we have non-monolithic techniques, among which we can distinguish Epitaxial Lift-Off (ELO) procedures and wafer bonding methods to report the AlGaAs structures on a low-index substrate (usually glass). In the next session I will provide a quick review of what has been achieved with all these methods and highlight the approach developed in our group, which relies on selective wet oxidation.

3.2 Non-monolithic approaches

We can start our review on AlGaAs integrated platforms by looking in detail at what has been achieved with non-monolithic fabrication methods. In this case we can distinguish between ELO and wafer bonding.

3.2.1 Epitaxial lift-off

This technique was first developed in the ‘80s for solar-cell applications [81], and it begins with the epitaxial growth of an active (Al)GaAs layer with low Al content on top of a GaAs substrate and a sacrificial AlAs layer sandwiched between them. The sample is then plunged into HF acid, which selectively attacks AlGaAs layers, while leaving GaAs layers untouched, with an etching rate that sensibly grows with the Al content x in the AlGaAs blend [82]. As the AlAs sacrificial layer gets eroded by the acid, the active layer we are interested in detaches from the substrate and forms a thin film. Finally the desired pattern is transferred on the active layer with standard lithographic processes (Fig. 27). Such approach has been successfully applied to nanophotonics, with the demonstration of zero linear backscattering from GaAs nanoparticles [85]. The main drawback of this technique is that of

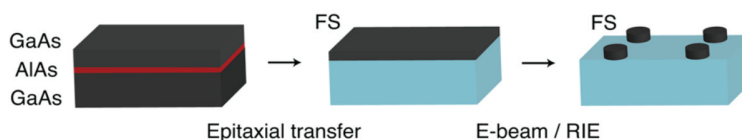


Figure 27: Fabrication procedure of GaAs nanoparticles on fused silica (FS) using the ELO technique. *Scheme reproduced from [85].*

the interaction of HF with the AlAs sacrificial layer can leave some AlF_3 or $\text{AlF}(\text{H}_2\text{O})$ impurities on the sample, which could be detrimental for some applications. To overcome this problem, the usage of lattice-matched sacrificial layers of materials such GaInP [83] or InAlP [84] has been shown to improve the quality of the fabricated films, with the surface mean squared roughness decreasing from $\sim 3\text{nm}$ for AlAs, to less than a nanometre (Fig. 28)

3.2.2 Wafer bonding

Other AlGaAs non-monolithic methods were also developed with the wafer bonding technique. In this process two sufficiently flat and clean surfaces are bond to each other with the help of an external applied pressure. In some cases this bonding is direct, not mediated by any surface activation. However, as AlGaAs does not glue well to glass, people have relied on the adhesive properties of Benzocyclobutene (BCB), a transparent polymer with a refractive index $n \approx 1.45$, which is compatible with optimal optical measurements.

Thanks to this method, efficient SHG from AlGaAs nanoantennas em-

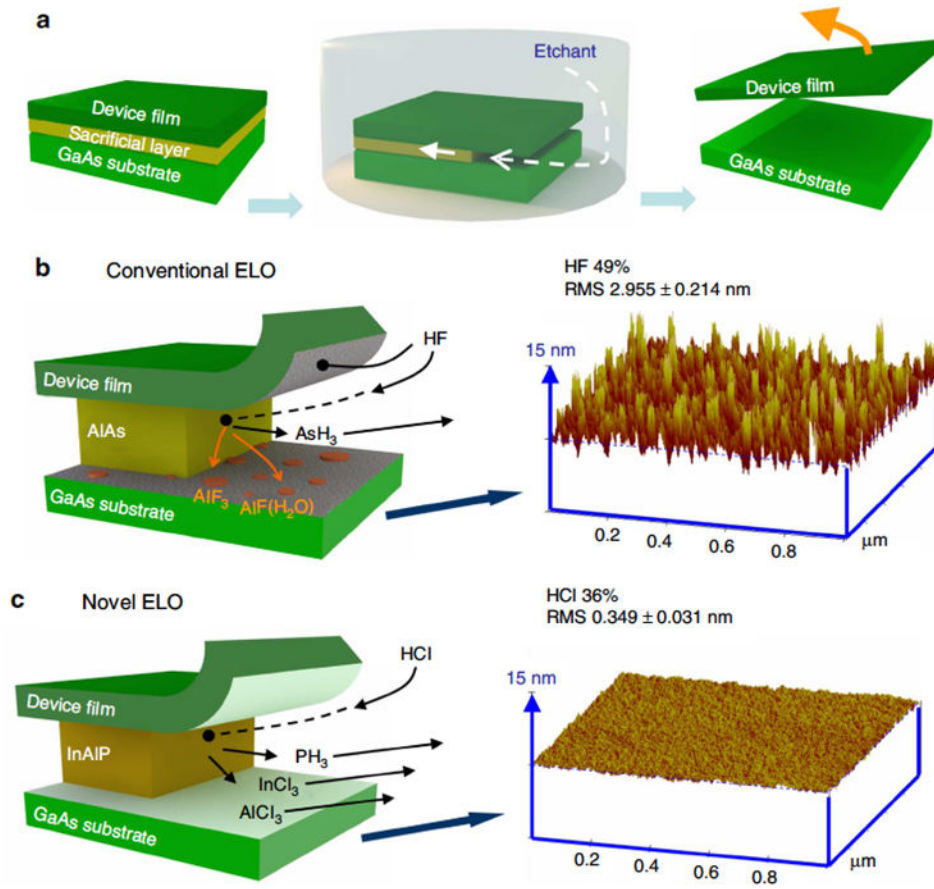


Figure 28: (a) Schematics of ELO procedure. (b) Case of AlAs sacrificial layer [81]. (c) Case of GaInP and InAlP sacrificial layers [83] [84].

bedded in a thin glass substrate was demonstrated [38]. In this work the nanoantenna pattern is first defined on an AlGaAs layer with EBL, followed by ICP. Afterwards, a Cl_2 -based chemical treatment, combined by HF-etching of an AlAs sacrificial layer, makes the sample surface non-adhesive, in a similar fashion to ELO. The nanoantennas are then embedded in BCB, which mediates the wafer bonding to a glass substrate, and finally the sample is peeled-off the GaAs substrate. Alternatively, the inverse strategy can be adopted as well, that is to perform the wafer bonding on a SiO_2 substrate first, and then pattern the AlGaAs layer at a later stage [86]. In this work, M. Pu and co-workers have also employed a GaInP sacrificial layer rather than an AlAs one, with all above mentioned benefits.

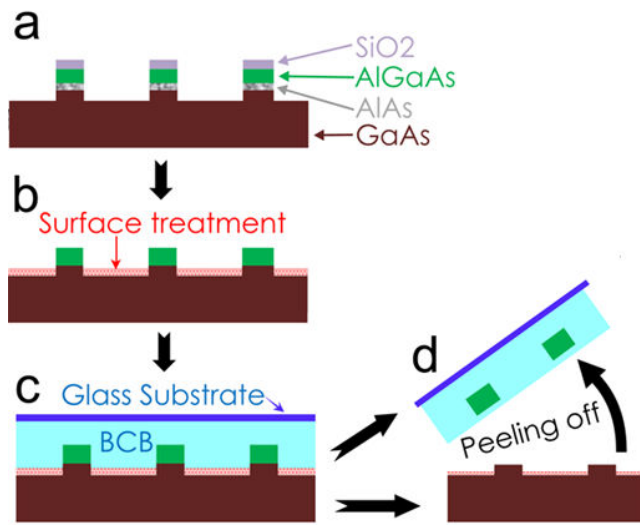


Figure 29: Fabrication protocol based on wafer bonding to obtain AlGaAs nanostructures embedded in glass. *The scheme is reproduced from ref. [38].*

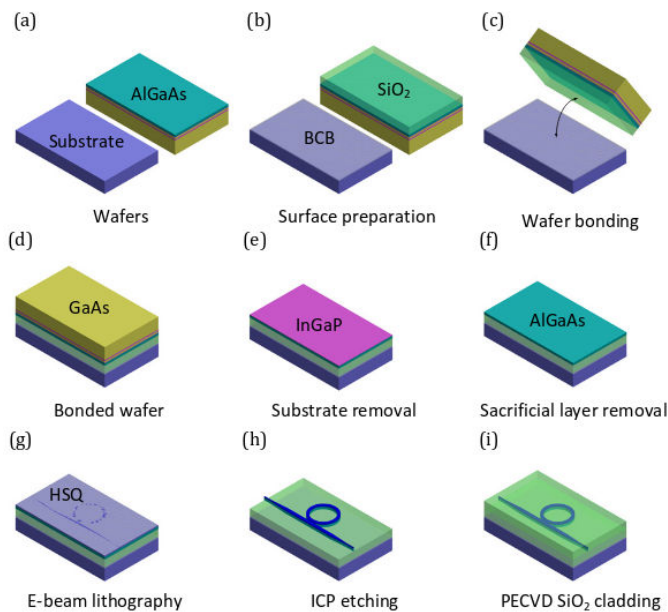


Figure 30: Alternative wafer bonding procedure, in which the wafer bonding step is performed before the structure patterning. *The figure is taken from [86].*

This process enabled the demonstration of efficient frequency-comb generation in AlGaAs waveguide+microring systems [86]. Despite the great success

of non-monolithic approaches, they entail a considerable technological burden, represented by the great number of steps needed, bonding processes and chemical treatments, which make the protocol reproducibility quite challenging.

Indeed all cleanroom users know that the more you process a sample, the more impurities are formed and the more the error probability increases, as well as the cost. For all these reasons, a monolithic fabrication process is preferable, provided that the number of steps and the burden imposed on the sample are decreased.

3.3 Monolithic approaches

The simplest monolithic approach developed so far takes advantage of the refractive index change in $\text{Al}_x\text{Ga}_{1-x}\text{As}$ as a function of the Al molar fraction x . This variation happens because the refractive index is related with the bandgap via the Kramers-Kronig relations [17]. Thus, the monotonic variation of the AlGaAs bandgap on the Al molar fraction implies the same kind of dependence on x of its refractive index.

The extremal values are exhibited by GaAs ($x = 0$) and AlAs ($x = 1$), corresponding to $n_{\text{GaAs}} \simeq 3.5$ and $n_{\text{AlAs}} \simeq 2.9$ respectively [87]. Usually however the maximum employed value of x is 0.7 ($n \simeq 3.1$), as greater values would imply high reactivity with air and native oxidation issues. Following this principle, two independent groups realised in 2011 AlGaAs monolithic waveguides consisting of stacked AlGaAs layers with different molar concentration for efficient, low-pump FWM [88], and SHG [89]. In both cases, the stacking was engineered so as to have high field confinement in a low-Al layer ($x = 0.18$ in [88], $x = 0.2$ in [89]), with TPA-free operation at 1550nm, by sandwiching it between two higher- x , i.e. lower refractive index, layers.

The main limitation of this approach however is that the vertical index contrast did not exceed $\Delta n \approx 0.2$, which is considerably lower than the $\Delta n \approx 1.6$ achieved in non-monolithic platforms based on wafer bonding and ELO. The consequence is that in order to properly confine the electromagnetic field inside the active region, etchings deeper than 1 μm are needed, limiting the miniaturization of the structures due to aspect-ratio issues.

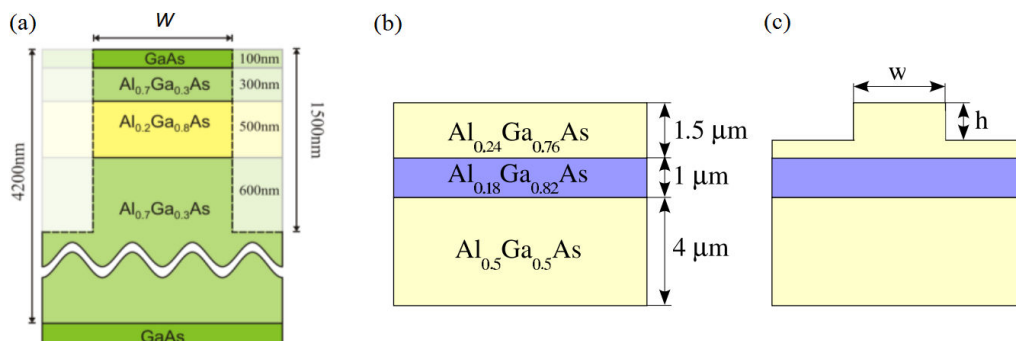


Figure 31: (a) All- $\text{Al}_x\text{Ga}_{1-x}\text{As}$ monolithic waveguides for low-power SHG. Figures reproduced from [89]. (b),(c) A similar monolithic platform engineered to demonstrate FWM. *These schemes appeared in refs. [88].*

A high-contrast monolithic all-AlGaAs platform has been developed as well, by exploiting the above mentioned selectivity of HF etching with respect to Al concentration [82]. The idea of this approach is to pattern the desired structures on low Al-content layers ($x \sim 0.2$) to again avoid TPA at $1.55 \mu\text{m}$, and to resist the HF attack, which in contrast almost completely erodes an Al-rich substrate (usually $x \sim 0.8$), only leaving a few anchoring points to maintain the structure suspension in air. This technology was developed at the MPQ lab, of Université Paris Diderot, and has lead to the demonstration of CW-driven SHG on AlGaAs waveguides fully-suspended on air [22]. Similar results were obtained with low-Al AlGaAs microdisks on an optically negligible pedestal supporting high-quality factor whispering gallery modes [91].

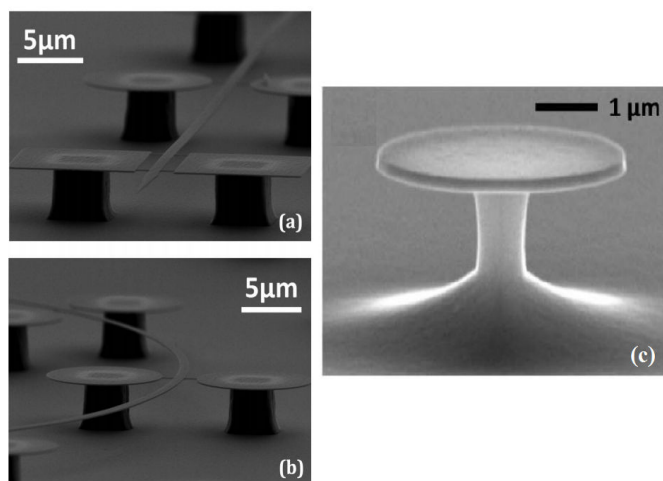


Figure 32: (a),(b) Fully suspended monolithic AlGaAs waveguides on air obtained by selective etching of an Al-rich layer with HF [22]. (c) Low-Al

content AlGaAs microdisks sustaining high-quality-factor whispering galley modes obtained with the same principle [91].

Despite the great field confinement achieved via this approach, the suspended structures are quite fragile, limiting the reproducibility of the process.

By exploiting yet another property of $\text{Al}_x\text{Ga}_{1-x}\text{As}$ that varies with the Al molar fraction x , that is the thermal wet oxidation rate [94], a third monolithic platform is possible, with an index step almost as high as the suspended-in-air structures, but without the fragility drawback. The idea is to pattern the optically relevant structures on a low-Al-concentration AlGaAs layer, resting on an Al-rich substrate. In such way wet oxidation produces a low-index AlOx substrate, while leaving the active structures basically unoxidised. Starting from the early '90, wet thermal oxidation of AlGaAs has been largely studied from a material science point of view [94, 95, 96, 97].

More recently, there have been a few groups specifically interested in AlOx as a low-index substrate for AlGaAs nonlinear photonics. Two of them, based in Stanford and Japan, focused on the fabrication and characterization of nonlinear waveguides consisting of an $\text{Al}_{0.5}\text{Ga}_{0.5}\text{As}$ core and a thick AlOx substrate, while a third one, based in Indiana, worked on full-oxide $(\text{Al}_x\text{Ga}_{1-x})_2\text{O}_3/(\text{Al}_y\text{Ga}_{1-y})_2\text{O}_3$ waveguide heterostructures. Stanford's group was the first to demonstrate SHG in such heterostructures driven by form-birefringence phase-matching [98], followed a few years later by the Japanese [99].

However both demonstrations suffered from high losses (> 20 dB/cm at the fundamental frequency (FF) and > 250 dB/cm at the SH), mainly due to interface defects, which are in turn caused by mechanical strains during the oxidation procedure [100]. In order to smoothen this effect it was proposed to slow down the oxidation kinetics by reducing the Al molar fraction in the AlGaAs layers to be oxidised from 0.93 to 0.8 [101]. Nonetheless, to our knowledge, no further literature demonstrating this prediction was published later. As for the full-oxide approach, losses as low as 3.6 dB/cm were measured [102], but no SHG measurement is feasible. In any case, the linear losses obtained in the above cited works were never as low as 1.4 dB/cm, that is the value measured in the wafer-bonded AlGaAs-on- SiO_2 waveguides [86].

More recently, this concept was translated as well to nanopillars including GaAs confining layers and $\text{Al}_{0.8}\text{Ga}_{0.2}\text{As}$ buffers, which are oxidized at a later stage [90]. In this case as well thicknesses no bigger than ~ 300 nm are demonstrated. Summing up, the main limitation of the wet oxidation based monolithic approach is the mechanical strain induced at the semiconductor/oxide interface, hindering both the AlOx layer maximum available

thickness, and the structure performances. Despite these limitations, an integrated OPO operating at $1.55\mu\text{m}$ was demonstrated on subwavelength-stacked GaAs/AlOx waveguides [103].

Finally, we developed in our group a monolithic fabrication technique to efficiently obtain $\text{Al}_{0.18}\text{Ga}_{0.82}\text{As}$ micro/nano-structures on a thick ($1\mu\text{m}$ - $2\mu\text{m}$) AlOx layer without any strain-induced wild delamination of the active layer [92]. The fabrication procedure is the following (Fig. 33):

- Starting from a [100] non-intentionally doped GaAs wafer, we grow $1\mu\text{m}$ of $\text{Al}_{0.98}\text{Ga}_{0.02}\text{As}$ and 400 nm of $\text{Al}_{0.18}\text{Ga}_{0.82}\text{As}$ with MBE.
- We define our structures on the $\text{Al}_{0.18}\text{Ga}_{0.82}\text{As}$ layer with EBL, followed by dry ICP, revealing the $\text{Al}_{0.98}\text{Ga}_{0.02}\text{As}$ layer.
- We selectively oxidise the Al-rich layer under water vapour flow at 390°C for 30 minutes.

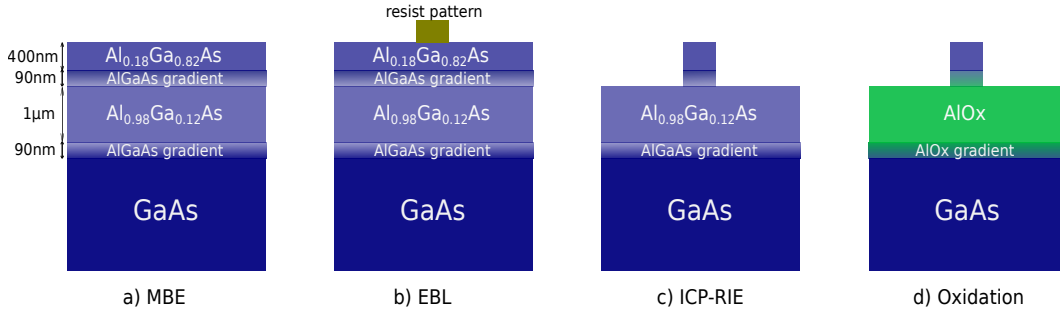


Figure 33: Fabrication procedure of our monolithic AlGaAs-on-AlOx platform. a) Molecular beam epitaxy (MBE). b) Electron beam lithography (EBL) defines the resist pattern on the top layer. c) The patterns are transferred on the $\text{Al}_{0.98}\text{Ga}_{0.02}\text{As}$ layer with inductively coupled plasma-reactive ion etching (ICP), revealing the Al-rich layer. d) The latter becomes low-index AlOx with selective oxidation.

The novelty of our method rests on the use of two 90 nm AlGaAs layers with linearly increasing/decreasing Al molar fraction sandwiching the Al-rich layer to be oxidised. In this way, the smooth transition between the amorphous AlOx and the crystalline AlGaAs layers solves the problem of mechanical stress on the micro/nano-structures, which was the most prominent hindering factors of the previous works. The fabrication procedure will be detailed in the next section.

3.4 Monolithic AlGaAs-on-AlOx platform: fabrication

This section will delineate the fabrication procedure developed by Oleksandr Stepanenko during his postdoc year at the MPQ Laboratory and the modifications I made in order to push forward the platform into the nanoscale.

3.4.1 Original fabrication protocol

MBE epitaxial wafers are grown in C2N lab in Marcoussis, by Aristide Lemaître and coworkers. Their typical structure consists of the following layers (from bottom to top):

- (100) non-intentionally doped GaAs wafer, with typical diameter of 2" (≈ 5 cm).
- 500 nm GaAs buffer.
- 90 nm AlGaAs transition layer with Al content linearly increasing from 5% to 98%.
- 1000 nm AlGaAs 98%.
- 90 nm AlGaAs transition layer with Al content linearly decreasing from 98% to 18%.
- Either 200 or 400 nm AlGaAs 18%.
- PMMA resist layer to prevent oxidation over time.

Starting from this epitaxial structure, a sample of ~ 1 cm² is cleaved with a diamond tip and undergoes a standard cleaning procedure. Organic residues and surface contaminants are removed with 3 min ultrasound bath first in acetone and then in isopropanol, followed by 2 min in an O₂ plasma asher. The cleaning is then concluded with a dehydration bake at 120 °C for 4 min for desorbing water from the surface. Immediately after, Ti-prime adhesion promoter is deposited on the surface, spun at 6000 rpm and baked at 120 °C for 2 min in order to make the surface hydrophobic and improve the adhesion of the resist after development.

In Stepanenko's original recipe the e-beam sensitive resist employed is ma-N 2403, that is a mixture of a polymeric bonding agent (novolac) and a photo-active compound, originally designed for UV photolithography, which nonetheless showed good performances in EBL too. Exposure of the resist to

electrons makes polymer chains in the mixture cross-link with each other to form bigger chains, thus locally reducing the resist solubility in the developer.

Few drops are collected with a pipette and deposited on the sample surface. Spin-coating at 3000 rpm leaves a 300 nm thick layer and a soft bake at 95 °C for 1 min helps evaporating any residual trace of solvent in the resist layer. EBL is then performed, with a beam aperture of 10 μm , a good compromise between resolution, focusing ease and patterning rate. The acceleration voltage is set at 20 kV, which again is a compromise between resolution and proximity effects. The typical dose suggested by the producer for exposure is 120 $\mu\text{C}/\text{cm}^2$. This value can be slightly reduced depending on the geometry of the patterns to reduce proximity effects.

After exposure the resist is developed in AZ 326 MIF, an alkali solution based on Tetramethylammonium hydroxide (TMAH). The development is performed in multiple steps by dipping the sample in the developer for 10 s and then in deionized water for 90 s. Three or four steps are usually sufficient to obtain a clean result and resolve critical features. Resist reflow is then performed by hot baking the sample at 150 °C for 3 min. At this temperature, as the resist softens, a balance is found between the tendency to subside under its weight and surface tension, keeping the resist in shape. In this ideal equilibrium position the resist remains perfectly smooth (Fig. 34). This step has been proved to be crucial to reduce sidewall roughness [104].

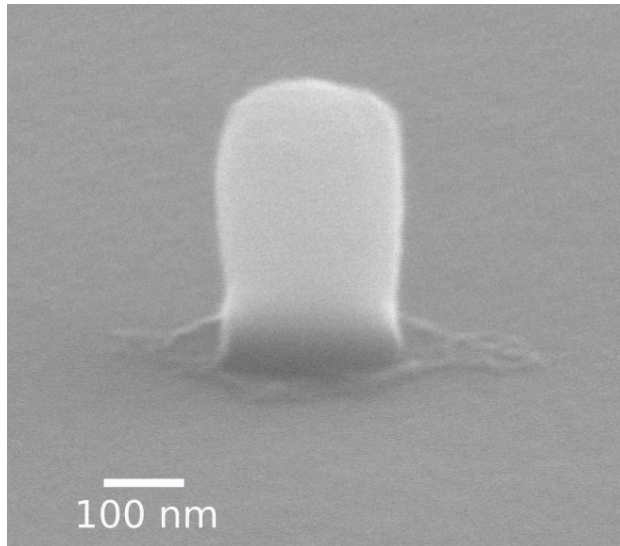


Figure 34: Resist pattern of a nanoantenna observed under SEM after development followed by reflow. The surface presents some nanometre-scale imperfections. Its removal will be described later.

Structures are then defined with ICP etching with the following parameters:

ICP power (W)	RF power (W)	Ar (sccm)	SiCl ₄ (sccm)	Temperature (°C)	Pressure (Pa)	RF Bias (V)
25	17	9	3	10	0.1	-100

The etching depth is controlled with an in-situ Fabry-Perot (FP) system. A low-power Continuous Wave (CW) laser centred at 633 nm passes through a high-reflectivity mirror and forms a cavity sample surface. The atomic level precision of MBE grants the necessary surface smoothness. In order for this system to properly work, the laser beam has to be focused on an unpatterned area. As the etching proceeds the reflectivity of the sample is recorded as a function of the time, revealing FP-like oscillations. When the interface with the Al_{0.98}Ga_{0.02}As layer is passed, the oscillation amplitude abruptly changes and the machine is stopped. As the transition layers are much thinner than the CW laser wavelength, their effect on the FP oscillations is negligible. This measurement allowed us to estimate the typical AlGaAs etching rate, that is $\sim 21\text{nm}/\text{min}$.

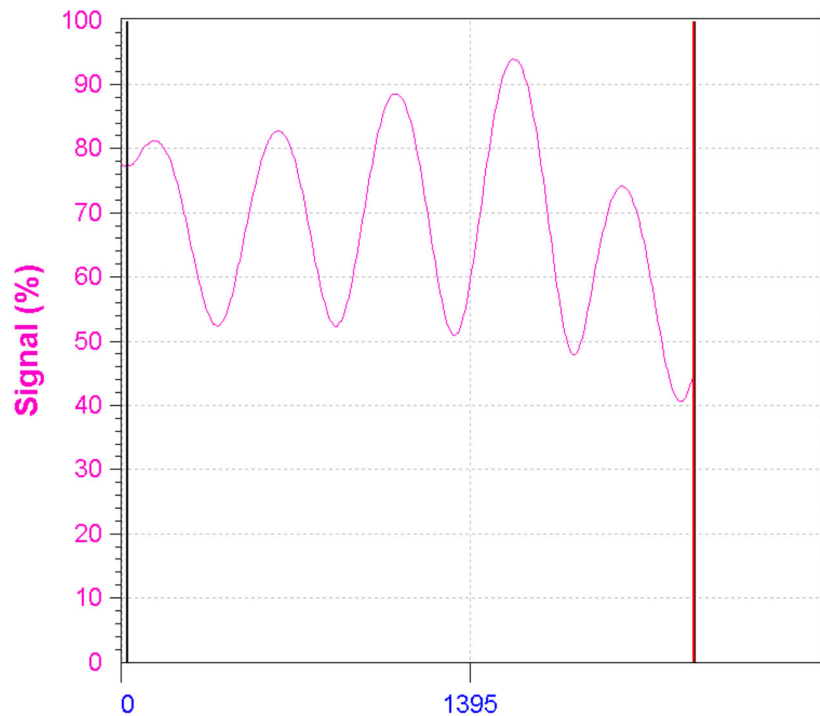


Figure 35: Screenshot of the in-situ sensor program allowing to register the variation in the sample surface reflectivity during the etching.

After ICP, the residual resist is removed by leaving the sample in acetone at 40 °C (near boiling point) for 20 min and then in isopropanol for 5 min. Oxidation during this time is negligible. After the resist is removed, the sample is immediately put in the oxidation oven under vacuum ($\sim 10^{-2}$ mbar), and it is oxidised at 390 °C for 30 min. As already stressed in the previous chapter, a very important aspect to be considered is the lateral oxidation under the Al_{0.18}Ga_{0.82}As structures. In our case we observed that for a 410 °C temperature, the lateral oxidation under a 50 μ m wide test mesa was limited in length at about 16.5 μ m (see Fig. 36), and this limit length was already reached after 1h of oxidation. Doubling the oxidation showed to have no impact.



Figure 36: A) SEM image of a 50 μ m wide test mesa oxidised at 410 °C for 1h. Oxidation fronts are clearly visible. B) SEM image of a similar structure oxidised at the same conditions for 2h. The extra hour of oxidation has no impact as the lateral oxidation length is diffusion limited.

It is important to underline that oxidation must be performed immediately after exposing the Al-rich layer to air with ICP. As a matter of fact, AlGaAs with Al molar fractions > 0.8 is very reactive in air, and native oxidation is much more violent than controlled one, causing cracking, and delamination. Oxidation must be complete as well, otherwise a considerable amount of strain accumulates at the interface between oxidised and un-oxidised zones,

causing severe delamination (see Fig. 37). The strain-induced surface cracking can be so intense to cause the detachment of large areas of the non-completely oxidised layer from the GaAs substrate. The latters end up forming several isolated islands, as shown in Fig. 38.

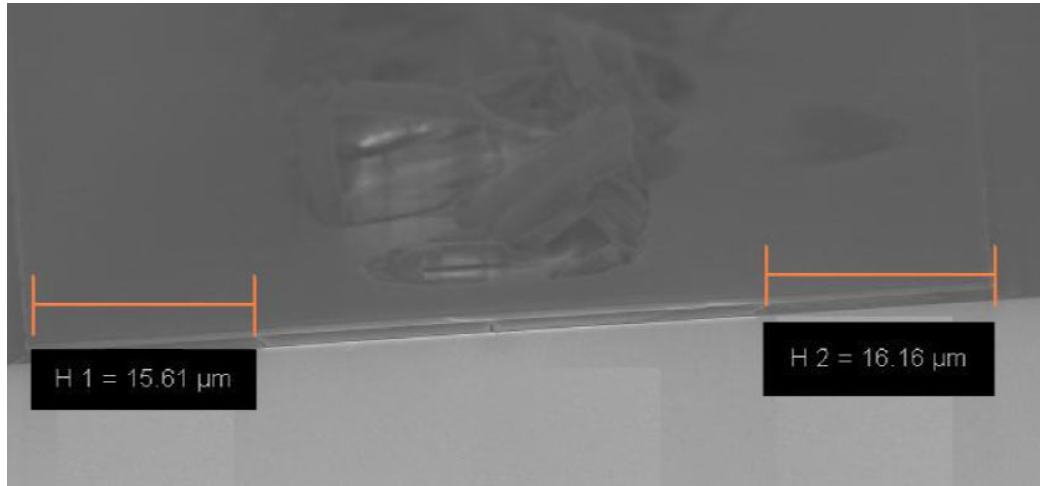


Figure 37: SEM image of a $70\mu\text{m}$ wide waveguide. After oxidation at 410°C for 1h, it was left in contact with air for 1 month. Severe surface delamination is present in the unoxidised central zone.

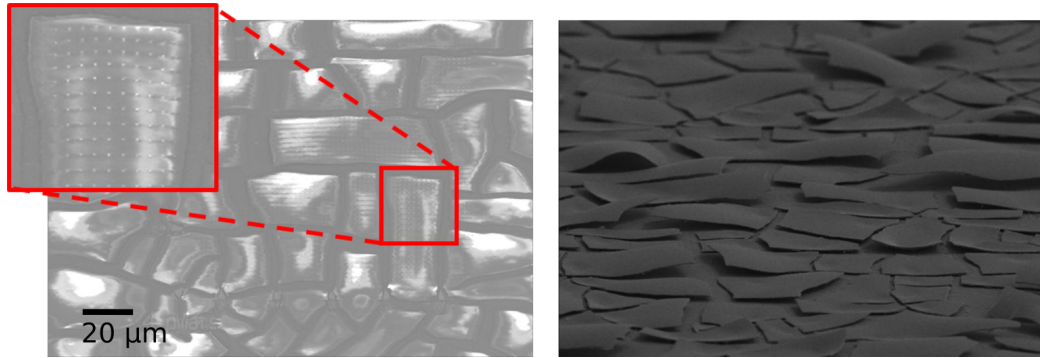


Figure 38: SEM micrograph of a sample containing nanostructure arrays. Left: top view. Right: tilted image. The scale-bar applies to both. Delamination and cracking in this case were much more severe, with the AlOx layer almost completely detaching from the GaAs substrate and forming isolated islands.

After some trial-and-error optimization, an acceptable recipe was found (Fig. 39). The main points are represented by the carrier gas, that is $\text{N}_2:\text{H}_2$, with a N_2 proportion of 95% and 5% of H_2 . The humid gas mixture evaporation temperature was chosen to be 95°C to increase the rate [7], while the flow was kept below 1 l/min as its increase would have a negligible effect [7].

3.4 Monolithic AlGaAs-on-AlOx platform: fabrication

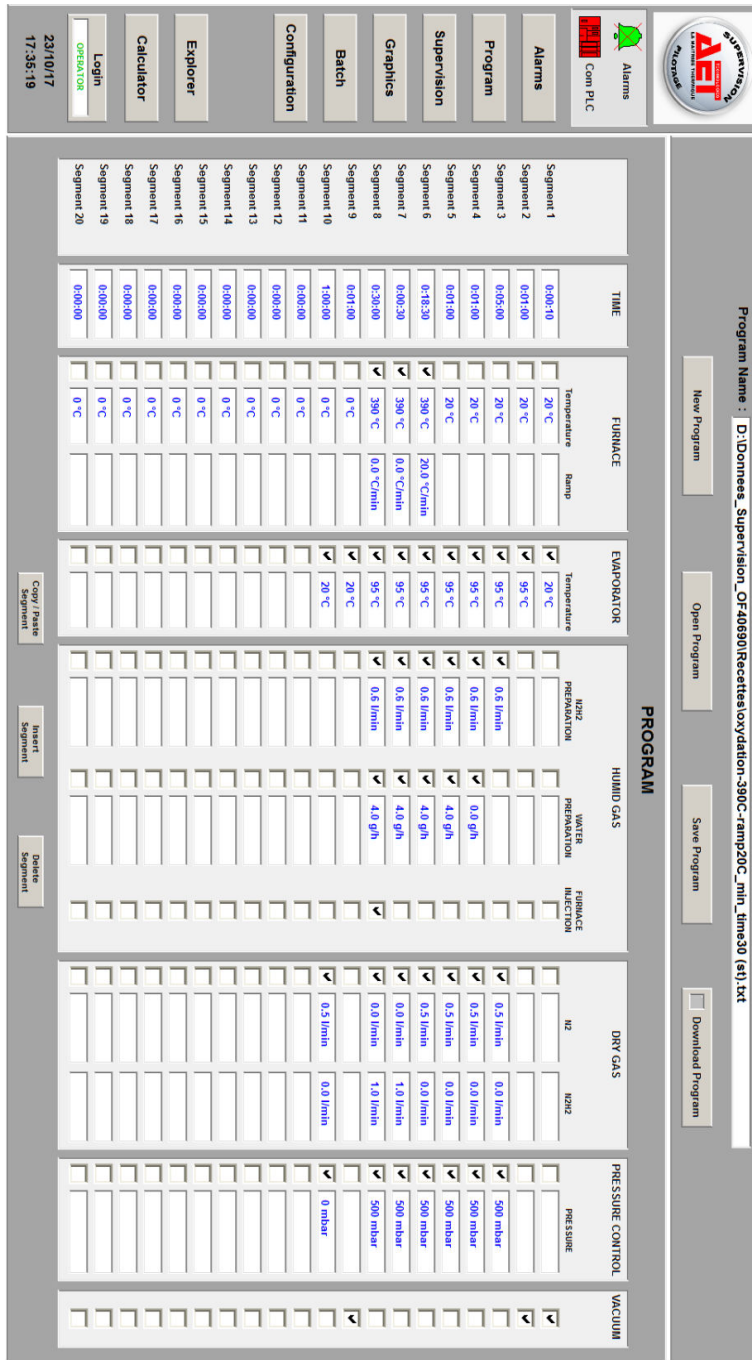


Figure 39: Oxidation program screenshot.

The recipe described so far allowed the successful fabrication of arrays of nanocylinders with radii spanning from 175 to 225 nm and distance of 3 μm , on which a record-high SHG conversion efficiency of 10^{-5} was measured [37].

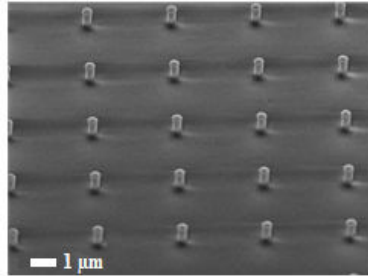


Figure 40: SEM picture of AlGaAs-on-AlO_x nanocylinder array [37].

Despite the initial success of this fabrication procedure however, its limitations manifested shortly after: as soon as we tried to fabricate two nanocylinders very close to each other in the so-called dimer configuration, we discovered that gaps smaller than 50 nm were impossible to achieve by only playing with the dose factor.

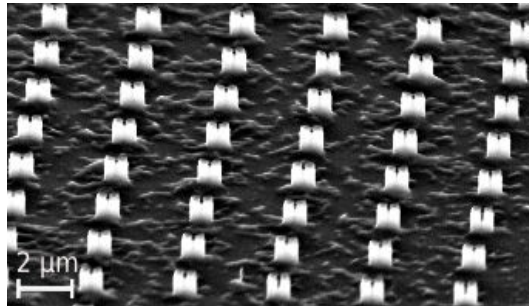


Figure 41: SEM micrograph of an array of nano-dimers with a nominal gap of 30 nm. The dimers are not perfectly resolved due to fabrication limitations.

3.4.2 Protocol improvement

In order to overcome the fabrication limitations and push the minimum gap below 50 nm, I first tried to improve the lithographic mask. The first change was to switch from ma-N 2403 to ma-N 2401, which is a more diluted solution. Same spin-coating parameters give a thickness of 100 nm instead of 300 nm, thus nominally improving the resolution. This change went along with a slight reduction of the dip time into the developer from 10 to 8 sec per iteration. After this I proceeded by systematically applying small perturbations of the parameters involved in each step to find a better optimum.

To further decrease the resist thickness (and increase the resolution), I tried to increase the number of rotations per minute during the spin-coating. However, no significant changes were seen in the up to 4000 rpm, while above

5000 rpm the mask became too fragile and completely dissolved in the developer after only a few seconds dipping. As for EBL, a small reduction of the beam aperture from 10 to 7 μm showed a slight improvement, though it came with more complicated adjustment of the beam parameters. The patterning speed was slightly decreased too with this change.

Following hints from a recent paper [105], I also tried to improve the e-beam mask quality by introducing a second reflow step consisting of UV exposure for 30s. Unfortunately, results proved to be not always reproducible and this step was discarded from protocol. A slight mask quality improvement came from introducing a non-isotropic O_2 plasma etching step immediately after development and before $\text{Ar}:\text{SiCl}_4$ ICP to remove any resist imperfections. Oxygen plasma is well known for rapidly attack any organic resist, thus this etching only lasts briefly (20 s) in order to obtain a planarization effect; the etching effect on AlGaAs during this time is negligible.

The reason for this extra step is that SEM images of the resist after development (see for example Fig. 34) often showed irregularities, and, as the ICP etching rate of AlGaAs is roughly ten times larger than that of the resist, getting rid of even nanometric-scale irregularities would yield an important improvement in the structure quality. The last significant change regarded the ICP recipe: following from useful discussions with William Hease and Mehdi Hamoumi I increased the Ar flow and decreased the SiCl_4 .

ICP power (W)	RF power (W)	Ar (sccm)	SiCl_4 (sccm)	Temperature ($^\circ\text{C}$)	Pressure (Pa)	RF Bias (V)
25	15	30	3	10	0.1	-80

The argument for preferring such strategy is twofold: on the one hand, as already explained in the ICP section, Ar^+ ions not only perform a mechanical sputtering action, but they also help “cleaning the surface” after chemical reaction with SiCl_x radicals and “clear the way for the next wave to come”, thus, at least intuitively, more Ar flow would imply a smoother etching. Moreover, increasing to Ar flow with respect to SiCl_4 slows down the chemical contribution to the overall etching and favours the anisotropic action.

Indeed, the chemical etching component of ICP induced by SiCl_4 can result in reduced verticality of the structure sidewalls, which in some cases is of paramount importance. Moreover this effect is also strictly dependent on the Al concentration in the blend. To support this, it is interesting to look at a deep-etching test with the “old” recipe in which I didn’t stop the process at the interface between the second transition layer and the $\text{Al}_{0.98}\text{Ga}_{0.02}\text{As}$, but I let the process continue up to the GaAs substrate.

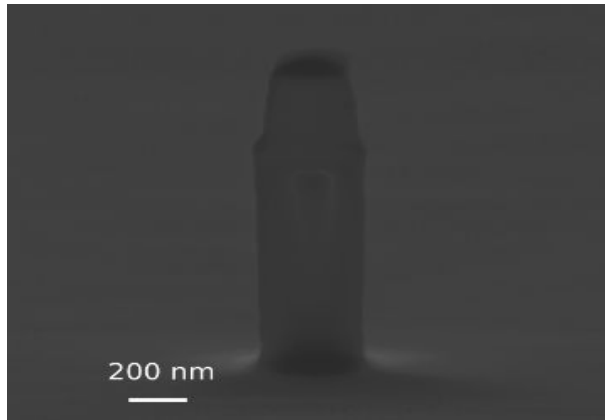


Figure 42: Deep-etched nanoantenna with the “old” recipe from Stepanenko. The $\text{Al}_{0.18}\text{Ga}_{0.82}\text{As}$ part is more inclined than the $\text{Al}_{0.18}\text{Ga}_{0.82}\text{As}$ as the chemical etching component of ICP due to SiCl_x radicals is sensitive to the Al concentration in the alloy.

Fig. 42 shows how the chemical etching component of ICP is sensitive to the Al concentration even for a relatively low 18% case. Overall, these small changes combined together helped improving the fabrication yield and allowed to push the minimum gap limit for dimers nanostructures down to 40 nm (Fig. 43).

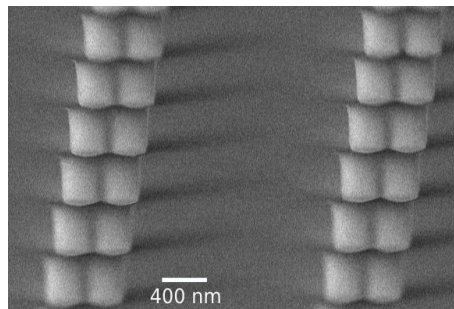


Figure 43: SEM image of an array of nanodimers with 40 nm gap. This achievement is the sum of all optimizations described in this section.

However, when we tried to pattern five coupled nanoantennas (pentamer) instead of two, the result was catastrophic. As at that time the limit was set by the resist resolution, in order to fabricate more complex structures we decided to employ a higher resolution e-beam resist called Hydrogen Silesquioxane (HSQ). Thus several steps of the fabrication recipe had to be changed accordingly.

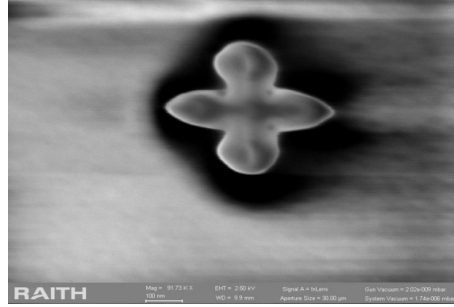


Figure 44: SEM micrograph of five coupled nanoantennas in the so called pentamer configuration. Even with further optimizations, this was the best result obtained with ma-N series resist.

3.4.3 Impact of dose factor

Particular attention has to be paid to the e-beam dose as it can dramatically change the overall fabrication yield. In this sense, the fabrication of an isolated nanoantenna surrounded by an asymmetric diffraction grating provides a good example. As shown in Fig. 45, it consists of a central pillar with nominal radius of 220nm, and two concentric half-gratings at a distance $d=500\text{nm}$. The asymmetry between left and right is defined in terms of a shift $s=290\text{nm}$. Each half-grating consists of three ridges with period $\Lambda=340\text{nm}$ and a duty cycle of 85%, corresponding to a ridge width of about 290nm.

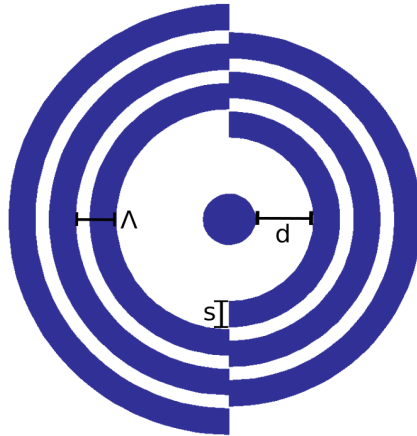


Figure 45: Schematics of the design for a nanoantenna surrounded by a diffraction grating.

The physical reasons for this particular design will be explained in the next chapter, while for now let us just focus on the fabrication challenges. Here

the biggest issue is represented by the ridges, as their nominal gap should be 50nm and, unlike the case of a dimer, it should be kept constant along their entire length, thus resulting in important proximity effects.

For the first fabrication test ma-N 2401 resist was used and the e-beam dose was fixed at $120 \mu\text{C}/\text{cm}^2$, however as Fig. 46 shows the proximity effects were so high that the actual duty cycle was 100%, i.e. the ridges were forming a continuum. The distance between pillar and grating was suffering from proximity effects as well, with an actual value of about 380nm instead of 500nm. In contrast the diameter of the central pillar was slightly smaller than the desired value.

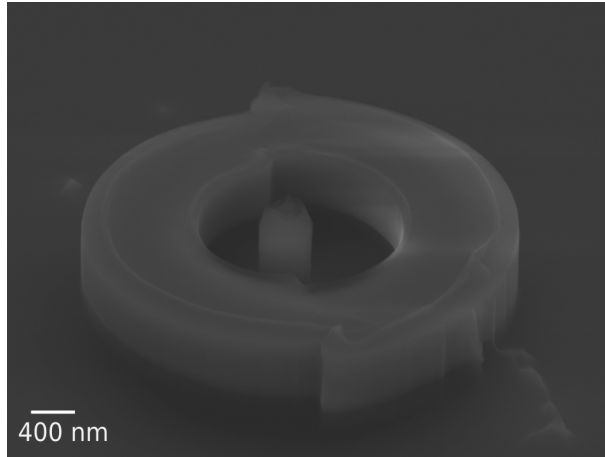


Figure 46: First fabrication test using a uniform dose of $120\mu\text{C}/\text{cm}^2$. The proximity effects with this dose are such that the gaps between the ridges are not resolved.

The lesson that this first test taught us was that the e-beam dose was too high in the grating and too low in the antenna. As a consequence we decided to introduce a different Dose Factor (DF) for the two types of structures to be multiplied by the standard base value of $120\mu\text{C}/\text{cm}^2$: $\text{DF}=1.1$ for the central pillar and $\text{DF}=0.85$ for the grating. As shown in Fig. 47, this second test showed a net improvement with respect to the previous one, especially for the gaps in the grating ridges, which were now well resolved almost everywhere.

In contrast, the dimension of the central pillar showed no significant increase despite the higher DF. The reason behind this effect can be attributed to the fact that the expected radius increase was exactly counter-balanced by the DF decrease in the grating, which caused smaller proximity effects between the two structures, and as a result no appreciable radius change.

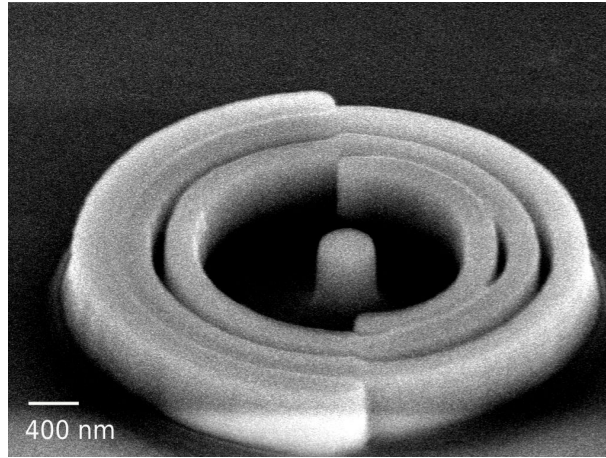
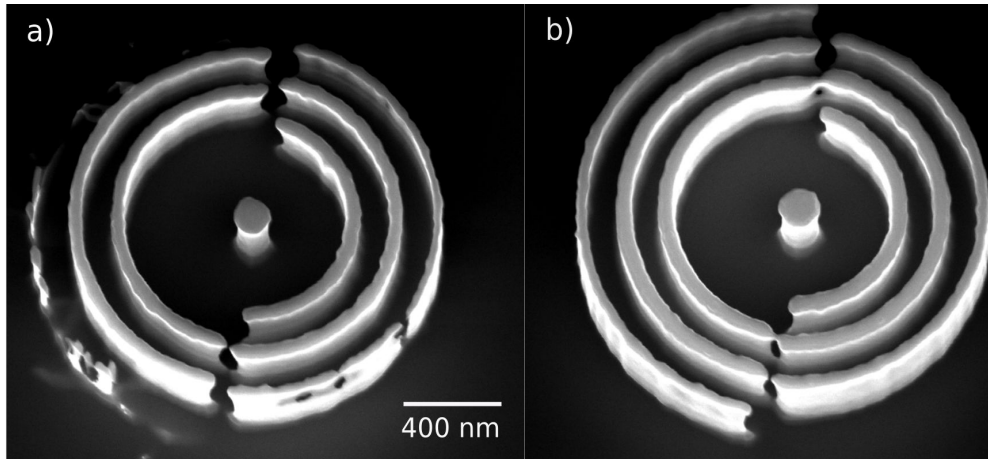


Figure 47: Second fabrication test with smaller e-beam dose ($DF=0.85$) for the grating. The result was promising as almost every ridge was well defined.

Intuitively at this point one could think of just decreasing a bit again the DF in the grating structures in order to obtain a good sample. There exists a dose threshold however, which depends non-trivially on the nominal dimensions, i.e. the exposed area, below which the cross-linking is not effective anymore, causing the resist to be partially affected by the ion bombardment during ICP. This effect is evident in case of $DF=0.65$ (Fig. 48a), while it is slightly mitigated for $DF=0.7$ (Fig. 48b).



400 nm

Figure 48: Third test showing two gratings with a $DF=0.65$ (a) and $DF=0.7$ (b). In this two cases the dose was too small to induce cross-linking in the resist, causing some damage during ICP.

The message of this test is that a trade-off between dose, proximity effects and structure dimensions must be found to optimize each fabrication recipe. This of course will sensibly depend on the particular design we are trying to implement. In this particular case a trade-off was found by anticipating the structure size reduction due to DF decrease. An increase of 50nm in the nominal dimensions of every structure, meaning an exposure area increase of the same amount on the resist, combined with a DF=0.65, was sufficient to obtain a sample good enough to be measured.

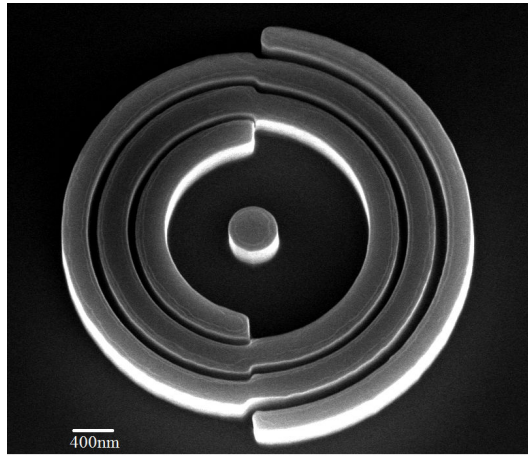


Figure 49: A good compromise between dose and proximity effects was found by increasing the nominal dimension of every structure by 50nm, anticipating that a DF of 0.65 would cause a decrease of the actual structure dimensions.

3.4.4 Switch to HSQ

As we approached the resolution limits of ma-N 2401 resist, we decided to switch to an inorganic resist called HSQ. It consists of HSiO clusters in a Metilisobutilchetone (MIBK), a solvent solution, and exposure to the e-beam causes cross-linking of Si and O atoms in the clusters, eventually forming SiO_x , i.e. glass. The advantage here is twofold: not only is the intrinsic resolution higher than that of ma-N series, but also the hardness, thus improving the ICP yield.

The first challenge of HSQ implementation regarded the adhesion enhancement after development, because standard Ti-prime treatment proved insufficient. Moreover, despite literature claiming improved adhesion of HSQ on III-V semiconductors with a cationic organic material (SurPass 3000) [106], we did not observe such amelioration.

A solution to the adherence problem was found by depositing 3 nm of

SiO_x with Plasma-Enhanced Chemical Vapour Deposition (PECVD). This technique allows to deposit thin layers of materials like SiO and SiN starting from gas-state precursor gases. These gaseous species are turned into plasma state with a RF discharge between two electrodes. In the SiO case the precursor gases are oxygen and silane (SiH₄). This PECVD step is performed right after the standard sample cleaning. Spin-coating of HSQ is then performed at 4000 rpm, followed by two hot plate baking steps at 150 °C and 200 °C for 2 min each, obtaining a layer ~100 nm thick.

As for e-beam lithography, the dose necessary to induce cross-linking in the resist molecular bonds at 20 kV is roughly an order of magnitude higher than the ma-N standard ($\sim 1800 \mu\text{C}/\text{cm}^2$), meaning that the average single-writing field patterning time increased from ~ 30 s to ~ 4 min. Development is achieved by dipping the sample in a KOH-based solution (AZ 400 K) for 1 min, plus rinsing in deionised water for 90 s. Unlike ma-N, HSQ development is single-step and no reflow is performed afterwards. Finally, just before ICP, a first CHF₃ plasma etching is performed to get rid of the 3 nm SiO layer, which would greatly slow down the SiCl₄:Ar ICP. The last two steps are unaffected by the resist change, and thus were not re-optimized. Thanks to this new recipe, structures impossible to fabricate with ma-N resist were achieved, such as dimers with 30 nm gap and pentamers (Fig. 50)

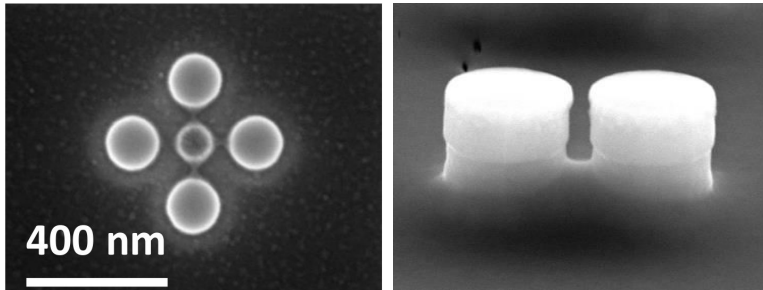


Figure 50: Left: top SEM image of a pentamer fabricated with HSQ lithographic mask. Right: tilted SEM image of a dimer with 30 nm gap.

The improved quality of dimers and pentamers demonstrates that HSQ is less sensitive to secondary electron exposure, mitigating proximity effects with respect to ma-N. Another interesting comparison between the two resists can be made in considering nanoantennas surrounded by diffraction gratings. It is indeed possible to appreciate a net roughness decrease in the HSQ case, due to enhanced lateral resolution (Fig. 51).

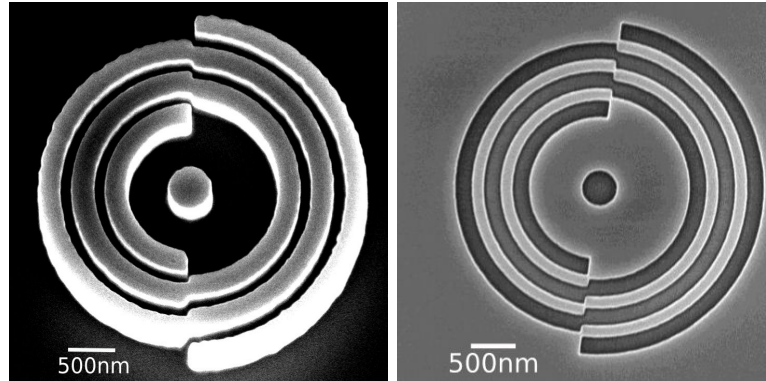


Figure 51: Left: tilted SEM image of a nanoantenna surrounded by a diffraction grating fabricated with ma-N 2401. Right: SEM image of the same structure with nominally identical parameters fabricated with HSQ (courtesy of Edmond Cambril). The latter presents both improved resolution and decreased lateral roughness.

The lateral resolution improvement is even more evident in Atomic Force Microscope (AFM) characterization, which I performed in the lab of Nordin Felidj with the help of Xiaonan Sun in Université Paris Diderot (Fig. 52).

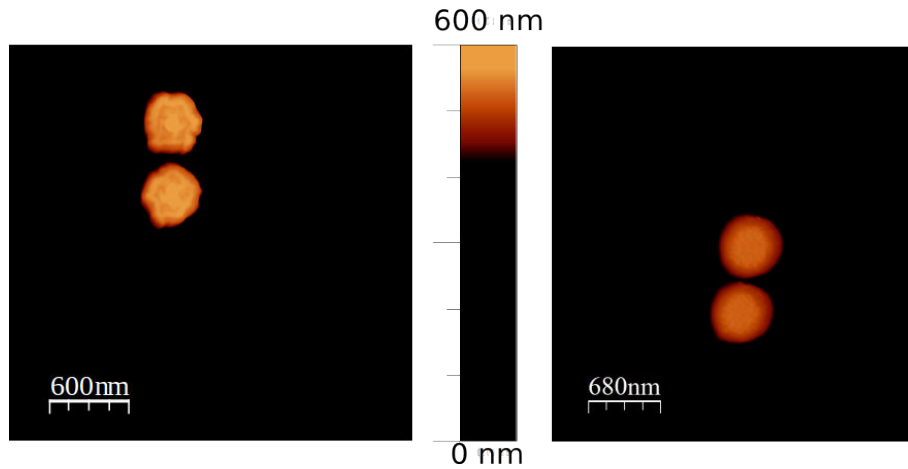


Figure 52: Left: AFM map of a dimer with 60 nm gap and a nominal radius of 225 nm fabricated with ma-N 2401. Right: dimer fabricated with HSQ technology. The nominal gap is the same (60 nm), while the nominal radius is 250 nm. The analysis is performed with WSxM software [108].

3.4.5 AlGaAs-Au hybrid integration

As a further technological validation of our AlGaAs-on-insulator platform, we demonstrated the possibility to integrate both metal (Au) and semiconductor nanostructures on the same chip. The motivation for doing so is far

from being of purely technological interest, as it was shown that plasmonic resonances of metallic nanostructures can enhance the field confinement in dielectric nanoantennas, boosting their nonlinear performances [107]. The basic hybrid nanostructure consists of a semiconductor nanoantenna surrounded by a metal ring helping the field confinement in the nanoantenna.

Unlike processes described so far, this fabrication requires multiple lithographies. Given that gold nanostructures do not need a MBE implementation and can be directly evaporated on the substrate, the correct workflow would consist of a first lithography to define AlGaAs nanostructures, followed by the oxidation of the substrate, and then definition of gold nanostructures with positive-tone lithography. In order to correctly align the mask of the second lithography to the first one, proper alignment marks have to be defined. These consist of three kind of structures which are key factors in an equal number of steps (Fig. 53):

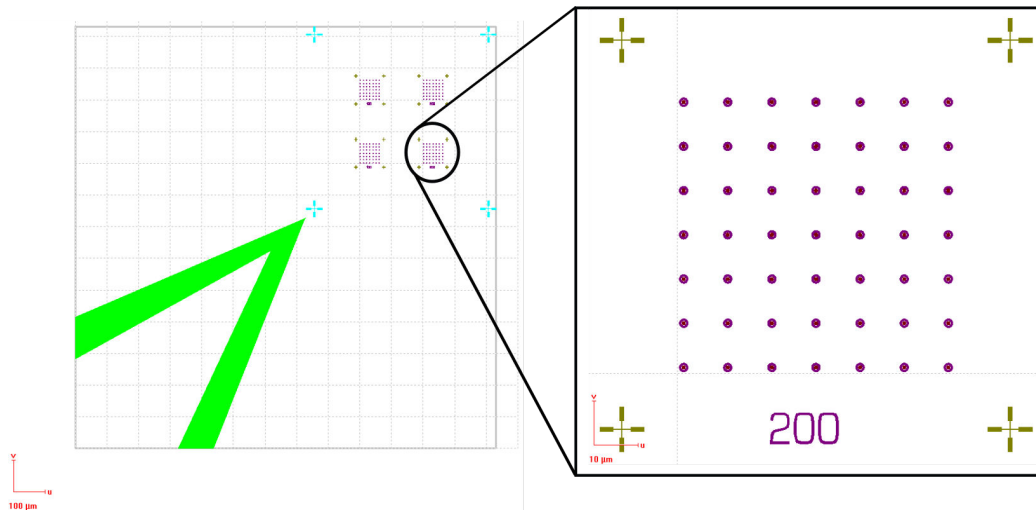


Figure 53: Alignment marks for hybrid dielectric-metal nanoantenna fabrication.

- Firstly a $700 \mu\text{m}$ large arrow guides the user to easily find the smaller structures.
- Secondly, a first coarse alignment is performed with the help of a series of four $50 \mu\text{m}$ wide crosses disposed at the vertices of an ideal square containing several nanoantenna arrays.
- Lastly each nanoantenna array, as large as a single writing field ($100 \times 100 \mu\text{m}^2$) to avoid stitching, is delimited by four $10 \mu\text{m}$ wide crosses allowing for fine alignment each time the beam translates to pattern a new array.

Unfortunately they cannot be patterned together with the AlGaAs nanostructures, as semiconductor materials do not offer enough contrast to be recognised under the resist layer in the second EBL, and the beam aperture during SEM imaging, i.e. $30\mu\text{m}$, is larger than the optimal one for EBL patterning, i.e. $10\mu\text{m}$ (see a few sections above). For these two reasons it was necessary to resort to gold alignment marks introducing a third (positive) EBL, performed before the patterning of AlGaAs nanoantennas.

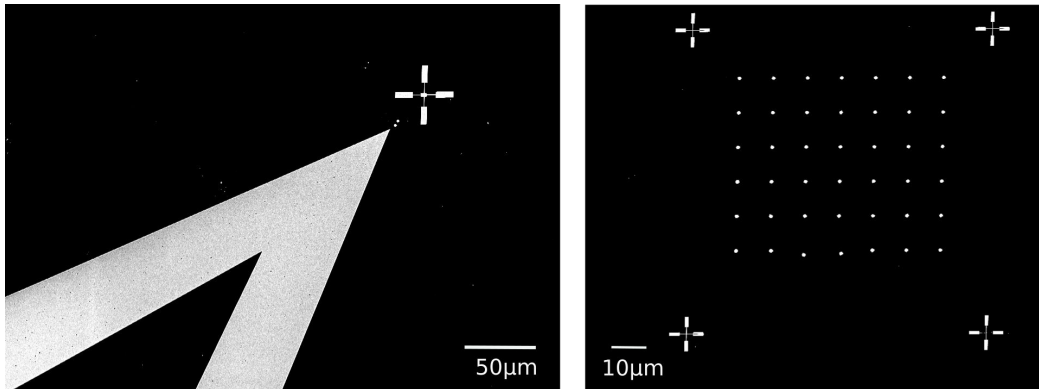


Figure 54: SEM micrograph of fabricated Au alignment arrow and big crosses (left) and a nanoantenna array with small crosses (right).

To sum-up hybrid semiconductor-metal nanoantenna fabrication requires three lithographies in total (Fig. 55), two of which (first and third) are positive-tone.

3.4 Monolithic AlGaAs-on-AlO_x platform: fabrication

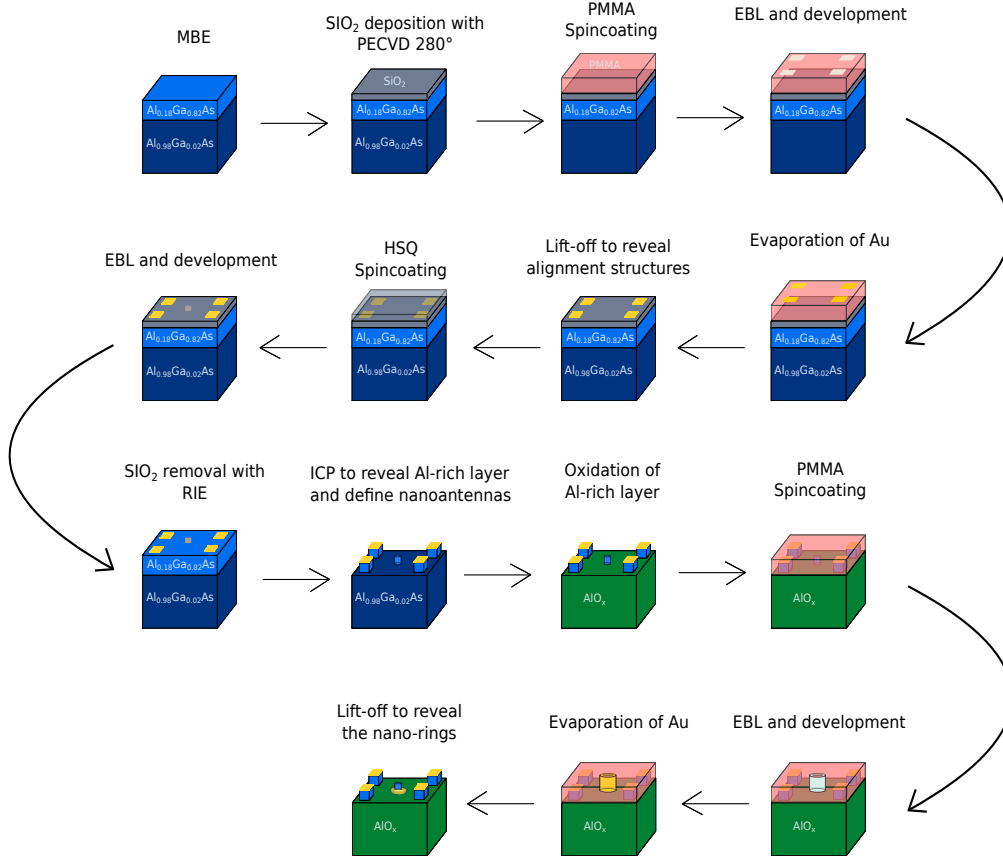


Figure 55: Fabrication scheme of hybrid AlGaAs-Au nanoantennas on AlO_x.

The positive-tone e-beam resist employed is Polymethyl methacrylate (PMMA), a synthetic polymer commonly used both in EBL and photolithography. Exposure to electrons or UV, opposite to ma-N and HSQ, causes de-cross-linking of the polymeric chains, rendering them removable via chemical development. The exposure parameters used to pattern PMMA are the same (20 kV voltage, 10 μm aperture), while the dose is $\sim 220 \mu\text{C}/\text{cm}^2$. Development is performed by dipping the sample first in MIBK diluted with isopropanol (1:3 ratio) for 40 s, then in isopropanol for 30 s.

The sample is then put in an O₂ plasma asher for 6 s to remove any resist residue. The metals are then evaporated by EBPVD. In both cases, a first 5 nm Ti layer is evaporated to promote adhesion to the substrate, followed by 80 nm of gold at a speed of 0.1 nm/s. At this deposition rate the uncertainty on the final thickness is 1-2 nm.

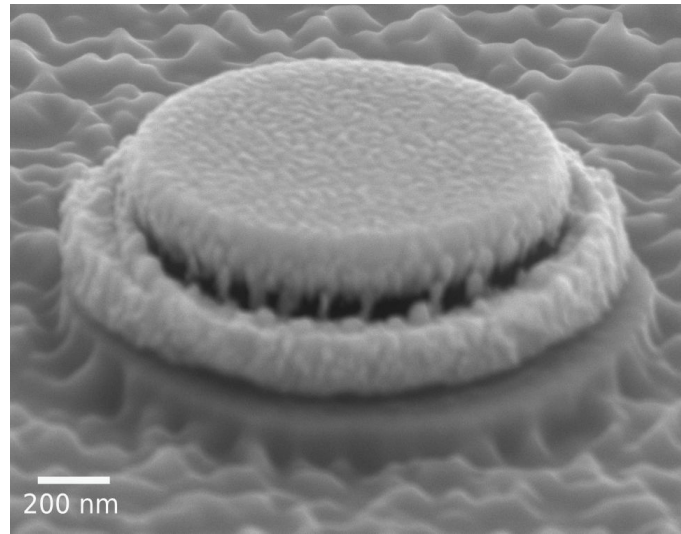


Figure 56: First unsuccessful attempt of final lift-off to reveal the hybrid structures.

Finally the lift-off allows to remove the unnecessary metal and reveal the desired structures. The first lift-off is performed in acetone brought to boiling point, while for the second one SVC-14 resist stripper is employed, as more resolution is needed to uncover the nanostructures and acetone proved not to be strong enough (Fig. 56). The final nanostructures are an AlGaAs nanoantenna surrounded by a Au nanoring with a gap as small as 100nm, both resting on the AlOx substrate (Fig. 57).

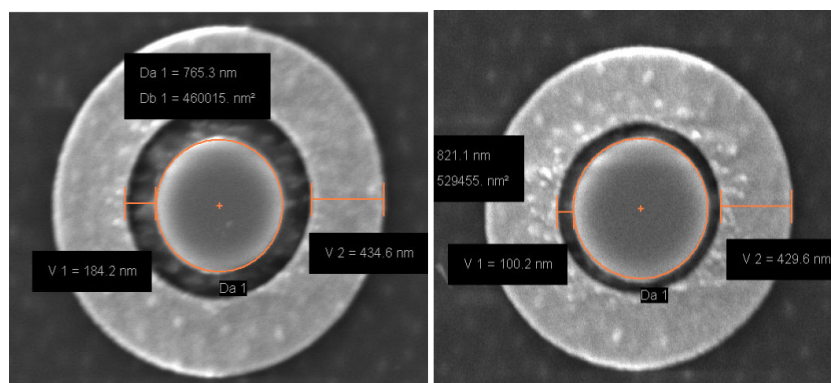


Figure 57: Fabricated AlGaAs-Au-on-AlOx nanostructures. Left: the gap between AlGaAs antenna and Au ring is 180 nm. Right: the gap is as small as 100nm.

3.5 TEM characterization

Prior to selective oxidation the AlGaAs layers are epitaxial with respect to the GaAs substrate, i.e. they are lattice-matched at the interface. In order to ascertain whether the wet oxidation of the $\text{Al}_{0.98}\text{Ga}_{0.02}\text{As}$ layer altered the crystallographic properties of the nanoantennas, we carried out a TEM characterization of AlGaAs-on- AlO_x nanoantennas.

3.5.1 Sample preparation

Before TEM analysis, a $5\text{ mm} \times 5\text{ mm}$ sample containing several nanoantenna arrays, with $3\ \mu\text{m}$ spacing and nominal radii spanning from 175 to 225 nm was fabricated following the protocol described in Section 2.2, with ma-N 2401 e-beam resist. The sample was then encapsulated in platinum via electron beam evaporation for metallization, and a cross section containing three nominally identical nanoantennas was extracted from the whole sample with Zeiss crossbeam Ga Focused Ion Beam (FIB) technique (Fig. 58). The plane of the obtained thin film is (001).

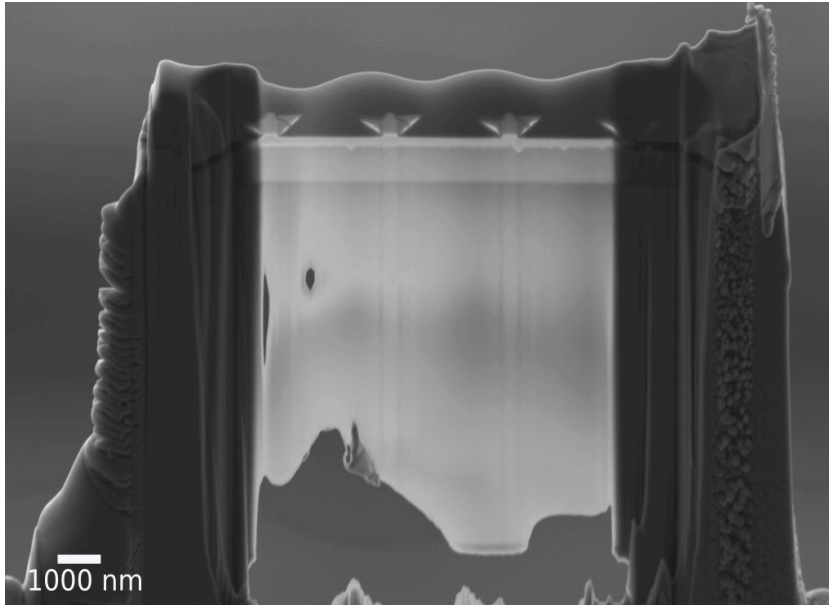


Figure 58: Cross section of the sample prepared for TEM characterization.

The FIB machine works in a similar fashion as a SEM system, with the only crucial difference that in the former ions are accelerated rather than electrons. Due to this similarity most commercially available machines have

two different columns, one for ions and one for electrons, to enable both FIB and SEM.

3.5.2 Results and discussion

After FIB processing, the sample was placed in a JEOL ARM 200F TEM. This microscope combines a cold field emission gun [109] and a CEOS hexapole spherical aberration corrector (CEOS GmbH) [110] to compensate for the spherical aberration of the objective lens. This TEM system is placed in MPQ laboratory, under the supervision of Guillaume Wang and Christian Ricolleau. Thanks to this TEM configuration a point resolution of 75 pm at 200 kV can be achieved [111].

High-resolution images of single nanoantennas confirm their crystalline nature, with the sole presence of a thin (~ 1 nm) passivated oxide layer at the interface with the platinum protection (Fig. 62), compatible with the exponential drop in the oxidation rate with decreasing Al content. In contrast, we could observe complete oxidation of the $\text{Al}_{0.98}\text{Ga}_{0.02}\text{As}$ layer, which presents an amorphous structure comprising the sporadic presence of polycrystalline islands due to the presence of 0.02 Ga molar concentration in the alloy (Fig. 60). We observe as well a volume shrinkage of the AlO_x layer after oxidation of $\sim 17\%$, in fair agreement with previous observations [71].

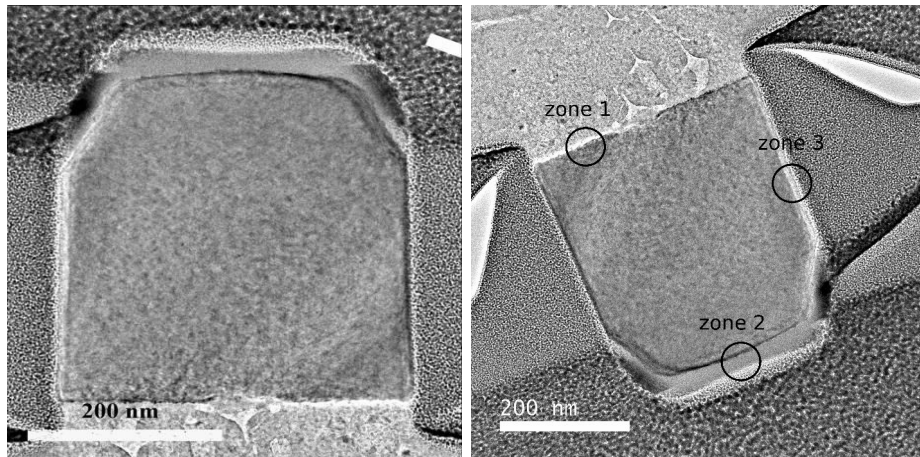


Figure 59: TEM images of $\text{Al}_{0.98}\text{Ga}_{0.02}\text{As}$ nanoantennas. The light grey area is the AlO_x substrate, whose amorphous nature is confirmed. The nanoantenna shape slightly deviates from that of a cylinder and its final 100 nm part resemble more a truncated cone.

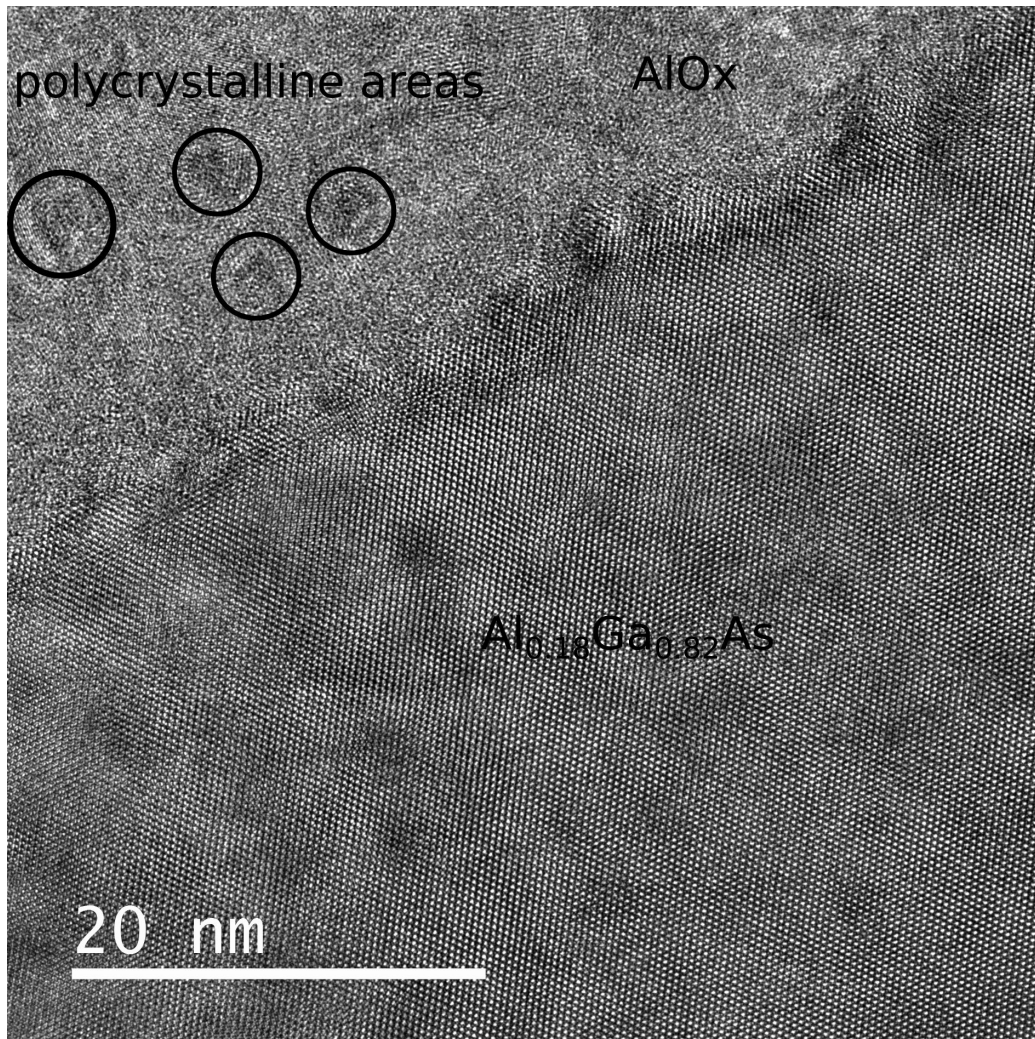


Figure 60: HR-TEM image of zone number 1, as labelled in Fig. 59, showing the semiconductor-oxide interface. The amorphous nature of the AlOx layer is confirmed, accompanied by polycrystalline islands (circled areas) which are attributed to the small Ga percentage. The Al_{0.18}Ga_{0.82}As nanodisk crystalline mesh can be appreciated as well. The interface roughness is as small as $\sim 1 - 2$ nm.

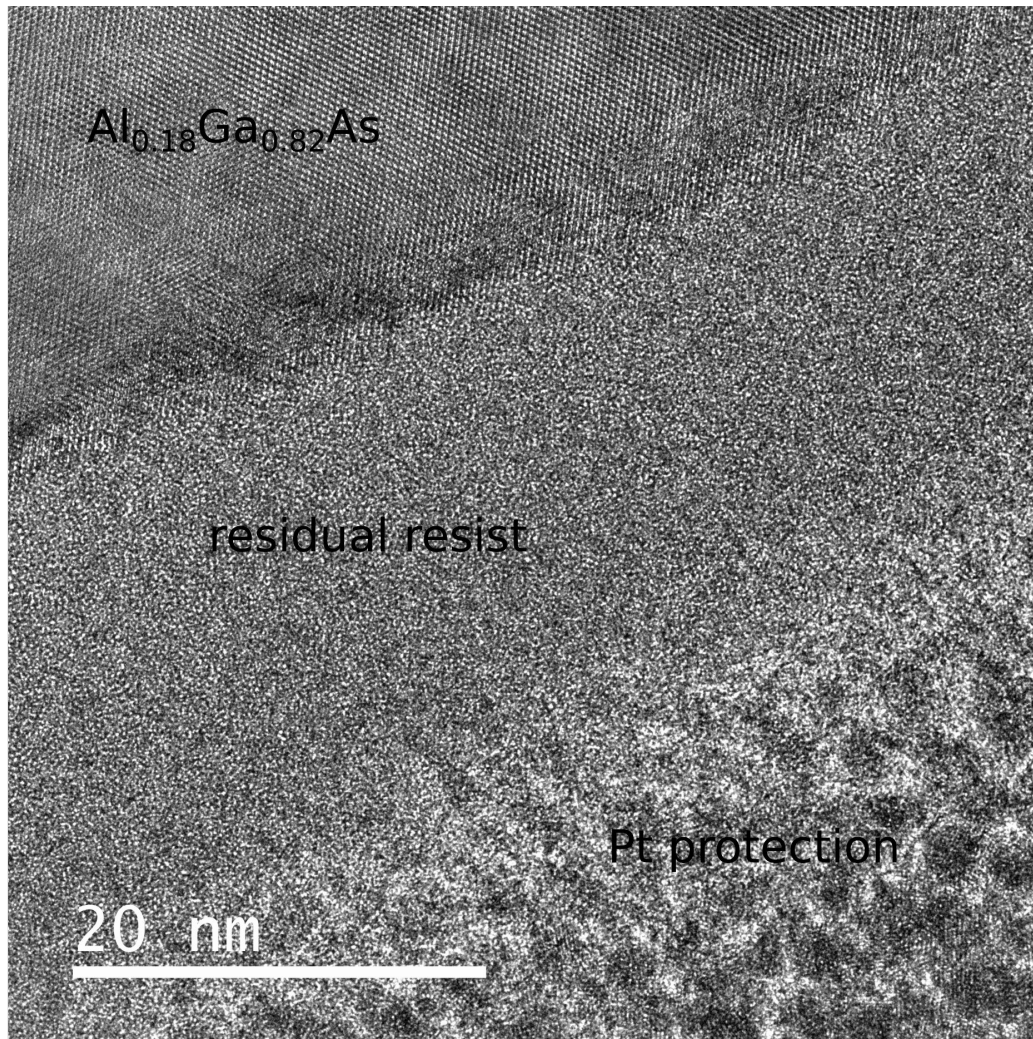


Figure 61: HR-TEM image of zone number 2, as labelled in Fig. 59, showing the top part of the pillar. Sandwiched between the nanodisk and the Pt protection, the presence of a residual ~ 20 nm thick ma-N resist layer can be inferred. The latter two have an amorphous structure.

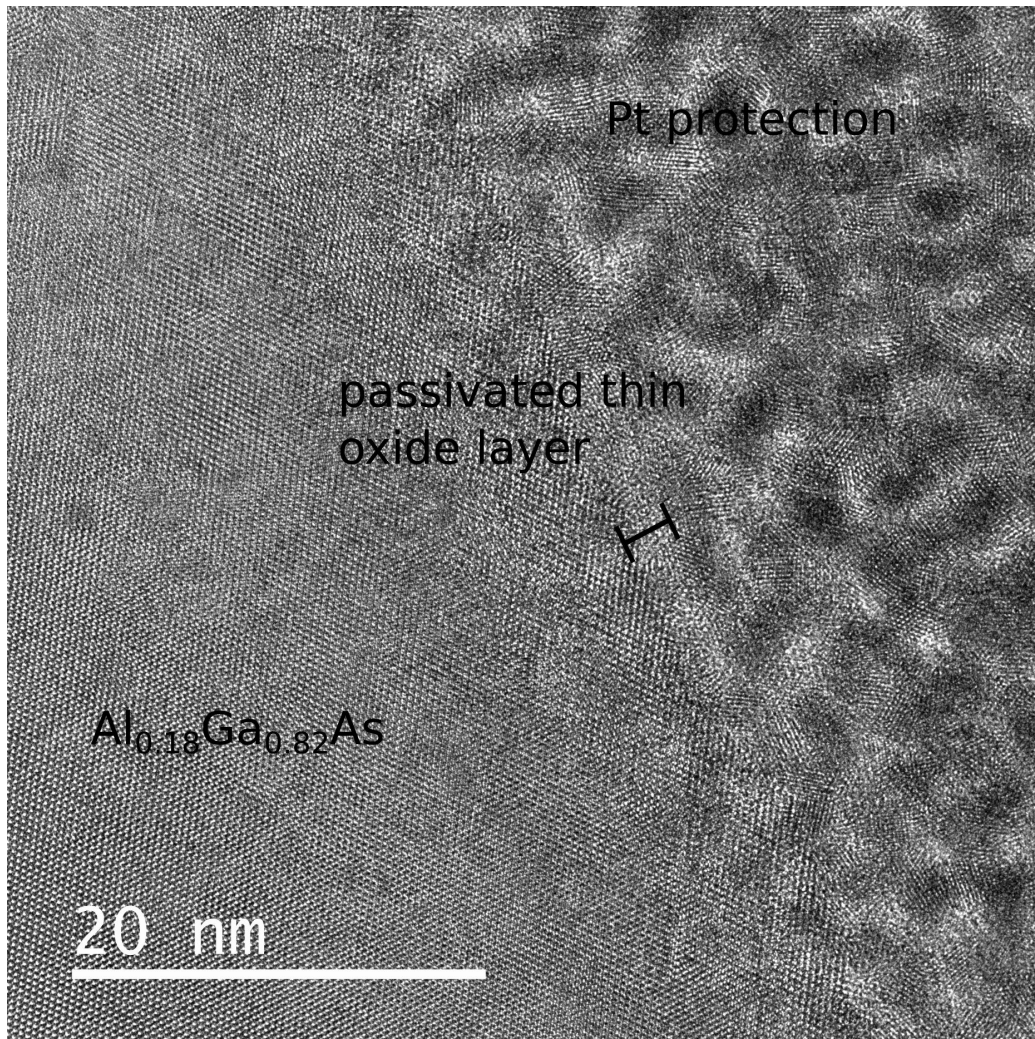


Figure 62: HR-TEM image of zone number 3, as labelled in Fig. 59, showing the side interface between the nanodisk and Pt. Compared with the images above, here it is easier to appreciate the ~ 1 nm AlO_x passivation layer formed during sample oxidation.

HR-TEM images highlighted as well the presence of nonidealities of several types [70]

- a deviation from the ideal cylindrical shape, with the last 100 nm in height resembling more a truncated cone. This defect is to be attributed to the ma-N fabrication procedure. FEM calculations on COMSOL show that this nonideality is optically negligible (Fig. 63).
- A ~ 20 nm layer of ma-N 2401 resist is still present on top of the nanoantennas even after removal with hot acetone. Fortunately this does not

affect optical measurements as ma-N has a refractive index ~ 1.6 in the range of our interest [112].

- Despite the absence of any alteration of the crystalline matrix, the crystallographic directions of the three nanoantennas are neither parallel to each other nor to the GaAs substrate. The loss of this epitaxial relationship is due to the inhomogeneous contraction of the $\text{Al}_{0.98}\text{Ga}_{0.02}\text{As}$ layer during wet oxidation.

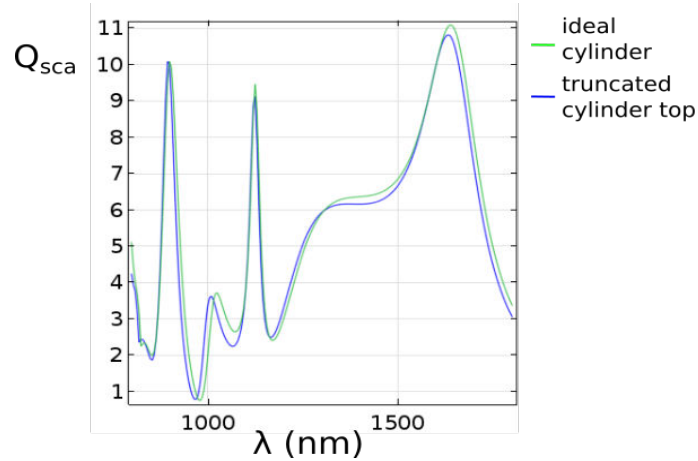


Figure 63: Scattering efficiency confrontation between an ideal cylinder and the actual one with a truncated cone top. The FEM calculation is performed on COMSOL.

More in detail, the tilt in the crystallographic directions of the nanoantennas was revealed with electron diffraction measurements, performed on the same machine with a double-tilt sample holder [111]. Using the GaAs substrate as a reference we determined the value of the tilt with respect to the $[001]$ (X) and $[1\bar{1}0]$ (Y) directions by comparing their electron diffraction maps in Fourier space.

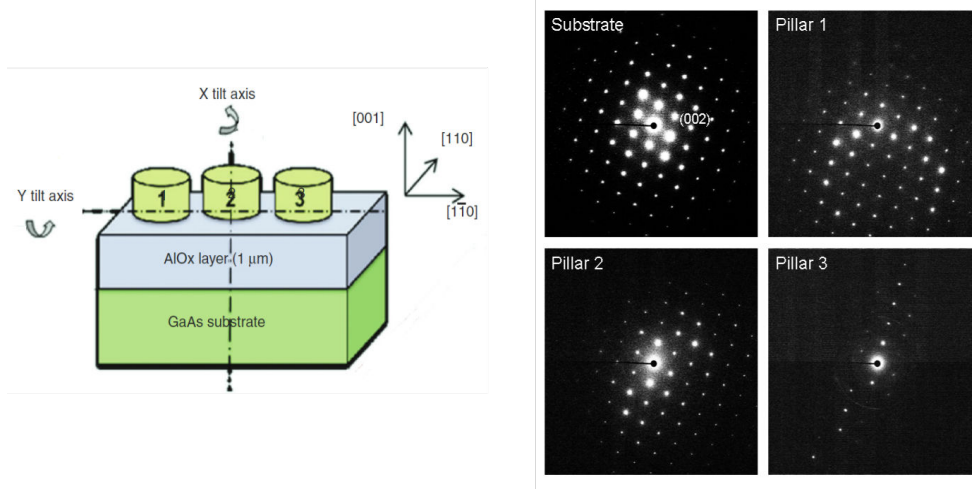


Figure 64: Left: schematics of the tilt axes with respect to the main crystallographic directions and the sample geometry. Right: electron diffraction patterns of GaAs substrate and the three nanopillars.

The measured values for these tilt angles are summarized in the table below.

Zone	X tilt	Y tilt
GaAs Substrate	0.2°	0°
Nanopillar 1	5.7°	1.8°
Nanopillar 2	-3.1°	-0.9°
Nanopillar 3	0.7°	-1.3°

Whereas the two other nonidealities proved to be negligible, the presence of these tilt angles is optically significant. This aspect will be clarified in the next chapter, which deals with the nonlinear response of nanostructures fabricated with the techniques above mentioned.

3.6 Conclusion

This chapter has provided in the first part a description of the AlGaAs integrated platforms state-of-the-art, both monolithic and non-monolithic. On the second part, a wet-oxidation based monolithic approach developed in MPQ laboratory was described, detailing all fabrication protocol steps and their optimization, and including SEM, TEM and AFM characterization of the fabricated samples. This concludes the technological part of my thesis and opens the way for the full experimental description, which will be provided in chapters four and five.

Chapter 4

Nonlinear response of single AlGaAs nanoantennas

In this chapter I will describe the nonlinear measurements carried out on isolated AlGaAs nanopillars. Following a thematic order, I will start by describing SHG measurements, including polarization and nonideality studies. I will then introduce the directivity problem, which has been addressed in two ways: by tilting the pump k-vector with respect to the cylinder symmetry axis and by surrounding the nanoantenna with an asymmetric diffraction grating. I will finally conclude by describing the measurements of different nonlinear effects, SFG and SPDC, linked together through a quantum-classical correspondence [20, 141].

4.1 SHG from isolated nanoantennas

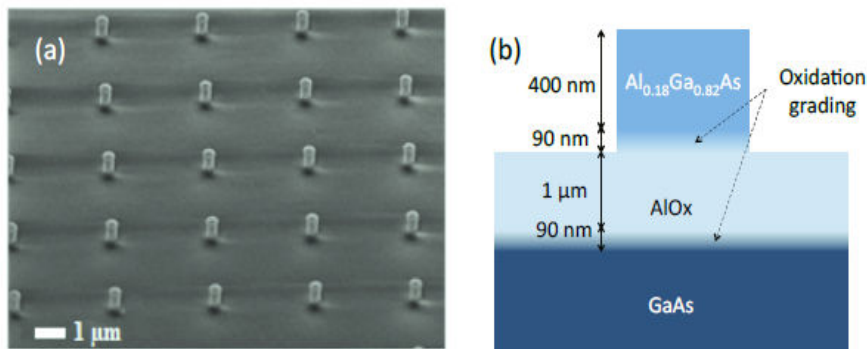


Figure 65: (a) SEM image showing an array of AlGaAs nanocylinders. (b) Vertical section of the sample showing the layer composition [37].

SHG nonlinear measurements on single pillars were carried out on a sample consisting of several arrays, in which a $3 \mu\text{m}$ spacing is chosen to ensure single-pillar investigation. Nominal radii span from 175 to 225 nm and the 400 nm height is fixed by the epitaxial growth. This sample was fabricated with the the non-optimized protocol, using ma-N 2401 as e-beam resist, with a dose varying from 100 to 200 $\mu\text{C}/\text{cm}^2$ to find optimal DF values (Fig. 65).

4.1.1 Numerical modelling

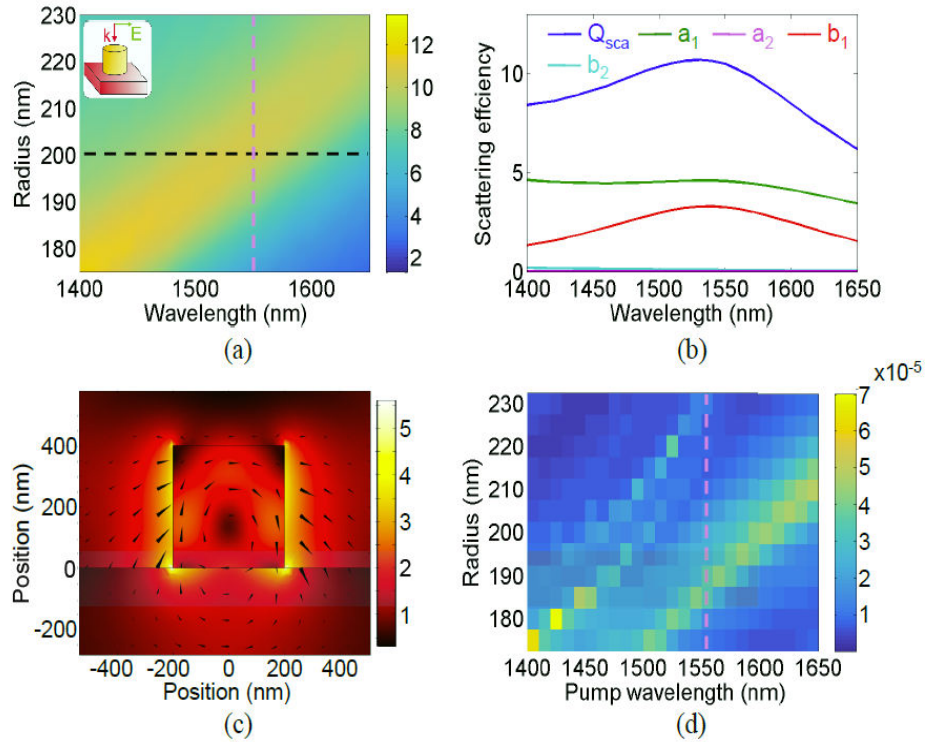


Figure 66: (a) Scattering efficiency spectra as a function of the nanoantenna radius and illumination wavelength. The horizontal dashed line represents a pillar with radius $r = 200$ nm while the vertical dashed line represents the wavelength of 1550 nm. The inset summarizes the geometry of the illumination. (b) Scattering efficiency (Q_{sca}) for a disk with $r = 200$ nm extracted from (a), with the multipole expansion terms of the optical response. The coefficients a_1 , b_1 , a_2 , and b_2 are due to ED, MD, EQ, and MQ contributions, respectively. (c) Electric field enhancement map in the incidence plane of a disk with $r = 200$ nm at the MD resonance ($\lambda = 1540$ nm). Black cones represent the electric field vector. (d) SH conversion efficiency as a function of the pump wavelength and nanoantenna radius. The vertical dashed line represents the wavelength of 1550 nm [37].

The linear and nonlinear optical response of a single nanoantenna on AlOx substrate was modelled in the group of Costantino De Angelis in Brescia University using FEM on COMSOL Multiphysics (Fig. 66) assuming plane-wave excitation with k-vector parallel to the cylinder symmetry axis and a field intensity of 1 GW/cm². In order to access the Mie theory regime and respect the constraint on the size parameter $x = 2\pi r/\lambda \sim 1$, the pump wavelength varies from 1400 nm to 1650 nm, while the cylinder radius span from 175 nm to 225 nm. The height is fixed at 400 nm, and we chose an Al concentration of 0.18. In such way we avoid the impact of TPA in the selected wavelength range. To model the material dispersion we resort to the phenomenological model presented in ref. [34].

First the scattering efficiency was calculated as a function of the radius and of the wavelength (Fig. 66a), then the spectrum of a pillar with radius 200 nm was extracted and decomposed in its multipolar contributions following the procedure described in [33]. In Fig. 66b a resonance around 1540 nm appears, mainly due to ED and MD moments. The electric field profile inside the pillar at such resonance (Fig. 66c) highlights the mostly magnetic nature of this resonance, with the presence of a circulating current generates a MD in the direction perpendicular to the pump k-vector.

SHG conversion efficiencies as a function of radius and wavelength are then obtained with the method described in Chapter 2, assuming a nonlinear coefficient value $\chi_{ijk}^{(2)} = 100$ pm/V for $i \neq j \neq k$ [36]. Nonlinear numerical simulations predict a maximum conversion efficiency of the order of 10^{-5} (Fig. 66d), with a two-order of magnitude drop with respect to the case of cylinder in air [32]. The reason for this striking difference is due to the presence of the AlOx layer ($n \simeq 1.6$). As the conversion efficiency is proportional to the following quantities:

$$\eta_{SHG} \propto (Q_{FF})^2 \cdot Q_{SH} \cdot \zeta \quad (4.1)$$

where Q_i are the scattering efficiencies at the FF and at the SH, while ζ is the overlap integral between the fields at the two involved wavelengths, defined as [32]:

$$\zeta = \frac{|\int E_i^{FF} E_j^{FF} (E_k^{SH})^* dV|}{\sqrt{\int |E_i^{FF} E_j^{FF}|^2 dV} \sqrt{\int |E_k^{SH}|^2}} \quad (4.2)$$

where the i, j, k -axes for FF and SH modes depend on the main field components to which a particular resonance couples and are bound to respect the $\chi^{(2)}$ symmetry, i.e. $i \neq j \neq k$. The presence of the AlOx substrate not only weakens the scattering resonances, but reduces the field confinement, due to the smaller Δn compared to air, thus diminishing the overlap integral ζ .

4.1.2 Experiments with fixed pump wavelength

In order to experimentally test the $\eta_{SHG} \approx 10^{-5}$ theoretical prediction, SHG experiments were performed in the group of Marco Finazzi, in Politecnico di Milano. Their nonlinear confocal microscopy setup (Fig. 67) allows lateral resolution as small as 700 nm in the nonlinear regime.

The illumination is provided by an Er^+ -doped fiber laser centred at 1554 nm laser emitting pulses of 150 fs duration. The pump polarization is controlled by means of a half-waveplate placed before the sample. The excitation beam is focused onto the sample through an objective with $\text{NA}=0.85$, with a measured spot-size of about $2\mu\text{m}$ allowing interrogation of individual nanoantennas (the spacing in this sample is $3\mu\text{m}$). It has to be stressed that even though the pump is fixed, it is still possible to access the various resonances involved in the SH process and retrieve spectral information on the system by analysing nanoantennas with different radii.

This approach is ideal to probe the nonlinear properties of $\text{Al}_{0.18}\text{Ga}_{0.82}\text{As}$ nanostructures, since the chosen Al molar fraction ensures transparency at both the pump and emission wavelengths and TPA-free operation. Results obtained in this way can still be compared with the ones employing a tunable pump since all the relevant phenomena occur at energies well below the material resonances, and other experiments are performed on relatively narrow spectral ranges so as to avoid dispersion.

Moreover, as Mie type resonances strictly depend on the size parameter x defined in Chapter 1, all the meaningful physics is expected to scale as the radius-to-wavelength ratio r/λ , regardless on which of these two parameters is fixed.

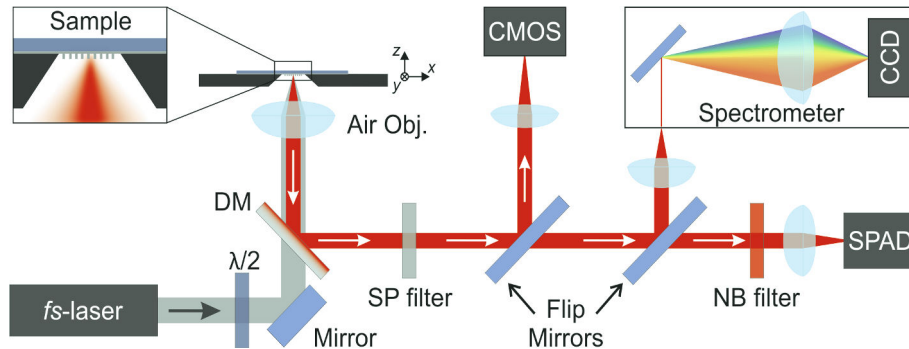


Figure 67: Experimental set-up for the nonlinear confocal microscopy experiments. Fs-laser: Er^+ -doped fiber laser delivering 150-fs pulses centered at 1554nm (light grey beam). $\lambda/2$: half-waveplate; Air Obj.: 0.85-NA air objective; DM: dichroic mirror; SP and NB filters: short-pass and narrow-band filter respectively. CMOS: imaging camera; SPAD: single-photon avalanche detector; CCD: spectrometer cooled camera [37].

The light emitted by the sample is collected in reflection geometry through the same optical path and separated from the pump by means of a polarization-maintaining DM. Moreover, a short-pass filter is inserted in the path just before the detection to clean-up the nonlinear signal from possible Two-Photon Luminescence (TPL). The nonlinear spectrum is investigated using two alternative paths divided by flip mirrors. The first consists of a visible/near-infrared grating-based spectrometer, while the second detection path consists of a narrow-band filter at 775 nm with 40 nm bandwidth followed by a silicon SPAD. The sample is mounted on a 3D-stage with a piezo allowing to move along the x and y directions with nanometric precision, thus allowing to record 2D SHG intensity maps (Fig. 68A).

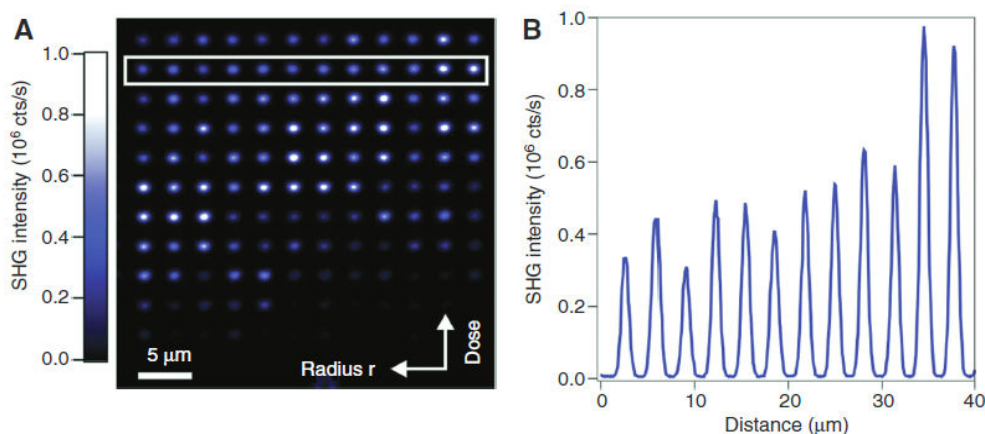


Figure 68: (A) SHG intensity map of a nanoantenna array with nominal radii spanning from 175 to 225 nm (x-axis) and e-beam dose varying from 100 to 200 $\mu\text{C}/\text{cm}^2$ (y-axis), obtained by scanning the hollow piezo on which the sample is placed. (B) Line profile of the second row of the array, marked by the white box in (A). [37].

Extracting data from a single row in the SHG intensity map (Fig. 68B) allows to confirm that the signal is coming from individual pillars, as individual peaks have the same spacing of $3\mu\text{m}$ of the nanoantennas, with a signal-to-noise ratio exceeding 10^4 . By subtracting the signal coming from the substrate of AlOx and GaAs, which is however three orders of magnitude lower than that of the pillars, it is possible to reveal the dependence of the experimental SHG on the nanodisk radius (Fig. 69a), with a maximum corresponding to a radius around 193 nm.

A direct comparison of the experimental plot with the numerical predictions (Fig. 69b) reveals a good agreement between the two, with a small frequency shift of the main peaks of around 5 nm which can be attributed to

fabrication tolerances between nominal and actual radii.

The SH emission of the most efficient nanoantenna was then studied as a function of the incident power ranging from 5 to 750 μW (Fig. 69c) both for increasing power (full circles) and decreasing power (hollow squares). The good overlap between the two curves indicates the absence of degradation during the measurements, while the quadratic fit confirms the second order nature of the process.

In particular the peak SH count rate at 750 μW incident power, corresponding to 1.6 GW/cm^2 peak intensity, gives a peak SH conversion efficiency of $1.1 \cdot 10^{-5}$, in good agreement with theoretical predictions. This figure of merit is obtained by accounting for the SPAD filling factor (0.34), the throughput of all the optical elements in the detection path including the objective (0.13), and the objective collection efficiency (0.1).

In order to compare the obtained SHG efficiency with other values reported in the literature for different peak intensity, we now normalize it to the pump power and obtain $\gamma_{SHG} = 1.5 \cdot 10^{-7} \text{ W}^{-1}$. In particular, comparing this value with the maximum SHG yield in engineered plasmonic nanostructures ($5 \cdot 10^{-10} \text{ W}^{-1}$ [46]) clarifies the advantage of bulk field confinement in Mie-type resonators with respect to surface confinement due to LSP in metallic nanostructures, and illustrates the potential of all-dielectric nanostructures for nonlinear light generation.

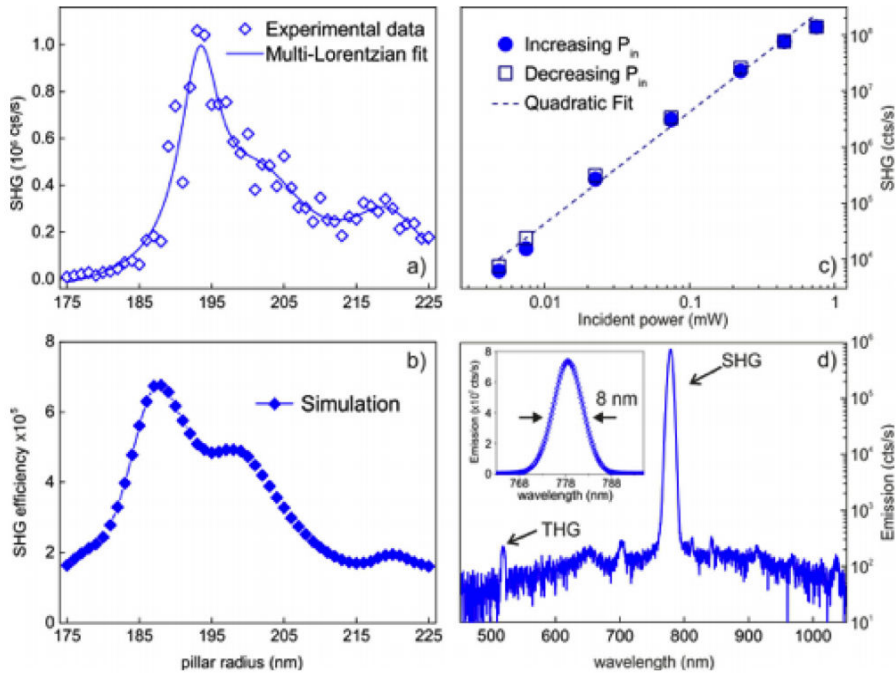


Figure 69: a) Measured SHG rate as a function of the nanoantenna

radius. As a guide to the eye a multi-Gaussian fit featuring three distinct peaks. b) Numerical calculations of the SHG efficiency on nanoantennas featuring the same geometrical parameters as the fabricated/measured ones. c) Power curve in Log/Log scale for the most efficient nanoantenna, with 193 nm radius. d) Emission spectrum of the most efficient pillar acquired at 500 μW incident power and plotted in Log scale. Inset: a zoom of the main SHG peak plotted in linear scale (void diamonds) and a Gaussian fit to it (straight line) [37].

We took a closer look to the emission spectrum by removing the short-pass filter, with incident power of 500 μW . Even at this relatively high pump power, Multi-Photon Luminescence (MPL) is barely detectable and only a very weak THG peak is observed (Fig. 69d).

This spectrum also allows us to safely claim that our signal is indeed coming from SHG and not from TPL. The argument is the following: while for both processes the efficiency scales with the square of the incident power, for a coherent process such as q th harmonic generation, the field scales as $E_{q\omega} \sim E_{\omega}^q$. Thus, in our case of Gaussian beam excitation, the SH Full-Width at Half Maximum (FWHM) is bound to be $\sqrt{2}$ times narrower than the FF laser line [17]. In our case, the FF FWHM is 15 nm, and the spectrum in the inset of Fig. 69d shows that the SH FWHM is about 8 nm, as expected from this process.

4.1.3 SHG polarization properties

We next analysed the polarization properties of the emitted SH signal by inserting a polarizer in the detection path [113]. This allowed us to study separately the SH components either co-polarized or cross-polarized with the pump, and compare them to unpolarized emission (Fig. 70). We observed a significant change in the SH polarization state with varying radius; indeed for smaller radius ($r/\lambda \simeq 0.123$) we found that the SH is mostly co-polarized with the pump, while for larger radii ($r/\lambda \simeq 0.140$) the behaviour is opposite and SH is mostly cross-polarized with the pump (Fig. 70b). These results might appear rather counter-intuitive compared to phase-matched structures, as for AlGaAs, which belongs to the $\bar{4}3m$ symmetry group, the only non-zero elements in the second-order nonlinear tensor are such that $\chi_{xyz}^{(2)} = \chi_{yzx}^{(2)} = \chi_{zxy}^{(2)} = 100 \text{ pm/V}$.

The consequence of such symmetry is that in case of an incident plane wave with a linearly polarized electric field along the bisector of two crystalline axes, say [100] and [010], SHG will occur in a way to be linearly polarized along the [001] direction in bulk AlGaAs. However, in Mie nanoresonators, the pump beam excites multipolar modes which do not exhibit pref-

erential k-vectors, contrarily to the phase-matched case. For example, in the case of an AlGaAs nanoantenna pumped at the MD the main the electric field components are E_x and E_z [32]. Moreover, the SH polarization will depend as well on the field distribution of the high-order multipolar mode at 2ω which best couples to the FF mode. As at 2ω the forest of modes is denser than at ω , small changes in the antenna geometry can result in great differences in the SH field distribution, and hence the nonlinear emission polarization.

Given the extreme polarization sensitivity of our system, we decided to further ameliorate our numerical model by explicitly allowing for Gaussian beam excitation rather than a plane wave one. Indeed, in this case, the plane wave approximation might not be adequately accurate. In addition to assuming Gaussian beam excitation with a beam-waist of $2\mu\text{m}$, the SHG signal was collected in reflection by integrating over a 0.85 NA. In this way we were able to obtain a good agreement between experiments and calculations for both cases of co and cross polarized SH light, with all relevant features being matched apart from one peak in the cross-polarized emission at low r/λ being stronger in the simulations than in the experiments (Fig. 70b). This discrepancy, as well as a small shift in radius of the resonances, are again to be attributed to fabrication tolerances.

In order to get further insight into the modes responsible for the nonlinear emission, the different resonances that characterize the SHG spectrum were decomposed and the multipolar contributions to the currents generated inside the resonator at the SH wavelength were analysed (Fig. 70c). The nonlinear emission peak occurring at lower r/λ is dominated by a Magnetic Hexapole (MH) resonance, while the nature of the secondary peak at higher radius values is mainly due to an overlap between electric and magnetic dipoles. Interestingly, here the magnetic quadrupole contribution is negligible, and we can attribute this to the specific values of the disk sizes and the wavelength employed.

However, as the nonlinear generation in such nanostructures is very sensitive to these parameters, in slightly different conditions the quadrupolar contributions can become dominant and the hexapole contributions negligible. It has to be stressed that since the computational model to identify the multipole contributions to the SH emission describes the fields emitted in the whole space, both the position and the spectral width of the peaks in Fig. 70c slightly deviate from the results reported in both Figs. 70a and 70b, which are obtained by considering only the limited collection angle of the objective.

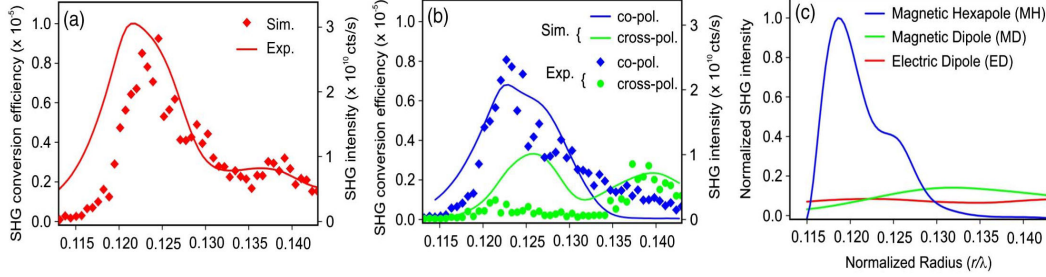


Figure 70: (a) Simulated (line) and experimental (diamonds) unpolarized emission replotted as a guide to the eye as a function of the normalized radius, r/λ . Results are plotted both as overall photon count and as equivalent conversion efficiency. (b) Calculated (lines) and experimental (dots) polarized emission as a function of r/λ . Co- and cross-polarized SHG are plotted in blue and green, respectively. (c) Multipole decomposition of the fields emitted at the SH wavelength as a function of r/λ [113].

This anomalous polarization behaviour was also studied by recording SHG confocal maps for the two resonant values of r/λ of 0.123 and 0.140 (Figs. 71a,b and 72a,b) for both cases of SH polarization parallel and orthogonal to the one of the pump. By changing the angular position of the polarizer in the collection path it was possible to extrapolate experimental polar plots from a series of SHG confocal maps (Figs. 71c and 72c).

In order to eliminate the effect of local nonidealities on the nanoantennas, such as the tilt in the crystallographic axes revealed by TEM characterization, an average of the SH emission over four nominally identical individual pillars was performed. In the case of $r/\lambda \simeq 0.123$ the experimental polar plot shows that the radiated SHG is polarized mainly parallel to the pump polarization, with an excellent agreement between the measurements and simulations. On the other hand, the cross-polarized SHG component is weaker.

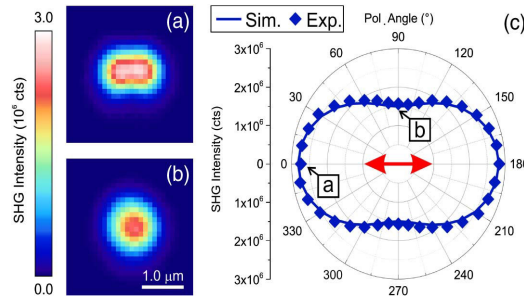


Figure 71: Confocal SHG maps acquired on a $r/\lambda \simeq 0.123$ nanodisk for nonlinear emission polarization (a) co-polarized and (b) cross-polarized

with the pump beam. (c) Simulated (solid line) and experimentally acquired (diamonds) polar plots of the emitted SH from the nanostructure. Red arrow: pump polarization direction. Boxed letters: SHG values corresponding to the images on the left [113].

In the case of $r/\lambda \simeq 0.140$, conversely the SH polarization component parallel to the one of the pump is only very weakly excited when focusing the excitation beam on the center of the nanoantenna, while for the stronger cross-polarized emission, optimized SHG is obtained when coupling to the side of the nanoantenna, in complete analogy to the case of smaller r/λ .

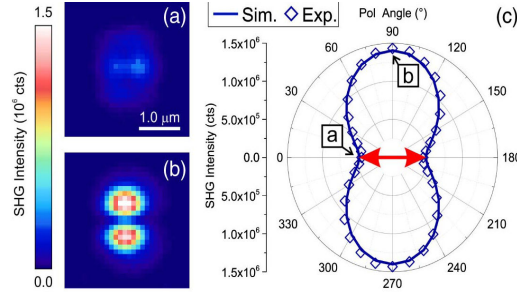


Figure 72: Same as Fig. 78 for $r/\lambda \simeq 0.140$ [113].

Fig. 72 also shows that in this last case, the polarization degree of the SH signal is higher than that of smaller nanoantennas, while the overall SH rate is lower. This feature again agrees with the simulations in Fig. 70b, and further confirms that the absence of one peak in the experimental cross-polarized SH component with respect to calculations can be attributed to local nonidealities due to fabrication tolerances. Finally these results shed light on the non-trivial polarization properties of SHG emission from nanoscale resonators and further validate the bulk- $\chi^{(2)}$ numerical model developed in Brescia.

4.1.4 Impact of nonidealities on SH emission properties

As already mentioned, the results described in the previous sections were obtained by averaging on four nominally identical nanoantennas. Conversely, the non-averaged polar plots, for example in the case of $r/\lambda \simeq 0.123$, present a polarization tilt with respect to the ideal case in the range $[-8.8^\circ; 6.6^\circ]$ (Fig. 73).

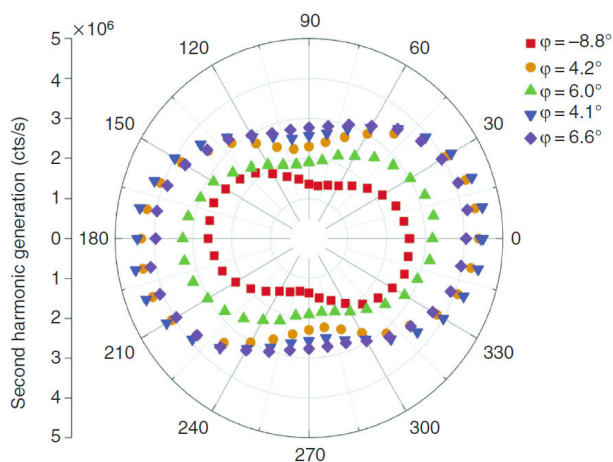


Figure 73: SHG polar plots of four virtually identical nanoantennas ($r/\lambda \simeq 0.123$). The tilt angle φ ranges from 8.8° to 6.6° [70].

In order to understand the origin of this angle we again resorted to FEM numerical simulations on COMSOL Multiphysics. First, we tested the hypothesis of a broken crystal symmetry in the nanoantennas induced by the volume shrinkage of the $\text{Al}_{0.98}\text{Ga}_{0.02}\text{As}$ layer during wet oxidation.

To this end we evaluated the strain distribution around the interface between the nanodisks and the oxide has been analysed by finite element modelling. Indeed several groups have shown that such symmetry breaking can affect the nonlinear response of a material, for example inducing SHG in Si, despite it being forbidden due to the crystal's centrosymmetry [114, 115, 116]. Similarly, the effect of uniaxial stress on coherence length for the second harmonic generation in GaAs and InAs has also been investigated [117].

In order to evaluate this strain on our AlGaAs-on-AlOx nanopillars and its possible effect on SHG, the strain distribution around the interface between the nano-disks and the oxide has been analysed with the mechanical module on COMSOL, treating $\text{Al}_x\text{Ga}_{1-x}\text{As}$ as an anisotropic material with mechanical properties described in [118]. As AlOx instead is amorphous, its exact mechanical properties are unknown. In this case $\gamma\text{-Al}_2\text{O}_3$ parameters can be used, as previously reported [100]. Those parameters are summarized in the following table:

Material	Young Modulus	Poisson's coefficient
$\text{Al}_x\text{Ga}_{1-x}\text{As}$	$C_{11}=(118.8+1.4x)$ GPa $C_{12}=(53.8+3.2x)$ GPa $C_{44}=(59.4-0.5x)$ GPa	$\nu=0.31+0.1x$
$\gamma\text{-Al}_2\text{O}_3$	$\ C\ =400$ GPa	$\nu=0.21$

We have considered an elastic strain of 13% in the oxide layer along the direction perpendicular to the substrate plane. The numerical results show that the strain in the nanodisks is mainly located close to the interface with the AlOx and seems too low (maximum 10^{-3} in the parallel direction) compared to the usual values employed for SHG enhancement in Si waveguides [114, 115, 116]. From these numerical results (Fig. 74), reinforced by the TEM observations described in the previous chapter, according to which only a small rotation of the crystallographic axes of the nanoantennas is present, we can safely claim that no significant deformation of the $\chi^{(2)}$ tensor occurs [70].

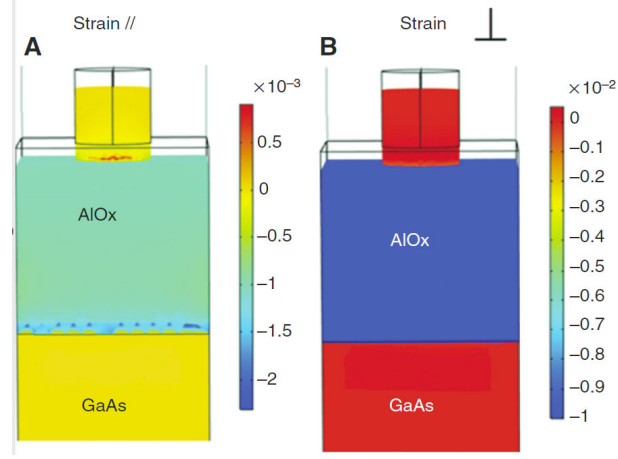


Figure 74: Finite-element map of the oxidation-induced strain on the nanoantenna parallel (A) and perpendicular (B) to the wafer plane. The latter is zero, whereas the former is much lower than the typical values that induce a non-vanishing $\chi^{(2)}$ in Si [70].

In order to infer whether the angles in the nanoantennas' crystallographic axes with respect to the $[001]$ (X) and $[1\bar{1}0]$ (Y) directions of the substrate measured by electron diffraction can explain the random tilt in the measured polar plots we performed fully vectorial frequency-domain FEM calculations. To model the stress induced rotation of the nanoantennas' principal axes we define an angle θ between the $[110]$ crystalline axis and the linearly polarized electric field of the pump impinging at normal incidence on an untilted nanoantenna (inset in Fig. 75).

Defined in this way, θ is thus completely equivalent to the tilt around the X axis, we measure with electron diffraction. The presence of this angle θ at the fundamental frequency then causes the presence of an angle ϕ between the prevailing SH linear polarization and the $[1\bar{1}0]$ axis which in general is different from θ . By performing FEM calculations with values of θ consistent

with electron diffraction measurements ($2^\circ - 5^\circ$), we indeed find that the latter give rise to a range of values for ϕ ($5^\circ - 13^\circ$) that are in good agreement with the SHG measurements (Fig. 75).

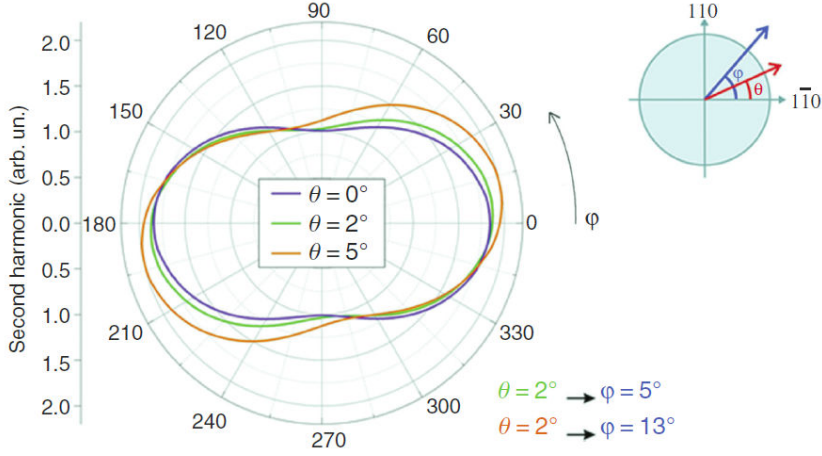


Figure 75: Calculated polarization plots of the emitted SH assuming an angle θ between the [110] crystalline axis and the linearly polarized electric field of the pump impinging at normal incidence on an untilted nanoantenna (see inset). The presence of θ gives rise to a tilt ϕ in the SH polar plots compatible with the experimental ones shown in Fig. 73 [70].

Interestingly, the message here is that we were able to get an agreement between calculations and experiments by only assuming the presence of a tilt around the [001] (X) principal direction.

4.1.5 Experiments with a tunable pump

A nominally identical sample of isolated nanoantennas with 400 nm height, $3\mu\text{m}$ spacing and radii in the range 175 nm-225 nm was also sent to King's College in London, and it was measured in the group of Anatoly Zayats using a broadband tunable femtosecond OPO (300 nm-2600 nm) as a pump for SHG. Apart from this difference their setup is essentially the same confocal microscope employed in Politecnico di Milano (Fig. 76).

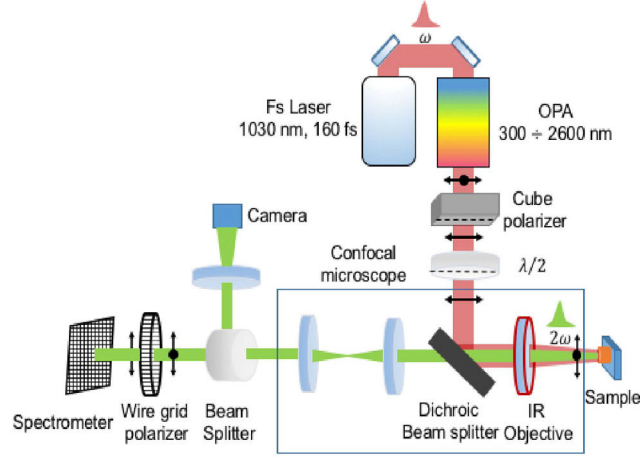


Figure 76: Experimental nonlinear confocal microscopy set-up in King's College. The pump beam is here delivered by a widely tunable ultra-fast OPA [119].

An x-polarized pump tuned in the range 1400-1750 nm with a 20 nm step is focused on a $4\mu\text{m}^2$ area, allowing to excite a single pillar with $r=225$ nm, whose nonlinear response is shown in Fig. 77 for both co-polarised (a) and cross-polarised (b) pump/SHG configurations [119]. Both cases present two resonances at approximately 1530 nm and 1670 nm. Two resonances can be observed in the SHG spectral range at the fundamental wavelengths of for both co-polarized and cross-polarized configurations. Despite the presence of TPA for $\lambda_p \leq 1480$ nm, as $E_g(\text{Al}_{0.18}\text{Ga}_{0.82}\text{As}) = 1.677$ eV corresponds to a $\lambda_g \approx 739.6$ nm, the agreement with numerics is again quite good.

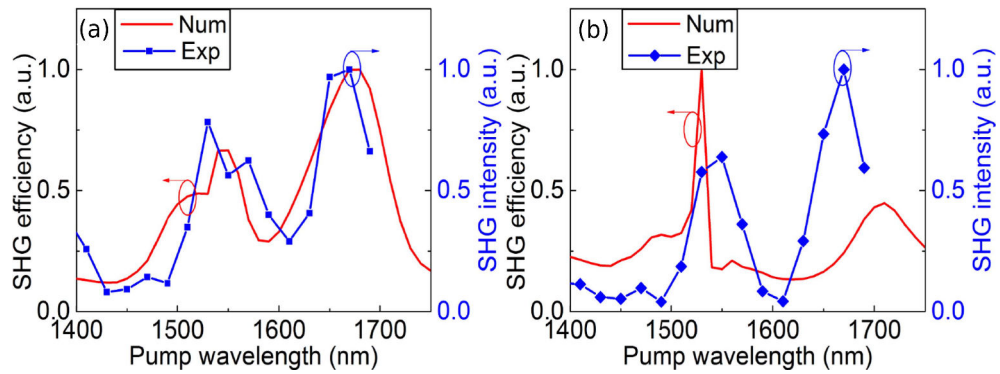


Figure 77: SHG spectra of a pillar with $r=220$ nm excited with a tunable pump in both co- (a) and cross- (b) polarized pump/SHG cases [119].

The novelty of these experiments is better represented by the SHG radiation pattern detection of the nanoantennas. To this end, a fixed X-polarized fundamental at 1064 nm was focused on a nanoantenna with $r=180\text{nm}$, and images of the radiated SHG at different focal planes along a single antenna optical axis were recorded on a camera (Fig. 78) [119]. A bright two-lobe green spot attributed to 532nm SHG is observed in the 60° light-cone accessible with the objective of 0.85 NA, surrounded by a weaker red background from the GaAs substrate attributed to TPL .

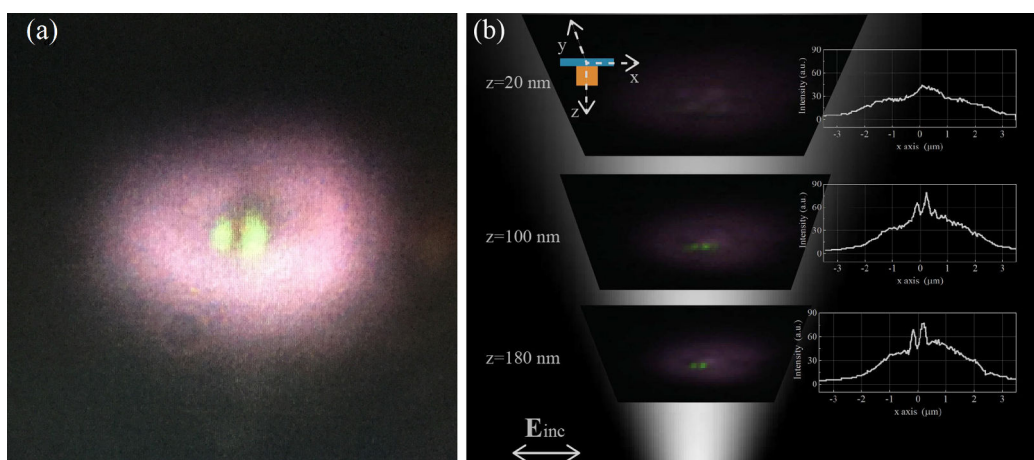


Figure 78: Camera images of the SH radiation pattern. (a) Snapshot taken at the nanoantenna focal plane; (b) The signal disappears as we scan along the z direction [119].

The presence of two lobes reveals the mainly quadrupolar nature of SH emission, in contrast with what observed in [113], and confirms again the extreme sensitivity of the SH multipolar nature to the nanodisk geometry and illumination conditions. In both fixed and tunable pump experiments, a common feature was observed which is due to symmetry reasons: the absence of emission in the direction of the antenna axis.

This effect can be seen as a direct consequence of the phase-matching absence in these nanoscale resonators, where the SHG radiation pattern is completely determined by high-order multipolar mode that couples to the nonlinear currents generated inside the nanoantennas. Of course, for applications in which a certain directivity is needed, the absence of the SH radiation in the direction of the nanoantenna axis constitutes a potential limitation.

4.2 Nonlinear emission directionality considerations

The origin of the null in SHG emission in the forward and backward directions for normal incidence pumping actually lies in the symmetry of the modes excited at 2ω frequency [120]. For FF in the NIR around 1550nm mostly dipolar resonances are excited, in the range of the SH wavelengths. However, a multitude of high-order multipolar modes exist, whose excitation depends on the nonlinear polarization the symmetry induced by the pump. For example, when we pump at the MD [37], the nonlinear current distribution is symmetric with respect to the xz and xy planes and gives rise to a nonlinear source that resembles an electric quadrupole.

This behaviour was also observed in [119], as the two-lobe emission in the backward direction shown in Fig. 78a suggests the excitation of a quadrupolar mode. Conversely, we have observed as well the case in which a MH contribution is predominant (Fig. 70c). In all above mentioned cases, the displacement current distribution inside the nanoresonator leads to excitation of modes that are in opposition of phase and thus have a zero in the normal forward and backward directions [120].

To date, several methods have been proposed to solve this issue including changing the pump polarization state, with a high degree of directionality achieved even in the simple case of a linearly polarized pump between 0° and 90° [120]. One of them is inspired to the so-called Kerker effect [122], in which for particular nanoparticle geometries, light is radiated as a superposition of equal strength of both electric and magnetic dipoles, with a high degree of directionality either in the forward or in the backward direction depending on the relative phase difference of these two modes. This effect was also experimentally observed in GaAs nanospheres [85]. The Kerker principle has also been extended to interference of higher order multipoles, finding that whenever multipoles with the same amplitude and opposite symmetry are present, the emission diagram becomes highly directive [123].

In the NANOPHI project, we preferred to focus on two other methods to overcome this issue: the first involves pump reconfiguration so as to couple the SH signal to a dipolar mode, which mainly radiates in the normal direction [120], while in the second we break the symmetry of the mode at 2ω surrounding the nanopillars with asymmetric diffraction gratings [121].

4.3 SH emission shaping through pump reconfiguration

The idea behind pump reconfiguration to achieve better directionality is that even though high SH conversion efficiency was achieved so far, the mode symmetry is such that there is a null both in the forward and backward direction, and as the collection efficiency is limited by the objective NA both in reflection and transmission geometries, most of the generated SH signal is lost.

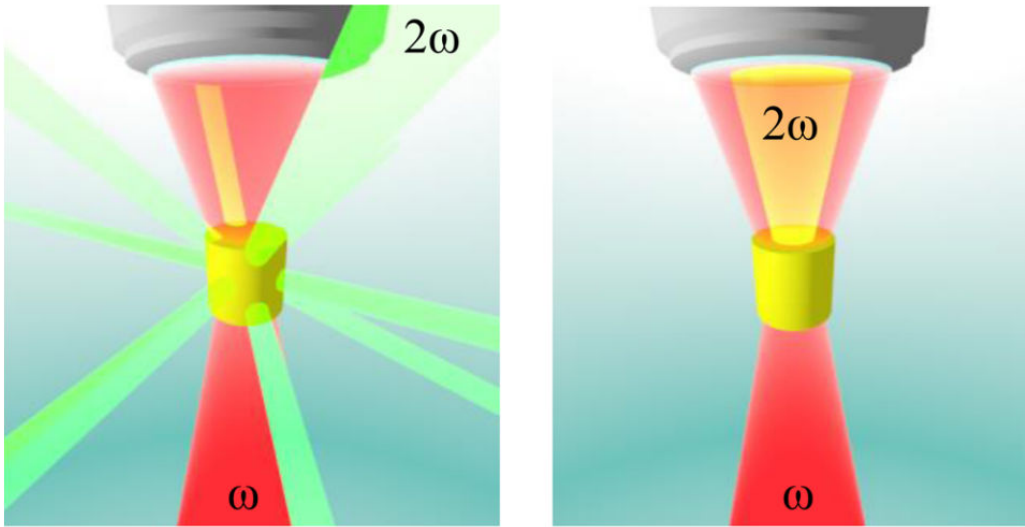


Figure 79: Conceptual scheme of the directionality problem: in all experiments described so far the nanoantennas do not emit in the normal direction (left), while in order to maximize the collection efficiency, the ability of radiation pattern engineering is of paramount importance (right). Figure taken from [120].

It was theoretically shown that, if we illuminate a nanoantenna of our typical dimensions with a pump around 1550 nm, the insertion of a tilt in the pump k -vector with respect to the cylinder axis allows to shape the far-field radiation pattern of the SHG so as to eliminate the null in the normal direction and obtain a high directionality in both forward and backward directions.

The origin of this effect is that while at normal incidence we excite a high-order multipolar resonance (quadrupolar or hexapolar as already shown), when we tilt the pump k -vector we are able to excite a dipolar mode at 2ω , which preferentially radiates in the direction parallel to the cylinder symmetry axis [120].

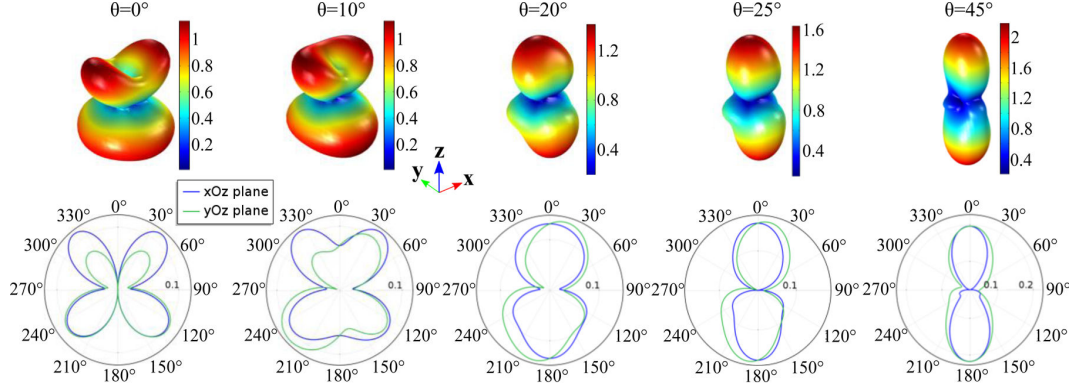


Figure 80: Top line: calculated far-field SH radiation patterns as a function of the pump incidence angle. Bottom line: Radiation pattern projected in the xz plane (blue line) and yz plane (green line). The results show that as the pump tilt increases, the SH radiation reshapes so as to increase directionality along the cylinder symmetry axis. Figure reproduced from [120].

In order to test these theoretical predictions, experiments were carried out on our samples in the group of Dragomir Neshev at the Australian National University in Canberra by Giuseppe Marino and Lavinia Ghirardini, who were visiting that group in the frame of the NANOPHI project. The experimental set-up (Fig. 81) is again a confocal microscope, in which the pump beam, an ultra-fast Er^+ -doped fiber laser emitting pulses centered at 1570 nm, is focused by a long focal-length lens ($f=500$ mm) onto the BFP of a high-NA objective (Olympus, NA 0.85).

The pump incidence angle is controlled by scanning the transverse position of the lens, which shifts the beam position on the input aperture of the objective with a maximum range from normal (beam at the center of the BFP) to 58° incidence (beam at the edge of the BFP). Here however we limited our experiments in the range 0° - 45° , as for angles $\theta > 45^\circ$ part of the pump beam was cut out due to the finite objective NA. The SH emitted from the sample is collected in epi-reflection through the same objective and filtered by a short-pass filter at 800 nm and a long-pass filter at 600 nm to remove any photoluminescence from the GaAs substrate and third harmonic emission component from the nanodisks, respectively. SHG emission is imaged on a cooled CCD camera in the real space, while the emission pattern in the Fourier space is studied by adding a confocal lens focusing at the objective BFP. [124].

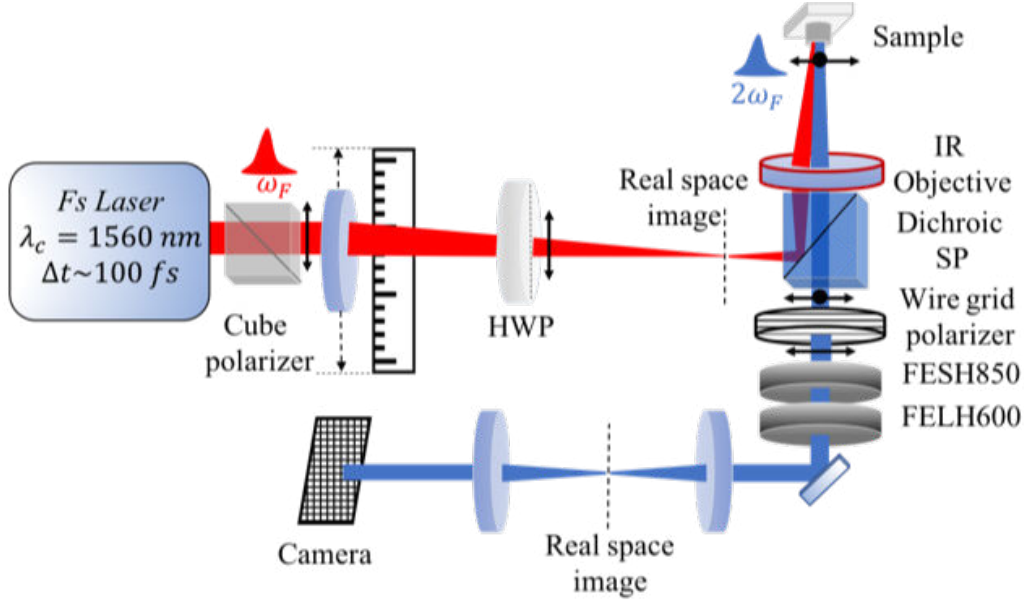


Figure 81: Nonlinear microscopy set-up for tilted pump measurements [124].

The SHG radiation pattern of a nanoantenna with $r=220$ nm in the far-field is studied in Fourier space as a function of the incident angle by adding a BL which focuses on the objective BFP for both cases of s and p polarized pump beam. As Figs. 89a,c show, for a pump at normal incidence the SH light is radiated only at large angles, while no light is detected in the normal direction (center in the BFP images), regardless of polarization.

As the angle of incidence increases we observe two distinct behaviours: for **p – polarized pump** beam the radiation pattern does not vary significantly as only a small SH radiation portion is redirected in the backward direction as θ is increased up to 45° . In contrast, for the case of an **s – polarized pump**, we observe that for $\theta \geq 10^\circ$ the SH radiation is redistributed. The emission lobes at large angles appear to merge in the lower side of the image into a single lobe along the normal direction (i.e. at the center of the BFP images). Moreover, the intensity of this lobe increases monotonically with θ . Full-wave FEM simulations performed on COMSOL show a good agreement between the measured and the calculated SH radiation patterns as a function of both pump polarization and angle of incidence.

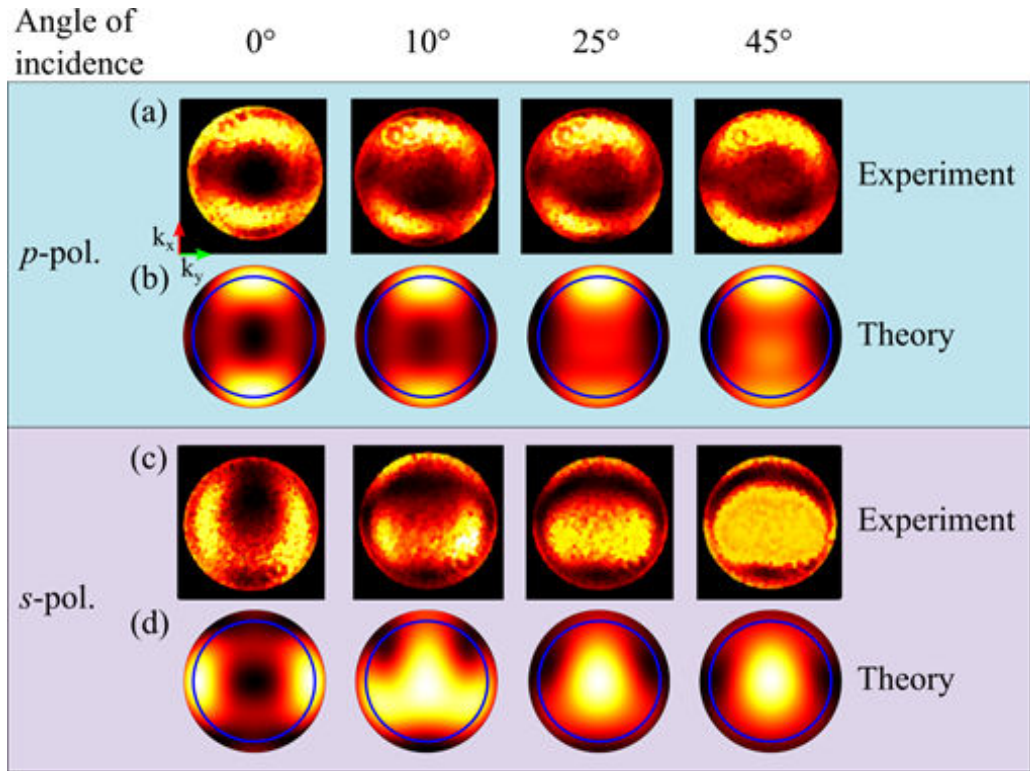


Figure 82: Measured (a,c) and simulated (b,d) BFP images of the SH radiation emitted in reflection geometry for different incidence angles θ . (a,b) regard the case of **s**-polarized fundamental excitation, while (b,d) refer to the case of **p**-polarization. The blue circle in (b,d) represents the objective NA=0.85 as a guide for the eye.

Figure 83 shows the SH collected power as a function of θ , for both of **s**- and **p**-input polarizations. Results exhibit a good superposition of the calculations (continuous line) with the experimental data (squares and diamonds). The numerical results achieved by Luca Carletti, presented in [120], show that the maximum SH collection efficiency is obtained for $\theta = 45^\circ$, which fortunately coincides with the maximum angle allowed by our objective NA.

Moreover, the collected SH power for the **s**-polarized pump beam is about 5 times larger than the **p**-polarized case as θ varies, underlining that SHG at the nanoscale is strongly sensitive to the pump polarization state. Overall, for **s**-polarized pump beam at 45° incidence, the collected SH power is enhanced by a factor 10. Remarkably, the collection efficiency enhancement increases monotonically with θ .

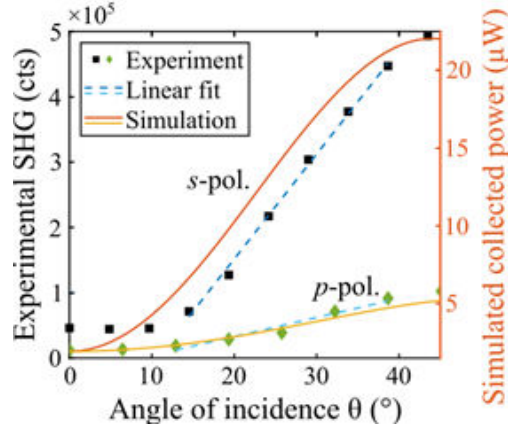


Figure 83: Angular dependence of the SH collection efficiency as a function of θ for both s and p polarized pump. The collected SH power is enhanced up to a factor 10.

As mentioned above, the physical reason for radiation redistribution and collection efficiency enhancement is revealed by the multipolar decomposition [33] of the SH field. As shown in Fig. 84, for s-polarized pump at $\theta = 0^\circ$ the SH radiation is mainly governed by an electric quadrupole, which mostly radiates at large angles and has a minimum along the normal axis. Conversely, as θ increases up to 45° , the electric dipole contribution builds up monotonically until it becomes the dominant one. In this case, the radiation pattern at the SH frequency is characterized by two main lobes pointing towards the forward and the backward directions along the disk axis.

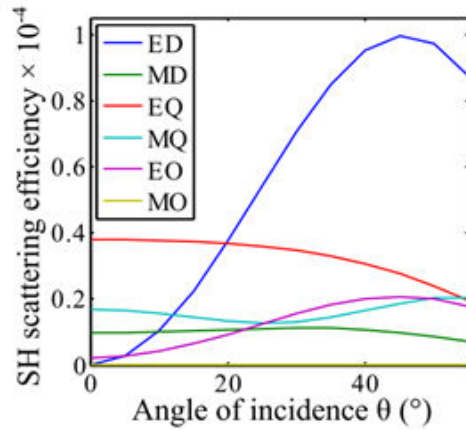


Figure 84: Multipolar decomposition of the SH emission according to [33]. The observed directionality increase and collection efficiency enhancement can be ascribed to the ED contribution building up for increasing pump incidence angles.

4.3.1 Towards nonlinear goniometry at the nanoscale

The monotonic collection efficiency increase with the angle θ is a rather interesting feature, which could find a practical application for the precise measurement of the angle between the pump-beam propagation direction and the disk symmetry axis. In other words a single nanoantenna can be considered a nanoscopic goniometer.

As seen in Fig. 83, the SH collected power increase is locally linear for θ in the range 15° - 40° . The slope, normalized to the lowest value of the SH power, is equal to $0.25(^\circ)^{-1}$ for **s**-polarization and $0.15(^\circ)^{-1}$ for **p**-polarization. To evaluate the angular sensitivity at small angles we can exploit the spatial intensity distribution revealed by BFP images in Fig. 82 and calculate the following quantity:

$$D_\theta = \frac{I_a - I_b}{I_a + I_b} \quad (4.3)$$

where I_a and I_b are respectively the measured intensities at one side and at the center of the BFP images. Defined in this way, D_θ is nothing but a normalized BFP intensity difference, and represents a good parameter to estimate the angular sensitivity of the nanoantennas. Looking at how this quantity varies with θ we find a good agreement between simulations and measurements, and most importantly we find a linear relation for angles in the range 0° - 10° , with slopes of $0.087(^\circ)^{-1}$ and $0.014(^\circ)^{-1}$ for s and p-polarizations respectively.

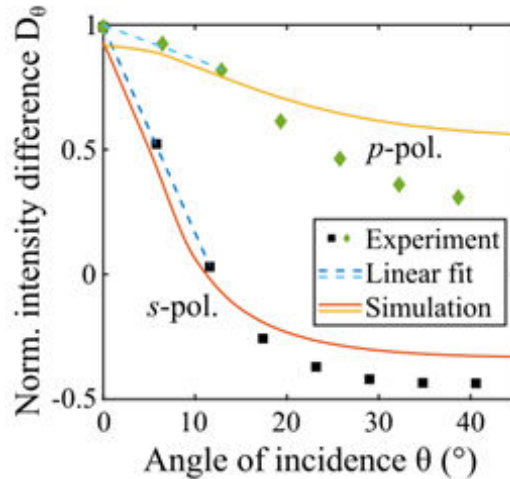


Figure 85: Normalized BFP intensity difference D_θ . This quantity can be used to estimate the angular sensitivity of our system especially in the range 0° - 10° where it varies linearly with θ . The resulting slopes are of $0.087(^\circ)^{-1}$ for s-polarized pump, and $0.014(^\circ)^{-1}$ for p-polarization.

A direct comparison with another nanoscale angular metrology system based on quantum-dot polarized emission, with a precision of 1° - 2° [125], suggests that our polarization-sensitive angular measurements of the pump inclination could potentially lead to a new technique for background-free nanoscopic nonlinear goniometry.

4.4 SH emission shaping through asymmetric diffraction gratings

An alternative method to reshape the SH radiation pattern relies on the integration of an asymmetric diffraction grating, which has the capability to reshape the far-field emission by operating in the near-field via interference effects [121]. The design of such structure involves the optimization of several parameters, including height, distance from the nanoantenna, asymmetry degree, period and duty cycle, defined as the ratio between air and high-index material. We first set the height of the grating at 400nm in order to facilitate its fabrication, allowing to integrate it directly in the $\text{Al}_{0.18}\text{Ga}_{0.82}\text{As}$ layer and avoid multiple EBL steps.

We then start with 2D simulations to find the optimal period and duty cycle parameters of the grating [126]. By taking advantage of the reciprocity principle, the structure is excited with a y-polarized Gaussian beam centred at the SH frequency, impinging at normal incidence (Fig. 86a). We measure the power that is scattered from one side of the grating towards a numerical probe (red line in Fig. 86a). Then a SH scattered power map is calculated as a function of the period Λ and the Duty Cycle (DC). In the simulations shown in Fig. 86b, the probe is 1200 nm far from the grating, however repeated simulations with different probe distance showed that the result at this stage is independent from the distance.

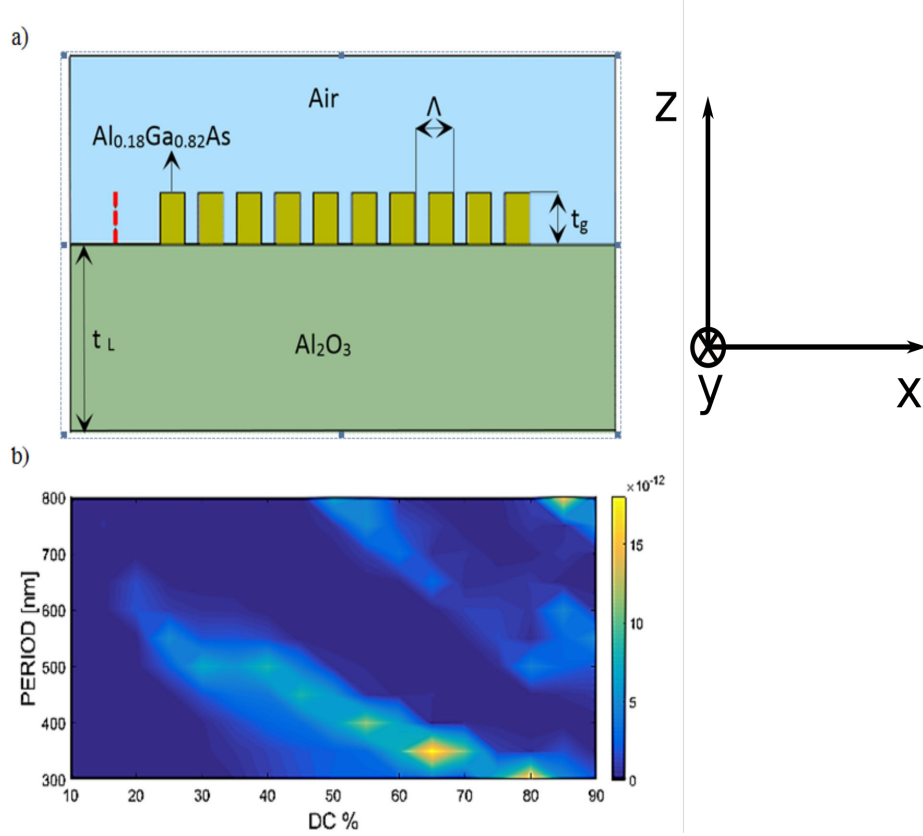


Figure 86: Asymmetric diffraction grating design. (a) Schematics of the sample, including the numerical probe (dashed line). (b) SH scattered power map as a function of the grating period (Λ) and DC [126].

The simulations show an optimal grating period of $\Lambda = 340$ nm and a DC of either 65% or 85%, corresponding to a ridge width of either 228 nm or 290 nm. Next, full-vectorial 3D simulations were performed surrounding a central nanoantenna with three concentric ridges resting on AlOx, to identify the optimal shift parameter to break the 2ω resonance symmetry (here assumed to be quadrupolar), and redirect the SH radiation into the normal direction. An optimal left-right shift of 290 nm was found, while the minimum distance between grating and central pillar was set at 500 nm so as that the grating structure does not affect the linear scattering properties of the nanocylinder at the fundamental frequency. The resulting structure was presented in Chapter 3, Fig. 45.

It is possible as well to write a simplified 2D analytical model to design the grating, which is based on the assumption that the radiated SH field mainly depends on the emission of the grating combined with the central pillar in the zx -plane with $y=0$. We can define a polar coordinate system (r, θ) whose origin is the nanopillar (Fig. 87).

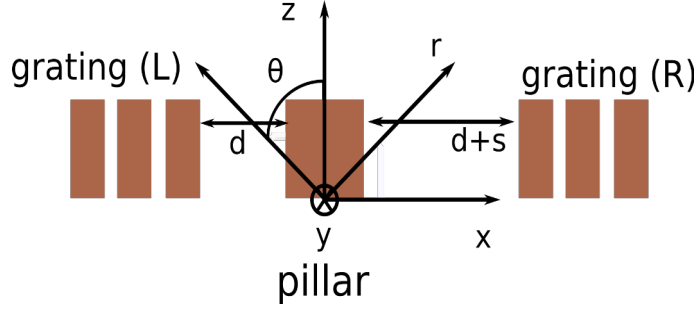


Figure 87: Schematics of 2D analytical model to design the grating. We consider an xz -plane with $y=0$ the largest cylinder section as well as the left and right sides of the grating consisting of three grooves. A polar coordinate system (r, θ) with origin in the nanopillar is defined.

The total SH signal observed in the far-field can then be written as follows:

$$\mathbf{E}_{total}^{SH}(r, \theta) = \mathbf{E}_{gr}^R(r, \theta) + \mathbf{E}_{gr}^L(r, \theta) + \mathbf{E}_p^{SH}(r, \theta) \quad (4.4)$$

where \mathbf{E}_{gr}^j , $j = (R, L)$ is the field radiated by the left (L) and right (R) sides of the grating, and \mathbf{E}_p^{SH} is the SH emitted by the nanoantenna. As we assume here that the gratings do not generate nonlinear signal themselves, but they just redirect the SH from the nanoantenna, \mathbf{E}_{gr}^j can be written in terms of the grating response function $\bar{G}(\theta)$. As we are interested in the field redirected in the normal direction ($r = z, \theta = 0$) we can rewrite Eq. 4.4 as:

$$\mathbf{E}_{gr}^L(z, 0) = \mathbf{E}_p^{SH}\left(\frac{\pi}{2}\right) e^{-ik_x d} \bar{G}(0) e^{-ik_0 z} \quad (4.5)$$

$$\mathbf{E}_{gr}^R(z, 0) = \mathbf{E}_p^{SH}\left(-\frac{\pi}{2}\right) e^{-ik_x(d+s)} \bar{G}(0) e^{-ik_0 z} \quad (4.6)$$

where k_0 and k_x are the vacuum and in-plane wavevector, respectively. As $\bar{G}(0)$ depends solely on the geometry of the grating, it will be the same both for left and right sections of the grating. Moreover, the expression can be further simplified by recalling that the SH emission of the nanoantenna in the xz -plane exhibits odd symmetry, with respect to z axis:

$$\mathbf{E}_p^{SH}\left(-\frac{\pi}{2}\right) = -\mathbf{E}_p^{SH}\left(\frac{\pi}{2}\right) \quad (4.7)$$

We can now introduce the phase-shift induced by the grating asymmetry: the pillar-grating distance on one side, say left ($\theta = \pi$), is d , while on the other, right ($\theta = 0$), it is $d + s$ (see Fig. 87). Then:

$$\mathbf{E}_{gr}^R(z, 0) = \bar{G}(0) \mathbf{E}_p^{SH}\left(-\frac{\pi}{2}\right) e^{-ik_x d} e^{-i\beta} = -\mathbf{E}_{gr}^L(z, 0) e^{-i\beta} \quad (4.8)$$

where $\beta = k_x s$ is the shift induced phase difference. If we now combine all expressions we find:

$$\mathbf{E}_{total}^{SH}(z, 0) = \bar{G}(0)\mathbf{E}_p^{SH}\left(\frac{\pi}{2}\right)(1 - e^{-i\beta}) + \mathbf{E}_p^{SH}(0)e^{-ik_0 z} \quad (4.9)$$

Let us now recall that we want to maximize the emission in the forward or backward direction, corresponding to $\theta = 0$. For symmetry reasons the nanopillar emission will be zero for this particular angle, thus the total field will only depend on the interference pattern generated by the grating. We now take the square modulus to maximize the intensity:

$$|\mathbf{E}_{total}^{SH}(z, 0)|^2 = \left| \bar{G}(0)\mathbf{E}_p^{SH}\left(\frac{\pi}{2}\right)(1 - e^{-i\beta})e^{-ik_0 z} \right|^2 = 2 \left| \bar{G}(0)\mathbf{E}_p^{SH}\left(\frac{\pi}{2}\right) \right|^2 (1 - \cos\beta) \quad (4.10)$$

This equation shows that in case of $s = 0$, the symmetry of the 2ω mode is not broken and the total field radiated in $\theta = \pi/2$ is 0 as expected. The SH intensity is maximized for $\cos\beta = 1$, which allows to find a bound for the optimal s values:

$$s_{opt} = (2m + 1)\frac{\lambda_{SH}}{2}, \quad m = 0, \pm 1, \pm 2... \quad (4.11)$$

Here however we obtain for s is slightly different from the $s = 290$ nm obtained with full-vectorial calculations, as the simplified model doesn't take into account the phase velocity of the in-plane propagating waves. Nevertheless this toy-model is a good starting point and could be refined in the future to potentially achieve precise far-field radiation pattern engineering [127].

Samples were fabricated in Paris according to the guidelines of FEM simulations and sent to ANU to be characterized with a setup similar to that of Fig. 81. In particular we were interested in looking at BFP images of grating+antenna structures, collected through a 0.7 NA objective, and compare them to the case of a bare pillar. As shown in Fig. 88, the grating indeed strongly reshapes the radiation pattern of the nanoantenna, which is redirected towards almost normal k-vectors.

Moreover, we observe a polarizing effect of the grating as well, as the SH emission becomes mainly co-polarized with the pump beam due to the redirection of the nonlinear signal towards the normal direction. While our numerical calculations correctly predict a negligible cross-polarized SH emission, we observe minor differences between theory and experiment, which are probably due to the fact that, as the spot size is around $2\mu\text{m}$, the first two ridges are slightly illuminated as well, and as they are also made of $\text{Al}_{0.18}\text{Ga}_{0.82}\text{As}$, they could contribute to the total observed SHG.

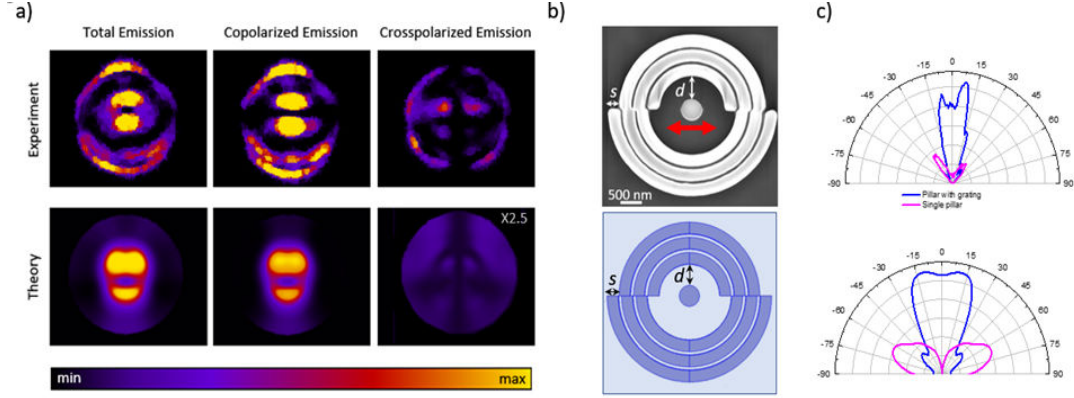


Figure 88: (a) Experimental (top) and theoretical (bottom) SH emission pattern for the pillar surrounded by the grating structure, assuming a collection $\text{NA} = 0.7$, decomposed in its contributions co-polarized and cross-polarized to the pump beam. (b) SEM image of the fabricated (top) and optimized theoretical structure (bottom). The red arrow indicates the input polarization of the pump beam. (c) Comparison of the experimental (top) and simulated (bottom) SH radiation pattern emitted in the air region in the case of a single cylinder (purple line) and of cylinder coupled to a $N = 3$ grooves grating structure (blue line).

The impact of the partial illumination of the grating was numerically studied by assuming Gaussian excitation with a beam waist of $2\mu\text{m}$ compatible with the experimental spot-size at the focal point. In particular we looked at the SH emission directed towards a $\text{NA}=0.2$ objective placed above the structures. Numerical results show that the pillar contribution to the total collected SHG is 76.5%, with only a minor contribution coming from the illuminated ridges (16%) and from the interference between them (7.5%). Fig. 88c shows the numerical and measured nonlinear emission in the z - x plane for both a bare pillar and a pillar “dressed” by the grating.

The influence of the beam collimator is evident as the zero in normal re-emission disappears. By integrating the SHG field within a 0.2-NA area it is possible to quantify the collection power enhancement due to the presence of the optimized diffraction grating, defined as the ratio between the SH power emitted in the collection cone by the structure with the grating and the one emitted by an isolated pillar in the same solid angle. The resulting collection power enhancement in the case of our collimator is about two orders of magnitude compared to the bare pillar.

4.4.1 Towards nonlinear background-free holography

The ability to shape the SHG radiation pattern by engineering the phase shift of the radiation diffracted by the two halves of the grating structure, as well as the emergence of different patterns depending on the pump polarization, is a quite interesting feature that can be interpreted as a nonlinear background-free holographic method, in which a desired image is generated at a frequency different from that of the pump.

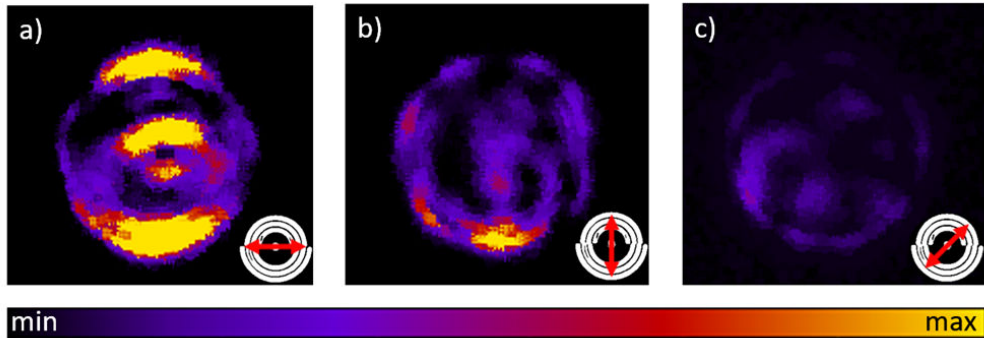


Figure 89: (a) Experimental SH radiation pattern from our grating structure for three different incident pump polarizations: (a) horizontal, (b) vertical and (c) 45, as shown by the red arrows in the corresponding insets. These results show the potential on-of switchability of a particular radiation pattern depending on the input polarization state.

We can indeed appreciate from Fig. 96 that the BFP image strictly depends on the pump polarization state, allowing almost on-off switching of a particular radiation pattern depending on the polarization angle of the linearly polarized pump. Moreover, different patterns emerge for different choices of design parameters such as the pillar-grating distance. For example, as shown in Fig. 97, we can imagine to encode the images of a flower ($d=450$ nm) or of an angel ($d=700$ nm) by simply playing with the design parameters.

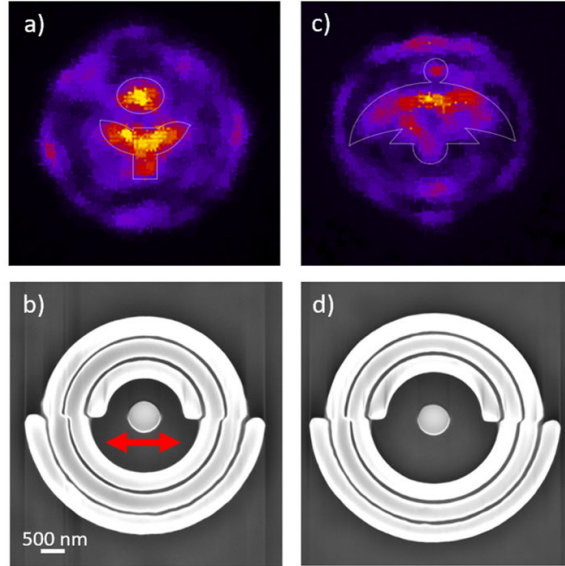


Figure 90: SHG far-fields resembling a flower (a) and a bird (d), obtained with the nanostructures (b), with $d = 450$ nm, and (d) $d = 700$ nm, respectively. The red arrow in (b) indicates the incident polarization of the pump beam.

A major obstacle remains to demonstrate nonlinear holography: full-vectorial simulations only allow to retrieve the output radiation pattern once a certain geometry is specified. The reverse problem instead, whose solution would allow to find the optimal fabrication parameters to obtain any desired pattern, is not trivial, if not impossible, to implement in COMSOL. On the other hand the simplified toy model we developed in [127] could potentially allow to solve the reverse problem, given that small corrections are performed in order to make it more realistic.

4.5 Quantum-classical correspondence: SFG and SPDC from isolated nanopillars

So far we focused our attention mainly on one second-order nonlinear process, that is SHG, however the analysis of other three-wave mixing effects is also interesting both for purely physical reasons and for applications. In particular, SPDC is nowadays the most widely used source of heralded and entangled single photon pairs for the photonic quantum information approach. In the last decade integrated AlGaAs chips at the microscale have already demonstrated the capabilities of this material to generate single photons at room

temperature with either optical [136] or electrical injection [137], exploiting its direct bandgap. More recently, a nearly deterministic single photon source at the nanoscale based on quantum dots was demonstrated [138], however, as their spatial position cannot be controlled yet, the spatial multiplexing of several coupled single photon sources, a key factor needed for photonic quantum computation [139] still seems science fiction.

These facts motivated us to study the generation of heralded photons in AlGaAs nanoantennas. Indeed, although single antennas are expected to exhibit lower SPDC brightness than other existing sources, we could imagine to multiplex an array of nonlinear nanoantennas to form a quantum metasurface for generation of photon states with complex spatial correlations. Before that, we first looked at the photon pairs generated in a single pillar. However, a single pillar tends to be a very weak source compared to already existing ones [140], therefore needing very long acquisition times of the photon-counting statistics, exhibiting as well a lack of correlation precision.

Thus, optimizing the experimental parameters directly through direct SPDC measurements seemed not the best way to approach the problem. To solve this issue, we first found the optimal SPDC conditions exploiting the quantum-classical correspondence between SPDC and its time-reversed process, namely SFG (see Fig. 17a,b) [20, 141]. This quantum-classical correspondence is based on Green-function formalism and allows to estimate the SPDC rate of any structure exhibiting quadratic nonlinearity by measuring the classical SFG conversion efficiency through the relation [142]:

$$\frac{1}{\Phi_p} \frac{dN_{pair}}{dt} = 2\pi \Xi_{SFG} \frac{\lambda_p^4}{\lambda_s^3 \lambda_i^3} \frac{c \Delta \lambda}{\lambda_s^2} \quad (4.12)$$

where λ_p , λ_s and λ_i are the pump, signal and idler wavelengths respectively, Φ_p the SPDC pump flux, Ξ_{SFG} the the ratio of sum-frequency photon power to the product of incident energy fluxes at signal and idler frequencies, $\Delta \lambda$ the nonlinear resonance bandwidth at the signal/idler wavelengths and dN_{pair}/dt the SPDC bi-photon generation rate. This relationship thus allows us to optimize the bi-photon pair generation rate before actually detecting it by maximizing the SFG efficiency, which is a classical, thus stronger and easier to detect process.

4.5.1 SFG experiments

SFG measurements were performed at ANU. The sample was fabricated in Paris Diderot with the HSQ recipe, and consists of several arrays of isolated

nanodisks with a radius of 215 nm, height of 400 nm and 10 μm separation, resting on 1 μm -thick AlOx (Fig. 91).

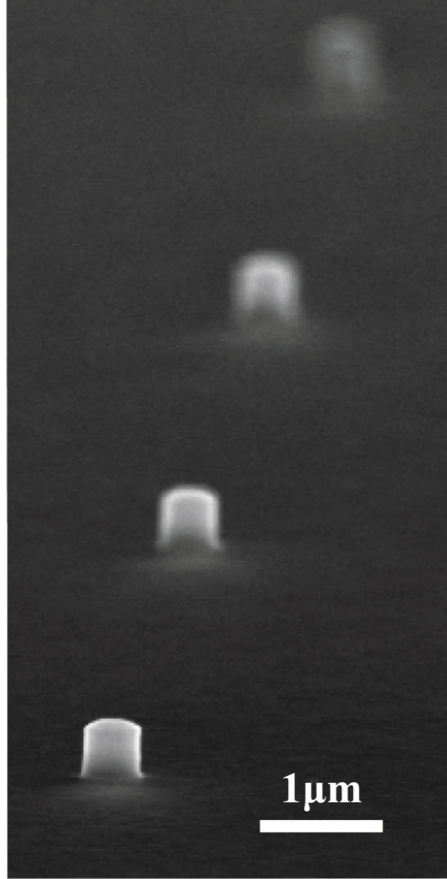


Figure 91: SEM tilted micrograph of the fabricated sample for SFG-SPDC measurements, consisting of AlGaAs nanoantennas [142].

The setup, sketched in Fig. 92, is illuminated by means of a femtosecond laser (100 fs) with central wavelength 1560 nm and FWHM of 80 nm. The beam is separated in two arms with a 50:50 Beam Splitter (BS). On one of the arms a bandpass filter centred at 1520 nm ($\Delta\lambda = 12$ nm) selects the λ_s for the SFG experiment. The λ_i is instead selected on the second arm by inserting another bandpass filter centred at 1560 nm ($\Delta\lambda = 12$ nm again). The two beams are then recombined in another BS and are focused on the sample with a 0.7-NA IR objective. The nonlinear signal coming from the sample is collected in reflection geometry through the same optical path and is filtered from the signal and idler with a dichroic BS. The polarization in each arm is controlled with half and quarter wave-plates. Finally a delay-line controls the the time delay at which the two pulses arrive on the sample.

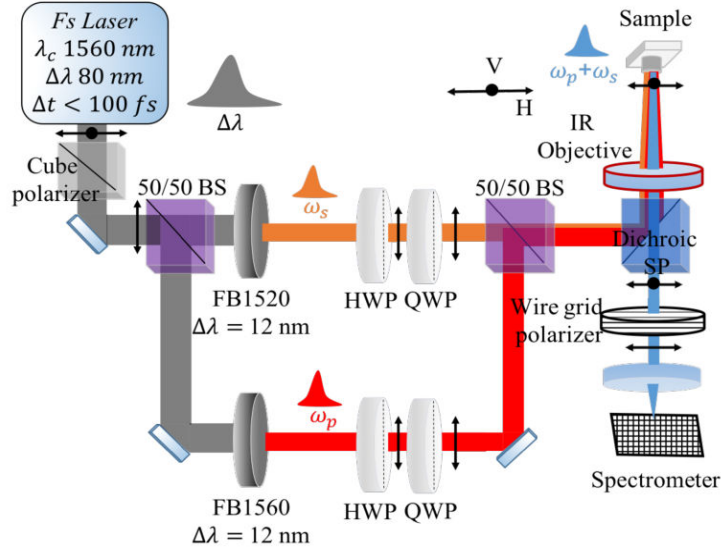


Figure 92: Nonlinear confocal setup for SFG characterization. A $\Delta\lambda = 80\text{nm}$ femtosecond ($\Delta t = 100\text{ ps}$) pump is divided in two arms with a 50:50 BS to generate the signal and idler pulses by means of two bandpass filters centred at 1520 nm and 1560 nm respectively, with a bandwidth of 12 nm. Their polarization is independently controlled with quarter and half waveplates, while a delay line controls the path-difference. The two pulses are then recombined in another balanced BS and focused. The SFG as well as the two SHG signals are collected in reflection through the same objective and separated from the signal and idler pulses by means of a dichroic BS [142].

SH signals from the two separate pulses at 760 nm and 780 nm are observed at all times, while the SFG at 770 nm is visible only for zero time delay (Fig. 93d). Different polarization combinations of the signal and idler pulses are then scanned to maximize the SFG signal with the help of the half and quarter waveplates. In particular we focus our attention on all sixteen combinations of horizontal (H), vertical (V), circular right (R) and circular left (L) polarizations (Fig. 93e). Here we find that the H-polarized SFG has a maximum when both signal and idler are V-polarized, corresponding to a $\Xi_{SFG} = 1.8 \cdot 10^{-5}$. It is important to note that due to the cylindrical symmetry of the nanopillar and the AlGaAs crystal symmetry, the detection of V-polarized SFG would give specular results. Radiation patterns are also registered with BFP measurements (Fig. 93f), showing as a general trend that almost no SFG is emitted in the backward direction.

4.5 Quantum-classical correspondence: SFG and SPDC from isolated nanopillars

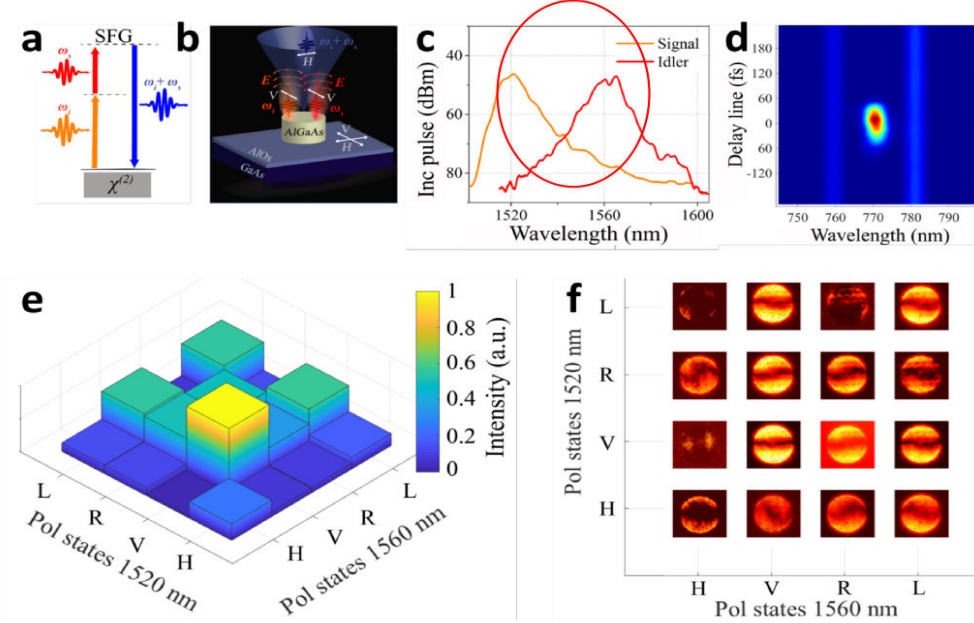


Figure 93: (a) Energy conservation diagram of the SFG process. (b) Schematics of the experimental geometry. (c) Signal (orange line) and idler (red line) spectra obtained by filtering the pump. (d) Spectrum showing the three nonlinear processes happening in the nanodisk as a function of the time delay between the signal and idler pulses. (e) Measured map of H-polarized SFG at 770 nm obtained with all 16 combinations of horizontal (H), vertical (V), right circular (R) and left circular (L) signal and idler polarization states. (f) SFG emission patterns obtained with a BFP lens for the same polarization combinations [142].

The measured peak $\Xi_{SFG} = 1.8 \cdot 10^{-5}$ for V-polarized signal and idler and H-polarized SFG allows us to calculate the expected SPDC photon-pair rate with Eq. 4.11, finding a value of 380 Hz, which is experimentally detectable, as it is above the dark count rate (5 Hz for a quantum efficiency of 10% and a temperature of 90 °C.).

4.5.2 SPDC experiment

Knowing the optimal SFG conditions, and thus being sure that the expected rate is detectable, we have performed SPDC measurements. The setup is slightly modified from that of SFG (Fig. 94). Here the IR pulsed laser is replaced with a 5 mW CW laser at 785 nm. The choice of a CW laser for this experiment is due to the fact that SPDC scales linearly with the pump power, thus the high peak powers of a femtosecond laser are not needed. Furthermore, since a CW source has a flat temporal profile and the coherence time is

much larger than the coincidence time window of the single photon detectors (162 ps), we can eliminate any possible time-correlated noise coming from the pulsed pump.

The relevant measurement to characterize the SPDC source is the second-order correlation $g^{(2)}$, which can be done in a typical Hanbury Brown-Twiss setup [143] consisting of four elements only: a balanced BS, two single photon detectors at each arm and some electronics to register the coincidences. The two detectors are fibre-coupled InGaAs/InP IR single-photon detectors, with 10% quantum efficiency (ID Quantique).

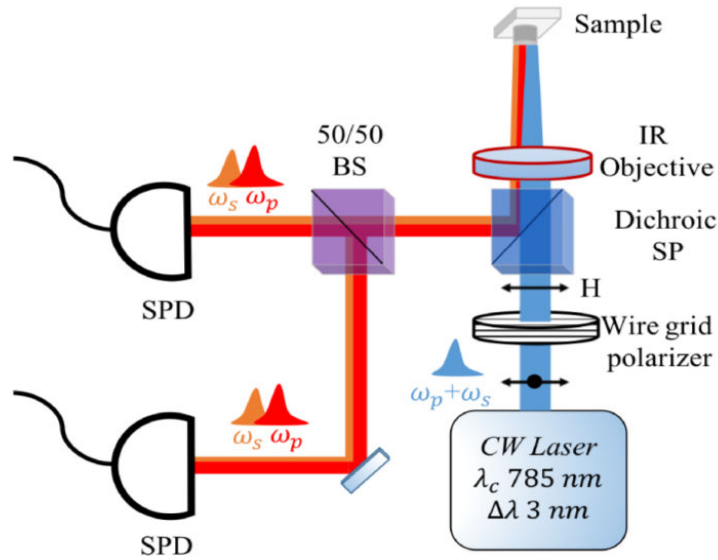


Figure 94: Experimental setup for SPDC measurement. SPDC photons are filtered from the pump with a short-pass dichroic BS, separated in two arms via a balanced BS and sent to single photon detectors to register the coincidences [142].

In this case the second-order correlation is given by $g^{(2)} = R_c/R_1R_2\tau_c$, where R_c is the coincidence rate, while the denominator indicates the accidental coincidence rate, which consist of the count rates R_1 and R_2 on each detector multiplied by the coincidence time window of the electronics. Being defined this way, a maximum $g^{(2)}$ is expected at the time delay of the simultaneous arrival of the two photons. The generated SPDC pairs are expected to have a large bandwidth of about 150 nm, as they couple to the broad MD resonance at 1550nm (see Fig. 66b). As a consequence, the expected temporal width ($\Delta\lambda/c$) of the heralded photons is sub 100 fs. The $g^{(2)}$ measurement was performed by detecting the photons at different time delays of the detectors,

accumulating statistics over a period of 24 hours (Fig. 95). Between 25 ns and 28 ns time difference we see an increase in the coincidence counting following a Gaussian fit, which we attribute to thermal excitation of the semiconductor materials [144]. The single-bin peak around 26.5 ns delay is instead attributed to SPDC, and is consistent with the expected photon temporal width. Measurements were repeated several times to make sure this was not a random fluctuation. This central bin coincidence count corresponds to a bi-photon rate of 34 Hz.

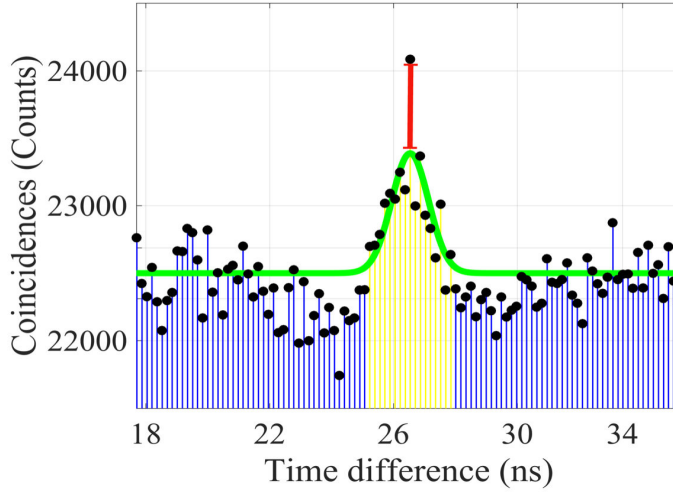


Figure 95: SPDC coincidence counts integrated over 24 hours on two single-photon InGaAs detectors after a beam splitter. Black dots are the measured coincidences at each time-bin [142].

Here it has to be pointed out that the obtained plot does not strictly represent a $g^{(2)}$ measurement, as it should be normalized with the accidental count rate of each channel. Nonetheless, the setup is a real Hanbury Brown-Twiss one, and the relevant physics is still present. The SPDC rate we obtained is modest itself, but if we define a figure of merit (FOM) for SPDC efficiency that takes into account the generation volume:

$$FOM = \frac{dN}{dt} \cdot (V_0 I_p Q_p)^{-1} \quad (4.13)$$

where $V_0 \sim 0.4 \mu\text{m}^3$ is the mode volume of the SPDC source, $I_p \sim 1.2 \text{mW}/\mu\text{m}^2$ the incident pump intensity and $Q_p \sim 52$ is the quality factor at the pump wavelength, we obtain a value four orders of magnitude higher than the typical value achieved in bulk BBO crystals ($V_0 \sim 10 \text{mm}^3$, $I_p \sim 50 \text{mW}/\text{mm}^2$,

$Q_p \sim 1$) [139], and about two orders of magnitude higher than the state-of-the-art value in integrated chips ($V_0 \sim 200 \mu\text{m}^3$, $I_p \sim 1.5 \text{ mW}/\mu\text{m}^2$, $Q_p \sim 10^5$) [145]. Moreover, the emitted photons are mode-entangled at the nanoscale. Indeed, for a H-polarized pump, based on scattering calculations and multipolar decomposition, we can calculate the field inside the nanoantenna at the FF as a superposition of ED and MD moments aligned along x,y, or z axes:

$$\begin{aligned}
 \mathbf{E}_{internal}^{(\omega)} \simeq & \left[\frac{a_{1,1} - a_{1,-1}}{k(\omega)} \mathbf{E}(p_x) + \frac{a_{1,1} + a_{1,-1}}{k(\omega)} \mathbf{E}(p_y) - \frac{\sqrt{2}a_{1,0}}{k(\omega)} \mathbf{E}(p_z) + \right. \\
 & \left. + (b_{1,1} - b_{1,-1}) \mathbf{E}(m_x) + (b_{1,1} + b_{1,-1}) \mathbf{E}(m_y) + \sqrt{2}b_{1,0} \mathbf{E}(m_z) \right] \quad (4.14)
 \end{aligned}$$

where p_i and m_i are the electric and magnetic dipole moments respectively, $a_{1,\pm 1}$ and $b_{1,\pm 1}$ the electric and magnetic multipolar coefficients. By decomposing the signal and idler photons exciting a superposition of ED and MD states, we then estimate the mode entanglement between the generated signal and idler photons by exploiting the quantum-classical correspondence again. The SFG output in the normal direction is calculated when exciting the idler and signal fields with the above superposition of ED (p_x, p_y, p_z) and MD (m_x, m_y, m_z) modes inside the nanopillar (Fig. 120). This calculation makes sense because, due to the SFG-SPDC correspondence, the SFG process has the same symmetry-group properties [146].

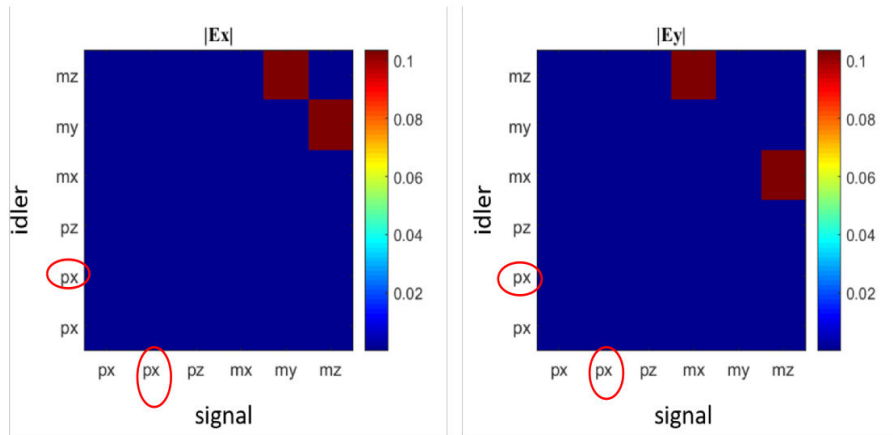


Figure 96: Mode entanglement in the AlGaAs nanodisk for H (left) and V (right) polarized pumps [142].

The result is that when we impinge with a H-polarized pump, the SPDC photons are dominantly coupled into m_x and m_z modes, while for V-polarized

pump the preferentially excited modes are m_y and m_z . This mode entanglement is then transferred into the far-field via antenna radiation, as the observed photon-pair coincidence plot suggests. This nanoscale SPDC source can obviously be improved by enhancing the emission directionality and conversion efficiency by careful engineering the nanostructures. Combining this with a better control over the nonidealities of each nanoantenna due to fabrication tolerances could potentially lead to efficient spatial multiplexing of entangled-pair sources for on-chip photonic quantum computation.

4.6 Conclusion

In this chapter I described the nonlinear experiments carried out within the NANOPHI consortium on single AlGaAs nanoantennas. Efficient SHG when exciting the MD resonance at 1550 nm was first demonstrated, obtaining a conversion efficiency of 10^{-5} with a pump intensity of 1.6 GW/cm^2 . The polarization behaviour of such emission as a function of the pillar radius was then analysed, highlighting different cases of SH radiation mostly co- or cross-polarized with the pump depending on the mode excited at 2ω frequency.

The impact on the SH polarization of oxidation-induced nonidealities was studied as well, and we were able to rule out the hypothesis of non-negligible $\chi^{(2)}$ tensor deformation. Subsequently, SH emission reshaping either through pump reconfiguration or the employment of integrated beam collimators was demonstrated, revealing as well the potential of these structures for background-free goniometry and holography respectively. Finally, I presented results on other second-order effects, namely SFG and SPDC, which point towards the realization of multiplexed nanoscale photon-pair sources.

Chapter 5

Nonlinear response of advanced AlGaAs nanostructures

This final chapter is dedicated to nonlinear experiments carried out on different nanostructures designed to enhance the conversion efficiency or develop new functionalities, that is dimers, hybrid metal-dielectric antennas, and metasurfaces. I will then conclude the chapter with a study of the linear multipoles supported in cylinders and dimers carried out with cathodoluminescence spectroscopy, allowing to access a wider range of resonances which are normally plane-wave forbidden.

5.1 Anapole-driven SHG enhancement: from single pillars to dimers

Nonlinear experiments carried out on single nanoantennas are extremely precious to understand the physics of these objects. Another important aspect to be studied is the engineering of more complex structures compared to the single pillar, in order to enhance SHG conversion efficiency. To this end we started by considering two pillars in a dimer configuration. To further enhance the nonlinear signal, we excited an anapole mode at the FF, as it was shown that it can highly boost THG in germanium nanopillars [52] and in hybrid silicon-gold nanostructures [128], as well as the intrinsic Raman scattering in silicon nanoparticles [56]. A particular effort on the anapole modelling was put by Davide Rocco in Brescia University.

5.1.1 Looking for the anapole in the linear scattering properties of a single pillar

In order to design an AlGaAs structure susceptible to support the anapole state, we started our analysis on a single nanocylinder.

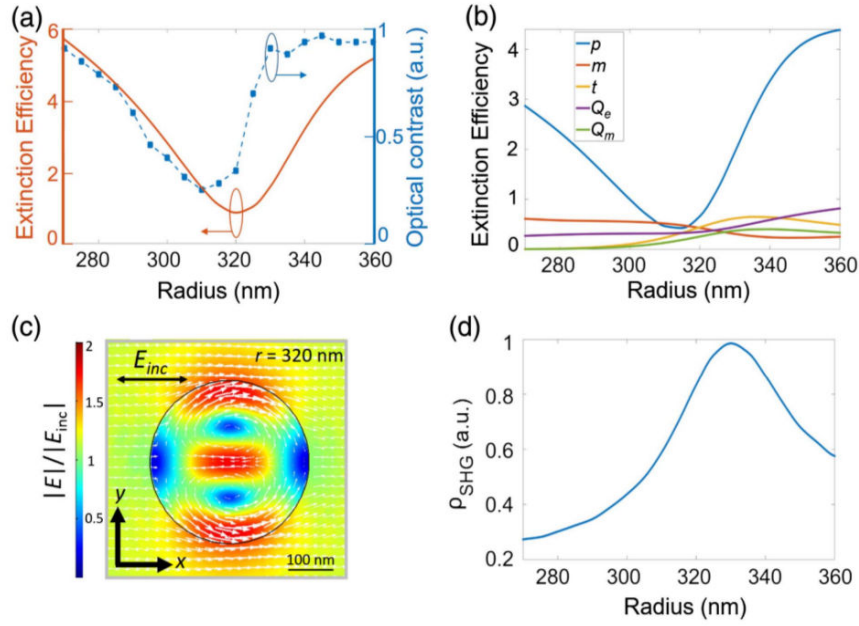


Figure 97: (a) Calculated extinction efficiency of an isolated cylinder as a function of the radius (orange line), compared with the experimental optical contrast (blue dots). (b) Extinction efficiency decomposed in ED (p), MD (m), TD (t), EQ (Q_e), and MQ (Q_m) contributions. (c) Electric field profile in the xy plane for a cylinder with $r=320$ nm. (d) Volume integral of the normalized nonlinear current density inside the cylinder as a function of the radius [55].

As the anapole is expected at larger radii than the ED and MD resonances, we calculated the extinction efficiency in the radius range between 270 nm and 360 nm, the height of the nanocylinder being set at 400 nm, and the illumination being a focused Gaussian beam centred at $\lambda = 1550$ nm. The calculated curve is then compared with the experimental optical contrast (Fig. 97a), defined as the relative reflected intensity normalized to the reference from the substrate: $(I_{cyl} - I_{ref})/I_{ref}$. We can notice a minimum in the extinction for $r = 320$ nm. To investigate what happens for this radius value, we perform a Cartesian multipolar decomposition (Fig. 97b), showing indeed that for $r = 320$ nm the dip in the extinction is mainly due to the drop in the ED moment p , which destructively interferes with the TD

moment t , as explained in Section 2.1.2. However here the exact anapole condition is perturbed by the non-zero contribution of the MD moment m , and the quadrupoles Q_e, Q_m , explaining the non-zero extinction. Nonetheless, if we look at the electric field profile in the xy plane for this specific radius (Fig. 97c), we can appreciate its similarity with the typical anapole [53]. Thus, in order to understand if this condition can still be useful to boost SHG conversion despite its nonideality, we calculated the volume integral of the nonlinear current density inside the AlGaAs cylinder as a function of the radius:

$$\rho_{SHG} = \left| 2\omega\epsilon_0 \sum_{i,j,k} \int \chi_{ijk}^{(2)} E_j(\omega) E_k(\omega) dV \right| \quad (5.1)$$

The resulting curve (Fig. 97d) shows a peak for $r = 330$ nm, shifted by 10 nm from the anapole, possibly due to the other multipole contributions.

5.1.2 Looking for the anapole in the linear scattering properties of a dimer

We next focused our attention on a dimer structure consisting of two identical pillars separated by a 30 nm gap (Fig. 98). We performed a linear analysis on this system to find anapole-like modes. Moreover, as the symmetry of the system has changed, we expect a different extinction behaviour depending whether the pump polarization is oriented parallel (X polarization) or perpendicular (Y polarization) to the dimer symmetry axis.

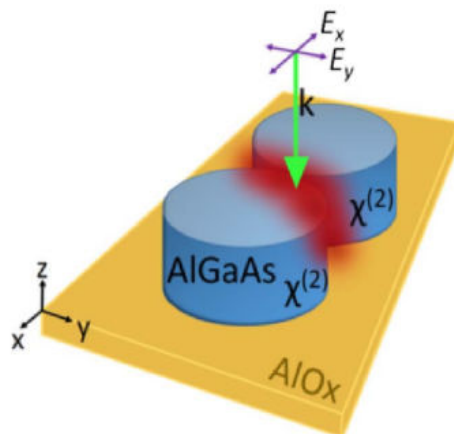


Figure 98: Geometry of the dimer structure: a plane-wave excitation at 1550nm impinges on the sample with a polarization either parallel (X) or perpendicular (Y) to the dimer axis. [55].

Multipolar decomposition in Cartesian coordinates reveals that for X polarization (Fig. 99a) the situation is similar to the case of the isolated pillar, with an anapole-like mode at $r = 330\text{nm}$ revealed by similar amplitudes of TD (t) ED (p). The non-ideal nature of this anapole-like mode is also revealed by the phase difference between TD and ED (Fig. 99c, blue curve), which is close to but not exactly $-\pi$ for $r = 330\text{nm}$.

In contrast, for Y-polarized excitation, ED and TD have the same amplitude for $r = 330\text{nm}$ (Fig. 99b), and in addition their phase difference (Fig. 99c, red curve) goes to $-\pi$, as required for exact anapole. Although the two main conditions are fulfilled for anapole excitation in this case, a certain degree of nonideality is still present due to non-zero contribution of higher-order multipoles.

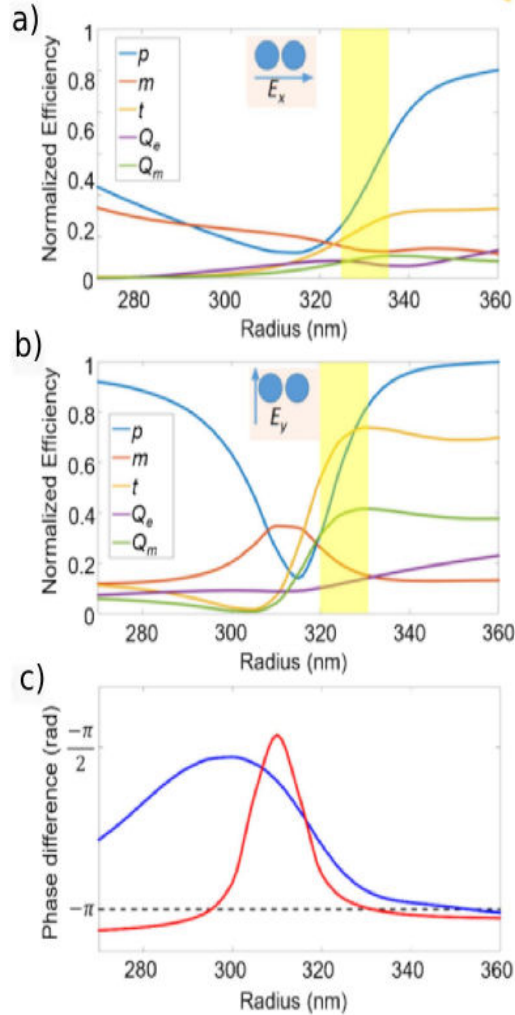


Figure 99: Calculated extinction efficiencies for a dimer, decomposed in its Cartesian multipolar contributions, in the case of X- (a) or Y- (b)

5.1 Anapole-driven SHG enhancement: from single pillars to dimers

polarised excitation. (c) Phase difference between ED (p) and TD (t) in the case of X-polarized (blue curve) or Y-polarized (red curve) light. A black dashed line corresponding to $-\pi$ is plotted as a reference [55].

By taking a closer look to the calculated electric and magnetic field profiles at the FF, we can appreciate another interesting property of the dimer structure, that is field enhancement in the gap. In particular we find that for X-polarized pump the electric field is the most enhanced in the gap ($E/E_0 \sim 8$), with a peak at $r = 335$ nm (Fig. 100a). In contrast, for Y-polarized illumination, the higher enhancement is exhibited by the magnetic field ($H/H_0 \sim 5$), with a peak at $r = 320$ nm, while the peak electric field enhancement is about 3 times weaker with respect to the X-polarized light case ($E/E_0 \sim 2.5$) (Fig. 100e). This preference for the electric field in the X-polarization case and for the magnetic field in the Y-polarization case can be understood by looking at how the various multipolar currents present in the bulk of the nanocylinders couple with each other.

For X-polarization, the induced ED and TD inside the cylinders are aligned with the dimer symmetry axis, thus strong coupling with each other and leading to the electric field hotspot in the gap (Fig. 100c, top). Conversely for Y-polarization, the TD moment is associated with a circulating magnetic field accompanied by a characteristic electric poloidal current distribution, which can be thought of as an ordinary solenoid with an even number of windings bent into a torus [54]. In this configuration, the induced TD in the two pillars are perpendicularly aligned to the symmetry axis of the dimer (Fig. 100c, bottom), causing a strong coupling between the two circulating magnetic fields inside the cylinders which is in turn responsible for the magnetic hotspot in the gap.

The generation of electromagnetic field hotspots in the dimer gap is a quite interesting feature that has been explored by several groups in the last years, showing its potential to enhance spontaneous emission [129, 130] and Raman scattering [131]. In our case of interest, we could for example take advantage of field enhancement in the gap, anapole mode at the fundamental and resonant SH emission from the bulk of the dimer to realize some background-free nonlinear sensing. In such a situation, changes in the gap region will be reflected in strong perturbations of the SH signal, while being transparent at the FF, due to the anapole state.

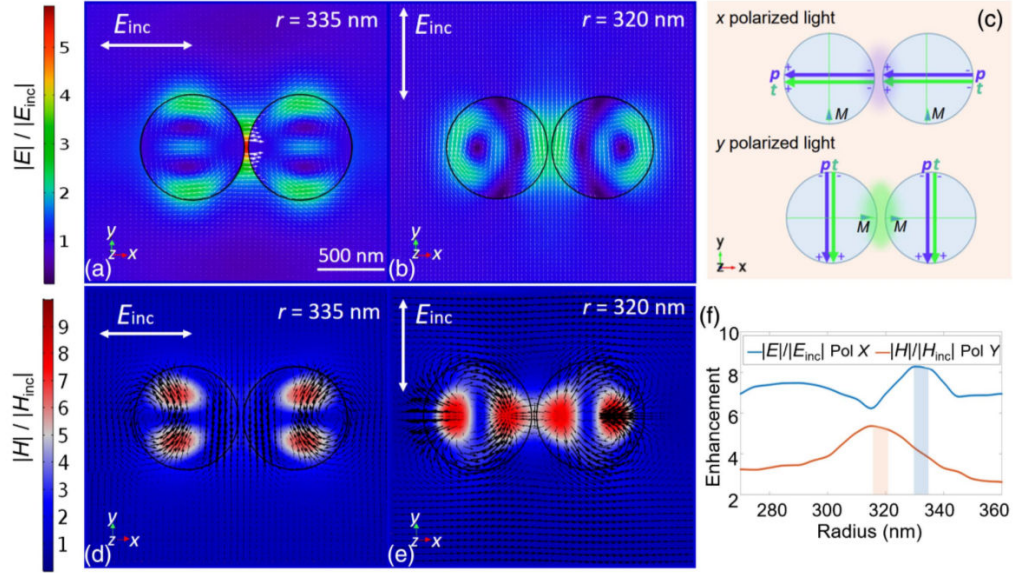


Figure 100: Electric (a,b) and magnetic (d,e) field distributions at $1.55 \mu\text{m}$ in the xy plane in the dimer structure for the two incident polarizations (white arrows): for a dimer with (a,d) a radius of 335 nm and (b,e) with a radius of 320 nm. (c) Schematic description of the coupling mechanism in the dimer responsible for the higher electric field enhancement for X-polarized light, and for the higher magnetic field enhancement for Y-polarized light. (f) Electric and magnetic field enhancement as a function of the dimer radius for X- (blue curve) and Y- (orange curve) incident polarizations. [55].

5.1.3 Nonlinear modeling and experiments

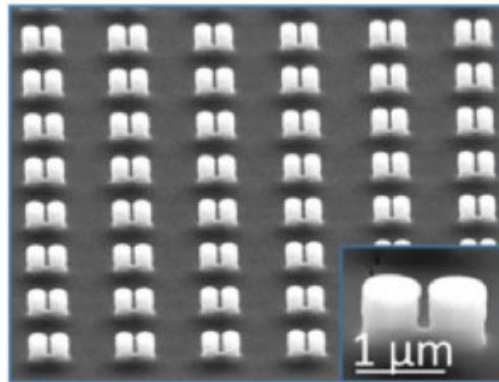


Figure 101: SEM micrograph of an array of AlGaAs-on-AlOx dimers with 30 nm gap [55].

5.1 Anapole-driven SHG enhancement: from single pillars to dimers

Following the guidelines provided by the above presented linear numerical calculations, a sample consisting of pillars and dimers with radii from 270 nm to 360 nm was fabricated using HSQ as negative e-beam resist (see Section 3.4.4), with gaps as small as 30 nm (Fig. 101). The sample was characterized at the Politecnico di Milano on the same setup used for SHG measurements from isolated nanoantennas (Fig. 67). Nonlinear measurements were performed in both cases of pump polarization, parallel and perpendicular to the dimer symmetry axis, to fully explore the response of this system (Fig. 102b). For X polarization, nonlinear simulations predict a peak at $r=335$ nm, while for Y-polarized light, the maximum is obtained for $r=320$ nm (Fig. 102a). Two things are worth noting at this point: SHG efficiency, for both incident polarizations, is about 5 times higher than that of a single cylinder of the same radius. Secondly, SHG peaks from the dimer structure in both polarization cases correspond to the maximum local electric (X polarization) and magnetic (Y polarization) field enhancement in the gap. Thus, this factor 5 increase can be explained by the coupling between the EDs in each cylinder forming the dimer for the X-polarized light, and between the TDs for the Y-polarized light. Experiments exhibit a good agreement with calculations, the only difference being a peak broadening, which can be ascribed to fabrication tolerances.

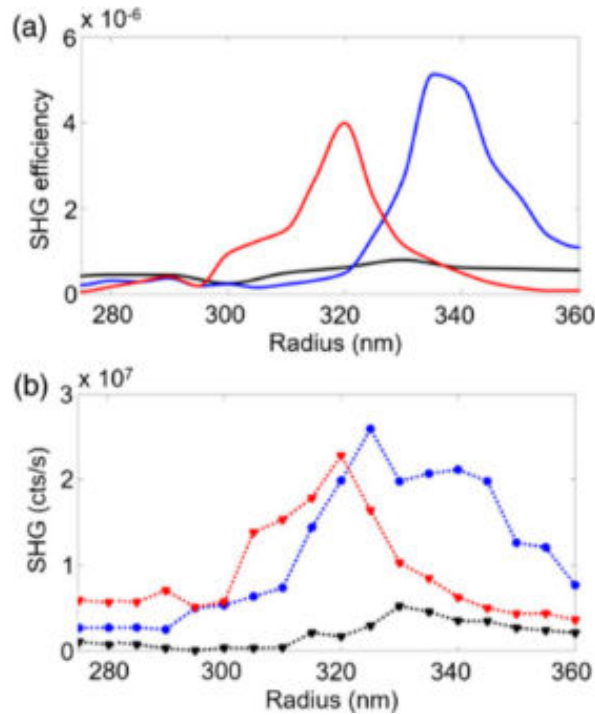


Figure 102: (a) Simulated SH conversion efficiency for a dimer excited

either by a X-polarized (blue line) or a Y-polarized pump (red line) compared with the reference of an isolated pillar (black line). (b) Measured SHG vs radius [55].

Unfortunately, despite the richness of phenomena in this dimer system, SHG efficiency does not exceed 10^{-6} at about 1.6 GW/cm^2 , i.e. one order of magnitude less than the one obtained by pumping at the MD resonance of an isolated pillar. Let us stress that this does not mean that dimers are useless, as the field hot-spots in the gap open up to sensing applications. Moreover, the presence of two different SHG maxima suggests the existence of an additional degree of freedom that could be exploited to modulate the SHG by tuning the pump polarization.

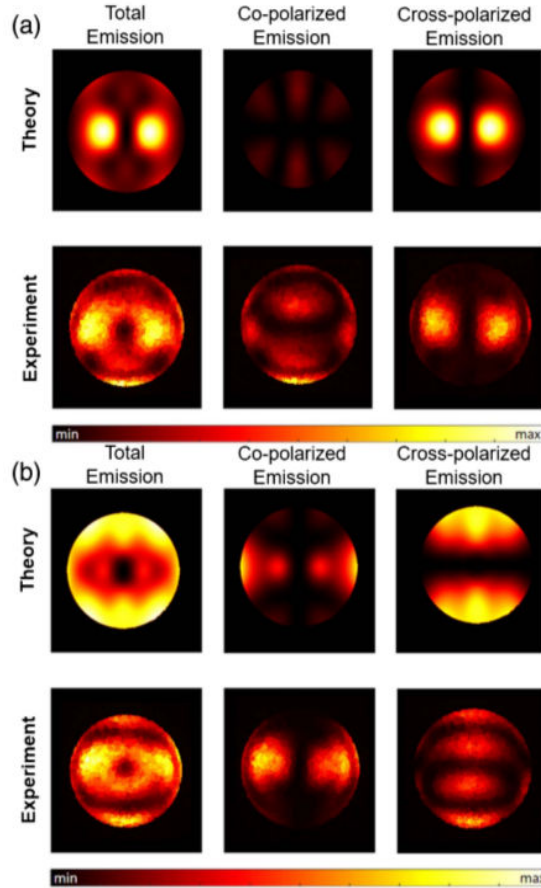


Figure 108: Calculated (top) and observed (bottom) SHG patterns decomposed in co-polarized and cross-polarized contributions with respect to the pump beam, in the case of: (a) a dimer with $r=335 \text{ nm}$, excited with a X-polarized pump; (b) dimer with $r=320 \text{ nm}$ and Y-polarized pump [55].

This peculiar feature becomes more evident if one analyses the radiation patterns of a dimer, obtained via BFP measurements performed at ANU with the same setup of the tilted pump experiments (Fig. 81). We looked in particular at the SHG components co- and cross-polarized with the pump coming from dimers with $r=320$ nm for X-polarized pump (Fig. 108a), and $r=335$ nm for Y-polarized pump (Fig. 108b). Apart from small deviations from the calculated radiation patterns, BFP measurements confirm the polarization switching of the nonlinear signal and show that in both cases SHG is mostly cross-polarized with respect to the pump, as already reported in the case of large single structures [113]. This feature can disclose new design approaches in building anisotropic nonlinear metasurfaces based on high-permittivity semiconductors.

5.2 SHG enhancement in hybrid AlGaAs-Au nanostructures

Another viable strategy to improve SHG efficiency is to exploit the coupling between plasmonic and Mie-type resonances. Indeed in the last years it was shown that such photonic-plasmonic mode hybridization allows to manipulate the in- and out-coupling of light to and from dielectric nanoantennas, and as such demonstrate a variety of effects due to its flexibility, including anomalous reflection and absorption [132], linear scattering redirection [133], enhanced SHG in hybrid perovskite-Au nanodimers [134], and enhanced THG in Si-Au nanostructures [128].

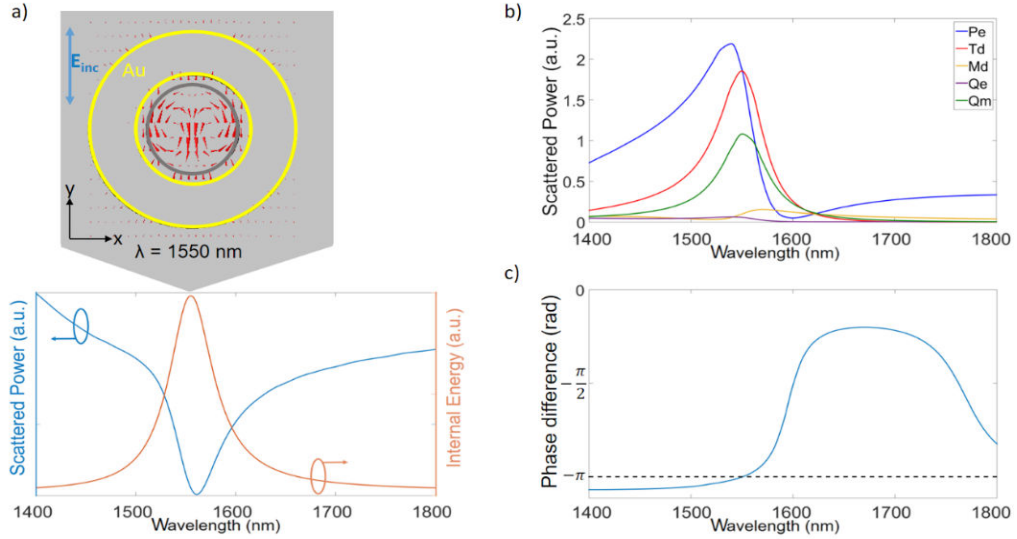


Figure 109: a) Scattered power (blue curve) and internal energy (orange curve) as a function of pump wavelength. The upper panel shows the electric field profile at 1550 nm, with the typical anapole shape. b) Cartesian multipolar decomposition of the scattered power. P_e refers to the ED, M_d to the MD, T_d to the TD, Q_e to the EQ and Q_m to the EM. P_e and T_e have the same amplitude at 1550nm wavelength. c) Phase difference between Cartesian ED and MD. A π phase opposition is reached for $\lambda_p = 1550$ nm [135].

In particular, Maier and co-workers (ref. [128]) merged the advantages of the anapole mode excitation at the fundamental and of the hybrid metal-dielectric integration to develop a nanoantenna composed of a silicon disk core surrounded by an annular plasmonic antenna, reporting a THG efficiency enhancement up to 3 orders of magnitude with respect to the bare disk [128]. We thus adopted the same approach to investigate SHG properties AlGaAs nanoantennas.

FEM simulations on COMSOL were first run to find the optimal excitation conditions for an anapole at the FF ($\lambda=1550$ nm). Two distinct geometries were identified: 1) with a central pillar radius of 410 nm and a gap of 100 nm from the Au nanoring; and 2) with a central pillar radius of 380 nm and a 200 nm gap. In both cases the nanopillar height is 200 nm, while the gold ring has a width of 410 nm and a height of 80 nm. The anapole state, as already stated, is revealed by the Cartesian ED and TD having the same amplitude and opposite phases. The fulfilment of such conditions is shown for example for the first structure (Fig. 109). Although we were not able to excite the exact anapole due to non-negligible contributions from the

quadrupoles (Fig. 109b), we still can appreciate the desired peak in stored internal energy at 1550 nm (Fig. 109a).

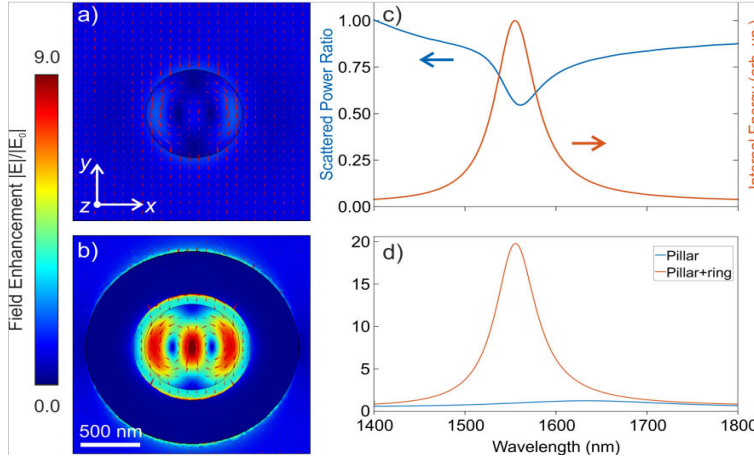


Figure 110: a) Electric field enhancement in the xy plane at 1550nm for an isolated $r=410$ nm nanocylinder and b) for its respective type-1 hybrid structure. c) Total scattered power (blue curve) and internal energy stored (orange curve) by the anapole in the bare pillar. d) Normalized electric field intensity averaged within the cylinder, as a function of pump wavelength for both isolated AlGaAs cylinder (blue curve) and hybrid nanoantenna (orange curve) [135].

The advantage of the gold nanoring integration is evident when we take a closer look at the field confinement (E/E_0). Even though we can have an anapole-like excitation in the naked pillar as well, the presence of the golden ring boosts the field enhancement up to a factor 6. Another way to quantify the advantage of the hybrid structure with respect to the bare pillar was proposed in [128] and involves the calculation of a figure of merit defined as the field intensity enhancement averaged over the whole cylinder volume. In type-1 hybrid structure, such figure of merit increases by a factor 20 with respect to the naked pillar (Fig. 110d).

Structures of type-1 and type-2 were fabricated along with bare pillars and rings following these design guidelines according to the recipe for hybrid metal-dielectric integration described Section 3.4.5. They were then sent to Politecnico di Milano and characterized with the same setup described in Section 4.1.2, enriched with an extra BL for BFP measurements (Fig. 111).

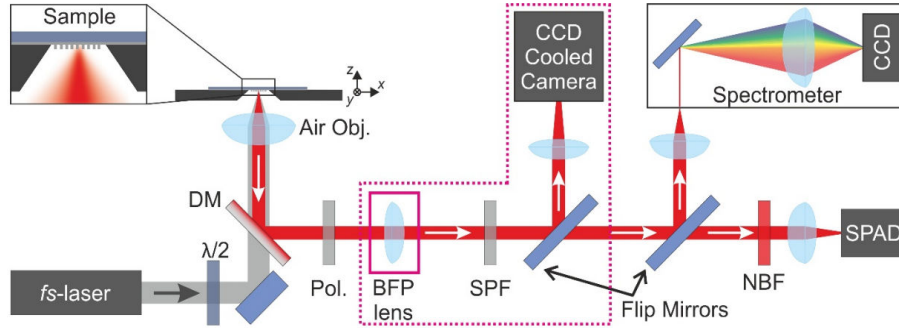


Figure 111: Nonlinear confocal microscope employed in Politecnico di Milano. The setup is essentially the same as in [37], with the addition of a BFP lens.

The nonlinear characterization of such sample was performed by registering SHG confocal maps (Fig. 112a) on arrays containing each type of element (bare ring, bare pillars and the two types of hybrid structures). Averaging the SHG within each array of nominally identical structures resulted in the histogram shown in Fig. 112b. Experimental results revealed that type-1 hybrid structure exhibits a factor-30 SHG enhancement with respect to the reference naked cylinder with $r=410\text{nm}$, while for type-2 configuration the enhancement is about one order of magnitude.

5.2 SHG enhancement in hybrid AlGaAs-Au nanostructures

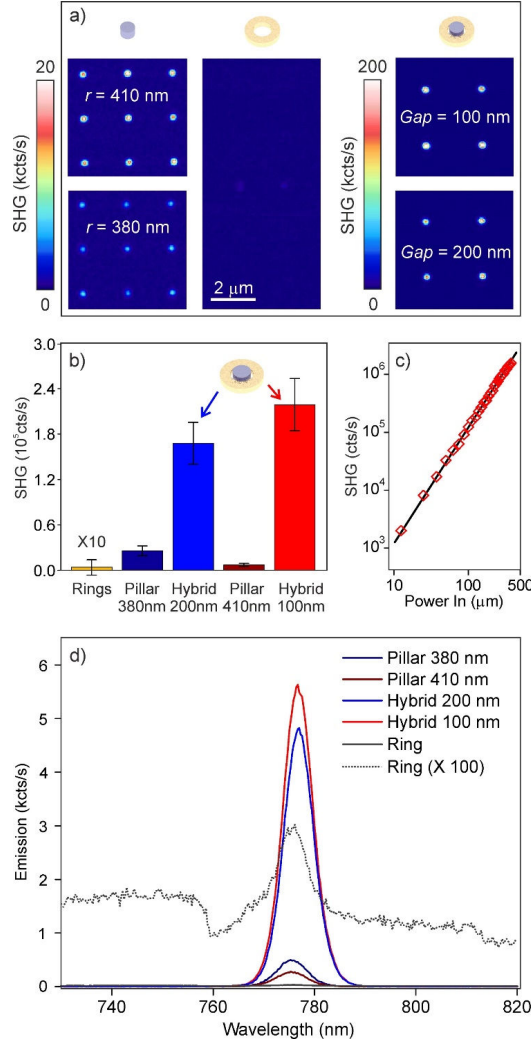


Figure 112: (a) Nonlinear confocal maps collected from the hybrid antennas and from the reference structures. From left to right: isolated pillars with $r=410$ nm (top), and $r=380$ nm (bottom); rings; and hybrid structures of type-1 (top) and type-2 (bottom). (b) Emission statistics averaged within an array for each element. (c) Log-log plot of the SHG power from type-2 hybrid structures. (d) Emission spectra from each different element of the sample, for the same pump intensity [135].

As the Au nanoring contribution to the overall SHG signal is several orders of magnitude lower, we can claim that the nonlinear signal enhancement is only the result of the better field confinement inside the dielectric material brought about by the hybrid configuration. A log-log plot of the SHG power dependence acquired from a type two nanostructure demonstrates the expected quadratic behaviour of this nonlinear process (Fig. 112c). To better

infer how the excitation of the anapole influences the SH emission with respect to the naked pillar case, we analysed both the polarization properties and the radiation pattern of the nonlinear signal. Polar plots acquired with a series of confocal maps as in [113] reveal indeed that the gold nanoring helps reshaping the SH emission, moving from a quadrupolar-like behaviour in case of the naked pillar to a more homogeneous dipolar-like for the hybrid structure (Fig. 113a,b).

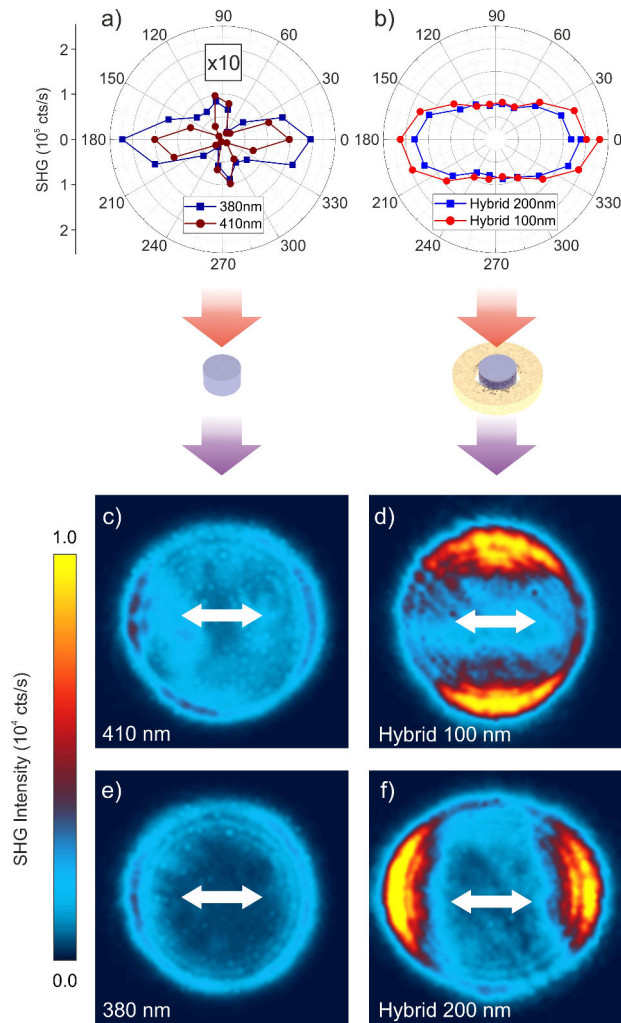


Figure 113: SHG polar plots for (a) the reference pillars and (b) the hybrid antennas. Experimental BFP images of the type-1 (c) and type-2 (e) nanopillars versus the respective hybrid antennas (d and f). White arrows indicate the pump polarization direction [135].

We can also appreciate the one-order-of-magnitude intensity difference in the two sets of polar plots, in agreement with the SHG enhancement factors

shown in the figure. Though this radiation reshaping happens at the SH and not at the fundamental as in [132], this suggests the existence of an underlying mechanism due to the plasmonic-Mie mode hybridization which is yet to be understood. As we have already mentioned a few sections above, when the SH emission is reshaped from quadrupolar-like to dipolar-like the collection efficiency is improved as well. This feature was indeed confirmed with BFP measurements, and a SH collection efficiency boost for the hybrid structures (Fig. 113d,f) compared to the naked pillars (Fig. 113c,e) was demonstrated. However, in contrast with grating+pillar structures and tilted pump configuration, here SHG still mostly occurs at large angles and not in the normal direction.

A substantial THG enhancement was observed as well with respect to the case of bare pillar excited at the MD resonance. As shown in Fig. 114, the improved field confinement provided by the Au ring allows achieving more than one order of magnitude enhancement in the THG, for type-2 structure. Thus for hybrid structures THG emission yields become comparable with SHG, when an average incident excitation power of about 1 mW is employed. In these conditions, THG is so strong that it can be easily seen by the naked eye as a bright green spot on the sample (Fig. 114, inset).

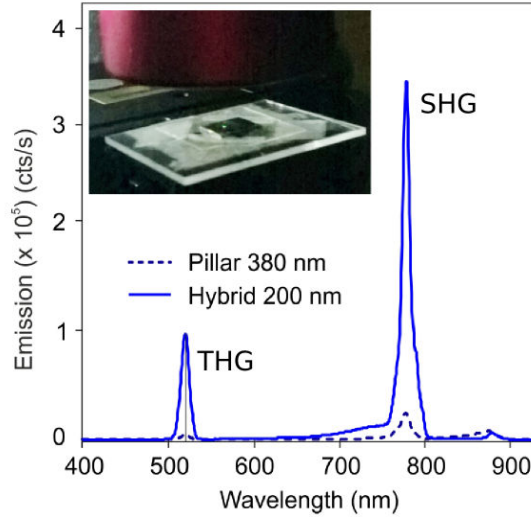


Figure 114: Emission spectrum of a type-2 hybrid structure and its relative reference pillar. THG is enhanced by more than one order of magnitude, and a bright green spot can be seen even at naked eye (inset) [135].

Overall, the maximum enhancement obtained in our hybrid structures leads to SHG efficiencies just as high as those of AlGaAs nanopillars excited at the MD resonance. Despite the efficiency improvement with respect to the

anapole in dimers, it still seems that the MD mode can overlap better than the anapole with the modes at 2ω . However this contrasts with numerical calculations, which predict a SHG normalized efficiency $\gamma_{SHG} = 9 \cdot 10^{-5} \text{ W}^{-1}$, for a pump fluency of 1.6 GW/cm^2 , corresponding to an enhancement factor of 600 with respect to the bare cylinder pumped at the MD. This two-order of magnitude discrepancy can be ascribed to the combination of two factors: fabrication tolerances and the extreme sensitivity of the anapole condition to the actual design parameters. In order to verify this point it will be interesting to re-do all the experiments with a tunable pump. If the above considerations are correct one should be able to observe the theoretically predicted SHG enhancement in the wavelength illumination range 1500 nm-1600 nm.

5.3 SFG from a transparent AlGaAs metasurface

This section is dedicated to the results that I obtained during a six-month visiting period in the group of Dragomir Neshev at the Australian National University, during my third year of PhD. My task was to demonstrate SFG-based nonlinear imaging from an AlGaAs metasurface, i.e. an array of coupled nanoantennas driven by a broadband OPO source and a pump-probe experimental configuration.

The sample was fabricated by Mohsen Rahmani according to the recipe developed in [38] and described in section 3.2.2 (see Fig. 29). It consists of a transparent glass chip containing the AlGaAs metasurfaces, with pillars of 300 nm height, 440 nm diameter and 850 nm edge-to-edge distance, to ensure optical coupling. The fabricated arrays have an area of $80 \mu\text{m}$. When I arrived in the Australian National University the optical setup for SFG measurements in pump-probe configuration was not yet ready, so it is worth spending a section to describe how it was mounted.

5.3.1 Setup

As the fabricated sample has a transparent substrate, the setup was designed to work in transmission geometry. This means that instead of having a single objective focusing the laser beam on the sample and collecting the nonlinear signal, we have a lens and an objective forming a conjugate pair. The sample is placed so as to have the metasurfaces at the focal point of both lens and objective. The setup is shown in Fig. 115.

The pump pulse is delivered by a tunable Ti:Sa tunable cavity (Coherent, Chameleon Vision) in the wavelength range 680 nm-1040 nm. About 80% of this first stage pumps an OPO cavity (Coherent, Chameleon compact OPO) which produces pulses in the range 1000nm-1600nm, with a dual output that allows to access to the remaining 20% power of the Ti:Sa, which simply passes through the OPO cavity. At the output of the OPO the two pulses have a path difference of about 1.6 m, which is basically the distance covered by the OPO signal inside the second cavity. For our purposes we choose to operate with a pump wavelength of 840 nm and a signal of 1550 nm. With this choice the expected SFG wavelength is around 545 nm. The path difference was recovered by making the pump (red line) travel 1.6 m more on the optical table than the signal (grey line). A Delay Line (DL) inserted in the pump path allows to finely tune the path difference. The two beams are then rejoined by means of a long-pass DM. A lens focuses both on the sample mounted on a 3D-stage and the light transmitted by the sample is collected with a 0.2-NA objective. The detection is performed either with a Si spectrometer for the visible range, or with a CCD camera and short-pass filters cut at 800 nm inserted in each detection arm allow to filter both pump and signal.

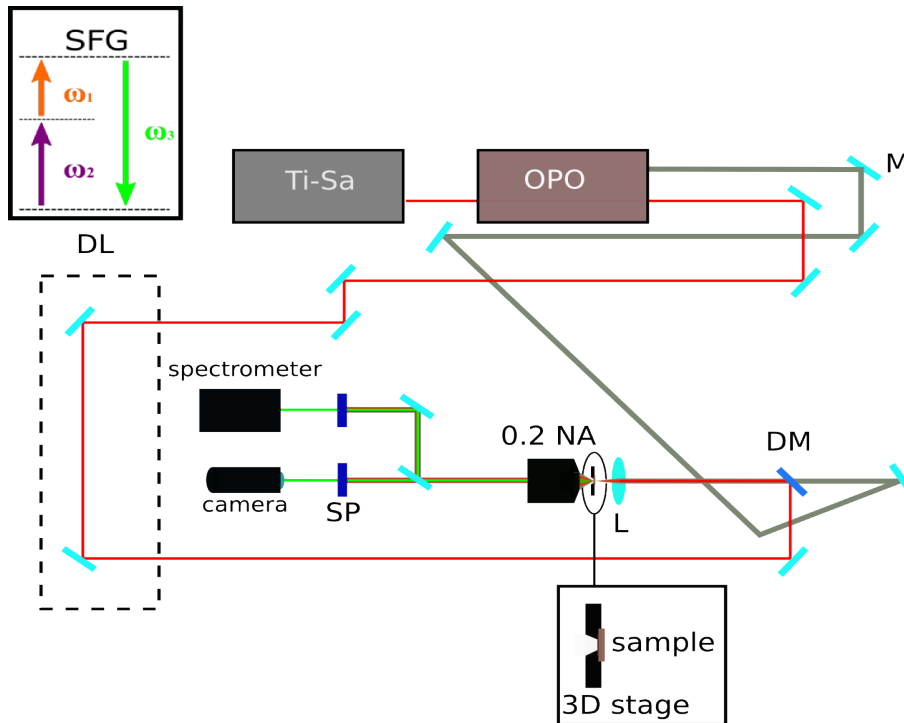


Figure 115: Nonlinear microscopy setup for SFG measurements on a transparent AlGaAs metasurface. Pump pulses at 840 nm (red line) are

delivered by a tunable Ti:Sa cavity, and pass through an OPO cavity to generate the 1550 nm signal (grey line). A Delay Line (DL) finely tunes their path difference. The two pulses recombine by means of a DM and are focused with on the sample, mounted on a 3D-stage. The SFG is collected in transmission by means of a 0.2-NA objective and is analysed by means of a CCD camera and a Si spectrometer. Short-pass filters cut at 650nm residual pump and signal. Top-left inset: energy level diagram for SFG process.

The most delicate part in a pump-probe setup is to find the spatio-temporal overlap between the two beams. To this end we replaced the sample with a 10^{-3} M Rhodamine 6G red dye solution in ethanol. This choice is due to the very strong fluorescence quantum yield (0.95) of this compound, with a broad peak around 530 nm [147]. We first found the optimal spatial overlap by exploiting the thermal lens effect. This occurs when light coming from a Gaussian is absorbed producing local heating the absorbing medium about the beam axis. This causes a radially dependent temperature distribution producing a refractive-index change dn/dT . As the refractive index dependence with the temperature is radial as well, this turns the host medium into an effective lens [148]. In our case we expected a maximum thermal lens effect with the two pulses spatially overlapping, with a subsequent broadening of the 840 nm pump coming out of the dye and observed in the far-field. As the employed dye is highly efficient this effect was clearly visible even by naked eye on a detector card (Fig. 116).

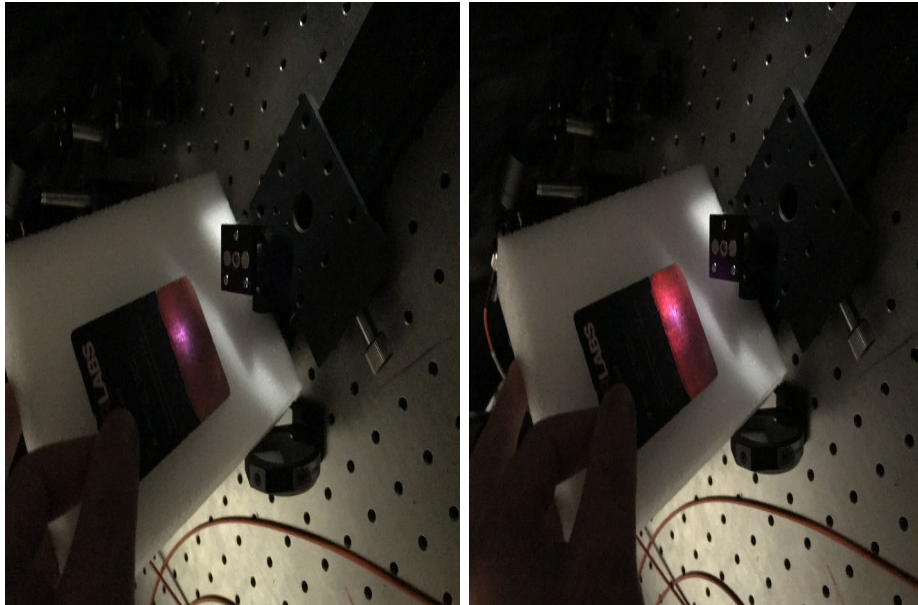


Figure 116: The spatial overlap of the two pulses is optimized by exploiting the thermal lensing effect, which induces a radial refractive index

gradient in the dye, effectively acting as a lens. When we are in the optimal overlap condition (right), the 840nm pump is much more broadened with respect to the out-of-matching situation (left).

Once the spatial overlap was found exploiting the thermal-lens effect, the temporal overlap was achieved by finely tuning the DL, knowing that the path difference of 1.6 m built-up in the OPO cavity was already recovered on the optical paths. The main observed signal coming from the dye is a strong TPL coming from the 840 nm pump, observed as a single bright spot in the vicinity of the focal point of the lens. A weaker luminescence trail is also present due to the high broadband of this peak. With the two pulses temporally overlapping we expected a considerable brightness increase of this luminescence trail due to the two pulses frequencies summing up to 545 nm and matching the luminescence peak. Again, the high efficiency of Rhodamine 6G allowed us to clearly see this effect with naked eye (Fig. 117).

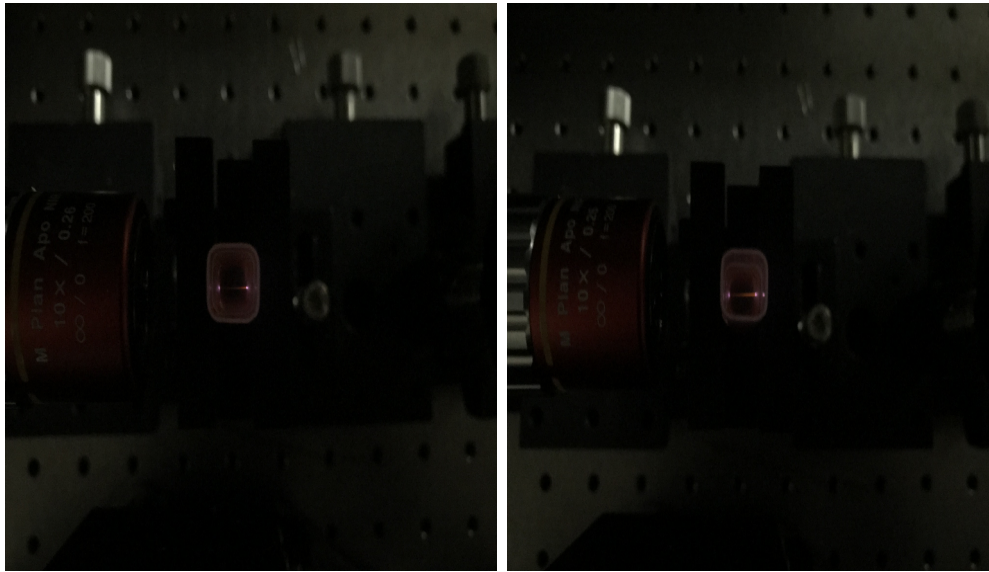


Figure 117: Smartphone camera images taken from the top of the Rhodamine 6G position when both pulses are shined on it. Left: when we are away from the temporal overlap condition a bright TPL spot due to the 840 nm pulse, localized at the right facet of the dye container, is clearly visible, accompanied by a weak luminescence trail. Right: when temporal overlap of the pulses is achieved, the luminescence trail brightness is clearly brighter, as the sum of pump and signal frequencies match pretty well the luminescence peak of the dye.

5.3.2 SFG measurement

Once the spatio-temporal overlap of the two pulses was found we replaced the dye with the above-mentioned sample. At this stage no numerical modelling

was supporting the experiments as that sample was just used as a test to see whether this pump-probe SFG idea would work. Surprisingly, a very strong SFG signal was observed even for this test sample, also accompanied by weaker THG from the 1550 nm signal and even a FWM peak of the type $\omega_{FWM} = 2\omega_p - \omega_s$, where ω_p and ω_s are the pump and signal frequencies respectively (Fig. 118). It is worth noting that the SFG signal is of the same order of the SHG obtained by illuminating the sample with the 1550nm pulse only. As expected, when we detune the DL the SFG and FWM peaks disappear.

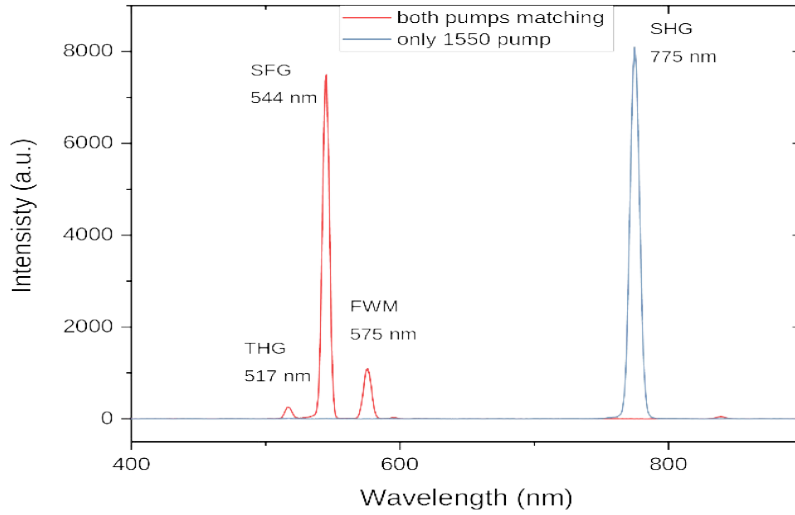


Figure 118: Spectra obtained by shining the sample with 1550 nm pulse only (blue line) and both 840 nm and 1550 nm pulses (red line). In the latter case, a strong SFG peak at 544 nm can be observed, at the spatio-temporal overlap condition, accompanied by THG and FWM peaks in its spectral vicinity.

This very strong signal is surprising also considering that we are employing an objective with NA=0.2 and, as the nonlinear signal is scattered mostly at large angles for symmetry reasons, we were collecting only a small part of the nonlinear emission. Thus, an SFG conversion efficiency estimation would not have made sense with this objective, as it would have been greatly underestimated. Measurements with an objective of 0.85 NA are currently in progress. Nevertheless the strong signals collected even with a small-NA objective were sufficient to perform a preliminary nonlinear imaging measurement.

5.3.3 SFG-based nonlinear imaging

The idea of nonlinear imaging is to encode an image on the pump path, i.e. induce some controlled light structuring, and try to retrieve the same image at the nonlinear frequency. The proper way of doing this would be to build a telescopic-like system at the infinity of the sample, consisting of the target image placed between two converging lenses at their focal points, as sketched in Fig. 119a. In particular, it is interesting to encode the image into the 1550 nm path as image transfer from NIR to the VIS could lead to night-vision applications. As my visiting period was reaching its end, we decided to encode the target image on the two pulses by mounting the target image on a 3D-stage and place it at about 0.5 mm from the sample (Fig. 119b). The target consists of a series of four identical squares with sides specified by a central number. This four-square series is repeated for side sizes of 25 μm , 50 μm , 100 μm and 200 μm (Fig. 119c,d).

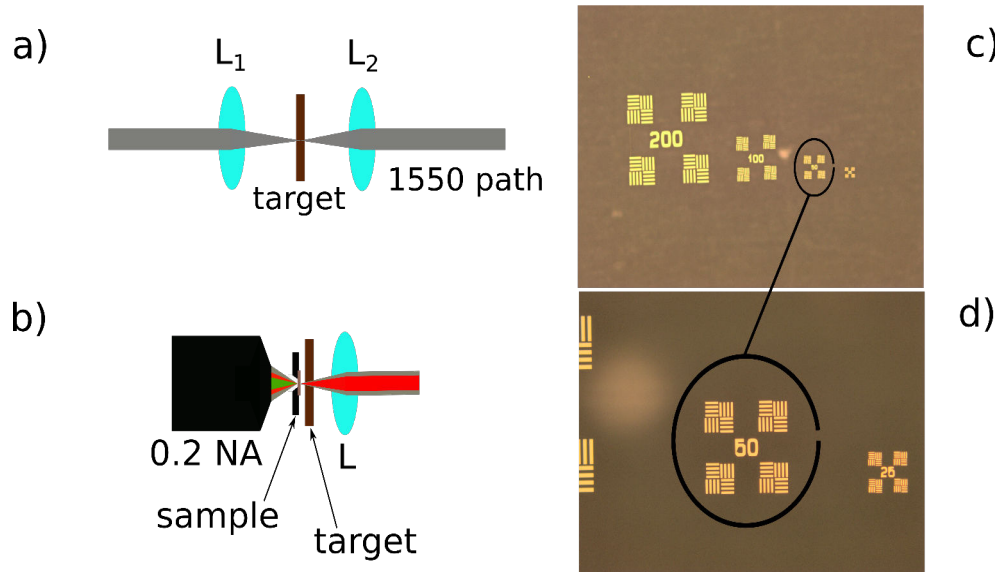


Figure 119: a) Ideal image encoding scheme. b) Actual implemented scheme. c) Optical microscope images of the target used for the nonlinear imaging experiment. These consists of four clusters each containing four squares with a reference number at the center indicating their sizes. d) Magnification of c).

The detection was done on a CCD camera with a relatively low integration time of 57ms. Four short-pass filters in total were used to filter out the pump at 840nm and the signal at 1550 nm: the first two cut at 650 nm and at 600 nm, (thus filtering out the 840nm pump) and the other two cut at 800 nm (thus filtering both 840 nm pump and 1550 nm signal). Unfortunately, as

the THG and FWM peaks are very close to SFG, we were not able to exclude them.

As shown in Fig. 120, the square pattern is correctly transferred to the harmonic wavelengths when both overlapping pulses are impinging on the sample. Conversely, when we shine only one of the pulses at a time on the sample, no significant contribution is observed, meaning that the four filters are working well. In addition, when we shine the 1550 nm signal only, we see that the THG contribution to the imaging is negligible.

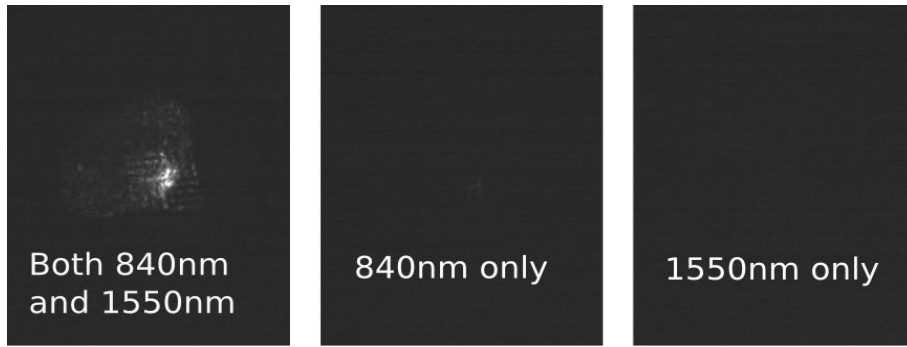


Figure 120: Left: image obtained when shining both 840 nm and 1550 nm pulses on the sample, showing correct image pattern transfer at the SFG wavelength. Center and right: camera images recorded when shining only the 840 nm pump and 1550 nm signal respectively.

We then registered a real-time video of the image on the camera while detuning the DL. We observed that after about a quarter of a turn of the screw into the DL, corresponding to a path difference of $75 \mu\text{m}$, the signal is significantly dropped. After an entire turn, corresponding to a delay of $300 \mu\text{m}$, the SFG and FWM signal is lost, while only a small visible-pump residue is present. Screenshots of the video at the aforementioned path differences are shown in Fig. 121.

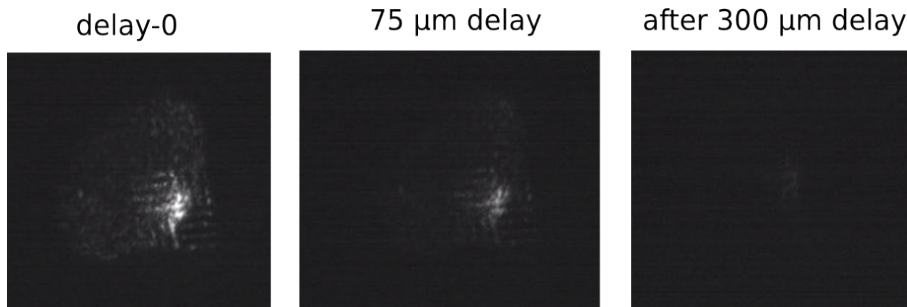


Figure 121: Screenshots of a real time video showing the SFG image variation while the DL detunes the path difference from from the 0-delay position. From left to right: screenshots at 0 delay, at $75 \mu\text{m}$, and at $300 \mu\text{m}$.

A real-time video was also recorded while moving the target position with its 3D stage. We can infer that the SFG image changes accordingly and, despite the low resolution, we can distinguish the reference numbers indicating the square dimensions. Screenshots of this video are shown in Fig. 122. Remarkably, in both videos the integration time is still 57 ms, and it is sufficient to yield a clear nonlinear image.

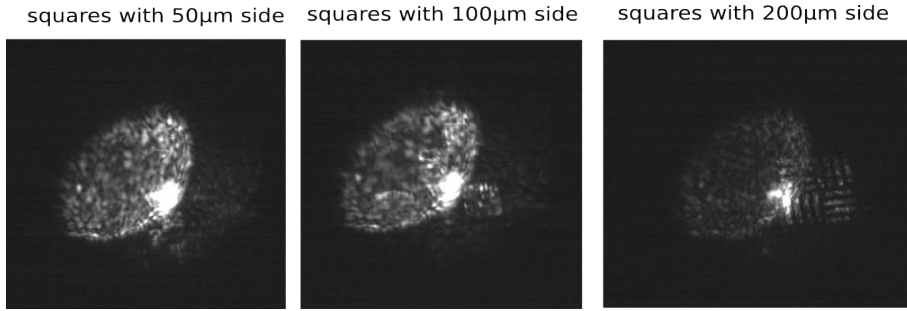


Figure 122: Screenshots of a real time video showing how the SFG image on the CCD camera changes as the position of the image target is moved. From left to right the screenshots show squares with 50 μm , 100 μm and 200 μm sides respectively.

Although these measurements should be repeated with an optimized setup, with a high-NA objective and with a proper image-encoding system, these results represent a proof-of-principle demonstration of the potential of AlGaAs metasurfaces for nonlinear imaging.

As already stated, the ability to convert images from the NIR to the VIS could potentially lead to night-vision applications, provided that the high peak-power 1550 nm signal is replaced by a weaker CW source.

5.4 Beyond plane-wave excitation: Cathodoluminescence spectroscopy of AlGaAs single pillars and dimers

So far, in all modelling and experiments performed on AlGaAs nanoantennas we were assuming either plane-wave, or focused Gaussian beam excitation. As we have seen in Section 1.2, this type of illumination dictates what kind of modes we are going to excite in the nanostructure. Interestingly also in the case of dimers, despite the symmetry of the system changes completely from the case of an isolated cylinder, we didn't observe any anti-symmetric modes, as of course a plane-wave would not "see" any difference between

right and left side of the dimer.

To better understand what are the modes supported by these nanostructures beyond the limits imposed by plane-wave excitation, we used CL imaging spectroscopy to investigate single AlGaAs nanoantennas and dimers.

5.4.1 Results and discussion

An array of AlGaAs nanopillars on AlOx substrate was fabricated according to the recipe described in Section 3.4.1. The diameter of such structures span between 300 nm and 450 nm, with a spacing of 3 μm . Dimers were patterned as well, with the same diameter range and a fixed gap of 110 nm (Fig. 123). The sample was then sent to the group of Anatoly Zayats in King's College, London where the CL experiments were performed. The setup is depicted in Fig. 26, and consists of a focused 30 keV electron beam impinging on the sample. The CL radiation is collected by means of a parabolic mirror and redirected towards Si (for the VIS) and InGaAs (for the NIR) spectrometers.

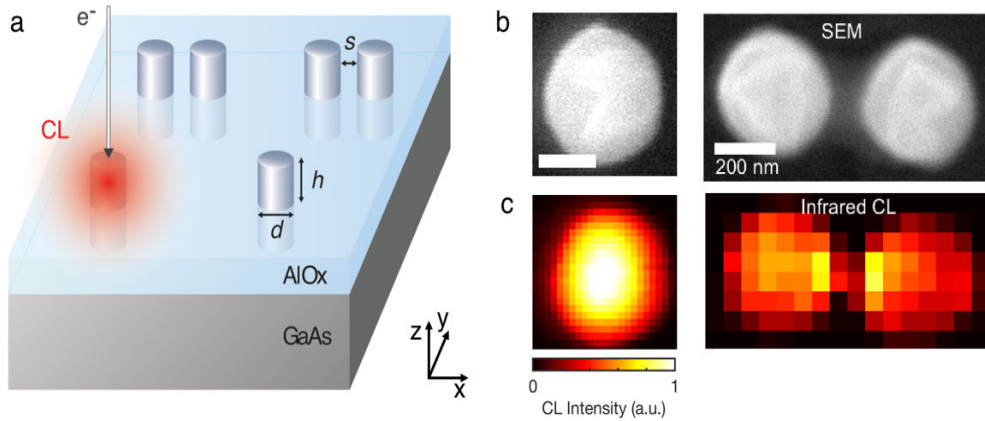


Figure 123: (a) Schematics of the sample consisting of isolated AlGaAs nanoantennas and dimers, characterized by a fixed height h of 400 nm, diameter d spanning from 300 nm to 450 nm, and dimer separation $s=110$ nm. (b) Scanning electron microscope image of a nanopillar with $d=400$ nm and the corresponding dimer. (c) CL intensity maps of a pillar at 730 nm (pixel size 20 nm) and of a dimer at 1 μm (pixel size 60 nm) [149].

By scanning the e-beam across the sample surface, two-dimensional CL intensity maps are obtained. The sensitivity of the spectrometers is such that the CL intensity maps in the VIS exhibit a pixel size of 20 nm, while in the NIR the pixel size is 60 nm. Then in order to produce a CL spectrum the signal was averaged over the pixels corresponding to the region of interest. CL originating from the GaAs substrate exhibits a luminescence peak at a

wavelength of 870 nm, corresponding to its bandgap ($E_g^{GaAs} = 1.424$ eV), which obscures the CL emission from the nanoantennas within its spectral vicinity. Figs. 124a (d=360 nm) and 124b (d=420 nm) show the CL spectra obtained by exciting the nanopillars at the centre. The grey shaded region corresponds to the above-mentioned GaAs luminescence.

The measurements are in good agreement with the extinction spectra calculated with FEM especially for wavelengths longer than the bandgap wavelength of $Al_{0.18}Ga_{0.82}As$ (~ 730 nm), whereas above the band-gap the CL signal is significantly suppressed. This behaviour contrasts with what previously reported for sample Si nanoantennas, where the role of interband emission is not significant due to the indirect bandgap and experimentally measured resonances are clearly visible even for wavelengths shorter than the bandgap [76, 78].

To shed light on the resonances responsible for the observed CL peaks, FEM eigenmode simulations are performed and contributions from magnetic (Figs. 124c,e,g,i) and electric (Figs. 124d,f,h,j) resonances are identified. As expected, the NIR is dominated by dipolar modes, while in the visible range we have higher order multipoles (quadrupoles, octupoles etc.). Moreover, we observe that for the largest pillar (d=420 nm, Fig. 124b) the resonances red-shift with respect to the pillar with d=360 nm (Fig. 124a), as expected from the intrinsic geometric nature of multipolar resonances at the nanoscale.

The change in the nanopillar size also brings about a change of the resonance spectral separation, leading to an overlap of the electric and magnetic modes, especially in the VIS.

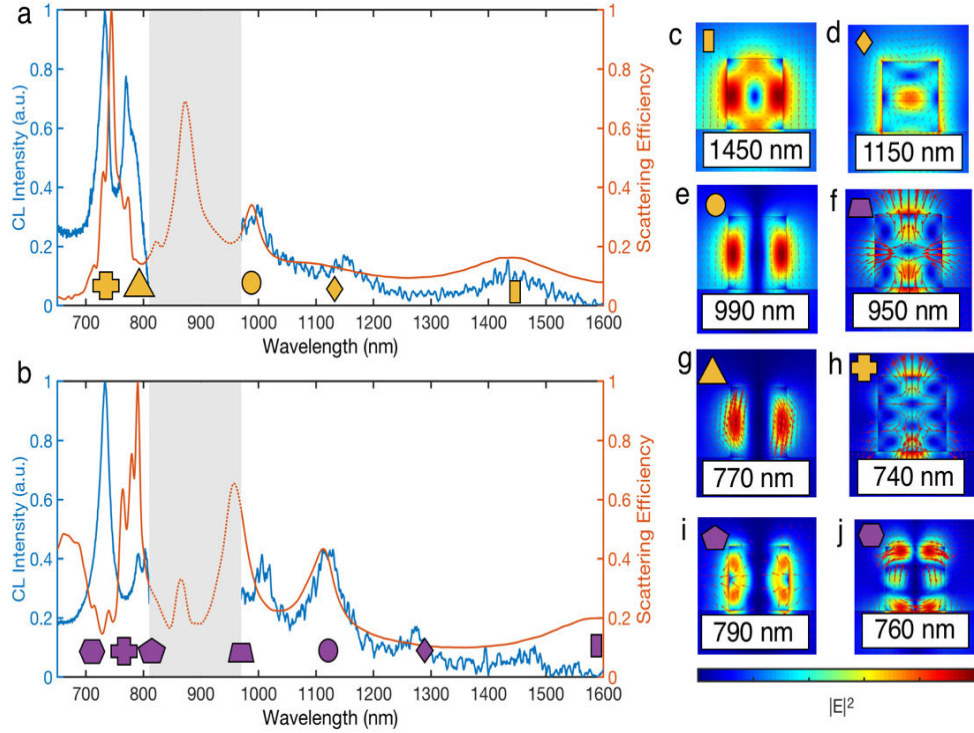


Figure 124: CL spectra (blue lines) and calculated scattering efficiency (red lines) for single AlGaAs pillars with (a) $d = 360$ nm and (b) $d = 420$ nm, excited at the centre. Grey shading indicates the spectral range wherein CL from the nanopillars is obscured by CL from the substrate. (c-j) Electric field distributions in the xz -plane of the modes responsible for the observed CL peaks, with magnetic (c,e,g,i) and electric (d,f,h,j) contributions. Their spectral positions are indicated in (a) and (b) with coloured markers. [149].

In the dimer case, the coupling between adjacent nanopillars and the different system symmetry give rise to mode hybridization modes, yielding both symmetric and anti-symmetric bonding modes. Again, this behaviour cannot be found in case of plane wave illumination at normal incidence, in which we can only find symmetric modes, where the multipolar moments are parallel.

These anti-symmetric modes concentrate energy and contribute as well to the radiative local density of states, making it possible to observe them with CL spectroscopy. The CL spectrum acquired from a dimer with pillar diameter of 330 nm and separation of 110 nm is shown in Fig. 125a, upon illumination at various positions of one of the pillars. Peaks in this case are broader compared to the isolated pillar. This is borne out by the corresponding simulated scattering efficiency as well (Fig. 125f).

A variation in the peaks intensity and wavelength as the excitation position is altered is also displayed. This effect is visible in the measured spectra

as well, especially for the peak at 1200 nm. It is apparent that, depending on the excitation position of the dimer, different modes are preferentially excited.

As a consequence, efficient excitation of a specific mode will occur when the highly localized electric field generated by the e-beam overlaps with the electric field of the mode. Spectra calculated via the eigenmode simulations (Fig. 125g), underline the multiple symmetric (solid lines) and anti-symmetric (dashed lines) resonances that overlap to produce the broad peaks observed in the experiment.

CL intensity maps at the resonance wavelengths of 1000 nm, 1100 nm, 1200 nm and 1350 nm are shown in Figs. 125b-e, highlighting the result of the overlap between all modes identified with the eigenmode simulation. For example, the CL map shown in Fig. e is the result of the contributions of three modes residing in the wavelength range 1350 nm - 1400 nm.

Another interesting feature revealed by the eigenmode simulations is that the two anti-symmetric mode peaks in the aforementioned range are narrower than the symmetric ones, suggesting lower radiative losses and that a greater contribution to the CL map may originate from the symmetric mode.

Conversely, for the CL map in Fig. 125b regarding the dip at 1000 nm, the brightest hotspots appear at the nanopillar edges close to the gap, an asymmetry which is proof of mode hybridization of symmetric and anti-symmetric contributions, revealed by the eigenmode simulations.

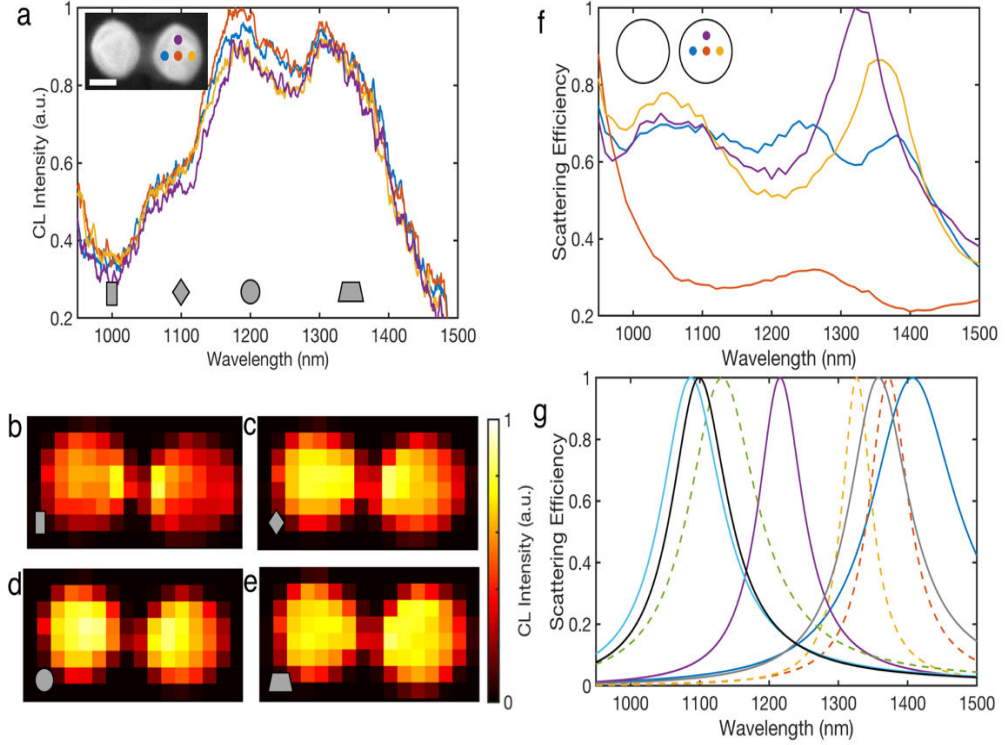


Figure 125: (a) CL spectra from an AlGaAs dimer with $s=110$ nm $d=330$ nm, for different excitation positions (see inset). (b-e) CL intensity maps for the wavelengths 1000 nm, 1100 nm, 1200 nm and 1350 nm. The spectral positions of the maps are indicated with grey markers in (a), the bandwidth for each map is 30 nm and the pixel size is 60 nm. (f) Simulated scattering spectra for different illumination positions (inset). (g) Individual mode contribution to the spectra via the eigenmode simulations. Solid (dashed) coloured lines correspond to symmetric (anti-symmetric) modes. The electric and magnetic dipole modes present in an isolated pillar with $d=330$ nm are shown by black and grey solid lines for reference [149].

The increased mode richness is harnessed when the simulated scattering of Fig. 125f is compared to plane wave excitation of the same dimer structure at normal incidence (Fig. 126). In the latter case, the scattering exhibits only two resonances for each incident polarization, corresponding to the excitation of the symmetric modes.

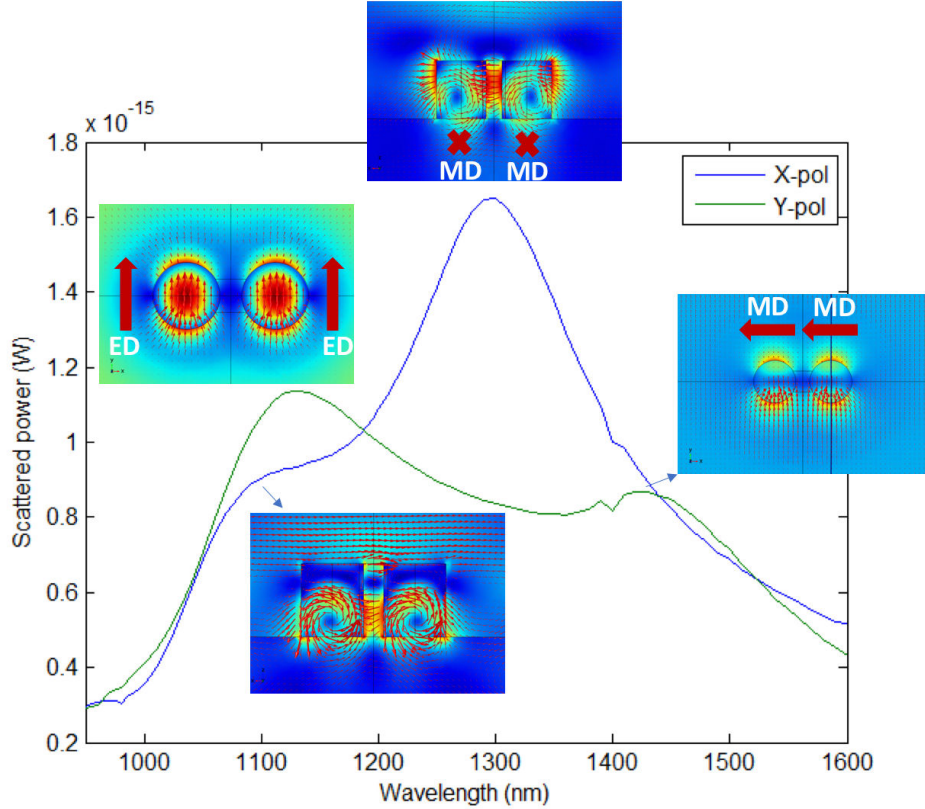


Figure 126: Simulated spectra for plane wave excitation at normal incidence of the same dimer for X (blue line) and Y (green line) polarizations. Insets display the electric field profiles of the hybridized symmetric modes [149].

Detailed field distributions of the modes involved in the CL emission from the dimer structure is shown in Fig. 127. The anti-symmetric (a-c) and symmetric (d-f) modes under exam appear to be the result of the coupling between ED and MD resonances excited in each of the two nanopillars. As expected, the symmetric and anti-symmetric hybridized modes due to coupling between EDs both occur in the spectral vicinity of the isolated ED mode (1100 nm). All four possible alignments of the MD hybridized modes residing in the 1220 nm-1410 nm region, are exhibited as well around the isolated MD mode at 1360 nm.

This splitting of the original single pillar modes is indeed the trademark of hybridization, induced by the fact that we pass from the single pillar case exhibiting circular symmetry to the dimer configuration with axial symmetry, somehow resembling the physical situation of atomic transitions in condensed

matter where the presence of a strong external magnetic field induces an axial symmetry on the system and causes the splitting of some transitions [150].

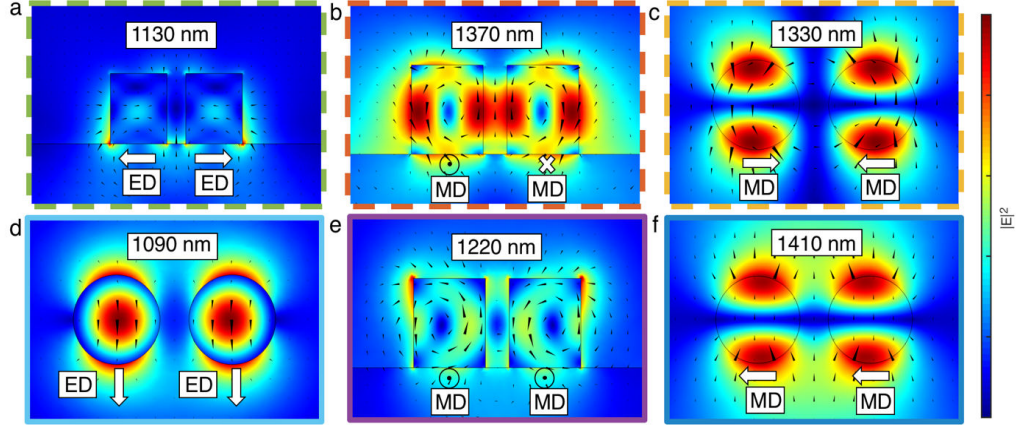


Figure 127: Simulated eigenmode electric field profiles of the modes shown in Fig. 125g. (a-c) correspond to anti-symmetric modes (dashed frame), and (d-f) to symmetric modes (solid frame). They are obtained by either cutting through the center of the nanopillars along the xz (a,b,e) and xy (c,d,f) planes. The directions of the electric and magnetic dipoles are shown, together with the wavelengths. The frame colors are the same of the corresponding peaks in Fig. 125g as a guide to the eye [149].

5.5 Conclusion

In this chapter we have reviewed the recent advances on second-order nonlinear optical generation at the nanoscale. The general message is that the physics in this regime is completely different from bulk and guided nonlinear optics, as the absence of phase-matching, i.e. the absence of a preferential k -vector for the generated nonlinear light, brings about new challenges for emission pattern and polarization control, due to the non-trivial mode mixing happening at 2ω . On the other hand, all cited works show a considerable mode volume shrinkage down to $\sim 10^{-3} \mu\text{m}^3$ with respect to previous results, potentially pushing the miniaturization of PICs further into the nanoscale.

General conclusion and perspectives

My PhD thesis has been focused on the fabrication of monolithic AlGaAs nanostructures for nonlinear frequency conversion, with significant experience in nonlinear measurements and good learning opportunities in numerical modelling. As already stated, the demonstration of such objects has been the result of a collaborative work involving several research groups within the EU-funded NANOPHI project.

My effort towards the efficient fabrication of an AlGaAs-on-AlOx monolithic platform, firstly led to the demonstration of enhanced SHG in isolated nanocylinders, exhibiting a conversion efficiency of $1.5 \cdot 10^{-7} \text{ W}^{-1}$, three orders of magnitude higher than the best achieved in specifically designed plasmonic nano-objects [46].

To further improve the conversion efficiency and SH directionality control I have reviewed the necessary steps to optimize the fabrication protocol and achieve ad-hoc engineered complex nanoscale patterns.

These technological efforts have led to the demonstration of emission control by tilting the pump k-vector and by employing asymmetric diffraction gratings. Conversely, even though dimers and dielectric-metal nanostructures provided further insight into the physics of Mie nanoresonators, the SHG conversion efficiency did not exceed that of isolated nanopillars excited at the MD resonance.

Our study also involved the measurement of other second-order nonlinear effects, such as SFG and SPDC, enabling the demonstration of the smallest, yet very efficient source of entangled photon pairs in terms of mode volume [142]. This PhD results point towards some interesting applications, including nonlinear goniometry [124], nonlinear holography [127], and night vision.

Perspective directions could be provided by diving deeper into four main research axes that have already underpinned the progress in Nanophotonics during the last decade:

- mode interference engineering
- identification of optimal nonlinear material properties
- wavefront shaping via metasurfaces
- active tunability of the metasurface optical properties

Starting with the first point, we have seen indeed the capabilities of anapoles [55, 135, 53], in which toroidal and electric dipoles destructively interfere to achieve ideally non-radiative objects. Another interference effect between electric and magnetic dipoles, the so-called Kerker effect, was briefly introduced as a way to achieve high radiation directivity [85, 123].

Other two interesting mode mixing effects recently explored are worth mentioning: on the one hand we have Fano resonances, defined as an interference effect between a broad bright mode, i.e. a mode which is excited by the incident wave, and a narrow dark mode which is not excited by the incident wave [151].

This gives rise to a narrow, high-Q and asymmetric resonance which has already proved its usefulness in nonlinear light generation [152] and in sensing applications [153].

On the other hand, another way to achieve high-Q cavities was found by tailoring the interference between Mie resonances and FP-modes, a concept inspired by bound states in the continuum [154], allowing a theoretical boost in the nonlinear frequency conversion by two orders of magnitude.

As for nanoscale nonlinear optical generation, Si was the first employed material for enhanced THG from SOI-nanopillars [155, 156]. However, its centrosymmetric structure and the TPA problem limit its applications even at the nanoscale.

Germanium (Ge), another $\chi^{(3)}$ material, was exploited as well to achieve higher THG conversion efficiency in nanodisks pumped at the anapole mode [52], as well as degenerate FWM [157].

Unfortunately, this material suffers from severe limitation, due to the fact that effective Top-down fabrication approaches were not demonstrated so far, especially due to the inexistence of an efficient ICP etching recipe. Thus, only bottom-up approaches are allowed, with a resulting amorphous material structure hindering further control.

Conversely, AlGaAs has proven to efficiently address all issues of the above mentioned materials, with the possibility to avoid TPA at $1.55\mu\text{m}$, the possibility to realize an integrated AlGaAs-on-Alox monolithic platform, and the huge $\chi^{(2)}$ and comparable-to-Si $\chi^{(3)}$ enabling a plethora of nonlinear frequency mixing effects.

It is worth mentioning that enhanced SHG was demonstrated as well on perovskite nanoparticles [158, 134], a promising material which is nowadays gaining wide attention in the opto-electronics field. However, conversion efficiency or effective $\chi^{(2)}$ coefficient measurements are still lacking, and a comparison with AlGaAs is not yet possible.

Another III-V candidate material with promising properties is Gallium Phosphide, which exhibits a two-fold advantage with respect to AlGaAs: its transparency range goes deep into the visible range, enabling to directly pump the nanostructures through the substrate, as reported in [160], and extend the TPA-free exploitable nonlinear wavelength range down to the green ($E_g = 2.26\text{eV}$). Moreover, similarly to AlGaAs, thermal wet oxidation of AlGaP has been reported [159], potentially enabling the development of an analogous nonlinear GaP-on-AlOx monolithic platform, enabling both transmission and reflection measurements with a $1.55\ \mu\text{m}$ pump. The sole drawback compared to AlGaAs would be represented by the lower nonlinear coefficient of $\sim 25\text{pm/V}$.

Another material allowing to bridge the gap between the visible and dielectric nanophotonics is AlAs, which has a bandgap close to that of GaP (2.12 eV). This material however could not allow a wet oxidation-based monolithic platform. Despite this, a wafer-bonding approach to transfer the nano-objects on a glass substrate could still be possible. To conclude this second point, despite all excellent results achieved with all aforementioned nonlinear materials, no wide consensus on an optimal one has been reached yet by the community.

A further leap forward in the all-dielectric Nanophotonics field requires also going beyond single-nanostructure illumination, and enter into the metasurface regime, as we did in the SFG-based nonlinear imaging project. This advancement could enable the unification of nonlinear material properties and mode interference engineering with the wavefront control capabilities already demonstrated in metasurfaces [13, 10, 11, 12]. Finally, the employment of liquid crystal-embedded samples has recently allowed for temperature [161] and electrical [162] tunability of the metasurface properties. To sum-up, so far only groups of two or three out of the four main paradigms in all-dielectric Nanophotonics have been studied at the same time. All cited works so far point towards virtually endless application possibilities in case of efficient merging of these four concepts altogether.

This research field offers interesting future developments to Giuseppe Leo's group as well: after the first results on SHG from single pillars demonstrating the capabilities of the platform we developed, our group was awarded two grants: one by the LabEx (a consortium of scientific universities in Paris) on the project "PANAMA", and one by ANR (French national re-

search agency) on the project “NOMOS”.

This funding allowed the acquisition of a broadband femtosecond OPA laser source by Amplitude (MANGO SP), and the subsequent construction of an optical setup for nonlinear confocal microscopy, also equipped with Fourier lenses for BFP imaging. The two cited grants also allowed to hire Giuseppe Marino as a postdoctoral fellow.

This, together with the arrival of a new PhD student, Carlo Gigli, allowed to expand the nanophotonic branch of our group. Moreover, the recent arrival of a new permanent member in our group, Dr. Aloyse Degiron, who is an expert in plasmonics, optoelectronics and metamaterials, opens up exciting research scenarios in hybrid nanophotonics.

I would like to conclude by giving a hint on the possible everyday-life technological applications offered by optical metasurfaces. We could imagine for instance a nonlinear quantum chip generating entangled photon pairs and operating as a quantum endoscope when placed on the tip of a $1.55\ \mu\text{m}$ fiber.

This configuration would allow new forms of spatial entanglement, which can give rise to new functionalities, and would enable quantum imaging techniques in environments where bulk crystal based sources could not be used, with possible in-vivo investigations. This technology could reduce cost and dimensions while improving the sensitivity of medical sensors and diagnostic systems.

Another possibility could be to deposit a metasurface on eyeglasses or car windshield, in order to enhance visibility in difficult conditions such as night, presence of fog or smoke, via frequency conversion from the NIR to the VIS, without supplementary ambient illumination. This would have important repercussions on road safety, auto and tele-guided systems and metrology.

List of acronyms

AFM Atomic Force Microscope

Al Aluminium

AlAs Aluminum Arsenide

AlGaAs Aluminum Gallium Arsenide

AlGaP Aluminum Gallium Phosphide

AlOx Aluminum oxide

Ar Argon

As Arsenide

Au Gold

BCB Benzocyclobutene

BFP Back Focal Plane

BL Bertrand Lens

BPM Birifringence Phase-Matching

BS Beam Splitter

CCD Charge-Coupled Device

CHF₃ Fluoroform

CL Cathodoluminescence

CMOS Complementary Metal-Oxide-Semiconductor

CW Continuous Wave

- DC** Duty Cycle
- DDA** Discrete-Dipole Approximation
- DF** Dose Factor
- DFG** Difference-Frequency Generation
- DL** Delay Line
- DM** Dichroic Mirror
- EBL** Electron Beam Lithography
- EBPVD** Electron-Beam Physical Vapour Deposition
- ED** Electric Dipole
- EELS** Electron Energy Loss Spectroscopy
- ELO** Epitaxial Lift-Off
- EO** Electric Octupole
- EQ** Electric Quadrupole
- Er** Erbium
- FDTD** Finite-Difference Time-Domain
- FEM** Finite-Element Method
- FF** Fundamental Frequency
- FIB** Focused Ion Beam
- FP** Fabry-Perot
- FWHM** Full-Width at Half Maximum
- FWM** Four-Wave Mixing
- Ga** Gallium
- GaAs** Gallium Arsenide
- GaP** Gallium Phosphide
- Ge** Germanium

- H** Horizontal
- HF** Fluoridric Acid
- HR-TEM** High-Resolution Transmission Electron Microscope
- HSQ** Hydrogen Silesquioxane
- ICP** Inductively Coupled Plasma - Reactive Ion Etching
- IR** Infrared
- In** Indium
- InAs** Indium Arsenide
- InGaAs** Indium Gallium Arsenide
- InP** Indium Phosphide
- LED** Light-Emitting Diode
- LSP** Localized Surface Plasmons
- MBE** Molecular Beam Epitaxy
- MD** Magnetic Dipole
- MH** Magnetic Hexapole
- MIBK** Metilisobutilchetone
- MOCVD** Metal-Organic Chemical Vapour Deposition
- MPL** Multi-Photon Luminescence
- MPM** Modal Phase-Matching
- MQ** Magnetic Quadrupole
- NIR** Near Infrared
- NA** Numerical Aperture
- O** Oxygen
- OPA** Optical Parametric Amplificator
- OPO** Optical Parametric Oscillator

- P** Phosphorus
- PECVD** Plasma-Enhanced Chemical Vapour Deposition
- PIC** Photonic integrated circuit
- PMMA** Polymethyl methacrylate
- PML** Perfectly-Matched Layer
- PPLN** Periodically Poled Lithium Niobate
- Pt** Platinum
- QPM** Quasi Phase-Matching
- RIE** Reactive Ion Etching
- RF** Radio Frequency
- RHEED** Reflection High Energy Electron Diffraction
- SEM** Scanning Electron Microscope
- SFG** Sum-Frequency Generation
- SH** Second Harmonic
- SHG** Second-Harmonic Generation
- Si** Silicon
- SiCl₄** Silicon Tetrachloride
- SiH₄** Silane
- SiO_x** Silicon Oxide
- SOI** Silicon-On-Insulator
- SP** Surface Plasmons
- SPAD** Single-Photon Avalanche Photodiode
- SPDC** Spontaneous Parametric Down-conversion
- SPP** Surface Plasmon-Polaritons
- TD** Toroidal Dipole

- TEM** Transmission Electron Microscope
- THG** Third-Harmonic Generation
- Ti** Titanium
- TL** Tube Lens
- TMAH** Tetramethylammonium Hydroxide
- TPA** Two-Photon absorption
- TPL** Two-Photon Luminescence
- UV** Ultraviolet
- V** Vertical
- VIS** Visible

List of publications

Journal articles

- V. F. Gili, L. Carletti, A. Locatelli, D. Rocco, M. Finazzi, L. Ghirardini, I. Favero, C. Gomez, A. Lemaître, M. Celebrano, C. De Angelis, and G. Leo, “Monolithic AlGaAs second-harmonic nanoantennas”, *Optics Express* 24, 15965 (2016).
- L. Ghirardini, L. Carletti, V. F. Gili, G. Pellegrini, L. Duò, M. Finazzi, D. Rocco, A. Locatelli, C. De Angelis, I. Favero, M. Ravaro, G. Leo, A. Lemaître, and M. Celebrano, “Polarization properties of second-harmonic generation in AlGaAs optical nano antennas”, *Optics Letters* 42, 559 (2017).
- L. Carletti, D. Rocco, A. Locatelli, C. De Angelis, V. F. Gili, M. Ravaro, I. Favero, G. Leo, M. Finazzi, L. Ghirardini, M. Celebrano, G. Marino, and A. V. Zayats, “Controlling second-harmonic generation at the nanoscale with monolithic AlGaAs-on-AlOx antennas”, *Nanotechnology* 28, 114005 (2017).
- V. F. Gili, L. Carletti, F. Chouchane, G. Wang, C. Ricolleau, D. Rocco, A. Lemaître, I. Favero, L. Ghirardini, M. Finazzi, M. Celebrano, C. De Angelis, and G. Leo, “Role of the substrate in monolithic AlGaAs nonlinear nanoantennas”, *Nanophotonics* 7, 2 (2018).
- D. Rocco, V. F. Gili, L. Ghirardini, L. Carletti, I. Favero, A. Locatelli, G. Marino, D. N. Neshev, M. Celebrano, M. Finazzi, G. Leo, and C. De Angelis, “Tuning the second-harmonic generation in AlGaAs nanodimers via non-radiative state optimization”, *Photonics Research* 6, 5 (2018).

- C. P. T. McPolin, G. Marino, A. V. Krasavin, V. F. Gili, L. Carletti, C. De Angelis, G. Leo, and A. V. Zayats, “Imaging Electric and Magnetic Modes and their Hybridization in Single and Dimer AlGaAs Nanoantennas”, *Advanced Optical Materials*, 1800664 (2018).
- V. F. Gili, L. Ghirardini, D. Rocco, G. Marino, I. Favero, I. Roland, G. Pellegrini, L. Duò, M. Finazzi, L. Carletti, A. Locatelli, A. Lemaitre, D. N. Neshev, C. De Angelis, G. Leo, and M. Celebrano, “Metal-dielectric hybrid nanoantennas for efficient frequency conversion at the anapole mode”, *Beilstein Journal of Nanotechnology* 9, 2306 (2018).
- L. Ghirardini, G. Marino, V. F. Gili, I. Favero, D. Rocco, L. Carletti, A. Locatelli, C. De Angelis, M. Finazzi, M. Celebrano, D. N. Neshev, and G. Leo, “Shaping the nonlinear emission pattern of a dielectric nanoantenna by holographic gratings”, *Nano Letters* 18, 6750 (2018).
- L. Carletti, G. Marino, L. Ghirardini, V. F. Gili, D. Rocco, I. Favero, A. Locatelli, A. V. Zayats, M. Celebrano, M. Finazzi, G. Leo, C. De Angelis, and D. N. Neshev, “Nonlinear goniometry by second harmonic generation in AlGaAs nanoantennas”, *ACS Photonics* 5, 4386 (2018).
- G. Marino, A. S. Solntsev, L. Xu, V. F. Gili, L. Carletti, A. N. Poddubny, M. Rahmani, D. A. Smirnova, H. Chen, G. Zhang, A. V. Zayats, C. De Angelis, G. Leo, A. A. Sukhorukov, and D. N. Neshev, “Optical nanoantenna for nonlinear generation of heralded photons”, submitted (2018).
- M. Rahmani, G. Leo, I. Brener, A. V. Zayats, S. A. Maier, C. De Angelis, H. Tan, F. Karouta, R. Oulton, M. Lysevych, I. Staude, L. Xu, V. F. Gili, A. Miroshnichenko, C. Jagadish, and D. N. Neshev, “Materials Evolution for Optical Frequency Conversion at the Nanoscale: From Metallic to III-V Semiconductor Resonators”, *Opto-Electronic Advances*, accepted (2018).

Conference acts

- L. Carletti, D. Rocco, A. Locatelli, V. F. Gili, G. Leo, and C. De Angelis, “Enhanced second-harmonic generation driven from magnetic dipole resonance in AlGaAs nanoantennas”, *SPIE Photonics Europe*, Brussels, Belgium, April 2016.

- D. Rocco, L. Carletti, A. Locatelli, V. F. Gili, G. Leo, and C. De Angelis, “Second harmonic generation from dielectric nanoantennas: control of the radiation pattern via phase gratings engineering”, ECMS 2016, Regensburg, Germany, May 2016.
- V. F. Gili, I. Favero, G. Leo, C. Gomez, A. Lemaître, L. Ghirardini, M. Finazzi, M. Celebrano, L. Carletti, D. Rocco, A. Locatelli, and C. De Angelis, “Monolithic AlGaAs Second Harmonic nanoantennas”, JNMO 15, Les Issambres, France, June 2016.
- V. F. Gili, L. Carletti, D. Rocco, A. Locatelli, A. Lemaître, M. Ravaro, I. Favero, L. Ghirardini, M. Finazzi, M. Celebrano, C. De Angelis, and G. Leo, “Monolithic AlGaAs-on-insulator second-harmonic nanoantennas” (post-deadline), EOSAM 2016, Berlin, September 2016.
- V. F. Gili, L. Carletti, D. Rocco, A. Locatelli, L. Ghirardini, I. Favero, C. Gomez, A. Lemaître, M. Finazzi, M. Celebrano, C. De Angelis, and G. Leo, “Second-harmonic generation in AlGaAs nanoantennas”, OSA Nonlinear Photonics, Sydney, Australia, September 2016.
- V. F. Gili, L. Carletti, D. Rocco, A. Locatelli, A. Lemaître, M. Ravaro, I. Favero, L. Ghirardini, M. Finazzi, M. Celebrano, C. De Angelis, and G. Leo, “AlGaAs monolithic nonlinear optical nanoantennas”, GDR PMSE, Toulouse, France, November 2016.
- V. F. Gili, L. Carletti, D. Rocco, A. Locatelli, A. Lemaître, M. Ravaro, I. Favero, L. Ghirardini, M. Finazzi, M. Celebrano, C. De Angelis, and G. Leo, “Second harmonic generation in monolithic AlGaAs nanoantennas” (invited), NANOP 2016, Paris, France, December 2016.
- V. F. Gili, L. Carletti, A. Locatelli, D. Rocco, M. Finazzi, L. Ghirardini, I. Favero, C. Gomez, A. Lemaître, M. Celebrano, C. De Angelis, and G. Leo, “Monolithic AlGaAs second-harmonic nanoantennas” (keynote), ICOPA 4, Bordeaux, France, December 2016.
- C. De Angelis, V. Gili, L. Carletti, D. Rocco, A. Locatelli, L. Ghirardini, I. Favero, C. Gomez, A. Lemaître, M. Finazzi, M. Celebrano, G. Leo, “Second harmonic generation in dielectric nanoantennas” (invited), Nanophotonics Workshop, Tequisquiapan, Queretaro, Mexico, January 2017.
- C. De Angelis, V. F. Gili, L. Carletti, D. Rocco, A. Locatelli, L. Ghirardini, I. Favero, C. Gomez, A. Lemaître, M. Finazzi, M. Celebrano,

and G. Leo, “Second harmonic generation in AlGaAs nanoantennas” (invited), SPIE Photonics West, San Francisco, USA, February 2017.

- V. F. Gili, L. Ghirardini, L. Carletti, G. Pellegrini, L. Duò, M. Finazzi, D. Rocco, A. Locatelli, I. Favero, M. Ravaro, A. Lemaître, M. Celebrano, C. De Angelis, and G. Leo, “Polarization properties of second harmonic signal from monolithic AlGaAs nanoantennas”, ECIO 2017, Eindhoven, The Netherlands, April 2017.
- C. De Angelis, L. Carletti, D. Rocco, A. Locatelli, V. F. Gili, M. Ravaro, I. Favero, G. Leo, M. Finazzi, L. Ghirardini, M. Celebrano, G. Marino, and A. V. Zayats, “Controlling Second-harmonic Generation at the Nanoscale with Monolithic AlGaAs-on-AlOx Antennas” (invited), PIERS 2017, St. Petersburg, Russia, May 2017.
- G. Marino, A. Solntsev, L. Xu, V. Gili, L. Carletti, A. N. Poddubny, D. Smirnova, H. Chen, G. Zhang, A. Zayats, C. De Angelis, G. Leo, Y. Kivshar, A. Sukhorukov, and D. N. Neshev, “Sum-Frequency Generation and Photon-Pair Creation in AlGaAs Nano-Scale Resonators”, CLEO 2017, San Jose, USA, May 2017.
- L. Carletti, L. Ghirardini, V. Gili, G. Pellegrini, L. Duò, M. Finazzi, D. Rocco, A. Locatelli, C. De Angelis, I. Favero, M. Ravaro, G. Leo, A. Lemaître, and M. Celebrano, “Polarization-resolved second harmonic generation measurements in AlGaAs monolithic nanoantennas”, CLEO-Europe, Munich, Germany, June 2017.
- G. Marino, C. McPollin, V. Gili, L. Carletti, C. De Angelis, G. Leo, A. V. Zayats, “Cathodoluminescence Imaging Spectroscopy of Single and Dimer AlGaAs Nano-disks”, CLEO-Europe, Munich, Germany, June 2017.
- L. Ghirardini, L. Carletti, V. Gili, G. Pellegrini, L. Duò, M. Finazzi, D. Rocco, A. Locatelli, C. De Angelis, I. Favero, M. Ravaro, G. Leo, A. Lemaître, and M. Celebrano, “Emission properties of second-harmonic generation in AlGaAs optical nanoantennas” (invited), META 2017, Seoul, South Korea, July 2017.
- V.F. Gili, D. Rocco, L. Ghirardini, L. Carletti, A. Locatelli, M. Celebrano, M. Finazzi, C. De Angelis, A. Lemaître, I. Favero, and G. Leo, “Second harmonic generation in AlGaAs nanodisk dimers”, NANOP 2017, Barcellona, Spain, October 2017.

- V. F. Gili, D. Rocco, L. Ghirardini, L. Carletti, A. Locatelli, M. Celebrano, M. Finazzi, C. De Angelis, A. Lemaître, I. Favero, and G. Leo, “Second-harmonic emission enhancement in monolithic AlGaAs-on-AlOx nano-dimers”, SPIE Nanophotonics Australasia, Melbourne, Australia, December 2017.
- D. Rocco, V. F. Gili, M. Celebrano, M. Finazzi, L. Ghirardini, L. Carletti, A. Locatelli, G. Leo, C. De angelis, “Enhanced second-harmonic generation from metal-dielectric hybrid nanoantennas”, SPIE Nanophotonics Australasia, Melbourne, Australia, December 2017.
- G. Marino, A. Solntsev, L. Xu, V. Gili, L. Carletti, A. N. Poddubny, D. Smirnova, H. Chen, G. Zhang, A. Zayats, C. De Angelis, G. Leo, Y. Kivshar, A. Sukhorukov, and D. N. Neshev, “Nonlinear AlGaAs nanodisks as sources of sum-frequency light and heralded photons”, ANZCOP 2017, Queenstown, New Zealand, December 2017
- G. Marino, A. Solntsev, L. Xu, V. Gili, L. Carletti, A. N. Poddubny, D. Smirnova, H. Chen, G. Zhang, A. Zayats, C. De Angelis, G. Leo, Y. Kivshar, A. Sukhorukov, and D. N. Neshev, “Sum-Frequency Generation and Creation of Photon Pairs In Nonlinear AlGaAs Nanodisks”, ICONN 2018, Wollongong, Australia, February 2018.
- V.F. Gili, “High-contrast monolithic photonic nanostructures in the AlGaAs-on-insulator platform”, (*invited*), Materials Congress 2018, Barcelona, Spain, June 2018.
- G. Marino, A. Solntsev, L. Xu, V. Gili, L. Carletti, A. N. Poddubny, D. Smirnova, H. Chen, G. Zhang, A. Zayats, C. De Angelis, G. Leo, Y. Kivshar, A. Sukhorukov, and D. N. Neshev, “Nonlinear AlGaAs nanodisks as sources of sum-frequency light and entangled photons”, META 2018, Marseille, France, June 2018.
- D. Rocco, V. Gili, L. Ghirardini, L. Carletti, I. Favero, A. Locatelli, G. Marino, D. Neshev, M. Celebrano, M. Finazzi, G. Leo, and C. De Angelis, “Nonradiating Modes for Tunable Second Harmonic Generation in AlGaAs Nanodimers”, Advanced Photonics 2018, Zurich, Switzerland, July 2018.
- L. Ghirardini, L. Carletti, V. Gili, G. Pellegrini, L. Duò, M. Finazzi, D. Rocco, A. Locatelli, C. De Angelis, I. Favero, I. Roland, G. Leo, A. Lemaître, and M. Celebrano, “Optical Switching of the Second

Harmonic Generation in AlGaAs Nanoantennas”, Advanced Photonics 2018, Zurich, Switzerland, July 2018.

- G. Marino, A. Solntsev, L. Xu, V. Gili, L. Carletti, A. N. Poddubny, D. Smirnova, H. Chen, G. Zhang, A. Zayats, C. De Angelis, G. Leo, Y. Kivshar, A. Sukhorukov, and D. N. Neshev, “Sum-Frequency- and Photon-Pair-Generation in AlGaAs Nano-Disks”, Advanced Photonics 2018, Zurich, Switzerland, July 2018.
- L. Ghirardini, L. Carletti, V. Gili, G. Marino, G. Pellegrini, L. Duò, M. Finazzi, D. Rocco, A. Locatelli, I. Favero, I. Roland, A. Lemaître, D. Neshev, G. Leo, C. De Angelis, and M. Celebrano, “Optimization and Control of the Second-Harmonic Generation in AlGaAs Dielectric Nanoantennas”, Plasmonica 2018 Workshop, Florence, Italy, July 2018.

Invited seminars

- V. F. Gili, “AlGaAs dielectric nonlinear optical nanoantennas”, Tor Vergata University, Rome, Italy, 22nd December 2016.
- V. F. Gili, “Nonlinear nanophotonics in AlGaAs-on-insulator monolithic platform”, CUDOS Workshop Nanophotonics 2018 - The Next Frontier, Canberra, Australia, 7th March 2018.
- V. F. Gili, “Monolithic AlGaAs-on-insulator platform for second order nonlinear nanophotonics”, Institute of Applied Optics, Jena, Germany, 5th September 2018.

Bibliography

- [1] E. Garmire, "Nonlinear optics in daily life", *Optics Express* 21, 25 (2013).
- [2] R. Piramidowicz, S. T. Stopinski, K. Lawniczuk, K. Welikow, P. Szczepanski, X. J. M. Leijtens, and M. K. Smit, "Photonic integrated circuits : a new approach to laser technology", *Bulletin of the Polish Academy of Sciences: Technical Sciences*, 60, 4 (2012).
- [3] R. N. Hall, G. E. Fenner, J. D. Kingsley, T. J. Soltys, and R. O. Carlson, "Coherent light emission from GaAs junctions", *Physical Review Letters* 9, 9, 366 (1962).
- [4] T. H. Maiman, "Stimulated optical radiation in ruby", *Nature* 187, 4736 (1960).
- [5] R. Braunstein, "Radiative transitions in semiconductors", *Physical Review* 99, 6, 18921893 (1955).
- [6] Editorial Board "Moore's deviation", *Nature Nanotechnology*, 12, 1105 (2017).
- [7] K. D. Choquette, K. M. Geib, C. I. H. Ashby, R. D. Twisten, O. Blum, H. Q. Hou, D. M. Follstaedt, B. E. Hammons, D. Mathes, and R. Hull, "Advances in selective wet oxidation of AlGaAs alloys", *IEEE Journal of Selected Topics in Quantum Electronics*, 3, 916 (1997).
- [8] B. Y. Nguyen, G. Celler, C. Mazuré, "A Review of SOI Technology and its Applications", *Journal of Integrated Circuits and Systems* 4, 2 (2009).
- [9] S. A. Maier "Plasmonics: fundamentals and applications", Springer 2007.

- [10] P. Lalanne, S. Astilean, P. Chavel, E. Cambril, and H. Launois, “Blazed binary subwavelength gratings with efficiencies larger than those of conventional échelette gratings”, *Optics Letters* 23, 14 (1998).
- [11] G. Biener, A. Niv, V. Kleiner, and E. Hasman, “Formation of helical beams by use of Pancharatnam-Berry phase optical elements” *Optics Letters* 27, 21 (2002)
- [12] U. Levy, C. H. Tsai, L. Pang, and Y. Fainman, “Engineering space-variant inhomogeneous media for polarization control”, *Optics Letters* 29, 15 (2004).
- [13] M. Khorasaninejad, W. T. Chen, R. C. Devlin, J. Oh, A. Y. Zhu, and F. Capasso, “Metalenses at visible wavelengths: Diffraction-limited focusing and subwavelength resolution imaging”, *Science* 352, 6290 (2016).
- [14] M. Decker, I. Staude, M. Falkner, J. Dominguez, D. N. Neshev, I. Brener, T. Pertsch, and Y. S. Kivshar, “High-Efficiency Dielectric Huygens Surfaces”, *Advanced Optical Materials* 3, 813 (2015).
- [15] A. Krasnok, M. Tymchenko, and A. Alú, “Nonlinear metasurfaces: a paradigm shift in nonlinear optics”, *Materials Today* 21, 1 (2018).
- [16] P. Franken, A. Hill, C. Peters, and G. Weinreich, “Generation of Optical Harmonics”, *Physical Review Letters* 7, 4, 118 (1961).
- [17] R. W. Boyd, “Nonlinear optics”, Burlington: Academic Press, 3rd edition (2008).
- [18] B. E. A. Saleh and M. C. Teich, “Fundamentals of photonics”, Series in Pure and Applied Optics, ed. Wiley. New York: John Wiley & Sons, Inc. (1991).
- [19] M. Tonouchi, “Cutting-edge terahertz technology”, *Nature Photonics* 1, 97 (2007).
- [20] A. N. Poddubny, I. V. Iorsh, A. A. Sukhorukov, “Generation of photon-plasmon quantum states in nonlinear hyperbolic metamaterials”, *Physical Review Letters* 117, 12, 123901 (2016).
- [21] S. P. Walborn, C. H. Monken, S. Pdua, P. H. Souto Ribeiro, “Spatial correlations in parametric down-conversion”, arXiv:1010.1236 [quant-ph] (2010).

- [22] N. Morais, I. Roland, M. Ravano, W. Hease, A. Lemaître, C. Gomez, S. Wabnitz, M. De Rosa, I. Favero, and G. Leo, “Directionally induced quasi-phase matching in homogeneous AlGaAs waveguides”, *Optics Letters* 42, 21 (2017).
- [23] S. Mariani, A. Andronico, A. Lemaître, I. Favero, S. Ducci, and G. Leo, “Second-harmonic generation in AlGaAs microdisks in the telecom range”, *Optics Letters* 39, 3062 (2014).
- [24] K. R. Parameswaran, J. R. Kurz, R. V. Roussev, and M. M. Fejer, “Observation of 99% pump depletion in single-pass second-harmonic generation in a periodically poled lithium niobate waveguide”, *Optics Letters* 27, 43 (2002).
- [25] S. Ducci, L. Lanco, V. Berger, A. De Rossi, V. Ortiz, and M. Calligaro, “Continuous-wave second-harmonic generation in modal phase matched semiconductor waveguides”, *Applied Physics Letters* 84, 2974 (2004).
- [26] H. C. Van de Hulst, “Light Scattering by Small Spheres”, Dover publications (1981).
- [27] C. F. Bohren and D. R. Huffman “Absorption and Scattering of Light by Small Particles”, New York: Wiley, 1983.
- [28] M. Quinten, “Optical Properties of Nanoparticle Systems: Mie and Beyond”, Wiley (2011).
- [29] A. Mirzaei and A. E. Miroshnichenko, “Electric and magnetic hotspots in dielectric nanowire dimers”, *Nanoscale* 7, 5963 (2015).
- [30] A. B. Evlyukhin, C. Reinhardt, and B. N. Chichkov, “Multipole light scattering by nonspherical nanoparticles in the discrete dipole approximation”, *Physical Review B* 84, 235429 (2011).
- [31] R. M. Bakker, D. Permyakov, Y. F. Yu, D. Markovich, R. Paniagua-Domínguez, L. Gonzaga, A. Samusev, Y. Kivshar, B. Luk’yanchuk, and A. I. Kuznetsov, “Magnetic and Electric Hotspots with Silicon Nanodimers”, *Nano Letters* 15, 2137 (2015).
- [32] L. Carletti, A. Locatelli, O. Stepanenko, G. Leo, and C. De Angelis, “Enhanced second-harmonic generation from magnetic resonance in AlGaAs nanoantennas,” *Optics Express* 23, 26544 (2015).

- [33] P. Grahn, A. Shevchenko, and M. Kaivola, “Electromagnetic multipole theory for optical nanomaterials”, *New Journal of Physics* 14, 093033 (2012).
- [34] S. Gehrsitz, F. K. Reinhart, C. Gourgon, N. Herres, A. Vonlanthen, and H. Sigg, “The refractive index of $\text{Al}_x\text{Ga}_{1-x}\text{As}$ below the band gap: accurate determination and empirical modeling”, *Journal of Applied Physics* 87, 11, 7825 (2000).
- [35] A. I. Kuznetsov, A. E. Miroshnichenko, Y. H. Fu, J. Zhang, and B. Lukyanchuk, “Magnetic Light”, *Scientific Reports* 2, 492 (2012).
- [36] Z. Yang, P. Chak, A. D. Bristow, H. M. van Driel, R. Iyer, J. S. Aitchison, A. L. Smirl, and J. E. Sipe, “Enhanced second-harmonic generation in AlGaAs microring resonators”, *Optics Letters* 32, 7, 826 (2007).
- [37] V. F. Gili, L. Carletti, A. Locatelli, D. Rocco, M. Finazzi, L. Ghirardini, I. Favero, C. Gomez, A. Lemaître, M. Celebrano, C. De Angelis, and G. Leo, “Monolithic AlGaAs second-harmonic nanoantennas”, *Optics Express* 24, 14 (2016).
- [38] R. Camacho-Morales, S. Kruk, M. Rahmani, L. Wang, L. Xu, D. Smirnova, A. Solntsev, A. Miroshnichenko, H. Tan, F. Karouta, S. Naureen, K. Vora, L. Carletti, C. De Angelis, C. Jagadish, Y. S. Kivshar, D. N. Neshev, “Nonlinear Generation of Vector Beams from AlGaAs Nanoantennas”, *Nano Letters* 16, 11, 7191 (2016).
- [39] S. Liu, M. B. Sinclair, S. Saravi, G. A. Keeler, Y. Yang, J. Reno, G. M. Peake, F. Setzpfandt, I. Staude, T. Pertsch, and I. Brener, “Resonantly Enhanced Second-Harmonic Generation Using III-V Semiconductor All-Dielectric Metasurfaces”, *Nano Letters* 16, 9 (2016).
- [40] P. Nordlander and E. Prodan, “Plasmon Hybridization in Nanoparticles near Metallic Surfaces” *Nano Letters* 4, 2209 (2004).
- [41] M. Kauranen, and A. V. Zayats, “Nonlinear Plasmonics”, *Nature Photonics* 6, 737 (2012).
- [42] F. X. Wang, F. J. Rodriguez, W. M. Albers, R. Ahorinta, J. E. Sipe, and M. Kauranen, “Surface and bulk contributions to the second-order nonlinear optical response of a gold film”, *Physical Review B* 80, 233402 (2009).

- [43] S. I. Anisimov, B. L. Kapeliovich, and T. L. Perelman, “Electron emission from metal surfaces exposed to ultrashort laser pulses”, *Sov. Phys. JETP* 39, 375 (1974).
- [44] N. Bloembergen, R. K. Chang, S. Jha, C. Lee, “Optical Second-Harmonic Generation in Reflection from Media with Inversion Symmetry”, *Physical Review* 174, 813 (1968).
- [45] G. Marino, P. Segovia, A. V. Krasavin, P. Ginzburg, N. Olivier, G. A. Wurtz, and A. V. Zayats, “Second-Harmonic Generation from Hyperbolic Plasmonic Nanorod Metamaterial Slab”, *Laser Photonics Review* 12, 1700189 (2018).
- [46] M. Celebrano, X. Wu, M. Baselli, S. Großmann, P. Biagioni, A. Locatelli, C. De Angelis, G. Cerullo, R. Osellame, B. Hecht, L. Duó, F. Ciccacci, and M. Finazzi, “Mode matching in multiresonant plasmonic nanoantennas for enhanced second harmonic generation”, *Nature Nanotechnology* 10, 412 (2015).
- [47] S. V. Boriskina, T. A. Cooper, L. Zeng, G. Ni, J. K. Tong, Y. Tsurimaki, Y. Huang, L. Meroueh, G. Mahan, and G. Chen, “Losses in plasmonics: from mitigating energy dissipation to embracing loss-enabled functionalities”, *arXiv:1802.01469* (2018).
- [48] M. L. Brongersma, N. J. Halas, and P. Nordlander, “Plasmon-induced hot carrier science and technology,” *Nature Nanotechnology* 10, 25 (2015).
- [49] M. Caldarola, P. Albella, E. Cortés, M. Rahmani, T. Roschuk, G. Grinblat, R. F. Oulton, A. V. Bragas, and S. A. Maier, “Non-plasmonic nanoantennas for surface enhanced spectroscopies with ultra-low heat conversion”, *Nature Communications* 6, 7915 (2015).
- [50] X. Huang, and M. A. El-Sayed, “Plasmonic photo-thermal therapy”, *Alexandria Journal of Medicine* 47, 1 (2011).
- [51] W. J. Padilla, A. J. Taylor, C. Highstrete, M. Lee, and R. D. Averitt, “Dynamical Electric and Magnetic Metamaterial Response at Terahertz Frequencies”, *Physical Review Letters* 96, 107401 (2006).
- [52] G. Grinblat, Y. Li, M. P. Nielsen, R. F. Oulton, and S. A. Maier, “Efficient Third Harmonic Generation and Nonlinear Subwavelength Imaging at a Higher-Order Anapole Mode in a Single Germanium Nanodisk”, *ACS Nano* 11, 953 (2017).

- [53] A. E. Miroschnichenko, A. B. Evlyukhin, Y. F. Yu, R. M. Bakker, A. Chipouline, A. I. Kuznetsov, B. Luk'yanchuk, B. N. Chichkov, and Y. S. Kivshar, "Nonradiating anapole modes in dielectric nanoparticles", *Nature Communications* 6, 8069 (2015).
- [54] V. Dubovik, and V. Tugushev, "Toroid moments in electrodynamics and solid-state physics". *Physics Reports* 187, 145 (1990).
- [55] D. Rocco, V. F. Gili, L. Ghirardini, L. Carletti, I. Favero, A. Locatelli, G. Marino, D. N. Neshev, M. Celebrano, M. Finazzi, G. Leo, and C. De Angelis, "Tuning the second-harmonic generation in AlGaAs nanodimers via non-radiative state optimization", *Photonics Research* 6, 5 (2018).
- [56] D. G. Baranov, R. Verre, P. Karpinski, and M. Käll, "Anapole-Enhanced Intrinsic Raman Scattering from Silicon Nanodisks" *ACS Photonics* 5, 2730 (2018).
- [57] J. S. T. Gongora, A. E. Miroschnichenko, Y. S. Kivshar, and A. Frat-alocchi, "Anapole nanolasers for mode-locking and ultrafast pulse generation", *Nature Communications* 8, 15535 (2017).
- [58] P. Frigeri, L. Seravalli, G. Trevisi, and S. Franchi, "3.12: Molecular Beam Epitaxy: An Overview", in P. Bhattacharya, R. Fornari, and H. Kamimura, "Comprehensive Semiconductor Science and Technology", Elsevier Amsterdam, pp. 480-522 (2011).
- [59] V. M. Donnelly, and A. Kornblit, "Plasma etching: Yesterday, today, and tomorrow", *Journal of Vacuum Science and Technology A: Vacuum, Surfaces and Films* 31, 050825 (2013).
- [60] M. Munsch, N.S. Malik, E. Dupuy, A. Delga, J. Bleuse, J. M. Gérard, J. Claudon, N. Gregersen, and J. Mørk, "Dielectric GaAs Antenna Ensuring an Efficient Broadband Coupling between an InAs Quantum Dot and a Gaussian Optical Beam", *Physical Review Letters* 111, 239902 (2013).
- [61] O. Kubaschewski, C. B. Alcock, and P. J. Spencer, "Materials Thermochemistry", Pergamon, United Kingdom, (1993).
- [62] C. I. H. Ashby, J. P. Sullivan, K. D. Choquette, K. M. Geib, and H. Q. Hou, "Wet oxidation of AlGaAs: the role of hydrogen", *Journal of Applied Physics* 82, 3134 (1997).

- [63] C. I. H. Ashby, M. M. Bridges, A. A. Allerman, B. E. Hammons, and H. Q. Hou, “Origin of the time dependence of wet oxidation of AlGaAs”, *Applied Physics Letters* 75, 1, 73 (1999).
- [64] A. R. Sugg, N. Holonyak Jr., J. E. Baker, F. A. Kish, and J. M. Dallesasse, “Native oxide stabilization of AlAs-GaAs heterostructures”, *Applied Physics Letters* 58, 1199 (1991).
- [65] S. K. Cheong, B. A. Bunker, T. Shibata, D. C. Hall, C. B. DeMelo, Y. Luo, G. L. Snider, G. Kramer, and N. El-Zein, “Residual arsenic site in oxidized Al_xGa_{1-x}As (x=0.96)”, *Applied Physics Letters* 78, 2458 (2001).
- [66] C. I. H. Ashby, J. P. Sullivan, P. P. Newcomer, N. A. Missert, H. Q. Hou, B. E. Hammons, M. J. Hafich, and A. G. Baca, “Wet oxidation of Al_xGa_{1-x}As: Temporal evolution of composition and microstructure and the implications for metal-insulator-semiconductor applications”, *Applied Physics Letters* 70, 18, 2443 (1997).
- [67] B. E. Deal and A. S. Grove “General Relationship for the Thermal Oxidation of Silicon”, *Journal of Applied Physics* 36, 3770 (1965).
- [68] P. Vaccaro, K. Koizumi, K. Fujita, and T. Ohachi, “AlAs oxidation process in GaAs/AlGaAs/AlAs heterostructures grown by molecular beam epitaxy on GaAs (n11)A substrates”, *Microelectronics Journal* 30, 4 (1999).
- [69] F. A. Kish, S. A. Maranowski, G. E. Höfler, N. Holonyak, S. J. Caracci, J. M. Dallesasse, and K. C. Hsieh, “Dependence on doping type (p/n) of the water vapor oxidation of high-gap Al_xGa_{1-x}As”, *Applied Physics Letters* 60, 25, 3165 (1992).
- [70] V. F. Gili, L. Carletti, F. Chouchane, G. Wang, C. Ricolleau, D. Rocco, A. Lemaître, I. Favero, L. Ghirardini, M. Finazzi, M. Celebrano, C. De Angelis, and G. Leo, “Role of the substrate in monolithic AlGaAs nonlinear nanoantennas”, *Nanophotonics* 7, 2 (2018).
- [71] O. Durand, F. Wyckzisk, J. Olivier, M. Magis, P. Galtier, A. De Rossi, M. Calligaro, V. Ortiz, V. Berger, G. Leo, and G. Assanto, “Contraction of aluminum oxide thin layers in optical heterostructures”, *Applied Physics Letters* 83, 13, 2554 (2003).
- [72] L. Novotny and B. Hecht, “Principles of Nano-Optics”, Cambridge: Cambridge University Press (2006).

- [73] M. Minsky, “Memoir on inventing the confocal scanning microscope”, *Scanning* 10, 128 (1988).
- [74] J. A. Kurvits, M. Jiang, and R. Zia, “Comparative analysis of imaging configurations and objectives for Fourier microscopy”, *Journal of the Optical Society of America A* 32, 11 (2015).
- [75] T. Coenen and N. M. Haegel, “Cathodoluminescence for the 21st century: Learning more from light”, *Applied Physics Reviews* 4, 031103 (2017).
- [76] T. Coenen, J. van de Groep, and A. Polman, “Resonant Modes of Single Silicon Nanocavities Excited by Electron Irradiation”, *ACS Nano* 7, 1689 (2013).
- [77] F. J. Garca de Abajo, “Optical excitations in electron microscopy”, *Review of Modern Physics* 82, 209 (2010).
- [78] J. van de Groep, T. Coenen, S. A. Mann, A. Polman, “Direct imaging of hybridized eigenmodes in coupled silicon nanoparticles”, *Optica* 3, 93 (2016).
- [79] A. Losquin and M. Kociak, “Link between Cathodoluminescence and Electron Energy Loss Spectroscopy and the Radiative and Full Electromagnetic Local Density of States”, *ACS Photonics* 2, 1619 (2015).
- [80] I. Shoji, T. Kondo, A. Kitamoto, M. Shirane, and R. Ito, “Absolute scale of second-order nonlinear-optical coefficients,” *Journal of the Optical Society of America B* 14, 2268 (1997).
- [81] M. Kongai, M. Sugimoto, and K. Takahashi, “High efficiency GaAs thin film solar cells by peeled film technology”, *Journal of Crystal Growth* 45, 277 (1978).
- [82] X. S. Wu, L. A. Coldren, and J. L. Merz, “Selective etching characteristics of HF for Al_xGa_{1-x}As/GaAs”, *Electronics Letters* 21, 13 (1985).
- [83] K. Lee, J. D. Zimmerman, X. Xiao, K. Sun, and S. R. Forrest, “Reuse of GaAs substrates for epitaxial lift-off by employing protection layers”, *Journal of Applied Physics* 111, 033527 (2012).
- [84] C. W. Cheng, K. T. Shiu, N. Li, S. J. Han, L. Shi, and D. K. Sadana, “Epitaxial lift-off process for gallium arsenide substrate reuse and flexible electronics”, *Nature Communications* 4, 1577 (2013).

- [85] S. Person, M. Jain, Z. Lapin, J. J. Sáenz, G. Wicks, and L. Novotny, “Demonstration of Zero Optical Backscattering from Single Nanoparticles”, *Nano Letters* 13, 1806 (2013).
- [86] M. Pu, L. Ottaviano, E. Semenova, and K. Yvind, “Efficient frequency comb generation in AlGaAs-on-insulator”, *Optica* 3, 8 (2016).
- [87] D. E. Aspnes, S. M. Kelso, R. A. Logan and R. Bhat, “Optical properties of Al_xGa_{1-x}As”, *Journal of Applied Physics* 60, 754 (1986).
- [88] K. Dolgaleva, W. C. Ng, L. Qian, and J. S. Aitchison, “Compact highly-nonlinear AlGaAs waveguides for efficient wavelength conversion”, *Optics Express* 19, 13 (2011).
- [89] D. Duchesne, K. A. Rutkowska, M. Volatier, F. Légaré, S. Delprat, M. Chaker, D. Modotto, A. Locatelli, C. De Angelis, M. Sorel, D. N. Christodoulides, G. Salamo, R. Arés, V. Aimez, and R. Morandotti, “Second harmonic generation in AlGaAs photonic wires using low power continuous wave light”, *Optics Express* 19, 13 (2011).
- [90] S. Liu, G. A. Keeler, J. L. Reno, M. B. Sinclair, and I. Brener, “III-V Semiconductor Nanoresonators-A New Strategy for Passive, Active, and Nonlinear AllDielectric Metamaterials”, *Advanced Optical Materials* 4, 10, 1457 (2016).
- [91] S. Mariani, A. Andronico, A. Lemaître, I. Favero, S. Ducci, and G. Leo, “Second-harmonic generation in AlGaAs microdisks in the telecom range”, *Optics Letters* 39, 10 (2014).
- [92] G. Leo, O. Stepanenko, and A. Lemaître, “Procédé de fabrication d’au moins une structure semi-conductrice présentant un empilement d’une ou de plusieurs couches d’Arséniure de Gallium-Aluminium”, *French Patent FR16 70043* (2016).
- [93] J. Leuthold, C. Koos, and W. Freude, “Nonlinear silicon photonics” *Nature Photonics* 4, 535 (2010).
- [94] J. H. Kim, D. H. Lim, K. S. Kim, G. M. Yang, K. Y. Lim, and H. J. Lee, “Lateral wet oxidation of Al_xGa_{1-x}As-GaAs depending on its structures”, *Applied Physics Letters* 69, 3357 (1996).
- [95] T. Langenfelder, St. Schröder, and H. Grothe, “Lateral oxidation of buried Al_xGa_{1-x}As layers in a wet ambient”, *Journal of Applied Physics* 82, 3548 (1997).

- [96] J. M. Dallesasse, N. Holonyak, A. R. Sugg, T. A. Richard, and N. ElZein, “Hydrolyzation oxidation of $\text{Al}_x\text{Ga}_{1-x}\text{As}/\text{AlAs}/\text{GaAs}$ quantum well heterostructures and superlattices”, *Applied Physics Letters* 57, 2844 (1990).
- [97] H. Nickel, “A detailed experimental study of the wet oxidation kinetics of $\text{Al}_x\text{Ga}_{1-x}\text{As}$ layers”, *Journal of Applied Physics* 78, 5201 (1995).
- [98] L. Scaccabarozzi, M. Fejer, Y. Huo, S. Fan, X. Yu et J. Harris, “Enhanced second-harmonic generation in $\text{AlGaAs}/\text{Al}_x\text{O}_y$ tightly confining waveguides and resonant cavities”, *Optics Letters* 31, 3626 (2006).
- [99] T. W. Kim, T. Matsushita, T. Kondo, “Phase-matched second-harmonic generation in thin rectangular high-index-contrast AlGaAs waveguides”, *Applied Physics Express* 4, 082201 (2011).
- [100] F. Chouchane, G. Almuneau, N. Cherkashin, A. Arnoult, G. Lacoste, and C. Fontaine, “Local stress-induced effects on $\text{AlGaAs}/\text{AlO}_x$ oxidation front shape”, *Applied Physics Letters* 105, 041909 (2014).
- [101] T. Matsushita, Y. Nakamura, S. Matsumoto, T. Onda, I. Shoji, and T. Kondo, “Fabrication of $\text{AlGaAs}/\text{AlO}_x$ waveguides with inversion-stacked core structure for higher-order modal-phase matching devices”, 2013 IEEE Conference on Lasers and Electro-Optics Pacific Rim (CLEO-PR), Kyoto, June 30-July 4 2013.
- [102] Y. Lou and D. C. Hall, “Low-loss nonselectively oxidized $\text{Al}_x\text{Ga}_{1-x}\text{As}$ heterostructure waveguides”, *Applied Physics Letters* 93, 261111 (2008).
- [103] M. Savanier, C. Ozanam, L. Lanco, X. Lafosse, A. Andronico, I. Favero, S. Ducci, and G. Leo, “Near-infrared optical parametric oscillator in a III-V semiconductor waveguide”, *Applied Physics Letters* 103, 261105 (2013).
- [104] A. Gondarenko, J. S. Levy, and M. Lipson, “High confinement micron-scale silicon nitride high Q ring resonator”, *Optics express* 17, 14, 11366 (2009).
- [105] G. A. Porkolab, P. Apiratikul, B. Wang, S. H. Guo, and C. H. Richardson, “Low propagation loss AlGaAs waveguides fabricated with plasma-assisted photoresist reflow”, *Optics Express* 22, 7 (2014).

- [106] W. Erfurth, A. Thompson, and N. Ünal, “Electron dose reduction through improved adhesion by cationic organic material with HSQ resist on an InGaAs multilayer system on GaAs substrate”, Proceedings of SPIE 8682, Advances in Resist Materials and Processing Technology, 86821Z (March 29, 2013).
- [107] T. Shibanuma, G. Grinblat, P. Albella, and S. A. Maier, “Efficient Third Harmonic Generation from Metal-Dielectric Hybrid Nanoantennas”, Nano Letters 17, 2647 (2017).
- [108] I. Horcas and R. Fernández, “WSXM: A software for scanning probe microscopy and a tool for nanotechnology”, Review on Scientific Instruments 78, 013705 (2007).
- [109] Y. Kohno, E. Okunishi, T. Tomita, I. Ishikawa, T. Kaneyama, Y. Ohkura, Y. Kondo, and T. Isabell, “Long-range chemical orders in Au-Pd nanoparticles revealed by aberration-corrected electron microscopy”, Microscopy and Analysis Supplement, 24, S9 (2010).
- [110] M. Haider, S. Uhlemann, E. Schwan, H. Rose, B. Kabius, and K. Urban, “Electron microscopy image enhanced”, Nature 392, 768 (1998).
- [111] C. Ricolleau, J. Nelayah, T. Oikawa, Y. Kohno, N. Braidy, G. Wang, F. Hue, I. Florea, V. Pierron Bohnes and D. Alloyeau, “Performances of an 80-200 kV microscope employing a cold-FEG and an aberration-corrected objective lens.”, Journal of Electron Microscopy 62, 283 (2012).
- [112] Micro Resist Technology, “Negative Tone Photoresist Series ma-N 2400 - Processing guidelines”.
- [113] L. Ghirardini, L. Carletti, V. F. Gili, G. Pellegrini, L. Duó, M. Finazzi, D. Rocco, A. Locatelli, C. De Angelis, I. Favero, M. Ravaro, G. Leo, A. Lemaître, and M. Celebrano, “Polarization properties of second-harmonic generation in AlGaAs optical nanoantennas”, Optics Letters 42, 3 (2017).
- [114] C. Schrieffer, C. Bohley, and R. B. Wehrspohn, “Strain dependence of second-harmonic generation in silicon”, Optics Letters 35, 3, 273 (2010).
- [115] M. Cazzanelli, F. Bianco, E. Borga, G. Pucker, M. Ghulinyan, E. Degoli, E. Luppi, V. Véniard, S. Ossicini, D. Modotto, S. Wabnitz, R.

- Pierobon, and L. Pavesi, “Second-harmonic generation in silicon waveguides strained by silicon nitride”, *Nature Materials* 11, 148 (2012).
- [116] C. Schriever, F. Bianco, M. Cazzanelli, M. Ghulinyan, C. Eisenschmidt, J. de Boor, A. Schmid, J. Heitmann, L. Pavesi, and J. Schilling, “Second-order optical nonlinearity in silicon waveguides: Inhomogeneous stress and interfaces”, *Advanced Optical Materials* 3, 129 (2015).
- [117] J. J. Wynne, and N. Bloembergen, “Measurement of the Lowest-Order Nonlinear Susceptibility in III-V Semiconductors by Second-Harmonic Generation with a CO₂ Laser”, *Physical Review B. Solid State* 2, 10, 4306 (1970).
- [118] S. Adachi, “GaAs and related materials: bulk semiconducting and superlattice properties”, *World Scientific* (1994).
- [119] L. Carletti, D. Rocco, A. Locatelli, C. De Angelis, V. F. Gili, M. Ravaro, I. Favero, G. Leo, M. Finazzi, L. Ghirardini, M. Celebrano, G. Marino, and A. V. Zayats, “Controlling second-harmonic generation at the nanoscale with monolithic AlGaAs-on-AlO_x antennas”, *Nanotechnology* 28, 114005 (2017).
- [120] L. Carletti, A. Locatelli, D. N. Neshev, and C. De Angelis, “Shaping the radiation pattern of second-harmonic generation from AlGaAs dielectric nanoantennas”, *ACS Photonics* 3, 1500 (2016).
- [121] K. Iwaszczuk, C. Bisgaard, A. Andronico, G. Leo, and P. U. Jepsen, “Numerical investigation of terahertz emission properties of microring difference-frequency resonators”, *IEEE Transactions on THz Sci. Technol.* 3, 192 (2013).
- [122] M. Kerker, D. S. Wang, and C. L. Giles, “Electromagnetic scattering by magnetic spheres”, *Journal of the Optical Society of America* 73, 765 (1983).
- [123] R. Alaei, R. Filer, D. Lehr, F. Lederer, and C. A. Rockstuhl, “Generalized Kerker condition for highly directive nanoantennas”, *Optics Letters* 40, 2645 (2015).
- [124] L. Carletti, G. Marino, L. Ghirardini, V. F. Gili, D. Rocco, I. Favero, A. Locatelli, A. V. Zayats, M. Celebrano, M. Finazzi, G. Leo, C. De Angelis, and D. N. Neshev, “Nonlinear goniometry by second harmonic generation in AlGaAs nanoantennas”, *ACS Photonics* 5, 4386 (2018).

- [125] T. Ichimura, T. Jin, H. Fujita, H. Higuchi, and T. M. Watanabe, “Nano-scale measurement of biomolecules by optical microscopy and semiconductor nanoparticles”, *Frontiers Physiol.* 5, 273 (2014).
- [126] D. Rocco, L. Carletti, A. Locatelli, C. De Angelis, V. F. Gili, and G. Leo, “Modelling And Optimization Of The Second-Harmonic Radiation Pattern In Dielectric Nanoantennas”, *European Conference on Modelling and Simulation*, Regensburg, Germany, June 2016.
- [127] L. Ghirardini, G. Marino, V. F. Gili, I. Favero, D. Rocco, L. Carletti, A. Locatelli, C. De Angelis, M. Finazzi, M. Celebrano, D. N. Neshev, and G. Leo, “Shaping the nonlinear emission pattern of a dielectric nanoantenna by holographic gratings”, *Nano Letters* 18, 6750 (2018).
- [128] T. Shibanuma, G. Grinblat, P. Albella, and S. A. Maier, “Efficient Third Harmonic Generation from MetalDielectric Hybrid Nanoantennas”, *Nano Letters* 17, 2647 (2017).
- [129] D. Bouchet, M. Mivelle, J. Proust, B. Gallas, I. Ozerov, M. F. Garcia-Parajo, A. Gulinatti, I. Rech, Y. De Wilde, N. Bonod, V. Krachmalnicoff, and S. Bidault, “Enhancement and inhibition of spontaneous photon emission by resonant silicon nanoantennas”, *Physical Review Applied* 6, 064016 (2016).
- [130] D. Rocco, L. Carletti, A. Locatelli, and C. De Angelis, “Controlling the directivity of all-dielectric nanoantennas excited by integrated quantum emitters,” *Journal of the Optical Society of America B* 34, 1918 (2017).
- [131] C. E. Talley, J. B. Jackson, C. Oubre, N. K. Grady, C. W. Hollars, S. M. Lane, T. R. Huser, P. Nordlander, and N. J. Halas, “Surface-Enhanced Raman Scattering from Individual Au Nanoparticles and Nanoparticle Dimer Substrates”, *Nano Letters* 5, 8, 1569 (2005).
- [132] M. Decker, T. Pertsch, and I. Staude, “Strong coupling in hybrid metaldielectric nanoresonators”, *Philosophical Transactions of the Royal Society A* 375, 20160312 (2017).
- [133] R. Guo, E. Rusak, I. Staude, J. Dominguez, M. Decker, C. Rockstuhl, I. Brener, D. N. Neshev, and Y. S. Kivshar, “Multipolar Coupling in Hybrid Metal-Dielectric Metasurfaces”, *ACS Photonics* 3, 349 (2016).
- [134] F. Timpu, N. R. Hendricks, M. Petrov, S. Ni, C. Renaut, H. Wolf, L. Isa, Y. S. Kivshar, and R. Grange, “Enhanced Second-Harmonic

- Generation from Sequential Capillarity-Assisted Particle Assembly of Hybrid Nanodimers”, *Nano Letters* 17, 9 (2017).
- [135] V. F. Gili, L. Ghirardini, D. Rocco, G. Marino, I. Favero, I. Roland, G. Pellegrini, L. Duò, M. Finazzi, L. Carletti, A. Locatelli, A. Lemaître, D. N. Neshev, C. De Angelis, G. Leo, and M. Celebrano, “Metal-dielectric hybrid nanoantennas for efficient frequency conversion at the anapole mode”, *Beilstein Journal of Nanotechnology* 9, 2306 (2018).
- [136] A. Orieux, A. Eckstein, A. Lemaître, P. Filloux, I. Favero, G. Leo, T. Coudreau, A. Keller, P. Milman, and S. Ducci, “Direct Bell states generation on a III-V semiconductor chip at room temperature”, *Physical Review Letters* 110, 160502 (2013).
- [137] F. Boitier, A. Orieux, C. Autebert, A. Lemaître, E. Galopin, C. Manquest, C. Sirtori, I. Favero, G. Leo, and S. Ducci, “Electrically injected photon-pair source at room temperature”, *Physical Review Letters* 112, 18, 183901 (2014).
- [138] P. Senellart, G. Solomon, and A. White, “High-performance semiconductor quantum-dot single-photon sources”, *Nature Nanotechnology* 12, 1026 (2017).
- [139] X. S. Ma, S. Zotter, J. Kofler, T. Jennewein, and A. Zeilinger, “Experimental generation of single photons via active multiplexing”, *Physical Review A* 83, 043814 (2011).
- [140] N. Somaschi, V. Giesz, L. De Santis, J. C. Loredó, M. P. Almeida, G. Hornecker, S. L. Portalupi, T. Grange, C. Anton, J. Demory, C. Gomez, I. Sagnes, N. D. Lanzillotti-Kimura, A. Lemaître, A. Auffeves, A. G. White, L. Lanco, and P. Senellart, “Near-optimal single-photon sources in the solid state”, *Nature Photonics* 10, 340 (2016).
- [141] F. Lenzini, A. N. Poddubny, J. Titchener, P. Fisher, A. Boes, S. Kастure, B. Haylock, M. Villa, A. Mitchell, A. S. Solntsev, A. A. Sukhorukov, and M. Lobino, “Direct characterization of a nonlinear photonic circuits wave function with laser light”, *Light: Science and Applications* 7, 17143 (2018).
- [142] G. Marino, A.S. Solntsev, L. Xu, V. F. Gili, L. Carletti, A. N. Poddubny, M. Rahmani, D. A. Smirnova, H. Chen, G. Zhang, A. V. Zayats, C. De Angelis, G. Leo, A. A. Sukhorukov, and D. N. Neshev, “Optical nanoantenna for nonlinear generation of heralded photons”, submitted.

- [143] R. Hanbury Brown and R. Q. Twiss, “Correlations between photons in two coherent beams of light”, *Nature* 177, 27 (1956).
- [144] E. B. Flagg, S. V. Polyakov, T. Thomay, and G. S. Solomon, “Dynamics of nonclassical light from a single solid-state quantum emitter”, *Physical Review Letters* 109, 163601 (2012).
- [145] X. Guo, C. L. Zou, C. Schuck, H. Jung, R. S. Cheng, and H. X. Tang, “Parametric down-conversion photon-pair source on a nanophotonic chip”, *Light: Science and Applications* 6, e16249 (2017).
- [146] M. S. Dresselhaus, G. Dresselhaus, and A. Jorio, “Group Theory. Application to the Physics of Condensed Matter”, Springer (2008).
- [147] D. Magde, R. Wong R, and P. G. Seybold, “Fluorescence quantum yields and their relation to lifetimes of Rhodamine 6G and fuorescein in nine solvents: improved absolute standards for quantum yields”, *Photochemical Photobiology* 75, 327 (2002).
- [148] J. P. Gordon, R. C. C. Leite, R. S. Moore, S. P. S. Porto, and J. R. Whinnery, “Long-Transient Effects in Lasers with Inserted Liquid Samples”, *Journal of Applied Physics* 36, 3 (1965).
- [149] C. P. T. McPolin, G. Marino, A. V. Krasavin, V. F. Gili, L. Carletti, C. De Angelis, G. Leo, and A. V. Zayats, “Imaging Electric and Magnetic Modes and their Hybridization in Single and Dimer AlGaAs Nanoantennas”, *Advanced Optical Materials*, 1800664 (2018).
- [150] B. H. Bransden and C. J. Joachain, “Physics of atoms and molecules”, Harlow : Prentice (2003).
- [151] A. E. Miroshnichenko, S. Flach, and Y. S. Kivshar, “Fano resonances in nanoscale structures”, *Reviews of Modern Physics* 82, 3, 2257 (2010).
- [152] Y. Yang, W. Wang, A. Boulesbaa, I. I. Kravchenko, D. P. Briggs, A. Puretzky, D. Geohegan, and J. Valentine, “Nonlinear Fano-Resonant Dielectric Metasurfaces”, *Nano Letters* 15, 11 (2015).
- [153] K. E. Chong, H. W. Orton, I. Staude, M. Decker, A. E. Miroshnichenko, I. Brener, Y. S. Kivshar, and D. N. Neshev, “Refractive index sensing with Fano resonances in silicon oligomers”, *Philosophical Transactions of the Royal Society A* 375, 2090 (2017).

- [154] L. Carletti, K. Koshelev, C. De Angelis, and Y. Kivshar, “Giant Non-linear Response at the Nanoscale Driven by Bound States in the Continuum”, *Physical Review Letters* 121, 033903 (2018).
- [155] M. R. Shcherbakov, D. N. Neshev, B. Hopkins, A. S. Shorokhov, I. Staude, E. V. Melik-Gaykazyan, M. Decker, A. A. Ezhov, A. E. Miroshnichenko, I. Brener, A. A. Fedyanin, and Y. S. Kivshar, “Enhanced Third-Harmonic Generation in Silicon Nanoparticles Driven by Magnetic Response”, *Nano Letters* 14, 6488 (2014).
- [156] M. R. Shcherbakov, A. Shorokhov, D. N. Neshev, B. Hopkins, I. Staude, E. V. Melik-Gaykazyan, A. A. Ezhov, A. E. Miroshnichenko, I. Brener, A. A. Fedyanin, and Y. S. Kivshar, “Nonlinear Interference and Tailorable Third-Harmonic Generation from Dielectric Oligomers”, *ACS Photonics* 2, 578 (2015).
- [157] G. Grinblat, Y. Li, M. P. Nielsen, R. F. Oulton, and S. A. Maier, “Degenerate Four-Wave Mixing in a Multiresonant Germanium Nanodisk”, *ACS Photonics* 4, 2144 (2017).
- [158] F. Timpu, A. Sergeyev, N. R. Hendricks, and R. Grange, “Second-Harmonic Enhancement with Mie Resonances in Perovskite Nanoparticles”, *ACS Photonics* 4, 76 (2016).
- [159] J. H. Epple, K. L. Chang, G. W. Pickrell, K. Y. Cheng, and K.C. Hsieh, “Thermal wet oxidation of GaP and Al_{0.4}Ga_{0.6}P”, *Applied Physics Letters* 77, 1161 (2000).
- [160] J. Cambiasso, G. Grinblat, Y. Li, A. Rakovich, E. Cortés, and S. A. Maier, “Bridging the Gap between Dielectric Nanophotonics and the Visible Regime with Effectively Lossless Gallium Phosphide Antennas”, *Nano Letters* 17, 1219 (2017).
- [161] J. Sautter, I. Staude, M. Decker, E. Rusak, D. N. Neshev, I. Brener, and Y. S. Kivshar, “Active tuning of All-Dielectric Metasurfaces”, *ACS Nano* 9, 4308 (2015).
- [162] A. Komar, Z. Fang, J. Bohn, J. Sautter, M. Decker, A. E. Miroshnichenko, T. Pertsch, I. Brener, Y. S. Kivshar, I. Staude, and D. N. Neshev, “Electrically tunable all-dielectric optical metasurfaces based on liquid crystals”, *Applied Physics Letters* 110, 071109 (2017).